Advances in Mechanics of Solids

In Memory of Prof. E. M. Haseganu

Ardéshir Guran • Andrei L Smirnov
David J Steigmann • Rémi Vaillancourt

SERIES ON STABILITY, VIBRATION AND CONTROL OF SYSTEMS

Series B

Volume 15

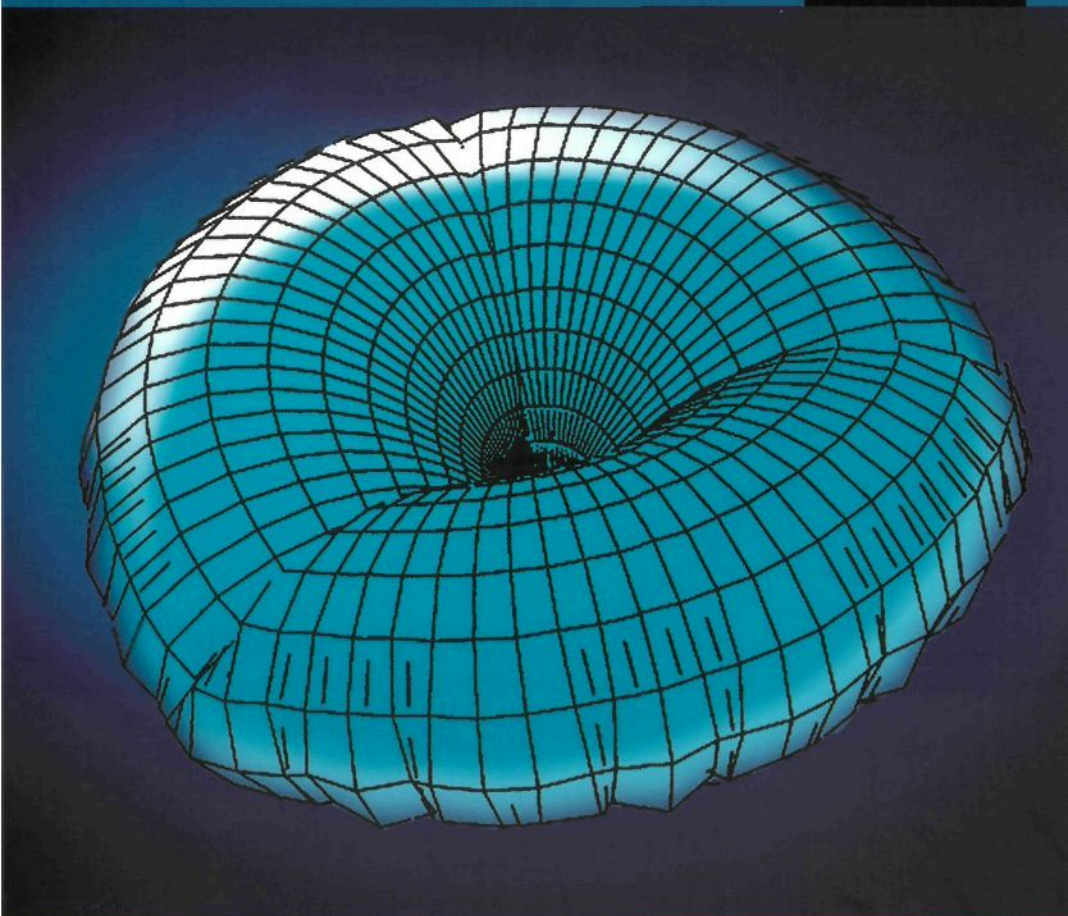

World Scientific

Advances in Mechanics of Solids

SERIES ON STABILITY, VIBRATION AND CONTROL OF SYSTEMS

Founder and Editor: Ardéshir Guran
Co-Editors: M. Cloud & W. B. Zimmerman

About the Series

Rapid developments in system dynamics and control, areas related to many other topics in applied mathematics, call for comprehensive presentations of current topics. This series contains graduate level textbooks, monographs, and collection of thematically organized research or pedagogical articles addressing key topics in applied dynamics.

The material is ideal for a general scientific and engineering readership, and is also mathematically precise enough to be a useful reference for research specialists in mechanics and control, nonlinear dynamics, and in applied mathematics and physics.

Reporting on academic/industrial research from institutions around the world, the SVCS series reflects technological advances in mechanics and control. Particular emphasis is laid on emerging areas such as modeling of complex systems, bioengineering, mechatronics, structronics, fluidics, optoelectronic sensors, micromachining techniques, and intelligent system design.

Selected Volumes in Series A

Vol. 12 The Calculus of Variations and Functional Analysis: With Optimal Control and Applications in Mechanics
Authors: L. P. Lebedev and M. J. Cloud

Vol. 13 Multiparameter Stability Theory with Mechanical Applications
Authors: A. P. Seyranian and A. A. Mailybaev

Vol. 14 Stability of Stationary Sets in Control Systems with Discontinuous Nonlinearities
Authors: V. A. Yakubovich, G. A. Leonov and A. Kh. Gelig

Vol. 15 Process Modelling and Simulation with Finite Element Methods
Author: W. B. J. Zimmerman

Vol. 16 Design of Nonlinear Control Systems with the Highest Derivative in Feedback
Author: V. D. Yurkevich

Vol. 17 The Quantum World of Nuclear Physics
Author: Yu. A. Berezhnoy

Selected Volume in Series B

Vol. 14 Impact and Friction of Solids, Structures and Intelligent Machines
Editor: A. Guran

SERIES ON STABILITY, VIBRATION AND CONTROL OF SYSTEMS

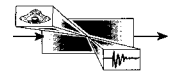

Series B Volume 15

Founder & Editor: **Ardéshir Guran**

Co-Editors: **M. Cloud & W. B. Zimmerman**

Advances in Mechanics of Solids

In Memory of Prof. E. M. Haseganu

Ardéshir Guran
Technical University of Graz, Austria

Andrei L Smirnov
St. Petersburg State University, Russia

David J Steigmann
University of California, Berkeley, USA

Rémi Vaillancourt
University of Ottawa, Canada

World Scientific

NEW JERSEY • LONDON • SINGAPORE • BEIJING • SHANGHAI • HONG KONG • TAIPEI • CHENNAI

Published by

World Scientific Publishing Co. Pte. Ltd.

5 Toh Tuck Link, Singapore 596224

USA office: 27 Warren Street, Suite 401-402, Hackensack, NJ 07601

UK office: 57 Shelton Street, Covent Garden, London WC2H 9HE

British Library Cataloguing-in-Publication Data

A catalogue record for this book is available from the British Library.

ADVANCES IN MECHANICS OF SOLIDS: IN MEMORY OF PROF. E. M. HASEGANU

ISBN 981-256-867-0

Printed in Singapore by World Scientific Printers (S) Pte Ltd

Eliza M. Haseganu (1940–2002)

This page is intentionally left blank

PREFACE

This volume is dedicated to the memory of Professor Eliza Maria Haseganu (1940-2002). Eliza was a highly regarded researcher and a meticulous and devoted teacher. She was also a warm and loving friend to many, including those whose work appears in these pages.

Educated in Romania, Professor Haseganu obtained her Diploma in Mechanical Engineering at the Polytechnic Institute of Brasov and had nearly finished her doctoral work when the political situation forced her to emigrate. She made a new start at the University of Alberta in Edmonton, Canada, and finally, in 1994, earned her doctorate under the supervision of D. Steigmann. Her thesis is entitled: *Analytical Investigation of Tension Fields in Lightweight Membrane Structures.*

In August of 1994 Eliza joined the Department of Mechanical and Industrial Engineering at Concordia University in Montréal, where she earned a tenured position shortly before her passing. Over the course of this brief period she published about 30 research papers in internationally recognized journals and conference proceedings. She also supervised one Ph.D. student and five MSc students.

Eliza's research and teaching activities were focused in the areas of Solid Mechanics, Structural Mechanics, Dynamics, Computational Mechanics and Biomechanics. She made her main research contributions to the field of Finite Elasticity, specializing in the nonlinear mechanics of thin shells and membranes. She made particularly important contributions to the development of robust numerical methods for ill-conditioned problems with emphasis on structural fabrics and stressed biological tissues.

Professor Haseganu had intended to publish additional results from her dissertation research on the deformations of highly elastic wrinkled membranes under pressure. These are very striking and reproduce a number of unusual and unexpected effects observed in experiments. Unfortunately, she delayed publication in the expectation that she would find sufficient time

to refine some of her more important analyses. A number of these results are presented on her behalf in Chapter 1 of this volume.

In her final years Eliza worked on the development of asymptotic techniques for the vibration and buckling analysis of thin-walled structural elements composed of composite materials. This body of work is described in three papers of the present collection.

Eliza's great warmth and extraordinary personal dedication permeated all aspects of her life and work. She is remembered as a most caring and devoted teacher with a genuine regard for the success and welfare of her students. In recognition of her great distinction in teaching, she was awarded the Department of Mechanical and Industrial Engineering Certificate of Recognition for Outstanding Teaching Excellence in 1997, The Concordia Council on Student Life Teaching Excellence Award in 1998, and the Faculty of Engineering and Computer Science award in 2000. For several years Professor Haseganu served as the Faculty Advisor to the Concordia Student Branch of the Canadian Society for Mechanical Engineers (CSME). With great pride she awarded the CSME Gold Medal to the most outstanding graduates in Mechanical Engineering. In addition, Eliza was often invited to speak on the subject of Women in Science and actively encouraged women to pursue engineering careers.

At the time of her passing, Eliza was planning a sabbatical leave to be spent in Russia. Tragically, she succumbed to cancer at the age of 62. She is warmly remembered and dearly missed by her colleagues, students and friends.

The Editors

CONTENTS

PART 1

Vibrations and Stability of Thin Structures

This page is intentionally left blank

CHAPTER 1

ELIZA HASEGANU'S ANALYSIS OF WRINKLING IN PRESSURIZED MEMBRANES

David J. Steigmann

Department of Mechanical Engineering, University of California Berkeley, CA 94720 USA

E-mail: steigman@me.berkeley.edu

Eliza Haseganu intended to publish results from her dissertation research on the numerical solution of highly elastic wrinkled membranes under pressure. These are quite striking and reproduce unusual and unexpected features observed in experiments. Her numerical analysis was sufficiently robust to achieve this without the need for any special measures. However, she delayed publication in the expectation that she would find the time to refine some of her more important analyses to take the effect of self contact of the membrane into account. Eliza's results are presented here on her behalf.

1.1. Introduction

This brief tribute to Dr. Eliza Haseganu collects some results contained in her thesis which would certainly have formed the basis of a substantial and influential paper, had she lived to prepare it. As her thesis adviser, I am both honoured and saddened to have the opportunity to summarize this body of work here on her behalf. Most of the essential details regarding the formulation and solution of mixed traction/displacement membrane boundary-value problems are summarized in her paper which appeared some years ago [Haseganu and Steigmann (1994)][1] and which has been cited quite frequently in the interim. In it she set a standard for the numerical analysis of wrinkling in finitely deformed membranes which has not been surpassed.

Eliza's achievement was the development and implementation of a numerical scheme for solving the ill-conditioned equilibrium equations generated by Pipkin's *relaxed* strain-energy function [Pipkin (1986)][2]. The re-

laxed formulation is motivated by the fact that the conventional theory admits compressive stresses in equilibrium. Although admissible in conventional two- and three-dimensional elasticity, in the setting of membrane theory such a state violates strong ellipticity, a well-known necessary condition for the existence of stable (energy-minimizing) equilibria. To rectify this Pipkin showed how to construct energy-minimizing sequences of deformations from the conventional strain energy which contain ever-more finely spaced wrinkles. The limit of such a sequence is a smooth deformation without compressive stress, and the strain energy function attributed to such a state, the so-called relaxed energy, may be used in place of the original when formulating equations of equilibrium. The relaxed energy also possesses certain convexity properties which are central to existence theorems based on the direct methods of the calculus of variations. In this way the problematic existence issue associated with membrane theory is addressed while the merits of its relatively simplicity are retained.

The obvious alternative to relaxation is to regularize the equations by including higher-order gradient (curvature) terms in the strain-energy function. This is tantamount to using a kind of shell theory in place of membrane theory. The advantage is that a length scale is built directly into the differential equations which effectively determines the wavelengths of wrinkles. Further, the energetic penalty associated with curvature sets a lower bound to the wavelength. This is clearly more realistic than the idealizations inherent in relaxed membrane theory; there the absence of bending resistance implies the absence of a lower bound and thus that wrinkles are continuously distributed over the surface. Fortunately, the associated equilibrium equations are statically determinate; therefore the stress distribution in a wrinkled region is insensitive to the details of the deformation and hence to the errors incurred in its description by using relaxed membrane theory. However, offsetting the advantages of relaxed membrane theory is the fact that the absence of stress in certain connected regions of strain space implies an absence of stiffness also, so that conventional stiffness-based solution strategies for the computation of equilibria are not effective. To overcome this difficulty, Eliza embedded the (relaxed) equilibrium problem into an artificial damped dynamical problem, constructed in such a way that the desired equilibria are globally and asymptotically stable relative to arbitrary initial data. One then discretizes this system in time using a simple difference scheme. Temporal accuracy is not an issue since it is only the asymptotic states which are of interest. This allows the use of simple explicit finite difference operators with mass-proportional damping to achieve

an efficient vectorized system for computations.

In this paper I describe the adjustments to Eliza's earlier work [Haseganu and Steigmann (1994)][1] needed to accommodate pressure loading. The basic formulation of relaxed membrane theory is described in section 2. The numerical method and the Lyapunov function associated with conservative pressure loads are discussed in section 3. Section 4 is devoted to specific simulations taken from Eliza's thesis. These examples, which are quite striking, illustrate her considerable achievement in this challenging branch of computational finite elasticity.

1.2. Relaxed Membrane Theory

The equilibrium equations for membranes, regarded as two-dimensional continua, have a simple structure identical to those for conventional bulk continua. For convenience, and with no essential loss of generality, I use a plane Ω as reference, which is here regarded as an unstressed configuration of the membrane. Let $\mathbf{e}_\alpha$, $\alpha = 1, 2$, be orthogonal unit vectors spanning (the translation space of) Ω, and let $\mathbf{e}_3 = \mathbf{e}_1 \times \mathbf{e}_2$. We use the usual summation convention with Greek subscripts taking values in $\{1, 2\}$ and Latin in $\{1, 2, 3\}$. Then the equilibrium equations in vector form are

$$\operatorname{div} \mathbf{T} + pJ\mathbf{n} = \mathbf{0}, \tag{1}$$

where

$$\mathbf{T} = T_{i\alpha}\mathbf{e}_i \otimes \mathbf{e}_\alpha \tag{2}$$

is the Piola stress, div is the (two-dimensional) divergence operator on Ω, p is the net lateral pressure across the membrane surface,

$$\mathbf{n} = \frac{\mathbf{F}\mathbf{e}_1 \times \mathbf{F}\mathbf{e}_2}{\mathbf{F}\mathbf{e}_1 \times \mathbf{F}\mathbf{e}_2} \tag{3}$$

is the unit normal to the membrane surface after deformation,

$$\mathbf{F} = F_{i\alpha}\mathbf{e}_i \otimes \mathbf{e}_\alpha \tag{4}$$

is the deformation gradient, where

$$F_{i\alpha} = r_{i,\alpha} \equiv \frac{\partial r_i}{\partial x_\alpha} \tag{5}$$

in which x_α and r_i are the Cartesian coordinates of a material particle before and after deformation, respectively, and

$$J = (\det \mathbf{C})^{1/2} \tag{6}$$

where

$$\mathbf{C} = \mathbf{F}^t\mathbf{F} \tag{7}$$

is the Cauchy–Green strain and the superscript ^{t} is used to denote transposition.

An elastic membrane possesses a strain-energy function W per unit area of Ω which depends on the deformation gradient and which delivers the stress through

$$\mathbf{T} = W_{\mathbf{F}}, \tag{8}$$

where the subscript identifies the gradient with respect to $\mathbf{F}$. Thus,

$$T_{i\alpha} = \frac{\partial W}{\partial F_{i\alpha}}. \tag{9}$$

These equations are augmented by traction data $t_i = T_{i\alpha}\nu_\alpha$ or position data $r_i = r_i^0$ on appropriate parts of the boundary, where ν_α are the components of the exterior unit normal to an edge in the reference configuration.

Isotropy of space requires that W depend on $\mathbf{F}$ through $\mathbf{C}$. If the membrane *material* is isotropic then the latter dependence occurs through the *principal stretches* λ and μ, the positive square roots of the eigenvalues of the strain $\mathbf{C}$. Thus,

$$\mathbf{T} = w_\lambda \mathbf{l}\otimes\mathbf{L} + w_\mu \mathbf{m}\otimes\mathbf{M}, \tag{10}$$

where $w_{\lambda,\mu}$ are the partial derivatives of the symmetric function

$$w(\lambda,\mu) = w(\mu,\lambda) = W(\mathbf{F}), \tag{11}$$

and $\{\mathbf{l},\mathbf{m}\}$, $\{\mathbf{L},\mathbf{M}\}$ are the orthonormal principal strain axes on the deformed surface and on Ω, respectively [Haseganu and Steigmann (1994)][1]. The latter generate a useful formula for the deformation gradient which is identical in form to (10):

$$\mathbf{F} = \lambda\mathbf{l}\otimes\mathbf{L} + \mu\mathbf{m}\otimes\mathbf{M}. \tag{12}$$

Relaxed membrane theory is based on the composite strain-energy function

$$\begin{aligned}
w(\lambda,\mu);&\quad \lambda > v(\mu) \quad \text{and} \quad \mu > v(\lambda)\\
w(\lambda,v(\lambda));&\quad \lambda > 1 \quad \text{and} \quad \mu \le v(\lambda)\\
w(v(\mu),\mu);&\quad \mu > 1 \quad \text{and} \quad \lambda \le v(\mu)\\
0;&\quad \lambda \le 1 \quad \text{and} \quad \mu \le 1,
\end{aligned} \tag{13}$$

where $v(x)$ is the (normally unique) solution of the implicit equation

$$w_y(x, y) = 0. \tag{14}$$

Thus the second and third branches of (13) correspond to states of uniaxial tension along the principal strain axes. These are valid even when λ or μ are less than the corresponding value of $v(\mu)$ or $v(\lambda)$, respectively, the difference being due to fine-scale wrinkling without further change of energy and with no compressive stress. The first branch corresponds to biaxial tension and the original strain-energy function is operative in the corresponding region of the plane of principal stretches. The fourth branch corresponds to double wrinkling without stress, this branch being operative in slack regions of the membrane. In general, the determination of the regions on the material surface Ω which correspond to the various branches of (13) constitutes a difficult free-boundary problem. In Eliza's work, such difficulties were avoided altogether by simply computing the stretches at any given stage of deformation and then selecting the appropriate branch for the subsequent calculation.

In the examples discussed here the specific strain-energy function used in the first branch of (13) is the specialization to membrane theory of Ogden's function [Ogden (1997)][3] for rubberlike solids that are incompressible in bulk, namely

$$w(\lambda, \mu) = \frac{G}{\alpha^r} \sum_{r=1}^{3} g_r \left[\lambda^{\alpha_r} + \mu^{\alpha_r} + (\lambda\mu)^{-\alpha_r} - 3\right], \tag{15}$$

where

$$\begin{gathered} \alpha_1 = 1.3, \quad \alpha_2 = 5.0, \quad \alpha_3 = -2.0; \\ g_1 = 1.491, \quad g_2 = 0.003, \quad g_3 = -0.0237 \end{gathered} \tag{16}$$

and the constant $G(> 0)$ may be regarded as the ground-state shear modulus multiplied by the initial membrane thickness. The associated functions $v(x)$ and $\hat{w}(x)[= w(x, v(x)) = w(v(x), x)]$ are

$$v(x) = x^{-1/2} \quad \text{and} \quad \hat{w}(x) = \frac{G}{\alpha_r} \sum_{r=1}^{3} g_r \left(x^{\alpha_r} + 2x^{-\alpha_r/2} - 3\right). \tag{17}$$

1.3. Numerical Scheme

The numerical method Eliza used is based on the *Green's theorem finite difference* technique [Haseganu and Steigmann (1994)][1] for the spatial discretization of the domain Ω. In this method the x_1, x_2-plane is sub-divided

into small quadrilateral cells that are arranged so as to cover the domain completely. Since the cells need not be rectangular, it is possible to approximate a domain with curved or irregular boundaries with high precision by using a sufficient number of cells. In contrast, conventional finite differences require computationally expensive boundary interpolation or grid-mapping to accommodate irregular domains. The procedure is known to be most effective when used in conjunction with spatial finite differences [Underwood (1983)][4]. It is for this reason that finite differences are used rather than the more widespread finite element method.

In the present method the divergence operator $T_{k\alpha,\alpha}$ appearing in (1) is approximated at node (i,j) by applying Green's theorem to a quadrilateral region enclosed by a contour described by node points in the material region of interest. The area integral in the theorem is estimated as the nodal value of the integrand multiplied by the enclosed area, while the contour integral is approximated by setting its integrand equal to the values it assumes at the midpoints on each of the four edges that make up the boundary. This yields the approximate divergence of stress at node (i,j) [Haseganu and Steigmann (1994)][1]:

$$\begin{aligned} f_k^{i,j} &\equiv A^{i,j}(T_{k\alpha,\alpha})^{i,j} \\ &= e_{\alpha\beta}\Big[T_{k\alpha}^{i+1/2,j+1/2}\left(x_\beta^{i,j+1}-x_\beta^{i+1,j}\right) \\ &\quad + T_{k\alpha}^{i-1/2,j+1/2}\left(x_\beta^{i-1,j}-x_\beta^{i,j+1}\right) \\ &\quad + T_{k\alpha}^{i-1/2,j-1/2}\left(x_\beta^{i,j-1}-x_\beta^{i-1,j}\right) \\ &\quad + T_{k\alpha}^{i+1/2,j-1/2}\left(x_\beta^{i+1,j}-x_\beta^{i,j-1}\right)\Big], \end{aligned} \tag{18}$$

where $e_{\alpha\beta}$ is the unit alternator ($e_{12}=-e_{21}=1$, $e_{11}=e_{22}=0$) and $A^{i,j}$ is the area of the quadrilateral.

The stresses on the right hand side in (18) are evaluated at the midpoints between nodes. These depend via the constitutive relations on the corresponding values of the deformation gradient, which are in turn computed using a second application of Green's theorem. As before, the associated area integral is estimated as the value of the integrand at the midpoints multiplied by the enclosed area. However, the four edge contributions to the boundary integral are now approximated by replacing the integrand in each with the average of their values at the node points. The resulting

difference formula is [Haseganu and Steigmann (1994)][1]

$$F_{k\alpha}^{i+1/2,j+1/2} = \left(A^{i+1/2,j+1/2}\right)^{-1} e_{\alpha\beta}\Big[\left(x_\beta^{i,j+1} - x_\beta^{i+1,j}\right)\left(r_k^{i+1,j+1} - r_k^{i,j}\right) + \left(x_\beta^{i+1,j+1} - x_\beta^{i,j}\right)\left(r_k^{i,j+1} - r_k^{i+1,j}\right)\Big], \quad (19)$$

where $A^{i+1/2,j+1/2}$ is the area of the associated quadrilateral.

Given the expression for the deformation gradient, the pressure term $pJ\mathbf{n}$ in the equilibrium equations integrates to yield the force

$$p_k^{i+1/2,j+1/2} = pe_{kmn}F_{m1}^{i+1/2,j+1/2}F_{n2}^{i+1/2,j+1/2}A^{i+1/2,j+1/2}, \quad (20)$$

where e_{ijk} is the three-dimensional unit alternator. Eliza [Haseganu (1994)][5] used this in the formula

$$p_k^{i,j} = \frac{1}{4}\left(p_k^{i+1/2,j+1/2} + p_k^{i-1/2,j+1/2} + p_k^{i-1/2,j-1/2} + p_k^{i+1/2,j-1/2}\right) \quad (21)$$

to generate the effective nodal force due to pressure. The total nodal force is then given by

$$g_k^{i,j} = f_k^{i,j} + p_k^{i,j}. \quad (22)$$

To solve the nonlinear algebraic system generated by the finite difference discretization, the equilibrium problem is embedded into an artificial dynamical problem with suitably chosen mass and viscosity. Since it is only the equilibrium configurations that are of interest, the dynamical system may chosen arbitrarily, subject to the requirement that the desired equilibria be asymptotically stable within the class of dynamics considered. Further, the system should be robust in the sense that its equilibria are not sensitive to the detailed features of the system on dynamical solution trajectories. This procedure is a variant of the method of relaxation*dynamic!relaxation.* In the present context, a convenient dynamical system, *not* equivalent to the actual equations of motion for the membrane, is

$$T_{i\alpha,\alpha} + pJn_i = \rho\dot{v}_i + c\rho v_i, \qquad v_i = \dot{r}_i, \quad (23)$$

subject to the kinematically admissible initial conditions

$$r_i(x_\alpha, 0) = R_i(x_\alpha), \qquad v_i(x_\alpha, 0) = 0. \quad (24)$$

Here $\rho(x_\alpha)$ is the mass per unit area of the reference plane and c is a positive damping coefficient.

Alternative formulations of dynamic relaxation have been based on the actual equations of motion for the system at hand. In such formulations

damping is introduced via the constitutive relations. The resulting discretization yields a coupled system for updating the configuration from one time step to the next. This is inconvenient in practice, but is generally necessary in problems for which the equilibria obtained are strongly influenced by the details of the dynamics in a given initial value problem. However, in the present application to membrane theory, the equations of equilibrium are derived from a strain energy that is modified to incorporate the effects of wrinkling automatically. In mixed position/traction problems without pressure, the resulting energy is often (for some strain-energy functions) a convex function of the deformation gradient in regions where the membrane is under stress [Haseganu and Steigmann (1994)][1]. Accordingly, these regions are uniquely determined if the membrane is in equilibrium, and are thus insensitive to the details of a dynamical system that exhibits such configurations as equilibria. The non-uniqueness of slack regions of the membrane is not a deficiency of the model, but instead reflects the fact that membrane equilibria are entirely arbitrary in the absence of stress (such states do not occur in equilibrium if pressure is present). The uniqueness of the stressed regions of equilibrium configurations together with the path-independence of the elastic constitutive relations were exploited by Eliza to construct a dynamical problem that is computationally efficient.

It remains to show that equilibria are asymptotically stable in the class of dynamics described by (23) and (24). Position/traction problems are discussed first. In view of the minimizing property of equilibria, it is sufficient to show that the total mechanical energy decreases on solution trajectories of (23). Asymptotic stability then follows by a theorem of Lyapunov. To this end (23) is scalar- multiplied by the velocity and the resulting equation is integrated over the reference plane Ω to derive

$$\frac{\mathrm{d}}{\mathrm{d}t}\left[K+\int_\Omega W(\mathbf{F})\mathrm{d}a\right]+c\int_\Omega \rho\,|\mathbf{v}|^2\,\mathrm{d}a=\int_{\partial\Omega}\mathbf{T}\nu\cdot\mathbf{v}\mathrm{d}a, \tag{25}$$

where

$$K=\frac{1}{2}\int_\Omega \rho\,|\mathbf{v}|^2\,\mathrm{d}a \tag{26}$$

is the kinetic energy and the relation $\dot{W}=T_{i\alpha}v_{i,\alpha}$ has been used together with Green's theorem. In a standard mixed boundary value problem with position assigned along a part of the boundary $\partial\Omega$ and traction assigned on the remainder, (25) reduces to

$$\frac{\mathrm{d}}{\mathrm{d}t}[K+E]=-c\int_\Omega \rho\,|\mathbf{v}|^2\,\mathrm{d}a\leq 0, \tag{27}$$

where

$$E = \int_{\Omega} W(\mathbf{F})\mathrm{d}a - \int_{\partial\Omega_t} \mathbf{t}\cdot\mathbf{r}\mathrm{d}a \tag{28}$$

is the total potential energy in which $\partial\Omega_t$ is the part of the boundary where the fixed traction $\mathbf{t}$ is assigned, position being assigned on the complementary part. Thus the total energy $K+E$ decays on the solution trajectories of (23) and the asymptotic stability of equilibria follows. Strictly, these statements are valid for the discretized equations. Their proof for the analytical model remains open due to certain difficulties associated with Lyapunov's theorem for continuous systems. Again, these issues are of no concern in the present context since the discrete dynamical problem merely serves to expedite the computation of equilibria.

Equation (27) remains valid for the pure displacement problem with prescribed pressure, provided that E is replaced by [Haseganu (1994)][5]

$$E' = \int_{\Omega} [W(\mathbf{F}) - (p/3)J\mathbf{n}\cdot\mathbf{r}]\mathrm{d}a. \tag{29}$$

The solution of eqs. (23) and (24) is based on the combination of the spatial difference formula (22) with central difference operators in time. This yields the explicit decoupled scheme [Haseganu and Steigmann (1994)][1]

$$\left(h^{-1}+\frac{c}{2}\right) m^{i,j}\dot{\mathbf{r}}^{i,j,n+1/2} = \left(h^{-1}+\frac{c}{2}\right) m^{i,j}\dot{\mathbf{r}}^{i,j,n-1/2} + \mathbf{g}^{i,j,n},$$
$$\mathbf{r}^{i,j,n+1} = \mathbf{r}^{i,j,n} + h\dot{\mathbf{r}}^{i,j,n+1/2}, \tag{30}$$

which is used to advance the solution in time node by node. In terms of a fixed orthonormal basis $\{\mathbf{e}_k\}$, $\mathbf{r} = r_k\mathbf{e}_k$ is the nodal position and $\mathbf{g} = g_k\mathbf{e}_k$ is the nodal force. In addition, $m^{i,j} = A^{i,j}\rho(x_\alpha^{i,j})$ is the nodal mass, t_n is the time after n cycles and h is the time step. This system is obtained by integrating (23) over the quadrilateral region formed by the four nearest neighbors of the node and setting the deformation in the interior equal to the nodal value. The starting procedure for (30) is derived from (24). Thus $\mathbf{r}^{i,j,0} = \mathbf{R}(\mathbf{x}^{i,j})$, $\dot{\mathbf{r}}^{i,j,0} = \mathbf{0}$ and the central difference formulas together with (30) yield

$$\frac{2}{h}\, m^{i,j}\dot{\mathbf{r}}^{i,j,1/2} = \mathbf{g}^{i,j,0}, \tag{31}$$

wherein the right hand side is determined by $\mathbf{R}(\mathbf{x})$. The system of equations is then non-dimensionalized and the solution advanced to the first time t_n such that $\max_{i,j}\left|\mathbf{g}^{i,j,n}\right|$ is less than some specified value.

Finally, it is noted that the convexity of the modified strain energy ensures that computations based on the foregoing scheme are not *mesh-dependent*. This property is fundamental to the convergence of the method with respect to mesh refinement.

For pure position boundary-value problems with assigned pressure, the foregoing claims regarding the convexity of the variational problem and the conclusions which follow therefrom are not valid, although the problem continues to satisfy important existence criteria such as the quasiconvexity condition [Dacarogna (1989)][6]. The stronger statement pertaining to (partial) uniqueness also does not apply, and this fact is reflected in some of the simulations to be discussed.

1.4. Examples

The examples discussed here are described in detail in Eliza's thesis [Haseganu (1994)][5] and pertain to the problem of assigned boundary position and simultaneous inflation by a uniform pressure of fixed intensity. Eliza had intended to collect these together into a paper for publication. Her previous work [Haseganu and Steigmann (1994)][1] was concerned exclusively with mixed position/traction data in the absence of pressure.

In the first example, a circular membrane of unit radius is subjected to a lateral dimensionless pressure $\tilde{p} = p/G = 2.0$ while the radius of the boundary is fixed at one-half its reference value. The meshed reference configuration is shown in Figure 1.1. Contraction of the boundary tends to promote membrane wrinkling whereas pressure tends to suppress it. The competition between these two influences is evident in Figure 1.2, in which dashed lines indicate trajectories of the active principal stress in wrinkled regions; elsewhere the membrane is under biaxial tension. From the figure it is evident that the large circumferential contraction of the boundary and the attendant wrinkling combine to yield a non-axisymmetric shape despite the axisymmetry of the data.

Figure 1.3 depicts a representative meridian corresponding to the same boundary data under a succession of pressures. A snap bifurcation from a low-volume solution to a shape enclosing a much larger volume was found to occur between $\tilde{p} = 2.675$ and 2.6775, the latter figure representing a 0.93% increase over the former. This kind of behaviour is a well-known feature of the response of spherical membranes inflated by a controlled pressure undergoing spherically symmetric deformations. In the latter case analytical solutions are available which exhibit an unstable branch of equilibria con-

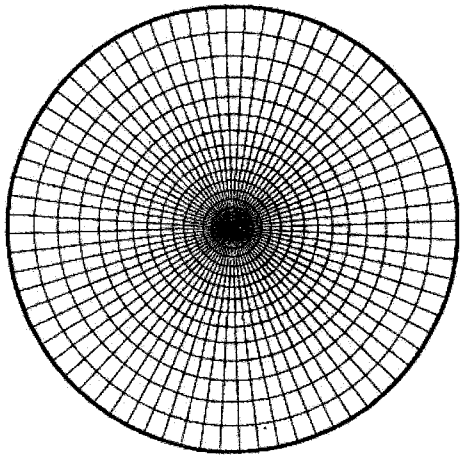

Fig. 1.1. Circular membrane; meshed reference configuration.

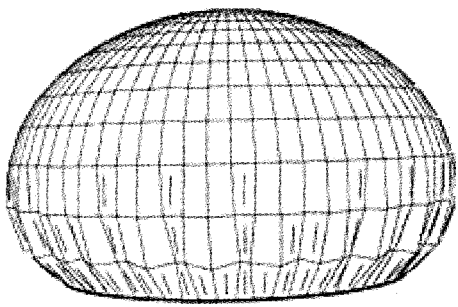

Fig. 1.2. Circular Ogden membrane subjected to a non dimensional pressure of 2.0 combined with a 50% reduction in the length of boundary circumference.

necting the stable branches, the latter requiring an increase in pressure to effect an increase in volume. It may be argued on physical grounds that the unstable equilibrium branch does not represent a meaningful solution, since the membrane is likely to undergo dynamical behaviour instead if subjected to even the smallest disturbance. The dynamic relaxation method mirrors this expectation as it never generates the unstable branch of equilibria. It is also noteworthy that computations using the neo-Hookean strain energy in place of (15)--(16) did not yield equilibria for pressures above $\tilde{p} = 2.612$. This is due to the insufficient growth of the latter strain-energy function at large stretches.

In the next class of examples the membrane is subjected to a relatively

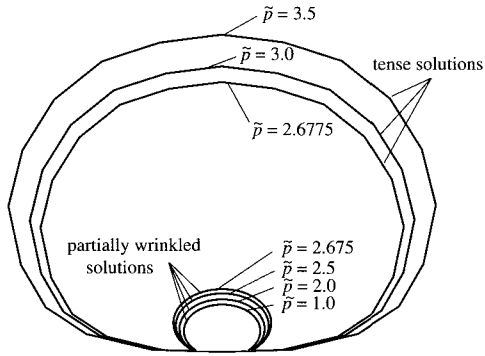

Fig. 1.3. Cross-sections through meridian of deformed configurations of circular Ogden membrane for different numerical values of pressure

modest pressure of intensity $\tilde{p} = 1.0$ while the central node of the mesh at the center of the membrane is displaced vertically downward by a fixed amount. The radius of the outer boundary of the membrane is decreased to 0.8. The resulting deformation is axisymmetric and exhibits wrinkling in a region adjoining the boundary, as depicted in Figure 1.4.

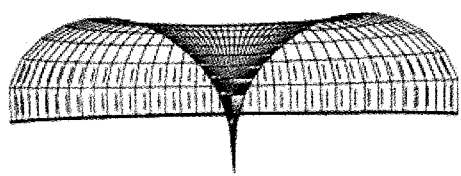

Fig. 1.4. Cross section through pressurized circular membrane subjected to a central vertical point load directed downwards, combined with a 20% reduction in the length of boundary circumference

A further reduction of the boundary radius to 0.5 holding the pressure and central displacement fixed generates a remarkable deformation in which the membrane exhibits pleats or *hinges* separating three distinct lobes. Oblique and overhead views are shown in Figures 1.5 and 1.6.

The computed solution is not to be regarded as definitive since the predicted deformation entails self penetration of the material. A refined solution would penalize self penetration through the introduction of a reactive contact pressure distribution. Eliza did not have the opportunity to incorporate this refinement into the computations. Nevertheless the results are remarkable to the extent that they capture the typical three-lobe pat-

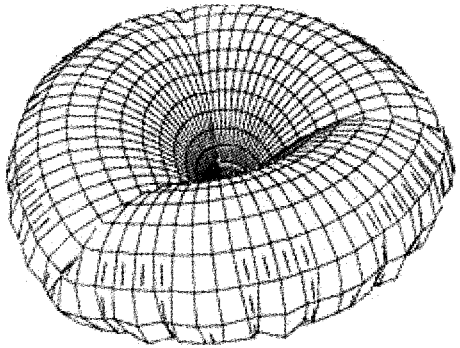

Fig. 1.5. Pressurized circular membrane subjected to a central vertical point load directed downwards, combined with a 50% reduction in the length of boundary circumference

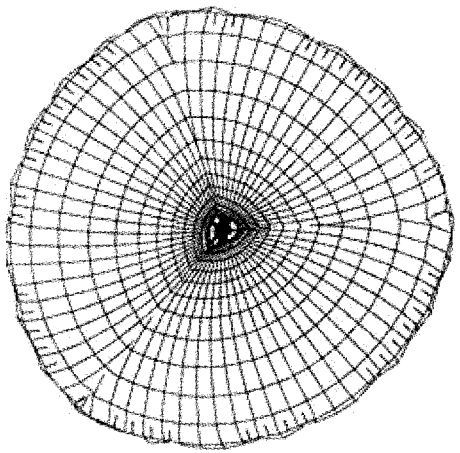

Fig. 1.6. Pressurized circular membrane subjected to a central vertical point load directed downwards, combined with a 50% reduction in the length of boundary circumference; top view

tern observed when a weight is suspended from the apex of a pressurized high-altitude balloon [Baginski (2002)][7].

Solutions possessing the unusual and unexpected features exhibited here were made possible by Eliza's pioneering efforts in this rich branch of computational elasticity. It is my hope that they will stimulate further advances in the study of the intricate and difficult problem of nonlinear membrane behaviour.

References

1. Haseganu, E., and Steigmann, D.J., (1994), "Analysis of partly wrinkled membranes by the method of dynamic relaxation", Computational Mechanics 14, 596–614.
2. Pipkin, A.C., (1986), "The relaxed energy density for isotropic membranes", IMA J. Appl. Math. 36, 85–99.
3. Ogden, R.W., (1997), "Non-linear Elastic Deformations", Dover Publications, New York.
4. Underwood, P., (1983), "Dynamic relaxation", Computational Methods for Transient Analysis, eds. T. Belytschko and T.J.R. Hughes, Elsevier, Amsterdam, pp. 245–265.
5. Haseganu, E., (1994), "Analytical investigation of tension fields in lightweight membrane structures", doctoral dissertation, University of Alberta, Edmonton AB.
6. Dacarogna, B., (1989), "Direct methods in the calculus of variations", Springer, Berlin.
7. Remarks by Dr. Frank Baginski at the George Washington University, Washington DC., 12 April 2002: 1st Capitol City Symposium on Ultra-Thin Membranes with Applications to Large Super-light Structural Systems.

CHAPTER 2

BUCKLING, VIBRATIONS AND OPTIMAL DESIGN OF RING-STIFFENED THIN CYLINDRICAL SHELLS

Sergei B. Filippov

Department of Theoretical and Applied Mechanics, St. Petersburg State University, St. Petersburg, Russia, 198504
E-mail: sbf@petrodvorets.spb.ru

This paper deals with the asymptotic analysis of linear buckling and free vibrations of ring-stiffened thin cylindrical shells. The simple approximate formulas for the fundamental frequency and the critical external pressure are obtained. The critical pressure and fundamental frequency of a stiffened shell are compared with the critical pressure and fundamental frequency of a non-stiffened cylindrical shell of the same mass. The optimal parameters for the stiffened shell, for which the fundamental frequency or the critical pressure is maximal, are found.

2.1. Introduction

Thin circular cylindrical shells are widely applied in engineering. The important characteristics of such shells are their critical external pressure and their fundamental vibration frequency. To effectively enhance the flexural stiffness to avoid premature elastic buckling failure and resonance, stiffening rings are frequently used. It is shown in [Filippov (1999)][7] that the critical external pressure of a ring-stiffened cylindrical shell can be five times higher than the critical pressure of a non-stiffened shell of the same mass.

The modelling techniques for stiffened shell may be divided into two types. Using the methods of the first type one smears the stiffness of the rings onto the shell and treats the stiffened shell as an orthotropic one. Such approach has been used in many papers, for example, see [Wang (1970)][16] and the references therein.

The orthotropic approximation is fine when the stiffeners are distributed evenly and closely spaced. If the stiffener spacing increase or become irreg-

ular, the orthotropic approximation becomes inaccurate. In this case one should consider stiffeners as discrete members, i.e. use the modelling techniques of the second type. In this paper we usually treat rings as discrete stiffeners, but sometimes we also apply one of the methods of the first type provided its error is small enough.

Recently, various analytical and numerical methods for stiffened shells have been developed: [Wang (1970)][16] and [Amiro and Zarutskii (1980)][2] used Fourier series for the solution of static and dynamic problems, [Yang and Zhou (1995)][17] obtained the natural frequencies and the buckling loads of stiffened shells by Fourier expansion with the corresponding transfer function formulation.

In the early studies on vibrations and buckling of stiffened shells, the Rayleigh–Ritz method was applied. Nowadays this technique is still popular, for example, in [Tian *et al.* (1999)][12] the Ritz method was used for buckling analysis of ring-stiffened cylindrical shells under general pressure loading.

It has been shown in [Ross *et al.* (1995)][10] that the finite element method is quite suitable to analyze the vibration characteristics of ring-stiffened cylindrical shells under external pressure.

The semi-momentless theory was applied in [Alfutov (1978)][1] for the construction of the buckling modes for stiffened cylindrical shells. The semi-momentless theory represents the first approximation to the asymptotic solution in linear buckling problems. The development of the asymptotic methods in the last decades (see [Bauer *et al.* (1993)][4] and [Tovstik and Smirnov (2001)][14]) allows one to extend the asymptotic approach to the wide range of problems of stiffened shells. Some asymptotic analysis results on linear buckling and free vibrations of ring-stiffened cylindrical shells are presented below.

The approximate values of the critical pressure and of the natural frequencies for thin ring-stiffened shells may be obtained by solving boundary value problems for systems of linear partial differential equations. The equations describing the vibration or the buckling of thin shells contain the dimensionless shell thickness as a small parameter. Therefore, these boundary value problems lend themselves to be solved by asymptotic methods.

The asymptotic results clarify the problem qualitatively and assist in gaining an understanding of the vibration and buckling mechanism. The understanding of the qualitative picture helps for further development of numerical methods.

By means of modern asymptotic methods, complex boundary value

problems for the stiffened shells theory are transformed into problems which have simple analytical solutions. The benefits of the asymptotic approach become apparent especially for the optimal design of the stiffened shells, since the numerical evaluation of the optimal parameters is time-consuming.

2.2. Equations of Cylindrical Shells

We consider the low-frequency free vibrations and buckling of a thin circular cylindrical shell presented in Fig. 2.1.

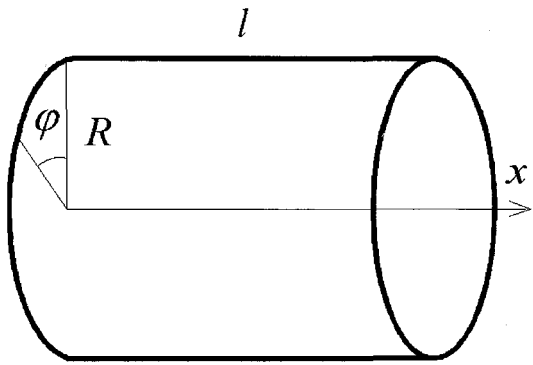

Fig. 2.1. Cylindrical shell.

We take the radius R of the cylindrical shell as the characteristic size. Then the approximate dimensionless equations of [Donnell (1976)][5] describing a cylindrical shell are

$$\varepsilon^8 \Delta\Delta w - \frac{\partial^2 \Phi}{\partial x^2} + \lambda Z = 0, \qquad \Delta\Delta\Phi + \frac{\partial^2 w}{\partial x^2} = 0, \tag{1}$$

where

$$\Delta w = \frac{\partial^2 w}{\partial x^2} + \frac{\partial^2 w}{\partial \varphi^2}, \qquad \varepsilon^8 = \frac{h^2}{12(1-\nu^2)},$$

x and φ are the coordinates on the shell neutral surface in the longitudinal and circumferential directions, $\varepsilon > 0$ is a small parameter, h is the dimensionless shell thickness, ν is Poisson's ratio, $w(x, \varphi)$ is the normal deflection and $\Phi(x, \varphi)$ is the force function.

In the case of free vibrations

$$Z = -w, \quad \lambda = \rho R^2 \omega^2 / E, \tag{2}$$

where λ is the frequency parameter, ω is the frequency, ρ is the mass density, and E is Young's modulus.

For buckling of the membrane stress-strain state under a uniform external pressure p in Eq. (1) we have

$$Z = \frac{\partial^2 w}{\partial \varphi^2}, \quad \lambda = \frac{p}{Eh}. \tag{3}$$

Four homogeneous boundary conditions are imposed on each edge, $x = 0$ and $x = l$, of the shell. We seek the lowest eigenvalues, λ, for which there exist non-trivial solutions of Eq. (1) satisfying the boundary conditions.

After separation of variables in Eq. (1),

$$w(x, \varphi) = w(x) \sin m\varphi, \quad \Phi(x, \varphi) = \Phi(x) \sin m\varphi,$$

where m is the circumferential wave number, we obtain the ordinary differential equations

$$\varepsilon^8 \Delta\Delta w - \frac{d^2\Phi}{dx^2} + \lambda Z = 0, \qquad \Delta\Delta\Phi + \frac{d^2 w}{dx^2} = 0, \tag{4}$$

where

$$\Delta w = \frac{d^2 w}{dx^2} - m^2 w. \tag{5}$$

2.3. Approximate Equations

The approximate solutions of the boundary value problems for Eq. (4) are obtained in [Bauer *et al.* (1993)][4]. If the shell edges are clamped or freely supported, then, for sufficiently small ε, the lowest eigenvalue, λ_1, corresponds to the large circumferential wave number $m \sim \varepsilon^{-1}$. Taking into account that $\Delta \sim m^2$ for $m \gg 1$, we obtain, in the first approximation, from Eq. (4):

$$\frac{d^4 w}{ds^4} - \alpha^4 w = 0, \tag{6}$$

where

$$\alpha^4 = m^4 \lambda M - \varepsilon^8 m^8, \quad M = \begin{cases} 1, & \text{for vibrations,} \\ m^2, & \text{for buckling.} \end{cases} \tag{7}$$

It follows from Eq. (7) that

$$\lambda(m, n) = \frac{1}{M} \left(\frac{\alpha_n^4}{m^4} + \varepsilon^8 m^4 \right). \tag{8}$$

Here α_n^4 $(n = 1, 2, \ldots)$ are the eigenvalues for which the boundary value problem for Eq. (6) has non-trivial solutions.

The problem of extracting two main boundary conditions for Eq. (6) out of four boundary conditions on the shell edges is discussed in detail in [Tovstik and Smirnov (2001)][14]. The boundary conditions for Eq. (6) in the case of freely supported shell edges (FS) have the form

$$w = \frac{d^2w}{dx^2} = 0 \quad \text{for} \quad x = 0, \quad x = l. \tag{9}$$

The boundary value problem (6), (9) also describes the flexural vibrations of a simply supported beam. The connection between the boundary value problems for a shell and a beam is shown in Fig. 2.2.

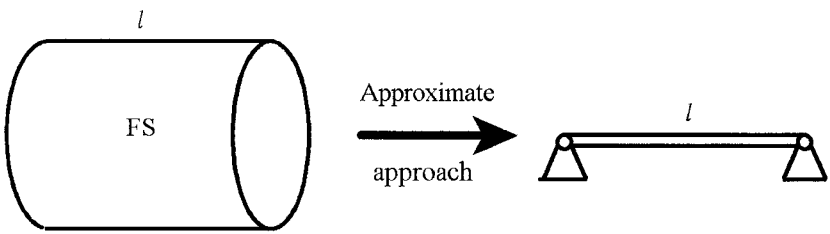

Fig. 2.2. Shell and beam.

Problem (6), (9) has a simple solution, presented for example in [Timoshenko (1955)][13]:

$$w_n = C \sin \alpha_n x, \quad \alpha_n = \pi n/l, \quad n = 1, 2, \ldots, \tag{10}$$

where C is an arbitrary constant.

If the shell edges are clamped, then

$$w = \frac{dw}{dx} = 0 \quad \text{for} \quad x = 0, \quad x = l. \tag{11}$$

Consequently, a clamped shell problem corresponds to a clamped beam problem.

The solutions of problem (6), (11) are well known (see [Timoshenko (1955)][13]) and have the form

$$w_n(x) = C[U(\alpha_n x) - \kappa_n V(\alpha_n x)], \tag{12}$$

where

$$\begin{gathered} U(x) = \cosh x - \cos x, \quad V(x) = \sinh x - \sin x, \\ \alpha_n = z_n/l, \quad \kappa_n = (\cosh z_n - \cos z_n)/(\sinh z_n - \sin z_n). \end{gathered} \tag{13}$$

The positive numbers z_n ($z_1 < z_2 < \cdots$) are the roots of the equation

$$\cosh z \cos z = 1. \tag{14}$$

To find the lowest eigenvalue

$$\lambda_1 = \min_{m,n} \lambda(m,n)$$

we calculate the partial derivative of the function $\lambda(m,n)$ given by (8) with respect to m and set it equal to zero. The solution of the equation $\partial\lambda/\partial m = 0$ has the form

$$m = m_* = \begin{cases} \sqrt{\alpha_n}/\varepsilon, & \text{for vibrations,} \\ 3^{1/8}\sqrt{\alpha_n}/\varepsilon, & \text{for buckling.} \end{cases} \tag{15}$$

The function $\lambda(m,n)$ attains its minimum, $\lambda_*(n)$, for $m = m_*$. It follows from (8) and (15) that

$$\lambda_*(n) = \min_m \lambda(m,n) \simeq \begin{cases} 2\varepsilon^4\alpha_n^2, & \text{for vibrations,} \\ 4\varepsilon^6\alpha_n/3^{3/4}, & \text{for buckling.} \end{cases} \tag{16}$$

If m_* is an integer, then formula (16) gives the exact result. Replacing m_* by one of the integers closest to m_* we introduce an error e whose absolute value is less than 1. Therefore, the relative error e/m_* in (16) decreases as m_* increases.

Taking into account the fact that $\alpha_1 < \alpha_2 < \cdots$ we obtain

$$\lambda_1 = \min_n \lambda_*(n) \simeq \begin{cases} 2\varepsilon^4\alpha_1^2, & \text{for vibrations,} \\ 4\varepsilon^6\alpha_1/3^{3/4}, & \text{for buckling.} \end{cases} \tag{17}$$

For a freely supported shell $\alpha_1 = \pi/l \simeq 3.14/l$ and for a shell with the clamped edges $\alpha_1 \simeq 4.73/l$. If one of the shell edges is clamped and the other is freely supported then $\alpha_1 \simeq 3.927/l$.

2.4. Ring-stiffened Shell

Consider low-frequency free vibrations and buckling of a thin circular cylindrical shell stiffened by n_r identical rings at the parallels $x = x_j$, $j = 1, 2, \ldots, n_r$ (see Fig. 2.3, where $n_r = 5$).

The dimensionless equations describing the vibrations and buckling of the ring-stiffened shell may be written as

$$\varepsilon^8\Delta\Delta w^{(j)} - \frac{\partial^2\Phi^{(j)}}{\partial x^2} + \lambda Z^{(j)} = 0, \qquad \Delta\Delta\Phi^{(j)} + \frac{\partial^2 w^{(j)}}{\partial x^2} = 0, \tag{18}$$
$$j = 1, 2 \ldots, n, \quad n = n_r + 1,$$

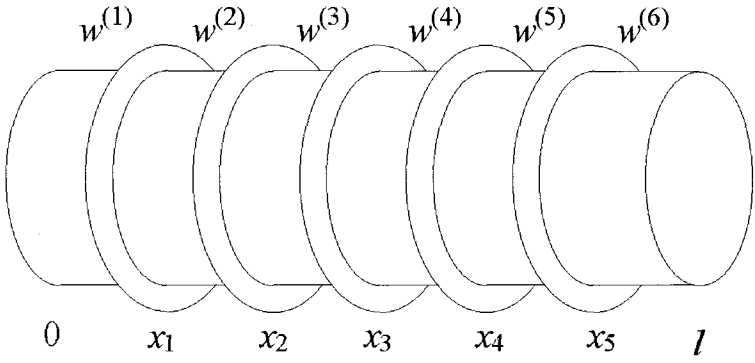

Fig. 2.3. Ring-stiffened cylindrical shell.

where the function $w^{(j)}$ is the normal deflection of the part of the shell situated between the rings or between the ring and the shell edge (Fig. 2.3),

$$Z^{(j)} = \begin{cases} -w^{(j)}, & \text{for vibrations,} \\ \dfrac{\partial^2 w^{(j)}}{\partial \varphi^2}, & \text{for buckling.} \end{cases}$$

The solutions of Eq. (18) have to satisfy eight boundary conditions on the shell edges $x = 0$, $x = l$ and $8n_r$ continuity conditions on the parallels $x = x_j$, $j = 1, 2 \ldots, n_r$.

Separating variables in Eq. (18)

$$w^{(j)}(x, \varphi) = w^{(j)}(x) \sin m\varphi, \quad \Phi^{(j)}(x, \varphi) = \Phi^{(j)}(x) \sin m\varphi$$

leads to the following system of ordinary differential equations:

$$\varepsilon^8 \Delta\Delta w^{(j)} - \frac{d^2 \Phi^{(j)}}{dx^2} + \lambda Z = 0, \qquad \Delta\Delta \Phi^{(j)} + \frac{d^2 w^{(j)}}{dx^2} = 0, \tag{19}$$

where the operator Δ is introduced in (5).

2.5. First Approximation

In the first approximation for $m \gg 1$ Eq. (19) reduces to the following equations

$$\frac{d^4 w^{(j)}}{ds^4} - \alpha^4 w^{(j)} = 0, \quad j = 1, 2 \ldots, n. \tag{20}$$

It is convenient to introduce the function $w(x) = w^{(j)}(x)$ for $x_{j-1} < x < x_j$, $j = 1, 2, \ldots, n$, $x_0 = 0$, $x_n = l$. Then the boundary conditions for

equations (18) corresponding to the freely supported or clamped shell edges $x = 0$ and $x = l$ are represented in the forms (9) or (11).

To determine the four boundary conditions for Eq. (20) from eight continuity conditions on the stiffened parallel $x = x_j$ in the general case is a difficult problem. This problem was analyzed in [Filippov (1999)][7]. We assume that the rings and the shell are made of the same material. The centers of gravity of the ring cross sections lie on the shell neutral surface and the characteristic size of the ring cross sections is $a = O(\varepsilon^3)$. Then the boundary conditions for Eq. (20) at the parallels $x = x_j$ are written as (see [Alfutov (1978)][1] and [Filippov (1999)][7])

$$w^{(j)} = w^{(j+1)}, \qquad \frac{dw^{(j)}}{dx} = \frac{dw^{(j+1)}}{dx},$$
$$\frac{d^2w^{(j)}}{dx^2} = \frac{d^2w^{(j+1)}}{dx^2}, \qquad \frac{d^3w^{(j)}}{dx^3} - \frac{d^3w^{(j+1)}}{dx^3} = -cw^{(j+1)}, \tag{21}$$

where

$$c = \frac{m^8 I}{h}, \tag{22}$$

I is the dimensionless moment of inertia of the ring cross-section with respect to the generatrix of the cylinder.

The boundary value problems (9), (20), (21) and (11), (20), (21) also describe the flexural vibrations of the simply supported and clamped beams, stiffened by n_r identical springs of stiffness c at the points $x = x_j$ (see Fig. 2.4).

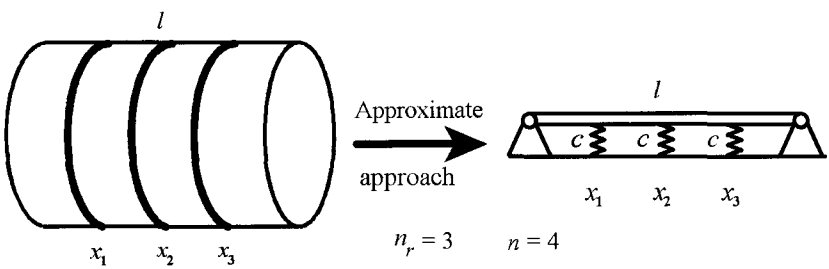

Fig. 2.4. Stiffened shell and stiffened beam

The solutions of Eq. (20) can be represented in the form

$$w^{(j)} = A_j S(z) + B_j V(z) + C_j U(z) + D_j T(z), \quad z = \alpha(x - x_{j-1}),$$
$$x_{j-1} < x < x_j, \quad j = 1, 2, \ldots, n, \quad x_0 = 0, \quad x_n = l, \tag{23}$$

where

$$S(z) = \cosh z + \cos z, \quad T(z) = \sinh z + \sin z,$$

the functions V and U are given in (13), A_j, B_j, C_j, and D_j are arbitrary constants. Substituting (23) into (9) or (11) and (21), we obtain $4n$ linear homogeneous algebraic equations in $4n$ unknowns A_j, B_j, C_j, and D_j. These equations have nontrivial solutions if the characteristic determinant $G(\alpha)$ is equal to zero:

$$G(\alpha) = 0. \tag{24}$$

In the general case one can find the roots α_n of Eq. (24) by means of numerical methods and then calculate the eigenvalue λ by formula (8). Unfortunately, in the case of a stiffened shell it is impossible to obtain a simple formula for the lowest eigenvalue λ_1 similar to formula (17), since c and, consequently, α_n depend on m.

From this point on, we focus our attention upon the evaluation of

$$\lambda_1 = \min_{m,n} \left[\frac{1}{M} \left(\frac{\alpha_n^4(m)}{m^4} + \varepsilon^8 m^4 \right) \right]. \tag{25}$$

The eigenvalue λ_1 is proportional to the fundamental vibration frequency in the case of vibrations and to the critical pressure in the case of buckling and, therefore, the first (lowest) eigenvalue is of interest in the industrial applications. We will also analyze how to find the values of the parameters corresponding to the largest value of λ_1.

2.6. Shell Stiffened with a Ring

We assume that the edges of a cylindrical shell are freely supported and a ring is located at the parallel $x = x_1$. In this case $n_r = 1$, $n = 2$ and the boundary value problem (9), (20), (21) describes the vibrations of a simply supported beam, stiffened with spring of stiffness c at the point $x = x_1$.

If $x_1 = l/2$, i.e. the spring is situated at the middle of the beam, Eq. (24) has the same roots as the following two equations

$$\tanh z - \tan z = 32z^3/c, \qquad \sin z = 0, \quad z = \alpha l/2.$$

If we denote by z_1 and z_2 the minimal positive roots of the first and second equations, then

$$\pi/2 \le z_1 < 3.927, \qquad z_2 = \pi.$$

The roots z_1 and z_2 are plotted as functions of c in the left part of Fig. 2.5.

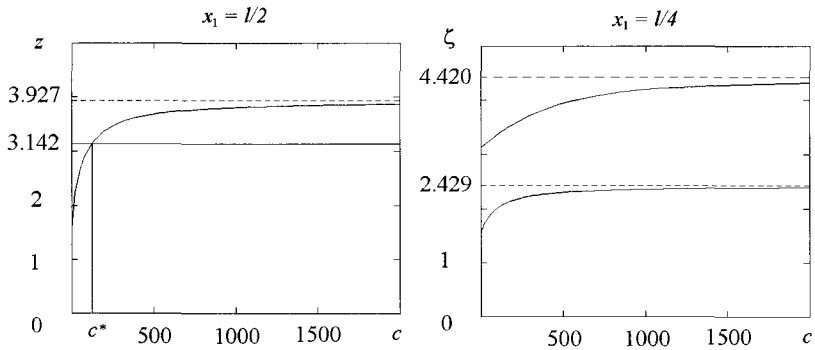

Fig. 2.5. Two minimal positive roots vs. the spring stiffness, c.

The asymmetric arrangement of the string $x_1 \neq l/2$ have been analyzed in [Sharypov (1997)][15]. Unlike the case of a symmetric string, when $x_1 = l/2$, in the asymmetric case Eq. (24) does not split into two simple equations.

Let $\zeta_k = 2\alpha_k/l$, where $0 < \alpha_1 < \alpha_2 < \cdots$ are the positive roots of Eq. (24). It is shown in [Sharypov (1997)][15] that

$$z_1 > \zeta_1, \quad z_2 < \zeta_2 \tag{26}$$

for all values of $c > 0$. The roots ζ_1 and ζ_2 are plotted as functions of c for $x_1 = l/4$ in the right part of Fig. 2.5. It follows from (26) that

$$\max_{x_1} \alpha_1(c, x_1) = \alpha_1(c, l/2),$$

i.e. the minimal positive root α_1 of Eq. (24) attains its maximum at the symmetric string position $x_1 = l/2$. Consequently, the first eigenvalue λ_1 of the simply supported cylindrical shell has its maximum at the symmetric ring position.

Usually a root of Eq. (24) increases with the stiffness c. The second characteristic property of the symmetric case is the existence of the root $\alpha_2^s = 2z_2/l = 2\pi/l$ which does not depend on c. One can easily understand the physical meaning of this fact by looking at Fig. 2.6, where the vibrations modes corresponding to $\alpha_1^s = 2z_1/l$ (on the left) and α_2^s (on the right) are shown.

The spring is deformed, when the beam vibrates with the first mode

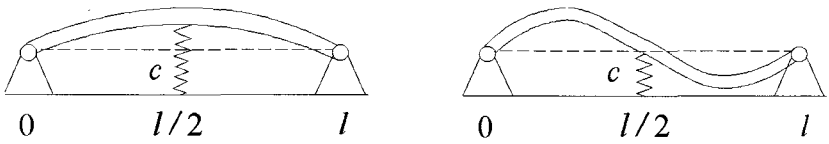

Fig. 2.6. Vibration modes of the stiffened beam.

and it is not deformed by the second mode. Therefore, the string stiffness, c, does not affect α_2^s.

We call the root c^* of the equation $\alpha_1^s(c) = \alpha_2^s$ the *effective stiffness of the spring* (see Fig. 2.5). The minimal positive root α_1 of Eq. (24) for $x_1 = l/2$ can be found from the relation

$$\alpha_1(c) = \begin{cases} \alpha_1^s(c), & c < c^*, \\ \alpha_2^s, & c \geq c^*. \end{cases} \tag{27}$$

It follows from this formula that, in case of symmetry, the root $\alpha_1(c)$ increases with the stiffness c only if $c < c^*$. Otherwise, $\alpha_1(c) = 2\pi/l$ and it does not change with an increase of c.

The lowest eigenvalue λ_1 for a freely supported shell stiffened by a ring located at the middle of the shell is

$$\lambda_1(\eta) = \min_m \frac{1}{M} \left(\frac{\alpha_1^4(\eta m^8 \varepsilon^8 l/n)}{m^4} + \varepsilon^8 m^4 \right). \tag{28}$$

Here

$$\eta = \frac{nI}{\varepsilon^8 hl} = \frac{cn}{m^8 \varepsilon^8 l}, \tag{29}$$

and α_1 may be found by (27). The dimensionless ring stiffness η is proportional to the ratio D_r/D, where $D_r = EIR^4$ and $D = Eh\varepsilon^8 R^3$ are the bending stiffness of the ring and the shell.

Consider first the case of vibration. Then for an unstiffened shell in compliance with (17)

$$\lambda_1(0) \simeq 2\varepsilon^4 \pi^2 / l^2.$$

If η is not very large, the eigenvalue $\lambda_1(\eta)$ increases with η since c and α_1 go up with η. However, for sufficiently large η the inequality $c > c^*$ is valid and $\alpha_1 = 2\pi/l$. Calculating the derivative of the function $\lambda_v(m) = [2\pi/(lm)]^4 + \varepsilon^8 m^4$ with respect to m we obtain

$$\lambda_1(\eta) = \min_m \lambda_v(m) \simeq 8\varepsilon^4 \pi^2 / l^2 = 4\lambda_1(0) \quad \text{for} \quad \eta \gg 1.$$

Consequently,

$$\lambda_1(0) \le \lambda_1(\eta) \le 4\lambda_1(0).$$

We call the root η_v^* of the equation $\lambda_1(\eta) = 4\lambda_1(0)$ the *effective stiffness of the ring*. For $\eta < \eta_v^*$, the eigenvalue $\lambda_1(\eta)$ increases with η, otherwise $\lambda_1(\eta) = 4\lambda_1(0)$.

The plot of the function $\lambda_1(\eta)/\lambda_1(0)$ for $l = 2$, $h = 1/500$, $\nu = 0.3$ is shown in Fig. 2.7.

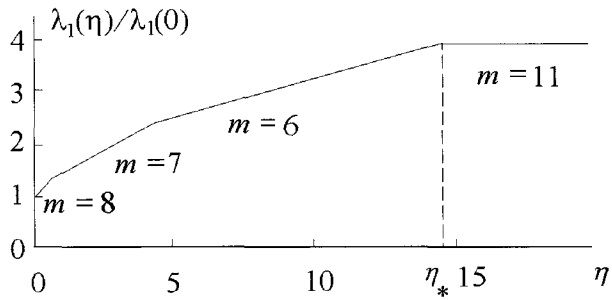

Fig. 2.7. Ratio between the eigenvalues $\lambda_1(\eta)$ and $\lambda_1(0)$ vs. the ring stiffness η.

The values of the circumferential wave number m for which the eigenvalue λ_1 attains its minimum are also presented in Fig. 2.7. These values depend on the variation interval of η. The effective stiffness $\eta_v^* = 14.6$. The spring stiffness $c = 71.9$ corresponding to η_v^* is large enough. We will see below that the effective stiffness is optimal from some point of view; therefore the case $c \gg 1$ is of interest in engineering.

Carrying out a similar calculation for the buckling problem, we obtain that

$$\lambda_1(0) \le \lambda_1(\eta) \le 2\lambda_1(0), \quad \lambda_1(0) \simeq 4\varepsilon^6\pi/(3^{1/4}l).$$

The effective stiffness η_b^* in the buckling problem is the root of the equation $\lambda_1(\eta) = 2\lambda_1(0)$.

2.7. Optimal Rings Arrangement

In the general case, the minimal positive root α_1 of Eq. (24) depends on the spring stiffness, c, and the set, $X = (x_1, x_2, \ldots, x_{n_r})$, of coordinates of

the springs. The set X is called the *arrangement.* If

$$\max_X \alpha_1(c, X) = \alpha_1(c, X^o),$$

we call $X^o(c) = (x_1^o(c), x_2^o(c), \ldots, x_{n_r}^o(c))$ the *optimal arrangement.* It follows from (25) that the optimal springs arrangement on the beam corresponds to the optimal rings arrangement on the shell.

Some optimal arrangements $X^o(c)$ of the springs have been found in [Sharypov (1997)][15] for simply supported and clamped beams. Eq. (24) have been solved numerically for $n_r \leq 6$ and various values of c. To find the optimal spring positions all possible variants of support have been analyzed. The conclusions are the following:

1) The optimal arrangement is symmetric with respect to the middle of the beam.

2) For small values of the stiffness c the optimal positions of the springs are located near the middle of the beam.

3) For $c \to \infty$ the optimal arrangement for a simply supported beam tends to the uniform one ($x_j = jl/n$) and to the almost uniform arrangement for the clamped beam.

In Fig. 2.8 the plots of x_1^o vs. c in the case of two ($n_r = 2$) symmetrically disposed ($x_2 = l - x_1$) springs are shown. The beam of length $l = 3$ is simply supported.

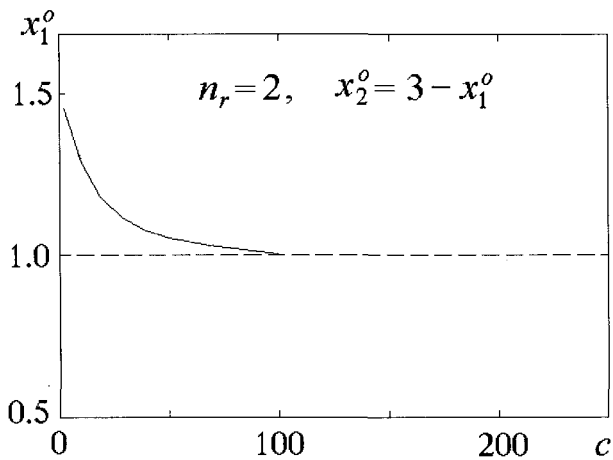

Fig. 2.8. The optimal string coordinate x_1^o vs. the spring stiffness c.

If the stiffness c is small, then $x_1^o \simeq x_2^o \simeq 1.5$. The distance between the strings and the ends of the beam decreases with the increase of c and $x_1^o \to 1$ and $x_2^o \to 2$ as $c \to \infty$.

We will call

$$X^* = \lim_{c \to \infty} X^o(c)$$

the *ultimate optimal arrangement*. For $c = \infty$ the last condition (21) takes the form $w(s_i) = 0$ and conditions (21) describe the joints of the hinges and the beam. Therefore, the ultimate optimal arrangement is the optimal arrangement of the hinges. If c is large then the optimal ring arrangement on the shell, $X^o(c)$, differs slightly from X^*.

As it was found in [Sharypov (1997)][15], if $n_r \leq 6$ then the ultimate optimal arrangement for a simply supported beam is the uniform arrangement, i.e. $X^* = X^u$, where $X^u = (l/n, 2l/n, \ldots, n_r l/n)$. Table 2.1 contains the data from [Sharypov (1997)][15] and shows some ultimate optimal arrangements for a clamped beam of length $l = n_r + 1$.

Table 2.1. Optimal hinges coordinates.

n_r	x_1^*	x_2^*	x_3^*	x_4^*	x_5^*	x_6^*
2	1.076	1.934	–	–	–	–
4	1.139	2.045	2.955	3.861	–	–
6	1.161	2.096	3.017	3.983	4.904	5.839

The nodes of oscillations of an unstiffened beam are the roots of the equation $w_n(x) = 0$, where w_n is the vibrations mode. For a simply supported beam, $w_n(x) = C\sin(\pi n x/l)$ (see (10)) and the nodes of oscillations $x_j = jl/n$ are uniformly arranged. Consequently, for a simply supported beam and $n_r \leq 6$

$$X^* = X^r, \tag{30}$$

where $X^r = (x_1^r, x_2^r, \ldots, x_{n_r}^r)$ is the roots arrangement for the equation $w_n(x) = 0$.

Comparing the data from Table 2.1 and the roots of the equation $w_n = 0$, where w_n is the vibrations mode of the clamped beam (see (12)), shows that for $n_r = 2, 4, 6$ equality (30) is valid also for a clamped beam.

It is proved in [Filippov and Lopatukhin (2001)][8] that equality (30) is valid for any homogeneous boundary conditions and any number of springs

n_r. Indeed, the condition $w(x_j) = 0$ is the equation of the constraint. Consequently, the beam stiffened by n_r hinges is a mechanical system made of an unstiffened beam by introducing n_r constraints. According to Rayleigh's theorem (see [Gould (1966)][9])

$$\alpha_1(0) \leq \alpha_1(\infty, X) \leq \alpha_n(0), \tag{31}$$

where $\alpha_1^4(0)$ and $\alpha_n^4(0)$ are the first and the n-th eigenvalues for an unstiffened beam and $\alpha_1^4(\infty, X)$ is the first eigenvalue for a beam stiffened by n_r hinges. If we assume that the coordinates of the hinges x_j are the nodes of the unstiffened beam vibrations mode, i.e. $X = X^r$, then $w_n(s)$ is also the first vibration mode of the stiffened beam corresponding to $\alpha_1(\infty)$ (see Fig. 2.9).

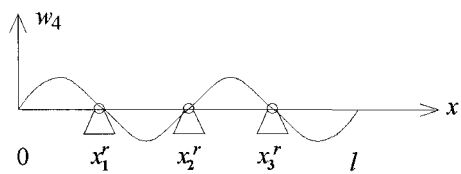

Fig. 2.9. First vibration mode of a beam stiffened by n_r hinges for $X = X^r$.

Therefore, $\alpha_1(\infty, X^r) = \alpha_n(0)$ and it follows from (31) that the eigenvalue $\alpha_1(\infty, X)$ attains its maximum value for $X = X^r$, i.e. $X^* = X^r$.

The root arrangement X^r depends only on the boundary conditions. The optimal ring arrangement in case $c \gg 1$ depends mainly on the boundary conditions, because $X^o \simeq X^* = X^r$ for the large values of stiffness c.

2.8. Homogenization

In this section we consider the uniform arrangement X^u of the rings on a freely supported cylindrical shell. This arrangement is often used in industrial applications and is the subject of theoretical considerations. On the other hand, the uniform arrangement is close to the optimal one if the edges of the shell are freely supported and $c \gg 1$.

If the number n_r of springs is large and the stiffness of each spring c is small, one can use the homogenization method (see [Babushka (1976)][3], [Sanchez-Palencia (1980)][11]) for the approximate evaluation of the eigenvalues α_k^4. Instead of the problem (9), (20), (21) we consider the equivalent

problem for the equation

$$\frac{d^4w}{dx^4} + cw\sum_{j=1}^{n-1}\delta(x-x_j) = \alpha^4 w$$

with the boundary conditions (9). Here $\delta(z)$ is Dirac's delta function, $x_j = jl/n$. In the new variables $x = sl$ and $w = \hat{w}l$ the equations are

$$\frac{d^4\hat{w}}{ds^4} + \hat{c}n\hat{w}\sum_{j=1}^{n-1}\delta(\xi - j) = \kappa\hat{w}, \tag{32}$$

where $\hat{c} = cl^3$, $\kappa = (\alpha l)^4$, and $\xi = ns$. The boundary conditions (9) take the form

$$\hat{w} = \frac{d^2\hat{w}}{ds^2} = 0 \quad \text{for} \quad s = 0, \quad s = 1. \tag{33}$$

Assuming that $n \gg 1$ and $\hat{c}n \sim 1$, we write the solution of Eq. (32) as

$$\hat{w}(s,\xi) = w_0(s,\xi) + n^{-4}w_4(s,\xi) + \cdots, \quad \kappa = \kappa_0 + n^{-4}\kappa_4 + \cdots, \tag{34}$$

where $w_i(s,\xi) = w_i(s,\xi+1)$ and, consequently,

$$< \frac{\partial^k w_i}{\partial\xi^k} >= \int_{\xi}^{\xi+1} \frac{\partial^k w_i}{\partial\xi^k} d\xi = 0, \quad i = 0,4,\ldots, \quad k = 1,2,\ldots \tag{35}$$

The operator $< \cdot >$ is called the homogenization operator. The application of this operator to both part of an equation is called the homogenization of the equation.

If we substitute (34) into (32) and (33), then we obtain the equations

$$\frac{\partial^4 w_0}{\partial\xi^4} = 0, \quad \frac{\partial^4 w_4}{\partial\xi^4} + \frac{\partial^4 w_0}{\partial s^4} + \hat{c}n\sum_{i=1}^{n}\delta(\xi - i)w_0 = \kappa_0 w_0 \tag{36}$$

and the boundary conditions

$$w_0 = \frac{\partial^2 w_0}{\partial s^2} = 0, \quad w_4 = \frac{\partial^2 w_4}{\partial s^2} = 0 \quad \text{for} \quad s = 0, \quad s = 1, \tag{37}$$

as a result of equating the coefficients of n^4 and n^0. From (35) and the first equation in (36) it follows that

$$\frac{\partial^3 w_0}{\partial\xi^3} = v_3(s), \quad v_3(s) =< v_3(s) >=< \frac{\partial^3 w_0}{\partial\xi^3} >= 0.$$

A further integration followed by a homogenization gives

$$\frac{\partial^2 w_0}{\partial\xi^2} = v_2(s) = 0, \quad \frac{\partial w_0}{\partial\xi} = v_1(s) = 0, \quad w_0(s,\xi) = v_0(s).$$

After the homogenization of the second equation in (36) we get

$$\frac{d^4 v_0}{ds^4} + \hat{c}nv_0 = \kappa_0 v_0. \tag{38}$$

Equation (38) describes the vibrations of a simply supported beam on an elastic base (see Fig. 2.10).

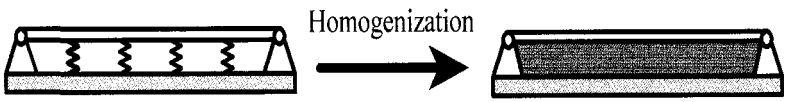

Fig. 2.10. Stiffened beam and beam upon an elastic base.

The solutions of Eq. (38) which satisfy the first of the boundary conditions (37) are $w_{0k} = \sin k\pi s$,

$$\kappa_{0k} = (k\pi)^4 + \hat{c}n, \quad k = 1, 2, \ldots \tag{39}$$

We seek the unknown function w_4 in the form

$$w_4(s, \xi) = v_4(s) + u_4(s, \xi),$$

where $< u_4 >= 0$.

It follows from (36) and (38) that

$$\frac{\partial^4 u_4}{\partial \xi^4} = \hat{c}nv_0[1 - \sum_{j=1}^{n-1} \delta(\xi - j)].$$

Integrating this equation gives

$$\frac{\partial^3 u_4}{\partial \xi^3} = \hat{c}nv_0[\xi - j - c_3(s)], \quad j \leq \xi \leq j + 1.$$

After the homogenization, the last equation takes the form

$$c_3 = \int_j^{j+1} (\xi - j) d\xi = \frac{1}{2},$$

and, after another integration followed by homogenization, we get

$$u_4(s, \xi) = \hat{c}nv_0[(\xi - j)^2(\xi - j - 1)^2 - 1/720], \quad j \leq \xi \leq j + 1.$$

Substituting (34) into (32) and equating the coefficients of n^{-4}, we obtain the equation of the next approximation. The homogenization of this equation yields

$$\frac{d^4 v_4}{ds^4} + \hat{c}nv_4 - \frac{\hat{c}^2 n^2}{720} v_0 = \kappa_0 v_4 + \kappa_4 v_0.$$

From the compatibility condition for the above equation we find

$$\kappa_4 = -\frac{c^2 n^2}{720}.$$

Consequently,

$$\kappa_k \simeq (k\pi)^4 + \hat{c}n - \frac{\hat{c}^2}{720n^2}, \quad k = 1, 2, \ldots \tag{40}$$

Table 2.2 lists the values of κ_1 calculated from the numerical solution of Eq. (24) and from the asymptotic formulas of the first and second approximations in (39) and (40).

Table 2.2. Comparison of numerical and asymptotic results.

n	$\hat{c}$	Parameter κ_1 calculated by (24)	(40)	(39)
2	1	99.41	99.41	99.41
	10	117.0	117.4	117.4
	10^2	278.7	293.9	297.4
3	10	127.4	127.4	127.4
	10^2	395.3	395.8	397.4
	10^3	2940	2942	3097
6	10^2	697.0	697.0	697.4
	10^3	6056	6059	6097
	10^4	56131	56236	60097

Although formulas (39) and (40) are derived for $n \gg 1$ and $\hat{c} \sim 1/n \ll 1$, they provide good approximations for the exact values of κ_1 even for $n = 2$ (for one ring) and for a sufficiently large stiffness $\hat{c}$ (for $\hat{c} = 100$ and more).

It follows from (29) and (39) that

$$\alpha_1^4 = (\pi/l)^4 + \eta(\varepsilon m)^8. \tag{41}$$

Substituting (41) into (28) and differentiating with respect to m give the following approximate formula

$$\frac{\lambda_1(\eta)}{\lambda_1(0)} \simeq \begin{cases} (1+\eta)^{1/2}, & \text{for vibrations,} \\ (1+\eta)^{3/4}, & \text{for buckling,} \end{cases} \tag{42}$$

where, in accordance with (17),

$$\lambda_1(0) \simeq \begin{cases} 2\varepsilon^4\pi^2/l^2, & \text{for vibrations,} \\ 4\varepsilon^6\pi/(3^{3/4}l), & \text{for buckling.} \end{cases}$$

2.9. Irregular Arrangement

Homogenization may be used only in the case of a uniform springs arrangement. Instead of the homogenization method for an irregular arrangement we apply Rayleigh's method. For example, we consider an irregular springs arrangement on a clamped beam. We recall here that the ultimate optimal arrangement for a clamped beam is irregular. Rayleigh's formula (see, in particular, [Gould (1966)][9]) for a stiffened beam may be written in dimensionless form as

$$\alpha_1^4 = (I_1 + I_2)/I_0,$$

$$I_1 = \int_0^l \left(\frac{d^2w}{dx^2}\right)^2 dx, \quad I_2 = c\sum_{j=1}^{n-1} w^2(x_j), \quad I_0 = \int_0^l w^2\,dx. \tag{43}$$

Substituting the first vibration mode $w_1(x)$ for a non-stiffened clamped beam (12) into (43) gives

$$\kappa_1(X) = [\alpha_1(X)l]^4 = z_1^4 + \gamma(X)\hat{c}n, \quad \hat{c} = cl^3. \tag{44}$$

Here z_1 is the minimal positive root of Eq. (14). The function

$$\gamma(X) = \frac{1}{n}\sum_{j=1}^{n-1}[U(\alpha_1 x_j) - \kappa_1 V(\alpha_1 x_j)]^2 \tag{45}$$

depends on the springs arrangement $X = (x_1, x_2, \ldots, x_{n_r})$.

In Table 2.3 we can see the values γ for the optimal ultimate X^* and uniform X^u springs arrangements.

Table 2.3. Values of the function $\gamma(X)$.

n	$\gamma(X^*)$	$\gamma(X^u)$
2	1.261	1.261
3	1.178	1.018
5	1.102	1.001

If $n = 2$, then $X^* = X^u$. In the case $n > 2$ it follows from (44) that κ_1, for the optimal ultimate arrangement, is greater than for the uniform one since $\gamma(X^*) > \gamma(X^u)$.

Table 2.4 lists the values of the parameter κ_1, obtained by means of different methods for a stiffened beam with clamped edges. The approximate values $\tilde{\kappa}_1(X^*)$ have been found by formula (44) for the optimal ultimate

arrangement of the strings. The values $\kappa_1(X^*)$ and $\kappa_1(X^u)$ were calculated by means of the numerical solution of Eq. (24) for the optimal ultimate and uniform arrangements, respectively.

Table 2.4. Numerical and asymptotic results for a clamped stiffened beam.

n	$\hat{c}$	$\tilde{\kappa}_1(X^*)$	$\kappa_1(X^*)$	$\kappa_1(X^u)$
2	1	503.0	505.6	505.6
	10	525.8	527.9	527.9
	100	752.7	747.2	747.2
3	10	533.6	538.3	532.2
	100	831.1	836.7	804.2
	1000	3806	3800	3363
5	100	1057	1046	1001
	1000	6070	5973	5523
	5000	28350	26124	25354

From Table 2.4 we can see that the relative error of the approximate formula (44) remains small when the parameters n and c widely vary. In the case $n > 2$, the values κ_1 for the optimal ultimate springs arrangement are larger than for the uniform arrangement.

Let us apply Rayleigh's method for the uniform springs arrangement X^u on a simply supported beam. Substituting the first vibration mode of a non-stiffened beam, $w_1 = \sin(\pi x/l)$, into (43) we obtain

$$\kappa_1 = \pi^4 + 2\gamma\hat{c}n,$$

where

$$\gamma = \frac{1}{n}\sum_{j=1}^{n-1} \sin^2(\pi j/n) = \frac{1}{2}.$$

Consequently, $\kappa_1 = \pi^4 + \hat{c}n$. Exactly the same formula for κ_1 gives the first approximation of homogenization (see (39)).

It follows from (44) that for clamped beams and shells

$$\alpha_1^4 = (z_1/l)^4 + \gamma\eta(\varepsilon m)^8. \tag{46}$$

Substituting (46) into (28), we have

$$\frac{\lambda_1(\eta)}{\lambda_1(0)} \simeq \begin{cases} (1+\gamma\eta)^{1/2}, & \text{for vibrations,} \\ (1+\gamma\eta)^{3/4}, & \text{for buckling,} \end{cases} \tag{47}$$

where $\lambda_1(0)$ can be found from (17).

2.10. Effective Stiffness

Usually, formulas (42) and (47) provide an approximation for the first (minimal) eigenvalue λ_1, but there is an important exception. For example, for a freely supported shell stiffened by a symmetrically positioned ring ($n_r = 1$, $x_j = l/2$) such an exceptional case takes place.

Then Eq. (24) has root $\alpha = 2\pi/l$, which is independent of the stiffness c. Hence there is a corresponding eigenvalue

$$\lambda = \begin{cases} 4\lambda_1(0), & \text{for vibrations,} \\ 2\lambda_1(0), & \text{for buckling.} \end{cases} \tag{48}$$

which does not depend on η (see Sect. 2.6). To find the first eigenvalue for $\eta > \eta^*$, where η^* is the effective stiffness, one has to use formula (48) instead of formula (42), which is valid only for $\eta < \eta^*$.

In the general case, Eq. (24) has a stiffness-independent or c-independent root if the arrangement of the rings is the following: $X = X^r = X^*$. The ultimate optimal arrangement X^* is important for engineering applications since, for $c \gg 1$, it differs only slightly from the optimal ring arrangement X^o.

Consider the ultimate optimal rings arrangement X^* for a freely supported shell. It is proved in Section 2.7 that, in this case, the ultimate optimal arrangement is uniform. The minimal c-independent root is $\alpha = \pi n/l$. The corresponding stiffness-independent eigenvalue] can be found as

$$\lambda = \begin{cases} n^2\lambda_1(0), & \text{for vibrations,} \\ n\lambda_1(0), & \text{for buckling.} \end{cases} \tag{49}$$

In the case of vibrations, the effective stiffness η_v^* is the root of the equation $\lambda_1(\eta) = n^2\lambda_1(0)$. In the case of buckling, η_b^* satisfies the equation $\lambda_1(\eta) = n\lambda_1(0)$. Using the approximate expression (42) we obtain the following approximate values of η_v^* and η_b^*

$$\eta_v^*(n) \simeq n^4 - 1, \quad \eta_b^*(n) \simeq n^{4/3} - 1. \tag{50}$$

The approximate values $\eta_v^*(2) \simeq 15$, $\eta_b^*(2) \simeq 1.52$, and $\eta_b^*(3) \simeq 3.33$ found by (50) are in good agreement with the exact ones $\eta_v^*(2) = 14.6$, $\eta_b^*(2) = 1.5$, and $\eta_b^*(3) = 3.2$. The two last results are reported in [Alfutov (1978)][1].

We use formula (42) for $\eta \leq \eta^*$ and formula (49) for $\eta > \eta^*$. Therefore, in the case of vibration of freely supported uniformly stiffened cylindrical shell,

$$\frac{\lambda_1(\eta)}{\lambda_1(0)} \simeq \begin{cases} (1+\eta)^{1/2}, & 0 \leq \eta \leq n^4 - 1, \\ n^2, & \eta > n^4 - 1. \end{cases} \tag{51}$$

In the case of buckling of such shell under external pressure,

$$\frac{\lambda_1(\eta)}{\lambda_1(0)} \simeq \begin{cases} (1+\eta)^{3/4}, & 0 \le \eta \le n^{4/3} - 1, \\ n, & \eta > n^{4/3} - 1. \end{cases} \tag{52}$$

The plots of the functions (51) and (52) for $n = 2$ practically coincide with the plots in Fig. 2.7 and in [Alfutov (1978)][1], respectively.

Consider the ultimate optimal arrangement X^* on a clamped shell stiffened by n_r identical rings. It is shown in Section 2.7 that, in this case, X^* coincides with the roots arrangement X^r for the equation $w_n = 0$, where w_n is the vibrations mode of a clamped unstiffened beam (see (12)). At the same time, the function w_n is the vibrations mode of a clamped stiffened beam for $X = X^r$. Therefore, Eq. (24) has the stiffness-independent root $\alpha = z_n/l$, where z_n is the root of Eq. (14). We use the following approximation to calculate z_n:

$$z_n \simeq \pi(2n+1)/2, \quad n = 1, 2, \ldots \tag{53}$$

The relative error of this formula is less than 0.1% for all n.

The frequency parameter corresponding to $\alpha = z_n/l$

$$\lambda = \begin{cases} r_n^2 \lambda_1(0), & \text{for vibrations,} \\ r_n \lambda_1(0), & \text{for buckling.} \end{cases} \tag{54}$$

does not depend on η. Here $r_n = z_n/z_1 \simeq (2n+1)/3$.

Using formulas (47) we obtain the following approximate values of the effective stiffness for the vibrations and buckling

$$\eta_v^*(n) \simeq \gamma^{-1}(r_n^4 - 1), \quad \eta_b^*(n) \simeq \gamma^{-1}(r_n^{4/3} - 1). \tag{55}$$

In Table 2.5 we can see the values η_v^* and η_b^* of the effective stiffness for various n. These values are less than the values of the effective stiffness

Table 2.5. Values of η_v^* and η_b^*.

n	η_v^*	η_b^*
2	5.326	0.774
3	25.99	1.906
5	161.4	4.179

for a shell with simply supported edges.

In the case of vibrations of a clamped stiffened cylindrical shell, the first eigenvalue is

$$\frac{\lambda_1(\eta)}{\lambda_1(0)} \simeq \begin{cases} (1+\gamma\eta)^{1/2}, & 0 \le \eta \le \eta_v^*, \\ r_n^2, & \eta > \eta_v^*. \end{cases} \tag{56}$$

In the case of buckling of such shell under an external pressure, we can find the first eigenvalue

$$\frac{\lambda_1(\eta)}{\lambda_1(0)} \simeq \begin{cases} (1+\gamma\eta)^{3/4}, & 0 \le \eta \le \eta_b^*, \\ r_n, & \eta > \eta_b^*. \end{cases} \tag{57}$$

It follows from formulas (51), (52), (56), and (57) that $\lambda_1(\eta) > \lambda_1(0)$ for $\eta > 0$, i.e. the fundamental vibration frequency and the critical pressure of a stiffened shell are higher than of an unstiffened one. All formulas are derived under the assumption that

$$M_s = M_0 + M_r,$$

where M_s is the mass of the stiffened shell, M_0 is the mass of the unstiffened shell, and M_r is the mass of the rings. This means that a stiffened shell is heavier than an unstiffened one. In the next sections we compare the vibrations frequencies and the critical pressures for stiffened and unstiffened shells of equal masses.

2.11. Optimal Design of Vibrating Stiffened Shells

We suppose that the mass, M_s, of a ring-stiffened cylindrical shell is given and seek the optimal parameters of the rings and the shell, for which the fundamental vibrations frequency have the largest value.

We consider both a freely supported (FS) shell and a clamped (CL) shell, assuming the rings arrangement $X = X^*$. From formulas (51) and (56)

$$\frac{\lambda_1(\eta)}{\lambda_1(0)} \simeq \begin{cases} (1+\gamma^*\eta)^{1/2}, & 0 \le \eta \le \eta_v^*, \\ r_n^2, & \eta > \eta_v^*, \end{cases} \tag{58}$$

where

$$\eta_v^* = \frac{1}{\gamma^*}(r_n^4 - 1), \quad \gamma^* = \begin{cases} 1, & \text{FS}, \\ \gamma(X^*), & \text{CL}, \end{cases} \quad r_n = \begin{cases} n, & \text{FS}, \\ z_n/z_1, & \text{CL}. \end{cases}$$

The function $\gamma(X)$ is given by (45).

The fundamental vibration frequency ω_0 of an unstiffened cylindrical shell of thickness h_0 and length l can be found by the approximate formula, following (2) and (17)

$$\omega_0^2 = \frac{E\lambda_1(0)}{\rho R^2}, \qquad \lambda_1(0) = \begin{cases} h_0\pi^2/(\sqrt{3\sigma}l^2), & \text{FS}, \\ h_0 z_1^2/(\sqrt{3\sigma}l^2), & \text{CL}, \end{cases} \tag{59}$$

where $\sigma = 1 - \nu^2$.

The mass of an unstiffened shell is $M_0 = Gh_0$, where $G = 2\pi R^3\rho l$. We compare ω_0 with the fundamental vibration frequency, ω_1, of an stiffened shell of thickness $h < h_0$ and mass

$$M_s = M + M_r = M_0, \tag{60}$$

where $M = Gh$ is the mass of the skin (the mass of the shell), M_r is the mass of the reinforcement (the mass of the rings). We consider rings with rectangular cross-sections of width a and height $b = ka$. In this case $M_r = 2\pi R^3\rho n_r a^2 k$.

Using relations (58) and (59), we obtain

$$f_v^2 = \frac{\omega_1^2}{\omega_0^2} = \begin{cases} d\sqrt{1+\gamma^*\eta}, & \eta \le \eta_v^*, \\ dr_n^2, & \eta > \eta_v^*, \end{cases} \tag{61}$$

where

$$d = \frac{h}{h_0}, \quad \eta = \frac{Ba^4}{d^3}, \quad B = \frac{\sigma n k^3}{h_0^3 l}. \tag{62}$$

It follows from (60) and (62) that

$$d = 1 - Aa^2, \quad A = \frac{n_r k}{l h_0}, \quad \eta = \frac{(1-d)^2 B}{d^3 A^2}. \tag{63}$$

Substituting the expression of η from (63) into (61) gives

$$f_v^2(d) = \begin{cases} dr_n^2, & 0 \le d \le d_v^*, \\ d\sqrt{1+\beta(d-1)^2/d^3}, & d_v^* \le d \le 1, \end{cases}$$

where $\beta = \gamma^* B/A^2$ and $d_v^* \in [0,1]$ is the root of the cubic equation

$$g(d) = d^3 - q(d-1)^2 = 0, \quad q = \beta/(\gamma^*\eta_v^*) > 0. \tag{64}$$

By the inequalities $g(1) = 1 > 0$ and $g(0) = -q < 0$, the function $g(x)$ has at least one root in the interval (0,1). This root is unique, since

$$g' = dg/dx = 3x^2 - 2q(x-1) > 0 \quad \text{for} \quad x \in [0,1].$$

The values of the parameters d, a, and η for which the function f_v attains its maximum are called the optimal values. To find the optimal value of d we study the behavior of the function $y(d) = f_v^4(d)$. This function increases for $0 \le d \le d_v^*$. Therefore, it attains its maximum for $d \in [d_v^*, 1]$. For these values of d the function $y(d)$ and its derivatives have the form

$$y = d^2 + \beta(d - 2 + 1/d), \quad y' = 2d + \beta - \beta/d^2, \quad y'' = 2 + 2\beta/d^3 > 0.$$

The first derivative $y'(d)$ increases for $d \in [d_v^*, 1]$ since $y''(d) > 0$. Consequently, the function $y(d)$ has no local maximum in the interval $[d_v^*, 1]$. This is also valid for the function $f_v = \sqrt[4]{y}$. It can attain its maximum f_v^* only at the ends of the interval $[d_v^*, 1]$, i.e.

$$f_v^* = \max[f_v(d_v^*), f_v(1)] = \max(r_n\sqrt{d_v^*}, 1).$$

The inequality $r_n\sqrt{d_v^*} > 1$ is valid if and only if $g(r_n^{-2}) < 0$. The last inequality holds if

$$h_0 < \sigma lk \frac{r_n^2(r_n^2 - 1)n}{(r_n^2 + 1)n_r^2}.$$

Therefore, for sufficiently thin shells,

$$f_v^* = f_v(d_v^*) = r_n\sqrt{d_v^*}, \tag{65}$$

and the optimal value of the parameter d is d_v^*. Substituting $d = d_v^*$ into (63) we obtain the optimal values of a and η,

$$a_v^* = \sqrt{(1 - d_v^*)/A}, \quad \eta_v^* = \frac{(1 - d_v^*)^2 B}{(d_v^*)^3 A^2}.$$

Hence, the effective stiffness η_v^* is at the same time the optimal stiffness ensuring the maximal value of the fundamental frequency.

It follows from (64) that, for $n \gg 1$,

$$d_v^* \sim q^{1/3} \sim n^{-5/3}, \quad f_v^*(n) \sim (nd_v^*)^{1/2} \sim n^{1/6}.$$

Therefore, the fundamental vibration frequency of a stiffened shell increases with n for large n. The following approximate expression for d_v^*

$$d_v^* \simeq q^{1/3}\left(1 - \frac{2}{3}q^{1/3}\right), \quad q \ll 1 \tag{66}$$

is derived by means of an asymptotic method (see [Bauer *et al.* (1993)][4]). Formula (66) is valid for $n \gg 1$ since, in this case, $q \ll 1$.

Consider a freely supported shell of length $l = 4$, thickness $h_0 = 0.01$, and Poisson's ratio $\nu = 0.3$, stiffened by $n_r = n - 1$ rings with square

Table 2.6. Approximate and exact values of d_v^*.

n	Appr. d_v^*	Exact d_v^*
6	0.297	0.316
7	0.245	0.254
8	0.204	0.209
9	0.172	0.175
10	0.147	0.148

cross-sections $k = 1$. The approximate values of d_v^* calculated in (66) and its exact values for various n are given in Table 2.6 . For $n > 6$ the error of formula (66) is less than 5%.

In Table 2.7 one can see the values of d_v^*, a_v^*, and f_v^* for the same stiffened shell. The optimal parameter for freely supported (FS) and clamped (CL) shells are given in the left and right columns, respectively.

Table 2.7. Optimal values of the parameters.

	FS shell			**CL shell**		
n_r	d_v^*	a_v^*	f_v^*	d_v^*	a_v^*	f_v^*
1	0.881	0.0689	1.88	0.924	0.0551	1.60
2	0.690	0.0788	2.49	0.785	0.0655	2.07
4	0.402	0.0773	3.17	0.535	0.0682	2.68
6	0.254	0.0705	3.53	0.370	0.0648	3.04
8	0.175	0.0642	3.76	0.268	0.0605	3.28

For the shells under consideration, the ratio $f_v^* = \omega_1^*/\omega_0$ increases with n_r. The fundamental vibration frequency ω_1^* of an optimal shell stiffened by eight optimal rings is about 3.5 times higher than the fundamental frequency ω_0 for an unstiffened shell of the same mass.

It follows from (60) that $d_v^* = M^*/M_s^*$, where M^* and M_s^* are the optimal masses of the skin and the whole stiffened shell, respectively. If the number n_r of rings is increased, then the ratio M^*/M_s^* decreases. For $n_r = 1$ and an FS shell, the optimal mass of the skin makes up 88.1% of the whole mass of the stiffened shell and for $n_r = 8$ it makes up only 17.5% whereas 82.5% falls at the reinforcement.

The ratio $f_v^* = \omega_1^*/\omega_0$, as a function of n_r and k for an FS shell with parameters $l = 4$, $h_0 = 0.01$, and $\nu = 0.3$, is shown in Fig. 2.11, where the points corresponding to the integer n_r are joined by line segments.

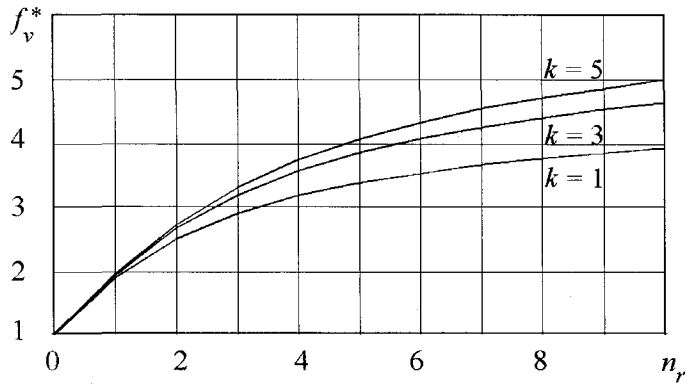

Fig. 2.11. The ratio $f_v^* = \omega_1^*/\omega_0$ vs. n_r and k for an FS shell.

The function $f_v^*(n_r, k)$ increases with k, but the suggested approximate approach is applicable only in the case $ka \ll 1$, since we use the beam model of the ring. For large values of k, the ring is wide and it must be treated as an annular thin plate.

2.12. Optimal Design of Buckling Shells

Consider the static buckling problem for a stiffened cylindrical shell under uniform external lateral pressure. Assuming that the shell edges are freely supported (FS) or clamped (CL) and the rings arrangement is $X = X^*$, we obtain, by means of (52) and (57), the following relation

$$\frac{\lambda_1(\eta)}{\lambda_1(0)} \simeq \begin{cases} (1+\gamma^*\eta)^{3/4}, & 0 \le \eta \le \eta_b^*, \\ r_n, & \eta > \eta_b^*, \end{cases} \tag{67}$$

where

$$\eta_b^* = \frac{1}{\gamma^*}(r_n^{4/3} - 1), \quad \gamma^* = \begin{cases} 1, & \text{FS}, \\ \gamma(X^*), & \text{CL}, \end{cases} \quad r_n = \begin{cases} n, & \text{FS}, \\ z_n/z_1, & \text{CL}. \end{cases} \tag{68}$$

The critical pressure p_0 of an unstiffened cylindrical shell of thickness h_0 is found from (3) and (17):

$$p_0 = Eh_0\lambda_1(0), \qquad \lambda_1(0) = \begin{cases} 2h_0^{3/2}\pi/(3l\sqrt{6}\sigma^{3/4}), & \text{FS}, \\ 2h_0^{3/2}z_1/(3l\sqrt{6}\sigma^{3/4}), & \text{CL}. \end{cases} \tag{69}$$

We compare p_0 with the critical pressures p_1 of a stiffened shell of the same mass, assuming that the rings cross-sections are rectangles with width

a and height $b = ka$. We find the ratio $f_b = p_1/p_0$ from (67) and (69):

$$f_b = \frac{p_1}{p_0} = \begin{cases} d^{5/2}(1+\gamma^*\eta)^{3/4}, & 0 \le \eta \le \eta_b^*, \\ d^{5/2} r_n, & \eta > \eta_b^*, \end{cases} \tag{70}$$

where d and η are given by (62).

Taking (63) into account, we write

$$f_b(d) = \begin{cases} d^{5/2} r_n, & 0 \le d \le d_b^*, \\ d^{5/2}[1+\beta(d-1)^2/d^3]^{3/4}, & d_b^* \le d \le 1, \end{cases}$$

where $\beta = \gamma^* B/A^2$, d_b^* is the root of the cubic equation

$$d^3 - q(d-1)^2 = 0, \quad q = \beta/(\gamma^* \eta_b^*).$$

This equation has a unique root in the interval (0,1).

The function $y = f_b^{4/3}$ increases with d for $d < d_b^*$. Consequently, it attains its maximum at $d \in [d_b^*, 1]$. For $d \in [d_b^*, 1]$ the function y takes the form

$$y = d^{10/3} + \beta d^{1/3}(d-1)^2.$$

If $h_0 \ll 1$, then $\beta \gg 1$ and the roots d_1, d_2, and d_3 of the equation

$$y' = [10d^3 + \beta(7d^2 - 8d + 1)]/(3d^{2/3}) = 0$$

have the following asymptotic expansions

$$d_1 \simeq -\frac{7\beta}{10}, \quad d_2 \simeq \frac{1}{7}\left(1 + \frac{5}{147\beta}\right), \quad d_3 \simeq 1 - \frac{5}{3\beta}.$$

The function $y(d)$ attains its local maximum and local minimum at $d = d_2$ and $d = d_3$, respectively. For h_0 sufficiently small, the inequality $d_2 < d_b^*$ is valid since $d_2 \to 1/7$ and $d_b^* \to 1$ if $h_0 \to 0$. Therefore, for small h_0 the function y does not have a local maximum at $d \in (d_b^*, 1)$ and attains its maximum only if $d = d_b^*$ or $d = 1$. The same is valid for the function $f_b = y^{3/4}$. Hence, for a sufficiently thin stiffened shell the largest value f_b^* of the function f_b is

$$f_b^* = \max\,[r_n (d_b^*)^{5/2}, 1].$$

For h_0 sufficiently small, the inequality $r_n (d_b^*)^{5/2} > 1$ holds, because $r_n > 1.5$ and $d_b^* \to 1$ if $h_0 \to 0$. Consequently,

$$f_b^* = r_n (d_b^*)^{5/2}$$

and at the same time the effective stiffness, η_b^*, is the optimal stiffness.

From the asymptotic formulas

$$d_* \sim n^{-7/9}, \quad f_b^* \sim n^{-17/18}, \quad n \gg 1 \tag{71}$$

it follows that the function $f_b^*(n)$ decreases for large n.

In Table 2.8 the values of d_b^*, a_b^*, and f_b^* for freely supported and clamped shells with $l = 4$, $h_0 = 0.01$, $\nu = 0.3$ and $k = 1$ are given.

Table 2.8. Optimal values of the parameters.

	FS shell			**CL shell**		
n_r	d_b^*	a_b^*	f_b^*	d_b^*	a_b^*	f_b^*
1	0.957	0.0414	1.79	0.969	0.0353	1.54
2	0.905	0.0436	2.34	0.926	0.0385	1.92
4	0.812	0.0434	2.97	0.850	0.0387	2.44
6	0.736	0.0420	3.25	0.786	0.0373	2.73
8	0.674	0.0404	3.36	0.731	0.0367	2.89

The ratio $f_b^* = p_1^*/p_0$ as a function of n_r and k for an FS shell and for the same values of the parameters l, h_0, and ν is shown in Fig. 2.12.

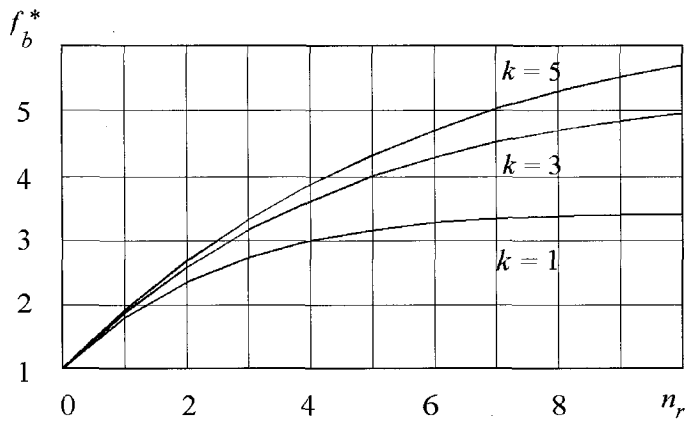

Fig. 2.12. The ratio $f_b^* = p_1^*/p_0$ vs. n_r and k for FS shell.

For a stiffened shell considered here, the ratio $f_b^*(n_r)$ increases with the number of rings, n_r, while n_r is not very large. However, this ratio decreases for sufficiently large n_r by (71). Hence, in contrast to vibrations,

the function $f_b^*(n_r)$ attains its local maximum for the finite number $n_r = n_r^*$, i.e. in the case of buckling the optimal number of the rings, n_r^*, exists.

In the case of $l = 4$, $h_0 = 0.01$, $\nu = 0.3$, and $k = 1$ for a freely supported shell, the optimal number of rings is $n_r^* = 9$, because the function $f_b^*(n_r)$ has the largest value 3.375 at $n_r = 9$ (see Fig. 2.12).

2.13. Conclusion

The asymptotic technique presented in this paper can be used for various stiffened thin-walled structures. The buckling and vibrations of a ring-stiffened cylindrical shell with a slanted edge have been considered in [Filippov (1997)][6]. For such shells, the vibrations and buckling modes are localized near the longest generatrix of the cylindrical shell. The evaluation procedure of the critical external pressure, the fundamental vibration frequency and the optimal parameters is similar to the procedure used for a shell with a straight edge.

Another interesting problem is the analysis of two joint shells with slanted edges. Often this type of structure is used in pipelines. The problem becomes more complicated, but even in this case the asymptotic approach allows one to obtain approximate analytical solutions and develop algorithms to compute the optimal parameters (see [Filippov (1999)][7]).

Acknowledgment

The author gratefully acknowledges the financial support provided by the Russian Foundation for Fundamental Research under Grant 04-01-00257.

References

1. Alfutov, N. A. (1978). Background of Elastic System Stability Design, Mashinostroenie, Moscow, 312 p. (in Russian)
2. Amiro, I. Y. and Zarutskii, V. A. (1980). Theory of ribbed shells, Naukova Dumka, Kiev, 368 p. (in Russian)
3. Babushka, I. (1976). Homogenization approach in engineering, *Lectures Notes in Economics and Math. System*, **134**, pp. 137–153.
4. Bauer, S. M., Filippov, S. B., Smirnov, A. L. and Tovstik, P. E. (1993). Asymptotic methods in mechanics with applications to thin shells and plates, in *Asymptotic Methods in Mechanics,* CRM Proc. and Lect. Notes, AMS, **3**, pp. 3–142.
5. Donnell, L. H. (1976). Beams, plates and shells, McGraw-Hill.
6. Filippov, S. B. (1997). Application of the asymptotic methods for the evaluation of optimal parameters for the ring-stiffened cylindrical shells, *Integral*

methods in science and engineering, C. Constanda et al., editors, Essex. Longman, **2**, pp. 79–83.
7. Filippov, S. B. (1999). Theory of joint and stiffened shells, St. Petersburg State University Press, St. Petersburg, 196 p. (in Russian)
8. Filippov, S. B. and Lopatukhin, A. L. (2001). Optimal arrangement of rings used for the reinforcement of thin cylindrical shells, *CD-Rom Proceedings of 2-nd European Conference of Computational Mechanics, Solids, Structures and Coupled Problem in Engineering*, Cracow, Poland.
9. Gould, S. H. (1966). Variational methods for eigenvalue problems, Oxford Univ. Press, London.
10. Ross, C. T. F., Haynes, P. and Richards, W. D. (1995). Vibration of ring-stiffened circular cylinders under external water pressure, *Computers & Structures*, **60**, pp. 1013–1019.
11. Sanchez-Palencia, E. (1980). Non-homogeneous media and vibration theory, Lectures Notes in Physics, **127**, Springer-Verlag, Berlin, 398 p.
12. Tian, J., Wang, C. M and Swaddiwudhipohg, S. (1999). Elastic buckling analysis of ring-stiffened cylindrical shell under general pressure loading via the Ritz method, in *Thin Walled Structures*, **35**, pp. 1–24.
13. Timoshenko, S. (1955). Vibration problems in engineering, Van Nostrand.
14. Tovstik, P. E. and Smirnov, A. L. (2001). Asymptotic methods in the buckling theory of elastic Shells, World Scientific, Singapore, 347 p.
15. Sharypov, D. V. (1997). Low-frequency vibrations of the ring-stiffened thin cylindrical shell, *St. Petersburg Univ. Mech. Bulletin*, **3**, pp. 29–34.
16. Wang, J. T. S. (1970). Orthogonally stiffened cylindrical shells subjected to internal pressure, *AIAA Journal*, **3**, pp. 455–461.
17. Yang, B. and Zhou, J. (1995). Analysis of ring-stiffened cylindrical shells, *J. of Applied Mechanics*, **62**, pp. 1005–1014.

This page is intentionally left blank

CHAPTER 3

ASYMPTOTIC ANALYSIS OF THIN SHELL BUKLING

Andreĭ L. Smirnov

Department of Theoretical and Applied Mechanics, St. Petersburg State University, St. Petersburg, Russia, 198504
E-mail: smirnov@AS1245.spb.edu

Buckling of thread-reinforced elastic thin shells is discussed in this paper. Smirnov's and Tovstik's results on the asymptotic analysis of thin isotropic shells are generalized to the case of a shell consisting of a matrix reinforced by fibers. In this work both localized and non localized bucklings are considered, Examples of these cases are, respectively, a convex shell under hydrostatic pressure and a cylindrical shell under axial or hydrostatic pressure. Special attention is devoted to the effect of anisotropy and boundary conditions on the critical buckling load.

3.1. Introduction

We consider a thin shell made of composite material, consisting of a matrix which is reinforced with threads situated in planes parallel to the midsurface. On the shell midsurface we introduce the curvilinear coordinates α_1, α_2 coinciding with the curvature lines. The coordinate z is directed along the normal to the midsurface. We assume that the shell is reinforced with N systems of fibers, inclined at angles $\theta^{(k)}$, $k = 1, 2, \ldots, N$, with respect to the axis α_1.

The shell stress σ_{ij} is a sum of the matrix stress $\sigma_{ij}^{(0)}$ and the averaged stress $\sigma_{ij}^{(k)}$, caused by the extensions of the fibers

$$\sigma_{ij} = \sigma_{ij}^{(0)} + \sum_{k=0}^{N} \sigma_{ij}^{(k)}. \tag{1}$$

The elastic energy Π of the shell can be expressed as the sum of the stretching energy Π_ε and the bending energy $\Pi_\varkappa$ [Tovstik and Smirnov

(2001)][1]

$$\Pi = \Pi_\varepsilon + \Pi_\varkappa,$$

where Π_ε and $\Pi_\varkappa$ are given by

$$\Pi_\varepsilon = \frac{1}{2}\iint (T_1\varepsilon_1 + T_2\varepsilon_2 + S\omega)\, d\Sigma = \frac{1}{2}\iint K_{ij}\varepsilon_i d\Sigma,$$
$$\Pi_\varkappa = \frac{1}{2}\iint (M_1\varkappa_1 + M_2\varkappa_2 + 2H\tau)\, d\Sigma.$$

Here T_1, T_2, and S are the stress resultants and M_1, M_2, and H are the moment resultants. ε_1, ω, and ε_2 are the stretching-shear strains and $\varkappa_1$, τ, and $\varkappa_2$ are the bending-twisting strains of the midsurface. $d\Sigma = A_1 A_2\, d\alpha_1 d\alpha_2$ is the area element and the integration in Π_ε and $\Pi_\varkappa$ is performed on the entire midsurface. K_{ij} are the coefficients in the constitutive relations whose expressions have been obtained in [Haseganu *et al.* (2000)][2]. For example, $K_{11} = E_1/(1 - \nu_1\nu_2)$ for an orthotropic shell with Young's moduli E_1 and E_2, Poisson's ratios ν_1 and ν_2 and shear modulus G.

We simplify the equilibrium equations by the usual assumptions for the Donnell equations for shallow shells. We assume that the values of the metric coefficients, A_1, A_2, and radii of curvature, R_1, and R_2, are approximately constant and $dx_1 = A_1 d\alpha_1$, $dx_2 = A_2 d\alpha_2$. If the reinforcing fibers are symmetric with respect to the directions α_1 and α_2, i.e. for each fiber system with an angle θ_k corresponding to a system with an angle $\theta_l = -\theta_k$, then

$$K_{i3} = D_{i3} = K_{3i} = D_{3i} = 0, \qquad i = 1, 2,$$

where $D_{ij} = \dfrac{1}{12}\tilde{K}_{ij}$. As a result we obtain the *constructive orthotropic* shell.

3.2. Bifurcation Equations

Under the assumptions which are usually made for the Donnell equations for shallow shells [Donnell (1976)][3], the following equilibrium equations have

been obtained in [Haseganu *et al.* (2000)][2]

$$\begin{aligned}
&\frac{\partial T_1}{\partial x_1} + \frac{\partial S}{\partial x_2} = 0,\\
&\frac{\partial T_2}{\partial x_2} + \frac{\partial S}{\partial x_1} = 0,\\
&T_1^0 \frac{\partial^2 w}{\partial x_1^2} + 2S^0 \frac{\partial^2 w}{\partial x_1 \partial x_2} + T_2^0 \frac{\partial^2 w}{\partial x_2^2}\\
&\quad - \left(\frac{\partial^2 M_1}{\partial x_1^2} + 2\frac{\partial^2 H}{\partial x_2} + \frac{\partial^2 M_2}{\partial x_2^2} \right) + \frac{T_1}{R_1} + \frac{T_2}{R_2} = 0.
\end{aligned} \tag{2}$$

Here we assume that the initial stress-strain state of a shell is determined only by the initial stress resultants T_1^0, T_2^0, S^0. Such stress-strain state is referred to as momentless or membrane-like. Below we analyze the stability of such a state.

Next we study the one-parameter loading by introducing the loading parameter λ as

$$\{T_1^0, T_2^0, S^0\} = -\lambda\{t_1, t_2, t_3\}$$

and seek the displacements under bifurcation in the form

$$u_1 = u_1^0 \sin z, \quad u_2 = u_2^0 \sin z, \quad w = w^0 \cos z, \quad z = k_1 x_1 + k_2 x_2, \tag{3}$$

where the amplitudes u_1^0, u_2^0, and w^0 and the wave numbers k_1 and k_2 must be determined.

The critical loading parameter λ is determined by the formula

$$\lambda = f(k_1, k_2) = \frac{B_\varepsilon + B_\varkappa}{B_t}, \tag{4}$$

where

$$\begin{aligned}
B_\varepsilon &= \frac{\Delta_k}{\Delta}\left(\frac{k_1^2}{R_2} + \frac{k_2^2}{R_1}\right)^2, \qquad \Delta_k = K_{11}A_{11} + K_{12}A_{12} + K_{13}A_{13},\\
B_\varkappa &= D_{11}k_1^4 + 4D_{13}k_1^3 k_2 + 2\left(D_{12} + 2D_{33}\right)k_1^2 k_2^2 + 4D_{23}k_1 k_2^3 + D_{22}k_2^4,\\
\Delta &= A_{22}k_1^4 - 2A_{23}k_1^3 k_2 + (2A_{12} + A_{33})k_1^2 k_2^2 - 2A_{13}k_1 k_2^3 + A_{11}k_2^4,\\
B_t &= t_1 k_1^2 + 2t_3 k_1 k_2 + t_2 k_2^2,
\end{aligned}$$

and A_{ij} are the coefficients whose relations have been obtained in [Haseganu *et al.* (2000)][2], for example, for an orthotropic shell $A_{11} = \dfrac{GE_2}{1 - \nu_1\nu_2}$. Here we denote by Δ_k the determinant of the matrix $\{K_{ij}\}$. The variables B_ε, $B_\varkappa$ and B_t are proportional to the bending-twisting shell energy $\Pi_\varkappa$, the tensile-shear shell energy for additional displacements Π_ε, and the work of

the initial momentless stress resultants on the additional rotations of the normal, respectively.

Relation (4) is rather general. It may be used for estimating the value of a critical loading and expected buckling modein many problems. We obtain the critical value λ_0 for the parameter λ by minimizing the function $f(k_1, k_2)$ over all real k_1 and k_2, such that $B_t > 0$.

Let

$$k_1 = r\cos\varphi, \qquad k_2 = r\sin\varphi.$$

Taking into account the fact that the functions are homogeneous in k_1 and k_2, we introduce

$$B_\varepsilon = B_\varepsilon^*(\varphi), \quad B_\varkappa = r^4 B_\varkappa^*(\varphi), \quad B_t = r^2 B_t^*(\varphi), \quad \Delta = r^4\Delta^*(\varphi).$$

Minimizing function (4) with respect to r, we obtain

$$\lambda_0 = \min_\varphi\{f^*(\varphi)\} = f^*(\varphi_0), \qquad f^*(\varphi) \equiv 2\frac{\sqrt{B_\varepsilon^*(\varphi)B_\varkappa^*(\varphi)}}{B_t^*(\varphi)},$$
$$r_0^4 = \frac{B_\varepsilon^*(\varphi_0)}{B_\varkappa^*(\varphi_0)}.$$

Due to the above formulas, the pits are significantly elongated at angle $-\varphi_0$ with respect to the axis x_2. This relation may be used to study the buckling of convex shells under compression, stretching, torsion, bending or combined loading. In the case of shells of zero Gaussian curvature, this relation provides a nontrivial result only for axial compression of cylindrical and conical shells.

In fact, the above algorithm may be applied only to shells of positive Gaussian curvature ($R_1R_2 > 0$). For shells of negative Gaussian curvature ($R_1R_2 < 0$), according to (4) we get

$$\lambda_0 = \min_\varphi\{f^*(\varphi)\} = 0, \qquad r_0 = 0 \quad \text{for} \quad \tan\varphi_0 = \sqrt{-\frac{R_1}{R_2}}. \tag{5}$$

Similarly, for shells of zero Gaussian curvature ($R_1^{-1} = 0$), i.e. cylindrical and conical, we obtain from (4)

$$\lambda_0 = \min_\varphi\{f^*(\varphi)\} = 0, \qquad r_0 = 0 \quad \text{for} \quad \varphi_0 = 0. \tag{6}$$

Relations (5) and (6) imply that, for shells of zero or negative Gaussian curvature, the order of the critical loading ($\lambda_0 = 0$) decreases and the buckling mode is not localized ($r_0 = 0$). To obtain the critical loading and buckling modes for such shells one should apply the method of asymptotic integration described below, for example, for a circular cylindrical shell.

The case of the axially compressed cylindrical shell $t_2 = t_3 = 0$, $t_1 > 0$, is the only one for which the application of relations (4) provides a nontrivial result.

3.3. Orthotropic Ellipsoid Under External Pressure

As an example, we consider an elliptical shell of revolution with semi-axes (a, a, b). The angle between the axis of symmetry and the normal to the surface is denoted by θ. We select the parameter $R = a$ as characteristic length. Then for the principal curvatures

$$\rho_2 = \frac{R}{R_2} = (\sin^2\theta + d^2\cos^2\theta)^{1/2}, \quad \rho_1 = \frac{R}{R_1} = \frac{\rho_2^3}{d^2}, \quad d = \frac{b}{a}. \tag{7}$$

Here d is the coefficient of ellipsoid compression (if $d > 1$ the ellipsoid is prolate and if $d < 1$ it is oblate).

The elliptical shell consists of the matrix made of uniform material of thickness h, with Young's modulus E and Poisson's ratio ν. The shell is reinforced with two similar systems of threads. The angles between the threads and the meridional direction are equal to $\pm\alpha$. The volume of the threads is $(1 - \delta_0)V$, where V is the total volume of the structure; Young's modulus of the thread material is e times larger than E.

The elliptical shell is under uniform normal (hydrostatic) pressure λ. The relations for the initial stresses are well known [Tovstik and Smirnov (2001)][1]

$$t_1 = \frac{1}{2\rho_2}\operatorname{sign}\lambda, \qquad t_2 = \frac{2\rho_2 - \rho_1}{2\rho_2^2}\operatorname{sign}\lambda, \qquad t_3 = 0.$$

For the external pressure $\operatorname{sign}\lambda > 0$, and for the internal pressure $\operatorname{sign}\lambda < 0$. Since B_t should be positive, buckling may occur under external pressure for elliptical shells of arbitrary form and under internal pressure only for shells for which $2\rho_2 < \rho_1$, i.e.

$$\rho_2^2 > 2d^2. \tag{8}$$

It follows from (7) that for ρ_2 the following relations hold

$$1 < \rho_2 < d, \text{ for } d > 1, \qquad d < \rho_2 < 1, \text{ for } d < 1. \tag{9}$$

Both inequalities (8) and (9) are satisfied only for $2d^2 < 1$.

For the system of threads described above, the shell is orthotropic and the relation for λ has the following form

$$\lambda_0 = \min_{\varphi,\theta}\{f^*(\varphi,\theta)\} = f^*(\varphi_0,\theta_0), \quad f^*(\varphi,\theta) \equiv 2\frac{\sqrt{B_\varepsilon^*(\varphi,\theta)B_\varkappa^*(\varphi,\theta)}}{B_t^*(\varphi,\theta)}, \tag{10}$$

where

$$B_\varepsilon^* = \frac{\Delta_k}{R^4\Delta}\left(\rho_2\cos^2\varphi + \rho_1\sin^2\varphi\right)^2, \qquad \Delta_k = K_{11}A_{11} + K_{12}A_{12},$$
$$B_\varkappa^* = D_{11}\cos^4\varphi + 2\left(D_{12} + 2D_{33}\right)\cos^2\varphi\sin^2\varphi + D_{22}\sin^4\varphi,$$
$$B_t^* = t_1\cos^2\varphi + t_2\sin^2\varphi,$$
$$\Delta = A_{22}\cos^4\varphi + \left(2A_{12} + A_{33}\right)\cos^2\varphi\sin^2\varphi + A_{11}\sin^4\varphi,$$
$$A_{11} = K_{22}K_{33} - K_{23}^2, \qquad A_{12} = K_{13}K_{23} - K_{12}K_{33},$$
$$A_{22} = K_{11}K_{33} - K_{13}^2, \qquad A_{33} = K_{11}K_{22} - K_{23}^2.$$

We first consider an isotropic elliptical shell under external pressure ($\delta_0 = 1$). In this case,

$$A_{11} = A_{22} = K^2\frac{1-\nu}{2}, \qquad A_{12} = -\nu A_{11},$$
$$A_{33} = K^2(1-\nu^2), \qquad K = \frac{Eh}{1-\nu^2}$$
$$\Delta_k = \frac{1-\nu}{2}K^3(1-\nu^2), \qquad \Delta = K^2\frac{1-\nu}{2}\left(\cos^2\varphi + \sin^2\varphi\right)^2,$$
$$B_\varepsilon^* = K\frac{1-\nu^2}{R^2\left(\cos^2\varphi + \sin^2\varphi\right)^2}\left(\cos^2\varphi\rho_2 + \sin^2\varphi\rho_1\right)^2,$$
$$B_\varkappa^* = \frac{h^2}{12}K\left(\cos^2\varphi + \sin^2\varphi\right)^2$$

and relation (4) may be written as

$$\lambda_0 = \frac{Eh^2}{R^2\sqrt{3(1-\nu^2)}}\min_{\varphi,\theta}\frac{\left(\cos^2\varphi\rho_2 + \sin^2\varphi\rho_1\right)}{t_1\cos^2\varphi + t_2\sin^2\varphi}.$$

Minimizing the above expression with respect to φ, we obtain

$$\frac{Eh^2}{R^2\sqrt{3(1-\nu^2)}}\rho_1/t_2, \qquad \text{for } \varphi = \pi/2 \text{ if } t_2\rho_2 > t_1\rho_1,$$
$$\frac{Eh^2}{R^2\sqrt{3(1-\nu^2)}}\rho_2/t_1, \qquad \text{for } \varphi = 0 \text{ if } t_2\rho_2 < t_1\rho_1,$$
$$\frac{Eh^2}{R^2\sqrt{3(1-\nu^2)}}\rho_2/t_1 = \frac{Eh^2}{R^2\sqrt{3(1-\nu^2)}}\rho_1/t_2, \qquad \text{if } t_2\rho_2 = t_1\rho_1.$$

In the last case, the angle φ is undefined. This means that there exist multiple buckling modes. At the same time the value of the buckling loading is unique.

In the case under consideration, the condition $t_2\rho_2 = t_1\rho_1$ may be rewritten as

$$\frac{\rho_1}{2\rho_2} = \frac{2\rho_2 - \rho_1}{2\rho_2},$$

or $\rho_1 = \rho_2$, which corresponds to $d = 1$, i.e. a spherical shell. For $d > 1$, $t_2\rho_2 > t_1\rho_1$, and for $d < 1$, $t_2\rho_2 < t_1\rho_1$.

Therefore the relation for critical loading is given as

$$\lambda_0 = \min_\theta \begin{cases} \dfrac{Eh^2}{R^2\sqrt{3(1-\nu^2)}} 2\rho_2^2, & \text{for } d \le 1, \\ \dfrac{Eh^2}{R^2\sqrt{3(1-\nu^2)}} \dfrac{2\rho_1\rho_2^2}{2\rho_2 - \rho_1}, & \text{for } d \ge 1. \end{cases}$$

Now minimizing with respect to θ we obtain

$$\lambda_0 = \begin{cases} \dfrac{Eh^2}{R^2\sqrt{3(1-\nu^2)}} 2d^2, & \text{for } d \le 1, \\ \dfrac{Eh^2}{R^2\sqrt{3(1-\nu^2)}} \dfrac{2}{2d^2 - 1}, & \text{for } d \ge 1. \end{cases}$$

For $d > 1$, the weakest parallel is on the equator ($\theta_0 = \pi/2$), and the pits are elongated in the direction of the meridian ($\varphi_0 = \pi/2$). For $d < 1$, the weakest parallel is the pole ($\theta = 0$). Note that, in the last case, the value of λ_0 does not depend on the angle φ which is, therefore, undetermined.

Now we consider an orthotropic shell. For such shell

$$A_{11} = \frac{E_2h^2}{1-\nu_1\nu_2}G, \quad A_{22} = \frac{E_1h^2}{1-\nu_1\nu_2}G, \quad A_{33} = \frac{E_1E_2h^2}{1-\nu_1\nu_2},$$
$$A_{12} = -\frac{\nu_1E_2h^2G}{1-\nu_1\nu_2}, \quad \Delta_k = \frac{E_1E_2h^3G}{1-\nu_1\nu_2}.$$

Here E_1 and E_2 are Young's moduli, ν_1 and ν_2 are Poisson's ratios in the x_1 and x_2 directions, respectively, and G is the shear modulus.

In the case of orthotropic shell, relation (4) cannot be simplified and one should numerically seek the minimum of function (10). For that, we fix the parameters α and δ_0 and find the different values of the parameter d which minimize the function

$$\lambda_0 = \min_{\varphi,\theta}\{f^*(\varphi,\theta)\}$$

$$= \begin{cases} \min\limits_{\substack{\varphi \in [0,\pi/2] \\ \rho_2 \in [1,d]}} f^*(\varphi,\theta), & \text{for } d \geq 1, \\ \min\limits_{\substack{\varphi \in [0,\pi/2] \\ \rho_2 \in [d,1]}} f^*(\varphi,\theta), & \text{for } \frac{\sqrt{2}}{2} \leq d \leq 1, \\ \min\limits_{\substack{\varphi \in \left[\operatorname{Arctan}\sqrt{\frac{d^2}{\rho_2^2-2d^2}},\pi/2\right] \\ \rho_2 \in [d,1]}} f^*(\varphi,\theta), & \text{for } d \leq \frac{\sqrt{2}}{2}, \end{cases} \tag{11}$$

where

$$f^*(\varphi,\theta) = 4\sqrt{\frac{B_{\varkappa}^*\Delta_k}{\Delta}}\,\frac{\rho_2^2 d^2\cos^2\varphi + \rho_2^4\sin^2\varphi}{d^2\cos^2\varphi + (2d^2-\rho_2^2)\sin^2\varphi}.$$

Numerical calculations revealed that this function attains its minimum at $\theta_0 = 0$ for $d < 1$ and at $\theta_0 = \pi/2$ for $d > 1$. This result does not depend on the values of the other parameters.

The effect of the shell compression parameter, d, on the relative critical loading is shown in Fig. 3.1. The values of the critical loading for an isotropic sphere is taken as 1. Poisson's coefficient is $\nu = 0.3$. Line 1 correspond to the isotropic case $\delta_0 = 1$, line 2 to the case $\delta_0 = 0.9$, $\alpha = 0$, line 3 to the case $\delta_0 = 0.9$, $\alpha = \pi/8$, line 4 to the case $\delta_0 = 0.9$, $\alpha = \pi/4$, and line 5 to the case $\delta_0 = 0.9$, $\alpha = \pi/2$.

As expected, increasing the thread stiffness and the threads relative volume leads to an increase in the critical loading. For very small values of the parameter δ_0 (the threads occupy almost the whole volume) the critical pressure comes down drastically since the shell, in this case, behaves like a system of threads.

The angle φ_0 depends on the values of the parameters d, α and δ_0. For large values of d, the pits are elongated in the direction of the meridian, so that the angle φ_0 converges to $\pi/2$, and, for highly elongated orthotropic elliptical shells, the buckling modes are similar to those of isotropic shells. Increasing the thread stiffness leads to a smaller angle φ_0.

The dependence of the critical loading and buckling modes on the angle between the system of threads is more complicated. For angles α larger

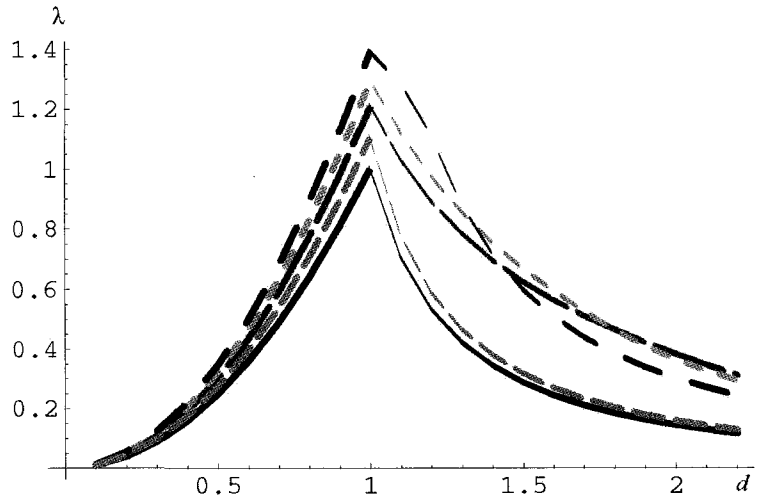

Fig. 3.1. Critical loading for an elliptical shell under external pressure

than $\pi/4$, the critical loading and buckling modes are equal to the critical loading and modes for an isotropic elliptical shell. For a slightly elongated ellipsoid, the critical loading attains its maximum for angles close to $\pi/8$.

For an oblate orthotropic elliptical shell ($d < 1$), the value of f_0 may be uniquely determined from the conditions:

$$\varphi_0 : \quad \lambda(\varphi_0, 0) = \min_{\varphi} \frac{B^*_{\varkappa}}{\Delta},$$

from which it follows that

$$\varphi_0 = \pm \mathrm{Arctan} \left(\frac{E_2}{E_1} \right)^{1/4}.$$

For small and large values of d, the following approximate formulas may be used to obtain the critical loadings:

$$\lambda_0 = \begin{cases} \dfrac{h^2\sqrt{E_1 E_2}}{R^2\sqrt{3(1-\nu_1\nu_2)}}\, 2d^2, & \text{for } d \ll 1, \\ \dfrac{h^2\sqrt{E_1 E_2}}{R^2\sqrt{3(1-\nu_1\nu_2)}}\, \dfrac{2}{2d^2-1}, & \text{for } d \gg 1. \end{cases}$$

3.4. Orthotropic Elliptical Shell Under Internal Pressure

As in the previous section, we start by considering the case of an isotropic shell (δ_0=1). Since, for the shell under internal normal pressure, $t_1 < 0$ and $t_2 > 0$, then the inequality $t_2\rho_2 > t_1\rho_1$ holds for any values of the parameter d and relation (4) has the form

$$\lambda_0 = \min_{\theta} \frac{Eh^2}{R^2\sqrt{3(1-\nu^2)}} \frac{\rho_1}{t_2}, \qquad \text{for } \varphi = \pi/2,$$

or

$$\lambda_0 = -\min_{\theta} \frac{Eh^2}{R^2\sqrt{3(1-\nu^2)}} \frac{2\rho_1\rho_2^2}{\rho_1 - 2\rho_2}, \qquad \text{for } d \le \frac{\sqrt{2}}{2}.$$

We seek the minimum of the function $\dfrac{2\rho_1\rho_2^2}{\rho_1 - 2\rho_2} = \dfrac{2\rho_2^4}{r_2^2 - 2d^2}$ under the condition $2d^2 < r_2^2 < 1$. For $d < 1/2$, the function attains its minimum at $\rho_2 = 2d$, i.e. on the parallel $\theta = \arcsin\sqrt{\dfrac{3d^2}{1-d^2}}$ and this minimum is equal to $16d^2$. For $1/2 < d < \frac{\sqrt{2}}{2}$, the minimum is attained at $\rho_2 = 1$, i.e. on the equator and it is equal to $\dfrac{2}{1-2d^2}$.

Hence, the pits are elongated in the direction of the meridian and they move from the equator to the pole as d decreases.

Consider the orthotropic elliptical shell described in the previous section. Then the relation for the critical loading may be written as

$$\lambda_0 = \min_{\varphi,\theta}\{f^*(\varphi,\theta)\} = \min_{\substack{\varphi \in \left(\operatorname{Arctan}\sqrt{\frac{d^2}{\rho_2^2-2d^2}},\,\pi/2\right] \\ \rho_2 \in (\sqrt{2}d,\,1]}} f^*(\varphi,\theta), \tag{12}$$

where

$$f^*(\varphi,\theta) = 4\sqrt{\frac{B_\varkappa^* \Delta_k}{\Delta}} \frac{\rho_2^2 d^2 \cos^2\varphi + \rho_2^4 \sin^2\varphi}{-d^2\cos^2\varphi - (2d^2 - \rho_2^2)\sin^2\varphi}.$$

As before, we seek the minimum for all positive λ_0. We remind that buckling of an elliptical shell under internal pressure may occur only if $d < \sqrt{2}/2$.

In Fig. 3.2 the dependence of the critical loading on the parameter d is plotted for the same set of parameters as in Fig. 3.1.

For a shell reinforced with the threads, the critical loading is higher than for an isotropic shell and the weakest parallel is closer to the equator

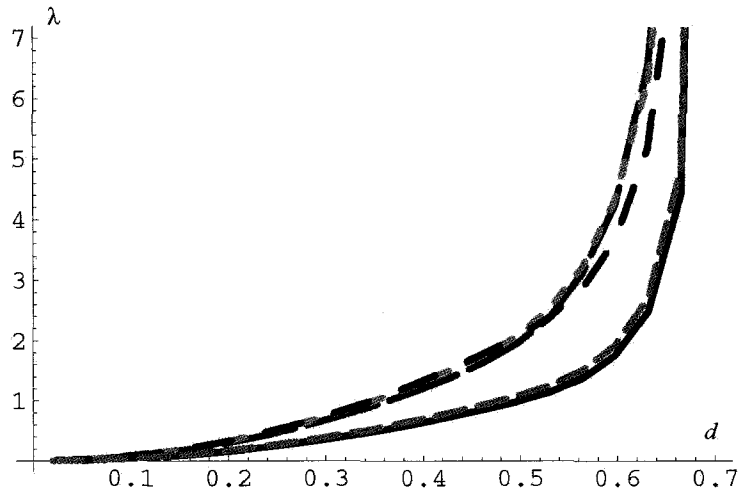

Fig. 3.2. Critical loading for an elliptical shell under internal pressure

for $1/2 < d < \sqrt{2}/2$. At the same time, the orientation of the pit axis, φ_0, changes significantly.

The critical loading decreases as the angle α increases. For $\alpha > \pi/4$, the buckling modes of isotropic and orthotropic shells practically coincide.

3.5. Buckling of Cylindrical Shells

We analyze the governing equations for buckling of the initial momentless (membrane) stress-strain state of thin anisotropic cylindrical shells obtained in [Haseganu *et al.* (2000)][2] for different cases of loading. The linearized system of the non-dimensional Donnell equations [Donnell (1976)][3] which describe buckling of such an orthotropic thin circular cylindrical shell of radius R has the form

$$D_{11}\frac{\partial^4 w}{\partial x_1^4} + 2(D_{12}+D_{33})\frac{\partial^4 w}{\partial x_1^2 \partial x_2^2} + D_{22}\frac{\partial^4 w}{\partial x_2^4} + \lambda\left(t_1\frac{\partial^2 w}{\partial x_1^2} + 2t_3\frac{\partial^2 w}{\partial x_1 \partial x_2} + t_2\frac{\partial^2 w}{\partial x_2^2}\right) - \frac{\partial^2 \Phi}{\partial x_1^2} = 0, \tag{13}$$

$$\frac{1}{\Delta_k}\left(A_{22}\frac{\partial^4 \Phi}{\partial x_1^4} + (2A_{12}+A_{33})\frac{\partial^4 \Phi}{\partial x_1^2 \partial x_2^2} + A_{11}\frac{\partial^4 \Phi}{\partial x_2^4}\right) + \frac{\partial^2 w}{\partial x_1^2} = 0.$$

Here the two unknown functions, w and Φ, are the shell deflection and stress function, respectively; x_1 and x_2 are the axial and circumferential coordi-

nates, respectively; D_{ij}, A_{ij}, and Δ_k are the constants given in [Haseganu *et al.* (2000)][2]; t_1, t_2 and t_3 are the initial membrane stress-resultants, μ is a small parameter and λ is a parameter of the buckling load. The analysis is made under the assumption that the remaining parameters have orders not larger than 1, in particular for the shell length $l = L/R \sim 1$. We study the one-parameter loading by introducing the loading parameter λ as

$$\{T_1^0, T_2^0, S^0\} = -\mu^4 \lambda \{t_1, t_2, t_3\}.$$

From now on, we use non-dimensional variables that are related to the dimensional ones (with $\tilde{}$) as

$$\begin{aligned} \{\tilde{x}, \tilde{x}_2, \tilde{u}_i, \tilde{w}\, \tilde{h}\} &= \tilde{R}\{x, x_2, u_i, w, h\}, \qquad \{\tilde{T}_i, \tilde{S}, \tilde{t}_i\} = \tilde{E}\tilde{h}\{T_i, S, t_i\}, \\ \tilde{K}_{ij} &= \tilde{E}\tilde{h}K_{ij}, \qquad \tilde{D}_{ij} = \tilde{R}^2\mu^8\tilde{E}\tilde{h}D_{ij} = \tilde{E}\tilde{h}^2 D_{ij}, \end{aligned} \tag{14}$$

$$\tilde{\Phi} = \tilde{R}^2\mu^4\tilde{E}\tilde{h}\Phi, \qquad \mu^4 = \frac{\tilde{h}}{\tilde{R}}, \qquad \tilde{E}_i = \tilde{E}E_i, \tilde{G} = \tilde{E}G. \tag{15}$$

As in the case of an isotropic shell, the buckling mode is formed as a system of pits strongly elongated in the axial direction from one shell edge to the other, covering the entire shell surface. The only exclusion is the case of an axially compressed shell.

As an example, we consider several problems: (i) anisotropic cylindrical shell under hydrostatic pressure, (ii) axially compressed orthotropic cylindrical shell, and (iii) torsion of orthotropic cylindrical shell.

The initial stresses may be sorted out in the order of intensity of their effects on the critical loading: t_2, t_3, and t_1. If $t_2 = 0$ or $t_2 < 0$, and $t_3 \neq 0$, then the order of the critical loading increases.

For case (i), i.e. for $t_2 > 0$ and $t_1 = t_3 = 0$, we have $\lambda = O(\mu^2)$, for case (ii), i.e. for $t_2 = t_3 = 0$ and $t_1 > 0$, we have $\lambda = O(1)$, and finally for case (iii), i.e. for $t_3 > 0$ and $t_1 = t_2 = 0$, we have $\lambda = O(\mu)$.

The order of the system of equations (13) does not permit to satisfy all boundary conditions, because, by using the proposed method of asymptotic integration, we, in fact, reduce the order of the initial system from 8 to 4 ignoring the edge effect integrals localized near the shell edges. Here the so called *regular degeneracy* (first studied in [Vishik and Lyusternik (1957)][4]) occurs. In the case of regular degeneracy, one should neglect the boundary condition containing the higher derivatives when studying the unperturbed problem. The neglected boundary conditions may be satisfied later while constructing the edge effect integrals.

For orthotropic shells, if $t_3 = 0$, we may avoid the complexity of the above consideration. For the simply supported shell (or if we ne-

glect the boundary conditions) the solution for the shell has the form $w = \sin kx \cos mx_2$, and the critical loading may be determined by minimizing the expression for λ with respect to the integer m while assuming that $k = \pi/l$ is given.

In this way the well-known formulas for the critical buckling loads for isotropic shells have been generalized to the case of anisotropic shells.

3.6. Buckling of Orthotropic Cylindrical Shell Under Hydrostatic Pressure

We start with the buckling of an orthotropic cylindrical shell under hydrostatic pressure ($t_2 = 1$, $t_1 = t_3 = 0$) for the case of simply supported edges

$$w = w'' = 0 \qquad \Phi = \Phi'' = 0 \qquad \text{at } x = 0, l. \tag{16}$$

Assuming a solution in the form

$$w = \sum_{j=1}^{8} C_j \exp(p_j x_1 + imx_2), \qquad \Phi = \sum_{j=1}^{8} C_j \delta_j \exp(p_j x_1 + imx_2), \tag{17}$$

where

$$\delta_j = -\frac{\Delta_k p_j^2}{\mu^4}\left(A_{22}p_j^4 - (2A_{12} + A_{33})p_j^2 m_*^2 + A_{11}m_*^4\right), \tag{18}$$

we obtain the characteristic equation for λ,

$$\begin{aligned}\left[\mu^4(D_{11}p^4 - 2(D_{12} + D_{33})p^2m^2 + D_{22}m^4) + \lambda(t_1p^2 + 2it_3mp - t_2m^2)\right] \\ + \left[\mu^4(A_{22}p^4 - (2A_{12} + A_{33})p^2m^2 + A_{11}m^4)\right] + \Delta_k p^4 = 0,\end{aligned} \tag{19}$$

and, hence, an expression for λ,

$$\begin{aligned}\lambda t_2 = \min_{m,p} \frac{\Delta_k p^4}{\mu^4(A_{22}p^4 - (2A_{12} + A_{33})p^2m^2 + A_{11}m^4)} \\ + \frac{\mu^4(D_{11}p^4 - 2(D_{12} + D_{33})p^2m^2 + D_{22}m^4)}{m^2},\end{aligned} \tag{20}$$

where $p = k\pi i/l$ for a simply supported cylindrical shell. After minimization with respect to m we get the following expression for the critical pressure

$$\lambda t_2 = \lambda_0 \mu^2 + \lambda_1 \mu^4 + O(\mu^6), \tag{21}$$

where

$$\lambda_0 = \sqrt{\frac{2}{27}} \frac{\pi E_2}{l} \left(\frac{E_1/E_2}{(1 - \nu_1\nu_2)^3}\right)^{1/4} \tag{22}$$

and

$$m_{\min} = 6^{1/4}\sqrt{\frac{\pi R}{L}}\left(\frac{E_1(1-\nu_1\nu_2)}{E_2}\right)^{1/8}\mu^{-1}.$$

In the case of an isotropic shell ($E_1 = E_1$ and $\nu_1 = \nu_2$) the first term in relation (21) transforms to Southwell–Papkovich's formula ([Tovstik and Smirnov (2001)][1]). Indeed, for dimensional variables, according to (14)

$$\tilde{T}_2 = \tilde{E}\tilde{h}\mu^4\lambda_0\mu^2 = \tilde{E}\tilde{h}\,\frac{1}{(1-\nu_1^2)^{3/4}}\sqrt{\frac{2}{27}}\,\frac{\pi}{l}\left(\frac{\tilde{h}}{\tilde{R}}\right)^{3/2}.$$

The next term in the expression for the critical pressure, λ_1, depends on both the shell anisotropy and the boundary conditions. To consider the effect of the boundary conditions we represent the solution in the form (17) and assume that $m \sim m_*\mu^{-1}$ and $\lambda \sim \lambda_*\mu^2$. The roots of (19) splits into two groups:

$$p^4_{1,2,3,4}(\lambda) = \frac{(\lambda_* t_2 m_*^2)A_{11}m_*^4 - A_{11}D_{22}m_*^8}{\Delta_k}, \qquad p^4_{5,6,7,8} = -\frac{1}{\mu^2}\frac{\Delta_k}{D_{11}A_{22}}.$$

Substituting solutions in the form (17) into the four boundary conditions, on each edge we obtain a system of eight equations. This system has a nontrivial solution if its determinant is equal to zero. In the case of a freely supported shell (16) the determinant $D(\lambda)$ consists of the following rows

$$\left\{1, p_j^2, \delta_j, \delta_j^2, e^{p_j l}, p_j^2\, e p_j l, \delta_j\, e^{p_j l}, \delta_j p_j^2\, e^{p_j l}\right\}, \quad j = 1, \ldots, 8. \tag{23}$$

After transformations, the frequency equation $D(\lambda) = 0$ reduces to $\sin(p_1 l) = 0$ or $p_1 l = \pi k$. The parameter of the critical loading may be obtained from the relation

$$\lambda = \min_{m_*} m_*^2 D_{22} + \frac{\Delta_k \pi^4}{l^4 A_{11} m_*^6},$$

which agrees with (20).

For boundary conditions which differ from (16), for example, for

$$w = w' = 0, \qquad \Phi = \Phi' = 0, \qquad \text{at } x_1 = 0, l, \tag{24}$$

the frequency equation will be more complicated. Denote $p^4_{1,2,3,4} = a^4$, $p^4_{5,6,7,8} = -\dfrac{b^4}{\mu^8}$ $(a, b > 0)$. Note also that

$$\delta_1 = \delta_2, \qquad \delta_3 = \delta_4, \qquad \delta_5 = \delta_8, \qquad \delta_6 = \delta_7. \tag{25}$$

Taking into account the fact that $\Re(p_5)$ and $\Re(p_6)$ are positive and $\Re(p_7)$ and $\Re(p_8)$ are negative, replacing $C_i \exp(p_i x_1)$ by $C_i' \exp(p_i(x_1 - l))$ ($C_i' = C_i \exp(p_i l)$) for $i = 6, 5$, and neglecting the terms containing the infinitely small multiplier e^{-bl/μ^2}, we obtain the frequency equation for $D(\lambda) = 0$, where

$$D(\lambda) =$$

$$\begin{vmatrix}
1 & 1 & 1 & 1 & 0 & 0 & 1 & 1 \\
a & -a & i\,a & -i\,a & 0 & 0 & \frac{(-1+i)\,b}{\mu^2} & \frac{(-1-i)\,b}{\mu^2} \\
\delta_1 & \delta_1 & \delta_3 & \delta_3 & 0 & 0 & \delta_5 & \delta_6 \\
a\,\delta_1 & -(a\,\delta_1) & i\,a\,\delta_3 & -i\,a\,\delta_3 & 0 & 0 & \frac{(-1+i)\,b\,\delta_5}{\mu^2} & \frac{(-1-i)\,b\,\delta_6}{\mu^2} \\
e^{a\,l} & e^{-(a\,l)} & e^{i\,a\,l} & e^{-i\,a\,l} & 1 & 1 & 0 & 0 \\
a\,e^{a\,l} & -\left(\frac{a}{e^{a\,l}}\right) & i\,a\,e^{i\,a\,l} & \frac{-i\,a}{e^{i\,a\,l}} & \frac{(1+i)\,b}{\mu^2} & \frac{(1-i)\,b}{\mu^2} & 0 & 0 \\
e^{a\,l}\,\delta_1 & \frac{\delta_1}{e^{a\,l}} & e^{i\,a\,l}\,\delta_3 & \frac{\delta_3}{e^{i\,a\,l}} & \delta_5 & \delta_6 & 0 & 0 \\
a\,e^{a\,l}\,\delta_1 & -\left(\frac{a\,\delta_1}{e^{a\,l}}\right) & i\,a\,e^{i\,a\,l}\,\delta_3 & \frac{-i\,a\,\delta_3}{e^{i\,a\,l}} & \frac{(1+i)\,b\,\delta_5}{\mu^2} & \frac{(1-i)\,b\,\delta_6}{\mu^2} & 0 & 0
\end{vmatrix}. \tag{26}$$

After expanding the above equation in a power series in μ we get

$$D(\lambda) = D_0(\lambda_0) + \mu^2 D_1(\lambda_0, \lambda_1) + \cdots = 0,$$

and, therefore,

$$D_0(\lambda_0) = 0, \qquad D_1(\lambda_0, \lambda_1) = 0.$$

From the first equation we obtain λ_0 that coincides with (22). Solving the second equation we get an expression for λ_1:

$$\lambda_1 = \frac{\pi}{36 l^2 G(1 - \nu_1\nu_2)}\Big[\pi E_1(-E_2 + 8G\nu_2) + 4G\left(\sqrt{2}\,3^{1/4}\left(E_1 E_2^3\right)^{1/4} + 3G\pi(1 - \nu_1\nu_2)\right)\Big]. \tag{27}$$

3.7. Buckling of Axially Compressed Orthotropic Cylindrical Shell

Now we examine the case of an axially compressed orthotropic cylindrical shell for which $t_2 = t_3 = 0$, $t_1 = -1$. Consider the boundary condition of a simply support type

$$w = w'' = 0, \qquad \Phi = \Phi'' = 0, \qquad \text{at } x_1 = 0, l. \tag{28}$$

We seek a solution in the form (17) where $p_1 = -p_2 = i\pi k/l$, $C_1 = -C_2$, and $C_j = 0$ for $j = 3, \ldots, 8$, i.e.

$$w = C \sin(\pi k x_1/l) \sin(m x_2) \qquad \Phi = C\delta \sin(\pi k x_1/l) \sin(m x_2). \tag{29}$$

Then the parameter of the critical loading may be obtained from relation

$$\lambda = \min_{m,k} \frac{\Delta_k (\pi k/l)^2}{\mu^4 \left[A_{22}(\pi k/l)^4 + (2A_{12} + A_{33})(\pi k/l)^2 m^2 + A_{11} m^4\right]} + \frac{\left[\mu^4 (D_{11}(\pi k/l)^4 + 2(D_{12} + D_{33})(\pi k/l)^2 m^2 + D_{22} m^4\right]}{(\pi k/l)^2} \quad (30)$$

Assuming $\pi k/l = r\cos\varphi$, $m = r\sin\varphi$, after minimization in r, we get

$$r_0 = \mu^{-2} \sin\varphi \left(\frac{\Delta_k}{D(\varphi)A(\varphi)}\right)^{1/4} \quad \text{and} \quad \lambda = 2\left(\frac{\Delta_k D(\varphi)}{A(\varphi)}\right)^{1/2}, \quad (31)$$

where

$$A(\varphi) = \left[A_{22}\sin^4(\varphi) + (2A_{12} + A_{33})\sin^2(\varphi)\cos^2(\varphi) + A_{11}\cos^4(\varphi)\right], \quad (32)$$

$$D(\varphi) = \left[(D_{11}\sin^4(\varphi) + (2D_{12} + D_{33})\sin^2(\varphi)\cos^2(\varphi) + D_{22}\cos^4(\varphi)\right]. \quad (33)$$

With dimensional variables,

$$T_1^0 = \frac{h^2}{R}\left(\frac{E_1 E_2}{3(1-\nu_1\nu_2)}\right)^{1/2} C, \quad (34)$$

where

$$C = \min_{\varphi}\left(\frac{E_1\cos^4\varphi + 2(2G(1-\nu_1\nu_2) + E_1\nu_2)\cos^2\varphi\sin^2\varphi + E_2\sin^4\varphi}{E_1\cos^4\varphi + (E_1E_2/G - 2E_1\nu_2)\cos^2\varphi\sin^2\varphi + E_2\sin^4\varphi}\right)^{1/2}. \quad (35)$$

Denote $E_1/E_2 = \xi$, $a_1 = 2(2G/E_2(1-\nu_1\nu_2)+\xi\nu_2)$, and $a_2 = (E_1/G - 2\xi\nu_2)$.

If $a_1 = a_2$, which is valid for isotropic shells since, in this case, $G = E/2/(1+\nu)$, then C does not depend on the angle φ and $C = 1$ (Lorenz–Timoshenko's formula). The buckling mode is not unique and the number of waves m is in the range from 0 (axisymmetric mode) to $O(\mu^{-2})$.

If $a_1 > a_2$, the minimum is attained at $\varphi = 0$ or $\varphi = \pi/2$ and $C = 1$. This seems to be impossible for real elastic constants.

If $a_1 < a_2$, then

$$\tan\varphi_0 = \left(\frac{E_2}{E_1}\right)^{1/4} \quad \text{and} \quad C = \left(\frac{\sqrt{E_1E_2} + 2G(1-\nu_1\nu_2) + E_1\nu_2}{\sqrt{E_1E_2} + E_1E_2/(2G) - E_1\nu_2}\right)^{1/2}. \quad (36)$$

These relations coincides with those given in [Hayashi (1949)][5].

A similar result may be obtained directly from formula (4). The inclination angle of the pits depend neither on Poisson's ratio nor on the shear modulus. If the material is almost isotropic, i.e. $E_1 \approx E_2$, $\nu_1 \approx \nu_2$, and $G \approx \frac{E}{2(1+\nu)}$, then $\tan\varphi^* \approx 1$. The last relation means that the "averaged" inclination angle of the set of pits for isotropic shell is equal to $\pi/4$.

3.8. Buckling of an Orthotropic Cylindrical Shell Under Torsion

For an orthotropic cylindrical shell under torsion $t_3 = 1$ and $t_1 = t_2 = 0$. Instead of (17) we represent the solution in the form

$$w = \sum_{j=1}^{8} C_j \exp(ip_j x_1 + imx_2), \qquad \Phi = \sum_{j=1}^{8} C_j \delta_j \exp(ip_j x_1 + imx_2), \quad (37)$$

and suppose that $m = m_*/\mu$ ($m_* \sim 1$) and $\lambda = \lambda_0 \mu$. The characteristic equation, in this case, is

$$\begin{aligned}&\left[\mu^4(D_{11}p^4 + 2(D_{12} + D_{33})p^2m^2 + D_{22}m^4) - 2\lambda t_3 mp\right] \\ &\quad + \left[\mu^4(A_{22}p^4 - (2A_{12} + A_{33})p^2m^2 + A_{11}m^4)\right] + \Delta_k p^4 = 0. \quad (38)\end{aligned}$$

Solving this equation, we get two groups of roots p_j. Four roots corresponding to the main integrals satisfy the equation

$$\Delta_k p^4 + \left(-2\lambda\rho p + \rho^4 D_{22}\right) A_{11} = 0. \quad (39)$$

Four other roots correspond to the edge effect integrals.

Consider the case where the same boundary conditions are introduced on both edges $x_1 = 0$ and $x_1 = l$. Substituting a linear combination of the main integrals into the boundary conditions we get the frequency equation, from which, after simplifications (see [Tovstik and Smirnov (2001)][1]), we obtain

$$\lambda_0 = K_s \sqrt{E_1 E_2} \left(\frac{1}{1 - \nu_1\nu_2}\right)^{5/8} \left(\frac{1}{l}\right)^{1/2},$$

where K_s is a constant given in [Tovstik and Smirnov (2001)][1]). The last formula is the generalization for orthotropic shells of the formula proposed in [Grigolyuk and Kabanov (1978)][6]. Indeed, in the isotropic case

$$\tilde{S}_0 = \tilde{E}\tilde{h}\mu^4\lambda_0\mu = \tilde{E}\tilde{h}K_s \left(\frac{1}{1-\nu^2}\right)^{5/8} \left(\frac{\tilde{R}}{\tilde{L}}\right)^{1/2} \left(\frac{\tilde{h}}{\tilde{R}}\right)^{5/4}.$$

3.9. Effect of Anisotropy on the Critical Loading

Last, we study the effect of anisotropy on the critical buckling loading. Consider an orthotropic cylinder under external hydrostatic pressure. We seek a solution in the form (29). We represent the functions Φ and w in

power series in μ. Then the governing equation for the term of the first approximation, Φ_1 and w_1, are the following (see [Haseganu *et al.* (2000)][2]):

$$\frac{d^2 w_1^s}{dx_1^2} + c\Phi_1^s - a\cos kx_1 = 0,$$
$$\frac{d^2 \Phi_1^s}{dx_1^2} + \frac{k^4}{c} w_1^s - b\cos kx_1 = 0,$$
$$a = \frac{2A_{13}k^3}{\rho A_{11}} \qquad b = -3D_{23}\rho^3 k \qquad c = \frac{A_{11}}{\Delta_k}\rho^4,$$

where with c and s denote the terms in sine and cosine, respectively. The terms a and b reflect the anisotropic properties of the shell. We cannot satisfy all boundary conditions and ignore the integrals of the boundary effect. Again here we have a case of regular singular perturbed system. So, we satisfy only the main boundary conditions

$$w = 0, \qquad \Phi = 0, \qquad \text{at } x_1 = 0, l.$$

Then

$$w_1^s = \frac{ak^2 + bc}{2k^3} X\cos kx_1 + \frac{ak^2 - bc}{4k^4}\left(\sin kx_1 - \frac{\sinh kX}{\sinh kl/2}\right),$$
$$\Phi_1^s = \frac{ak^2 + bc}{2kc} X\cos kx_1 - \frac{ak^2 - bc}{4kc}\left(\sin kx_1 - \frac{\sinh kX}{\sinh kl/2}\right),$$
$$a = \frac{2A_{13}k^3}{\rho A_{11}}, \qquad b = -3D_{23}\rho^3 k, \qquad c = \frac{A_{11}}{\Delta_k}\rho^4, \qquad X = x_1 - \frac{l}{2}.$$

For the second approximation,

$$\frac{d^2 w_2^c}{dx_1^2} + c\Phi_2^c + f_1 = 0,$$
$$\frac{d^2 \Phi_2^c}{dx_1^2} + \frac{k^4}{w_2^c} + \rho^2 t_2 \lambda_4 w_0^c + f_2 = 0,$$

where

$$f_1 = \frac{1}{\Delta_k}\left(2\rho^3 A_{11}\frac{d\Phi_1^s}{dx} + \rho^2(2A_{12} + A_{33})\frac{d^2\Phi_0^c}{dx^2}\right)$$
$$= \frac{\pi^4 \sin\dfrac{\pi x}{l}\; E_1(E_2 - 2G\nu_2 - (E_1 - 2G\nu_1)\nu_2^2)}{Gl^4\rho^2 E_2(-1 + \nu_1\nu_2)},$$
$$f_2 = 2(D_{12} + 2D_{33})\rho^2\frac{d^2 w_0^c}{dx^2} + 4D_{23}\rho^2\frac{dw_1^s}{dx}$$

$$= -\frac{h^3\pi^2\rho^2 \sin\dfrac{\pi x}{l}\left(2G + \dfrac{E_1\nu_2}{1-\nu_1\nu_2}\right)}{6l^2}.$$

From the compatibility condition

$$\int_0^l \left(f_1 \frac{\Delta_k k^2}{A_{11}\rho^4} \sin[kx_1] + \left(\rho^2 t_2 \lambda_4 \sin[kx_1] + f_2\right) \sin[k\ x_1]\right) dx_1 = 0,$$

we finally obtain the second term

$$\lambda_4 = \frac{\pi^2\ h^3\ (2\ G + (E_1 - 2\ G\ \nu_1)\ \nu_2)}{6\ l^2\ (1 - \nu_1\ \nu_2)}$$

in the expression for the critical loading

$$\lambda = \mu^2\lambda_2 + \mu^4\lambda_4 + O\left(\mu^6\right).$$

The orders of the terms due to the anisotropy and due to the boundary effect appear to be equal (see Section 3.6).

Acknowledgment

The author gratefully acknowledges the financial support provided by the Russian Foundation for Fundamental Research under Grant 04-01-00257.

References

1. Tovstik, P. E., and Smirnov, A. L., (2001), "Asymptotic Methods in the Buckling Theory of Elastic Shells", World Scientific, Singapore.
2. Haseganu, E. M., Smirnov, A. L., and Tovstik P. E., (2000), "Buckling of thin anisotropic shells", Transactions of the CSME, 24(1B), pp. 169–178.
3. Donnell, L. H., (1976), "Beams, Plates and Shells", McGraw-Hill, New York.
4. Vishik, M. I., and Lyusternik, L. A., (1957), "Regular degeneracy and boundary layer for linear differential equations with small parameter", Uspekhi Mat. Nauk (N.S.), vol. 12, no. 5(77), pp. 3–122, (in Russian).
5. Hayashi, T., (1949), "On the elastic instability of orthogonal anisotropic cylindrical shells, especially the buckling load due to compression, bending and torsion", J. Soc. Naval Arch. Japan, No.81, pp. 85–98.
6. Grigolyuk, E. I., and Kabanov, V. V., (1978), "Stability of Shells", Nauka, Moscow, (in Russian).

This page is intentionally left blank

CHAPTER 4

THIN-WALL STRUCTURES MADE OF MATERIALS WITH VARIABLE ELASTIC MODULI

Andrei L. Smirnov

Department of Theoretical and Applied Mechanics, St. Petersburg State University, St. Petersburg, Russia, 198504
E-mail: smirnov@AS1245.spb.edu

Petr E. Tovstik

Department of Theoretical and Applied Mechanics, St. Petersburg State University, St. Petersburg, Russia, 198504
E-mail: peter.tovstik@pobox.spbu.ru

In this paper, one considers the bending of structures made of specific materials with different resistance to tensile and compressive loadings. Two types of structures are analyzed, and for each a non-linear boundary problem is formulated. The first problem is the bending of a vertical steel-reinforced concrete beam loaded on the upper end. The second problem is the deformation of a fiber-reinforced cylindrical shell under internal pressure. In the first problem, steel-reinforced concrete offers less resistance to tensile than to compressive loadings. In the second problem, fibers hardly resist compression. The results obtained by Haseganu, Smirnov and Tovstik are generalized to the case where the compressive stiffness of the fibers is less than their tensile stiffness or is equal to zero.

4.1. Introduction

One of the best elaborated problems of elasticity theory is the analysis of bending of thin-wall structures. In numerous papers and books starting in the 18th Century the bending of thin-wall structures such as beams, plates and shells made of either isotropic or anisotropic materials has been examined.

In this paper we consider bending of structures made of specific mate-

rials with different resistance to tensile and compressive loadings; thus, the elastic coefficients for the stress-strain states under tension and compression are different. The general properties of the structures made of materials with different elastic moduli have been considered in [Ambartsumian (1982)][1]. In this paper we analyze two specific problems both of which may be modelled as non-linear boundary value problems.

The first problem is the bending of a vertical steel-reinforced concrete beam loaded on the upper end. Such a model may be used to describe the bending of an off-shore oil platform. In the unperturbed state, the beam is compressed along the axial direction under the weight of the platform. For small deviations from the equilibrium position, the material of the beam is also entirely under compressive loading, but for large deflections there exist areas where the beam resists to tensile deformations. As a result, the total beam bending stiffness decreases. The beam bending stiffness depends on the amplitude of the deviation and on the ratio of tensile to compressive stiffness for the beam material. The relation for the beam bending stiffness is obtained in this paper.

The second problem is the deformation of a fiber-reinforced cylindrical shell under internal pressure. In the first problem, the resistance of steel-reinforced concrete to tensile loading is less than to compressive loading, but in the second problem the fibers have almost no resistance to compression. In [Haseganu *et al.* (2000)][2] the two-dimensional equations for thin shells, reinforced with elastic fibers, have been obtained under the Kirchhoff–Love hypotheses and have been used for the analysis of shell buckling. However the approach used in that paper does not permit the analysis of structures made of materials with variable elastic moduli because the fiber tensile and compressive stiffnesses were assumed to be equal. Here we use a more general approach assuming that the compressive stiffness of the fibers is less than their tensile stiffness or the compressive stiffness of the fibers is equal to zero. The detailed formulation of these assumptions and their discussion is given below. Under these assumptions the non-linear elasticity relations for the stress-resultants/bending couples and tensile-shear/bending-twisting deformations of the neutral surface have been obtained. Then these relations are used in the analysis of the bending of cylindrical shell under uniform internal pressure. The shell is reinforced with loop fibers that resist internal pressure. In the neighborhood of the clamped edges there appear areas with large bending deformations, where some parts of the fibers are under compressive loading. The purpose of this research is to study the effect of this compression on the stress-strain state of the shell.

The idea of analyzing thin-wall fiber-reinforced structures with variable elastic moduli was discussed with Prof. E. Haseganu while we were working on the paper [Smirnov and Tovstik (2002)][3]. During the Summer 2001, we were planning future joint research in this area. Unfortunately, the tragic death of Prof. E. Haseganu put an end to these plans.

4.2. Relations Between the Curvature of the Beam Neutral Line and the Bending Moment

Consider a beam under compressive force $P < 0$. We intend to calculate the bending stiffness of the steel-reinforced concrete beam with rectangular cross-sectional area $h \times b$, $h < b$ bent in the plane with the smallest stiffness by the moment M.

Let ε and κ be the tensile and bending deformations of the beam axis (under compression $\varepsilon < 0$). Assuming the plane cross-section hypothesis, we find that the tensile deformation $e(z)$ in a fiber parallel to the beam axis at distance z is

$$e(z) = \varepsilon + \kappa z. \tag{1}$$

The corresponding stress $\sigma(z)$ is equal to

$$\sigma(z) = \begin{cases} E_1 e(z) & \text{for} \quad e(z) > 0, \\ E_2 e(z) & \text{for} \quad e(z) < 0, \end{cases} \qquad 0 \le E_1 < E_2, \tag{2}$$

where E_1 and E_2 are the elastic moduli under tension and compression, respectively (see Fig. 4.1).

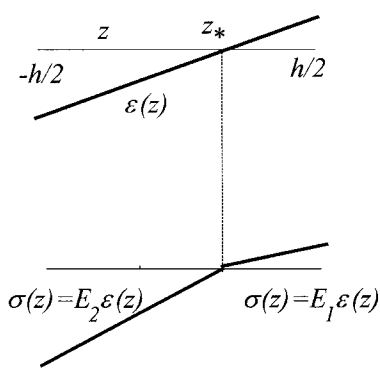

Fig. 4.1. Elasticity relation σ vs. ε

The axial force, P, and bending moment, M, with respect to the center of the cross-sectional area of the beam are

$$P = b\int_{-h/2}^{h/2} \sigma(z)\,dz, \qquad M = b\int_{-h/2}^{h/2} \sigma(z) z\,dz. \tag{3}$$

We introduce the parameter η as

$$\eta = -\frac{\varepsilon}{\varepsilon_m}, \qquad \varepsilon_m = \frac{|\kappa|\,h}{2}. \tag{4}$$

If $\eta > 1$, then the fibers are compressed throughout the entire cross-sectional area and to calculate the moment M the following well-known relation may be applied:

$$M = E_2 J\kappa, \qquad J = \frac{h^3 b}{12}. \tag{5}$$

If $\eta < 1$ in the domain $z_* < z < h/2$, $z_* = -\varepsilon/\kappa$ of the cross-sectional area, the fibers are under tension and to calculate the force P and the moment M due to (3) one should use the relations of the variable elastic modulus theory (2). Substituting (2) into (3) we obtain

$$\begin{aligned} P &= \frac{S\varepsilon\left(E_2(1+\eta)^2 - E_1(1-\eta)^2\right)}{4\eta} = E_2 S\varepsilon + \frac{(E_2 - E_1)(1-\eta)^2 S\varepsilon}{4\eta}, \\ M &= E_2 J\kappa - \frac{(E_2 - E_1)(2+\eta)(1-\eta)^2}{4} J\kappa, \qquad S = bh. \end{aligned} \tag{6}$$

Here the force P is assumed to be given; therefore the first formula in (6) is the relation between the parameters ε and η or, by (4), it is the relation between the parameters κ and η. Now (4) may be represented in the form of a quadratic equation in η:

$$1 - \gamma - 4\xi^{-1} + 2(1+\gamma)\eta + (1-\gamma)\eta^2 = 0, \tag{7}$$

where

$$\gamma = \frac{E_1}{E_2}, \quad \xi = \frac{\varepsilon_m}{\varepsilon_0} = \frac{\kappa}{\kappa_0} > 1, \quad \varepsilon_0 = -\frac{P}{E_2 S}, \quad \kappa_0 = \frac{2\varepsilon_0}{h}. \tag{8}$$

Here ε_0 in the initial compressive deformation, ε_m is the bending deformation of a fiber on the boundary.

Now the second relation in (6) may be represented as

$$M = E_* J\kappa = E_2 J\kappa_0 \xi f(\xi), \tag{9}$$

where E_* is the reduced elastic modulus and

$$E_* = E_2 f(\xi,\gamma), \; f(\xi,\gamma) = \begin{cases} 1 & \text{for} \quad \kappa < \kappa_0, \\ 1 - (\xi^{-1} - \eta)(2+\eta) & \text{for} \quad \kappa > \kappa_0. \end{cases} \tag{10}$$

By equation (7)

$$\eta = \frac{-(1+\gamma) + 2\sqrt{\xi^{-1} + \gamma(1-\xi^{-1})}}{1-\gamma}. \tag{11}$$

The dependence of the ratio E_*/E_2 on the parameter ξ for different values of the ratio $\gamma = E_1/E_2$ is plotted in Fig. 4.2. In particular, for the

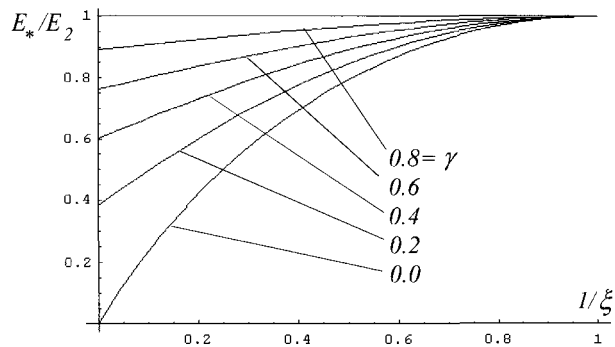

Fig. 4.2. Bending stiffness of a beam made of material with variable moduli

lower curve $E_1 = 0$ in the left side of the plot, the axial compression is equal to 0 ($\varepsilon_0 = 0$, $\xi = \infty$).

Let the lower end of the beam, $x = 0$, be clamped and, at the upper end, $x = l$, let the applied vertical compressive force be P and the transverse force be Q as shown in Fig. 4.3.

If the bending stiffness is assumed to be constant and equal to $E_2 J$ then the deflection $w(s)$ is well known:

$$w(x) = \frac{Q}{P\lambda\cos(\lambda l)}[\sin(\lambda l) - \sin(\lambda(l-x)) - \lambda x\cos(\lambda l)], \qquad \lambda = \sqrt{\frac{P}{E_2 J}}. \tag{12}$$

In particular, the beam stiffness under the transverse force Q is

$$c^{cl} = \frac{Q}{w(l)} = \frac{P\lambda\cos(\lambda l)}{\sin(\lambda l) - \lambda l\cos(\lambda l)} \tag{13}$$

and the stiffness converges to $c = 3E_2 J/l^3$ as $P \to 0$.

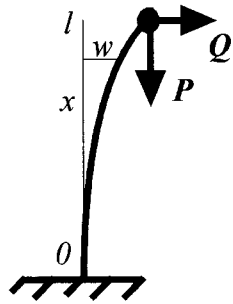

Fig. 4.3. Bending of a vertical beam loaded at the upper end

For $\cos(\lambda l) = 0$ or

$$P = P_0 = \frac{\pi^2 E_2 J}{4l^2} \tag{14}$$

the beam buckles under axial compression, and its stiffness becomes equal to 0.

Solutions (12)–(14) are later compared with similar solutions for variable modulus material. Those solutions depend non-linearly on the force Q.

4.3. Stiffness of a Beam Made of Variable Modulus Material

By relation (9), the bending moment in the cross-section x is equal to

$$M(x) = P(w(l) - w(x)) + Q(l - x) = E_2 J \kappa_0 \xi f(\xi), \quad \xi = \frac{1}{\kappa_0}\frac{d^2 w}{dx^2}, \tag{15}$$

where $w(x)$ is the deflection of the beam.

Reduce equation (15) to dimensionless form (the dimensionless variables are marked with *) and assume the following relations:

$$\begin{aligned} x &= lx^*, \quad w = w^* h/2, \quad w_0 = w_0^* h/2, \\ P &= P_0 P^*, \quad Q = Q_0 Q^*, \quad Q_0 = E_2 J \kappa_0 / l, \end{aligned} \tag{16}$$

where the force P_0 is defined in (3) and the force Q_0 is the threshold force. For forces larger than Q_0 tensile stresses develop. Now equation (15) may be written as

$$\xi f(\xi) = 3(w^*(1) - w^*(x^*) + w_0^*) + Q^*(1 - x^*), \qquad \xi = \frac{12}{P_* \pi^2}\frac{d^2 w^*}{(dx^*)^2}. \tag{17}$$

Equation (17) is a nonlinear differential equation for $w^*(x^*)$, which we integrate using the boundary conditions of the clamped edge

$$w^* = 0, \qquad \frac{dw^*}{dx^*} = 0 \quad \text{for} \quad x^* = 0. \tag{18}$$

After the equation is solved, the beam stiffness may be obtained in the form

$$c = \frac{Q}{w(l)} = c_0 \frac{P^* Q^*}{3w^*(1)}, \qquad c_0 = \frac{P_0}{l}. \tag{19}$$

By relations (16), formula (2) may be written in the form

$$c^{cl} = \frac{Q}{w(l)} = c_0 \frac{P^* y \cos y}{\sin y - y \cos y}, \qquad y = \frac{\pi\sqrt{P^*}}{2}. \tag{20}$$

Let us compare the results for variable modulus material obtained by formula (19) and the results for material with a constant modulus of elasticity obtained by formula (20). The stiffness ratio for the beams made of materials with variable and constant moduli is denoted with ζ,

$$\zeta = \frac{c}{c^{cl}} = \frac{Q^*(\sin y - y \cos y)}{3w^*(1) y \cos y}, \qquad y = \frac{\pi\sqrt{P^*}}{2}. \tag{21}$$

In Figs. 4.4(a) and 4.4(b), the stiffness, ζ, of a beam made of variable modulus material is plotted against the dimensionless horizontal deflection of the upper beam end, $w^*(1) = 2w(l)/h$.

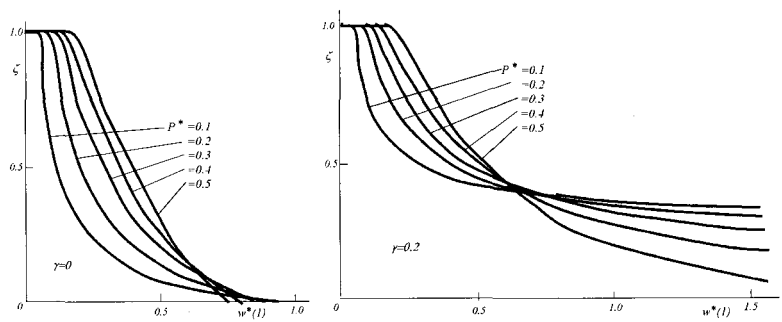

Fig. 4.4. Relation ζ vs. $w^*(1)$ for $\gamma = 0$ (a) and $\gamma = 0.2$ (b)

The curves are plotted for five values of the dimensionless axial compressive force P^* and two values of the parameter γ which is the ratio of elastic moduli under tension and compression. The decrease in stiffness is clearly shown. Note that, in the case $\gamma = 0$, the material does not resist

tension at all. A value of ζ equal to zero means that the beam buckles under axial compression. Numerical experiments show that for $\gamma = 0.2$ the beam buckling may also occur for large values of $w^*(1)$. For example, for $P^* = 0.5$ beam buckling occurs if $w^*(1) = 1.99$. The horizontal parts of the curves $\zeta(w^*(1)) = 1$ correspond to the case where there are no fibers in tension in the beam cross-sections.

4.4. Fiber-reinforced Shell

Consider a thin elastic shell made of composite material. The shell consists of an elastic isotropic matrix and N systems of elastic fibers placed parallel to the neutral surface of the shell. In [Haseganu *et al.* (2000)][2], the equations describing the stress state of such shell have been obtained for a 2D shell model satisfying Kirchhoff–Love's hypotheses. The fibers were assumed to be linear elastic and resistant to both compressive and tensile stresses.

In this paper we consider fibers with essentially non-lineal properties under compression. Indeed, we assume that the fiber stiffness is negligibly small under sufficiently large compressive stresses. Under these assumptions, the relations for internal stresses and moments and deformations of the neutral surface of the shell are significantly nonlinear. Both stresses and moments depend on both types of deformations of the neutral surface, i.e. tangential and bending. As an example, we consider a cylindrical shell reinforced with fibers under internal pressure.

4.5. Strains and Stresses in a Shell Made of Composite Material

We introduce the curvilinear coordinates α_1 and α_2 on the neutral surface, which coincide with the lines of curvature. The third coordinate z is directed normal to the surface. It is assumed that the shell is reinforced with N systems of fibers inclined at angles θ_k with respect to the axis α_1, $k = 1, 2, \ldots, N$. The stresses in the shell, σ_{ij}, are the sum of the stresses in the matrix $\sigma_{ij}^{(0)}$ and the average stresses $\sigma_{ij}^{(k)}$ due to tension/compression of the fibers

$$\sigma_{ij} = \sigma_{ij}^{(0)} + \sum_{k=1}^{N} \sigma_{ij}^{(k)}. \tag{22}$$

According to Kirchhoff's hypothesis, $\sigma_{33} = 0$ and the stresses σ_{i3} may be found from the equilibrium equations. We write the relations for the stresses

σ_{ij} and deformations ε_{ij} for $i, j = 1, 2$. For the matrix

$$\sigma_{11}^{(0)} = F_0(\varepsilon_{11}+\nu_0\varepsilon_{22}), \quad \sigma_{12}^{(0)} = \frac{1-\nu_0}{2}F_0\varepsilon_{12}, \quad \sigma_{22}^{(0)} = F_0(\varepsilon_{22}+\nu_0\varepsilon_{11}), \tag{23}$$

where $F_0 = E_0\delta_0/(1-\nu_0^2)$, E_0 is Young's modulus and ν_0 is the matrix of Poisson coefficient. The coefficient $\delta_0 < 1$ defines the relative volume occupied by the matrix. The case $\delta_0 = 1$ corresponds to the non-stiffened shell. In accordance with Kirchhoff's hypothesis [Haseganu *et al.* (2000)][2], the deformations ε_{ij} are a linear functions of the coordinate z,

$$\varepsilon_{11} = \varepsilon_1 + \kappa_1 z, \quad \varepsilon_{12} = \omega + 2\tau z, \quad \varepsilon_{22} = \varepsilon_2 + \kappa_2 z. \tag{24}$$

Here ε_1, ω, and ε_2 are the tensile-shear deformations and κ_1, τ, and κ_2 are the bending-twisting deformations of the neutral surface of the shell. Consider one system of fibers inclined at angle θ_k to the axis α_1. The deformations $\varepsilon^{(k)}$ in the fibers are found to be

$$\varepsilon^{(k)} = \varepsilon_{11}c_k^2 + \varepsilon_{12}c_k s_k + \varepsilon_{22}s_k^2, \quad c_k = \cos\theta_k, \quad s_k = \sin\theta_k, \tag{25}$$

where the deformations ε_{ij} are as in relations (23) and (24). If a fiber is under tension then, by Hooke's law, the axial force in the fiber is equal to

$$P^{(k)} = E_k S_k \varepsilon^{(k)}, \tag{26}$$

where E_k is Young's modulus and S_k is the fiber cross-section area. If a fiber is under compression, then we use more general relations than (26). For this purpose we introduce the following fiber model: if $\varepsilon^{(k)} \geq -\varepsilon_0$ then relation (26) holds, otherwise, i.e. if $\varepsilon^{(k)} < -\varepsilon_0$, then $P^{(k)} = 0$. The meaning and value of the threshold constant ε_0 is discussed in Section 6. According to the above model, the average stresses in the direction $\theta^{(k)}$ for the k-th system of fibers are determined by the formulas

$$\sigma^{(k)} = \begin{cases} F_k\varepsilon^{(k)} & \text{for } \varepsilon^{(k)} \geq -\varepsilon_0, \\ 0 & \text{for } \varepsilon^{(k)} < -\varepsilon_0, \end{cases} \qquad \varepsilon_0 \geq 0, \quad F_k = E_k\delta_k, \tag{27}$$

where δ_k is the relative volume filled with the fibers of the k-th system. Naturally, $\sum_{k=0}^{N}\delta_k = 1$. Here and below we neglect Poisson's effect, which states that the cross-section of a fiber changes under tension. The stresses $\sigma_{ij}^{(k)}$ in relation (22) are the following:

$$\sigma_{11}^{(k)} = c_k^2\sigma^{(k)}, \qquad \sigma_{12}^{(k)} = c_k s_k \sigma^{(k)}, \qquad \sigma_{22}^{(k)} = s_k^2\sigma^{(k)}. \tag{28}$$

4.6. The Threshold Constant ε_0

If $\varepsilon_0 = 0$, then the fiber stiffness under tension is equal to zero. The inequality $\varepsilon_0 > 0$ may be justified in the following way. Firstly, the fibers may be initially stressed. Secondly, if we consider a fiber as a beam on an elastic foundation under compressive load, then the beam deflection, $w(s)$, may be obtained from the equation

$$D\frac{d^4w}{ds^4} + P\frac{d^2w}{ds^2} + cw = 0, \tag{29}$$

where s is the axial coordinate, D is the bending stiffness, P is the compressive force and c is the foundation (matrix) stiffness.

Equation (29) has the nontrivial bounded solution $w(s) = w_0 \sin(\lambda s)$ if

$$P(\lambda) = D\lambda^2 + \frac{c}{\lambda^2}. \tag{30}$$

Then the minimal value of P and the corresponding value of the threshold stress ε_0 are

$$P_{\min} = \min_{\lambda} P(\lambda) = 2\sqrt{Dc}, \qquad \varepsilon_0 = \frac{2\sqrt{Dc}}{E_k S_k}. \tag{31}$$

4.7. Elasticity Relations for a Shell Made of a Composite Material

Neglecting the small terms h/R_1 and h/R_2 compared to 1, where h is the shell thickness and R_i are the principal radii of curvature of the neutral surface, we get an expression for the stress-resultants T_1, T_2 and S and the stress-couples M_1, M_2 and H in the form

$$\begin{aligned} &T_1 = \int_{-h/2}^{h/2} \sigma_{11}\, dz, \quad T_2 = \int_{-h/2}^{h/2} \sigma_{22}\, dz, \quad S = \int_{-h/2}^{h/2} \sigma_{12}\, dz, \\ &M_1 = \int_{-h/2}^{h/2} \sigma_{11} z\, dz, \; M_2 = \int_{-h/2}^{h/2} \sigma_{22} z\, dz, \; H = \int_{-h/2}^{h/2} \sigma_{12} z\, dz, \end{aligned} \tag{32}$$

where the stresses σ_{ij} are calculated by formulas (23) and (27)–(28). If, for all $z \in [-h/2, h/2]$ and for all $k = 1, 2, \ldots, N$, the inequality $\varepsilon^{(k)} \geq \varepsilon_0$ holds, then the stress resultants and couples depend linearly on the deformations of the neutral surface ε_1, ε_2, ω, κ_1, k_2, and τ. Assuming that the shell is symmetric with respect to the neutral surface we obtain elasticity relations similar to those found in [Ambartsumian (1982)][1],

$$T_i = \sum_{j=1}^{3} K_{ij}\varepsilon_j, \quad M_i = \sum_{j=1}^{3} D_{ij}\kappa_j, \quad j = 1, 2, 3, \tag{33}$$

where, for short, we denote $\varepsilon_3 = \omega$, $\kappa_3 = 2\tau$, $T_3 = S$, and $M_3 = H$. The coefficients K_{ij} and D_{ij} are determined in [Haseganu *et al.* (2000)][2] and, for example, K_{11} and D_{11} are given by formulas

$$\begin{bmatrix} K_{11} \\ D_{11} \end{bmatrix} = \int_{-h/2}^{h/2} \left(F_0 + \sum_{k=1}^{N} F_k c_k^4 \right) \begin{bmatrix} 1 \\ z^2 \end{bmatrix} dz. \tag{34}$$

If the inequality $\varepsilon^{(k)} < -\varepsilon_0$ is valid only for some specific values of k and/or z, then relations (34) do not hold any more since the dependence of the stress resultants and couples on the deformations of the neutral surface becomes nonlinear. In this case, it is more convenient to analyze the effect of each of the fiber systems separately. For that we represent the stress resultants and couples in the form

$$T_i = T_i^{(0)} + \sum_{k=1}^{N} T_i^{(k)}, \quad M_i = M_i^{(0)} + \sum_{k=1}^{N} M_i^{(k)} \quad i = 1, 2, 3. \tag{35}$$

Here the variables $T_i^{(0)}$ and $M_i^{(0)}$ depend linearly on the deformations of the neutral surface and may be calculated by formulas (33)–(34) for $F_k = 0$ ($k \neq 0$). The remaining variables in (35) are

$$T_i^{(k)} = C_i^{(k)} \delta_k \int_{-h/2}^{h/2} \sigma^{(k)}(e^{(k)})\, dz, \quad M_i^{(k)} = C_i^{(k)} \delta_k \int_{-h/2}^{h/2} \sigma^{(k)}(e^{(k)})\, z\, dz. \tag{36}$$

Here $C_1^{(k)} = c_k^2$, $C_2^{(k)} = s_k^2$, and $C_3^{(k)} = c_k s_k$, and, by relations (24)–(25), the deformations $\varepsilon^{(k)}(z)$ are linear functions of z $\varepsilon^{(k)} = \varepsilon_m^{(k)} + \kappa^{(k)} z$, where

$$\varepsilon_m^{(k)} = \sum_{i=1}^{3} C_i^{(k)} \varepsilon_i, \qquad \kappa^{(k)} = \sum_{i=1}^{3} C_i^{(k)} \kappa_i, \tag{37}$$

and the functions $\sigma^{(k)}(\varepsilon^{(k)})$ are given by relation (28). Here $\varepsilon_m^{(k)}$ are the tensile–compressive deformations in the directions θ_k. Below the subscript k is omitted.

Let $\varepsilon_b = |\kappa| h/2$ be the maximal value of the second term in the expression for $\varepsilon^{(k)}$ corresponding to the bending deformations. We should consider the following three cases.

Case 1. If $\varepsilon_m \geq \varepsilon_b - \varepsilon_0$, then the fibers of the k-th system are under tension for all values of z and one should use relations (34) obtained in [Smirnov and Tovstik (2002)][3]. In this case, the deformations ε_j and κ_j are independent, i. e. $T_j^{(k)} = T_j(k)(\varepsilon_i)$ and $M_j^{(k)} = M_j(k)(\kappa_i)$.

Case 2. If $\varepsilon_m \le -\varepsilon_b - \varepsilon_0$, then, by relations (36), $T_j^{(k)} = M_j^{(k)} = 0$. So, in this case, the fibers of the k-th system do not resist compression.

Case 3. In the intermediate case $|\varepsilon_0 + \varepsilon_m| < \varepsilon_b$, the fibers resist compression only in a part of the shell volume and relations (36) for the shells for symmetric cross-section lead to the formulas, according to which the stress resultants, $T_i^{(k)}$, and couples, $M_j^{(k)}$, depend on both the tensile-shear deformations ε_j and the bending-twisting deformations κ_j. If the fibers are uniformly distributed along the shell thickness, then, after calculating the integrals in (36), we obtain

$$T_j^{(k)} = C_j F_k \delta_k \frac{\varepsilon_m + \varepsilon_b + \varepsilon_0}{2|k|}(\varepsilon_m + \varepsilon_b - \varepsilon_0),$$
$$M_j^{(k)} = C_j F_k \delta_k \frac{\varepsilon_m + \varepsilon_b + \varepsilon_0}{6k|k|}(2\varepsilon_b^2 - \varepsilon_m^2 + \varepsilon_0^2 + \varepsilon_m\varepsilon_b + \varepsilon_m\varepsilon_0 - 2\varepsilon_b\varepsilon_0). \tag{38}$$

These relations are valid for $\kappa > 0$ and $\kappa < 0$. Formulas (38) are not used for $\kappa = 0$ since, for small $|\kappa|$, either case 1 or case 2 may occur.

4.8. Cylindrical Shell Under Internal Pressure

As an example, we consider the axisymmetric deformation of a circular cylindrical shell of radius R under uniform internal pressure q. The shell is reinforced by two systems of fibers inclined at angles $\theta_{1,2} = \pm\pi/4$ from the generatrix (this means that, for all coefficients, $C_j^{(k)} = 1/2$) and uniformly distributed along the shell thickness.

Let δ be the relative volume of each fiber system and $1 - 2\delta$ be the relative volume of the matrix. The moduli of elasticity for the matrix and fibers are E_0 and E_1, respectively.

Far away from the shell ends, the fibers are under tension resisting internal pressure. It could be obtained from the equilibrium equations that

$$T_1 = \frac{qR}{2} = K_0(\varepsilon_1 + \nu_0\varepsilon_2) + T^{(1)}, \quad K_0 = \frac{E_0 h(1-2\delta)}{1-\nu_0^2},$$
$$T_2 = qR = K_0(\varepsilon_2 + \nu_0\varepsilon_1) + T^{(1)}, \quad T^{(1)} = \frac{E_1 h\delta}{2}(\varepsilon_1 + \varepsilon_2), \tag{39}$$

where the variable $T^{(1)}$ is the term in the stress resultants T_1 and T_2 due to stresses in the fibers. This term appears to be equal for both stress

resultants since $\theta_{1,2} = \pm\pi/4$. From relations (39) one can find

$$\varepsilon_1 = \frac{\varepsilon_q - (\nu_0 + \gamma)\varepsilon_2}{1+\gamma}, \qquad \varepsilon_q = \frac{qR}{2K_0}, \quad \gamma = \frac{E_1 h\delta}{2K_0},$$
$$T_2 = K_0 \frac{(1-\nu_0)(1+\nu_0+2\gamma)}{1+\gamma}\varepsilon_2 + \frac{(\nu_0+\gamma)qR}{2(1+\gamma)}. \tag{40}$$

Consider a shell with clamped edge $s = 0$. First, it is assumed that the parameter ε_0 is such that there does not exist such part of the shell volume where the fibers do not resist the stress. In the neighborhood of the edge, the shell deformations are described by the equations

$$\frac{d^2M_1}{ds^2} + \frac{T_2}{R} = q, \quad w(0) = w'(0) = 0, \tag{41}$$

where

$$M_1 = \frac{K_0 h^2}{12}(1+\gamma)\kappa_1, \qquad \kappa_1 = \frac{d^2w}{ds^2}, \quad \varepsilon_2 = \frac{w}{R}.$$

Transforming equation (41) to the dimensionless variables $s_1 = s/R$ and $w_1 = w/R$ we have

$$\mu^4 \frac{d^4 w_1}{ds_1^4} + w_1 = w_0, \qquad \mu^4 = \frac{a_\mu h^2}{12R^2}, \tag{42}$$

where

$$a_\mu = \frac{(1+\gamma)^2}{(1-\nu_0)(1+\nu_0+2\gamma)}, \qquad w_0 = \frac{(2+\gamma-\nu_0)qR}{2(1-\nu_0)(1+\nu_0+2\gamma)K_0}.$$

Here w_0 is the normal dimensionless deflection far from the shell edge and μ is a small parameter. The solution of equation (42) that we are interested in is

$$w = w_0\left(1 - e^{-s_2}(\cos s_2 + \sin s_2)\right), \qquad s_2 = \frac{s_1}{\mu\sqrt{2}}. \tag{43}$$

The minimal value $\varepsilon_{\min}$ of the expression $\varepsilon_m - \varepsilon_b$ is attained at $s = 0$ and is equal to

$$\varepsilon_{\min} = \frac{qR(1-\xi)}{4K_0(1+\gamma)}, \qquad \xi = \frac{(2+\gamma-\nu_0)\sqrt{3}}{\sqrt{(1-\nu_0)(1+\nu_0+2\gamma)}}. \tag{44}$$

It is easy to show that, for all values $\gamma \geq 0$ and $\nu_0 \leq 0.5$, the inequality $\xi > 1$ holds, from which it follows that $\varepsilon_{\min} < 0$, i. e. in the neighborhood of the shell edge some fibers are compressed. For $\varepsilon_{\min} + \varepsilon_0 \geq 0$, solution (43) is valid, otherwise (case 3) some of the fibers do not resist tension and, to calculate the stress resultants and couple, one should use formulas (38). In

the following consideration, it is assumed that $\varepsilon_0 = 0$ for the fibers which do not resist tension.

Under the above assumptions

$$T_1 = K_0\left(\varepsilon_1 + \nu_0\varepsilon_2 + \gamma\frac{(\varepsilon_m+\varepsilon_b)^2}{2\varepsilon_b}\right) = K_0\varepsilon_q,$$
$$T_2 = K_0\left(\varepsilon_2 + \nu_0\varepsilon_1 + \gamma\frac{(\varepsilon_m+\varepsilon_b)^2}{2\varepsilon_b}\right), \tag{45}$$
$$M_1 = \frac{K_0h^2\kappa_1}{12}\left(1+\gamma\frac{(\varepsilon_m+\varepsilon_b)^2(2\varepsilon_b-\varepsilon_m)}{4\varepsilon_b^3}\right),$$

where

$$\varepsilon_m = \frac{\varepsilon_1+\varepsilon_2}{2}, \quad \varepsilon_2 = \frac{w}{R} = w_1, \qquad \kappa = \frac{\kappa_1}{2}, \quad \kappa_1 = \frac{d^2w}{ds^2},$$
$$\varepsilon_b = \frac{|\kappa|h}{2} = a\left|\frac{d^2w_1}{ds_2^2}\right|, \quad a = \frac{h}{8R\mu^2} = \frac{\sqrt{3}}{4\sqrt{a_\mu}}. \tag{46}$$

From the first equation in (45) we obtain

$$\varepsilon_1 = \frac{1}{\gamma}\left(\sqrt{8\varepsilon_b(2\varepsilon_b(1+\gamma)+\gamma(\varepsilon_2+\varepsilon_q)-\nu_0\varepsilon_2)} - 2\varepsilon_b(2+\gamma) - \gamma\varepsilon_2\right).$$

Now all variables in relations (45) for T_2 and M_1 are expressed through the deflection w and its derivatives and equation (41) may be written as the following system of two equations

$$\frac{1}{2}\frac{d^2y}{ds_2^2} = \frac{a_\mu}{1+\gamma}\left(2\varepsilon_q - \varepsilon_2 - \nu_0\varepsilon_1 - \gamma\frac{(\varepsilon_m+\varepsilon_b)^2}{2\varepsilon_b}\right),$$
$$\frac{1}{2}\frac{d^2w_1}{ds_2^2} = (1+\gamma)\left(1+\gamma\frac{(\varepsilon_m+\varepsilon_b)^2(2\varepsilon_b-\varepsilon_m)}{4\varepsilon_b^3}\right)^{-1} y. \tag{47}$$

For $\varepsilon_m \geq \varepsilon_b$, system (47) reduces to equation (42),

$$\frac{1}{4}\frac{d^4w_1}{ds_2^4} + w_1 = w_0, \qquad y = \frac{1}{2}\frac{d^2w_1}{ds_2^2}.$$

One of the obstacles for the numerical solution of system (47) is the fact that the second equation in (47) is not resolved with respect to d^2w_1/ds_2^2, whereas the right side of the equation implicitly depends on this value through ε_b. We solve system (47) by the shooting method. The initial conditions are imposed at the point $s_2 = s_2^0$, which is located far enough from the edge $s_2 = 0$, to satisfy the condition $\varepsilon_m > \varepsilon_b$. Under such conditions

all fibers in the cross-section s_2^0 are in tension. The initial condition are imposed on the solution

$$w_1 = w_0 \left(1 - e^{-s_2}(B_1 \cos s_2 + B_2 \sin s_2)\right), \tag{48}$$

and then one evaluates the constants B_1 and B_2 to satisfy the clamped conditions at the other end $s = 0$, $w_1(0) = w_1'(0) = 0$.

Numerical results are obtained for $\nu_0 = 0.45$ and several values of the relative stiffness parameter γ. Table 4.1 lists the dimensionless coordinate of the generatrix s_2^* which bounds the domain where the compressed fibers exist ($0 \leq s_2 < s_2^*$), and the curvature of the generatrix $s_2 = 0$.

Table 4.1. Relative stiffness γ, dimensionless coordinate s_2^* and curvature of the generatrix.

$\gamma =$	0.00	0.30	1.00	3.00	10.00
$s_2^* =$	0.00	0.22	0.29	0.42	0.60
$w_1''(0) =$	2.00	1.94	1.81	1.61	1.35

Acknowledgment

The authors gratefully acknowledge the support provided for this work by the Russian Foundation for Basic Research through grant number 04-01-00257.

References

1. Ambartsumian, S. A. (1982) "Theory of Elasticity for Materials with Variable Moduli". Moscow, Nauka, 320 pp.
2. Haseganu, E. M., Smirnov, A. L., and Tovstik, P. E., (2000), "Buckling of thin anisotropic shells", Transactions of the CSME, 24(1B), 169–178.
3. Smirnov, A. L., and Tovstik, P. E., (2002), "Thin shells reinforced with nonlinear elastic fibres", in Problems in Mechanics of Solids, St. Petersburg University Press, pp. 277–282.

This page is intentionally left blank

CHAPTER 5

ASYMPTOTIC INTEGRATION OF FREE VIBRATION EQUATIONS OF CYLINDRICAL SHELLS BY SYMBOLIC COMPUTATION

Eliza M. Haseganu

Department of Mechanical Engineering, Concordia University, Montral QC H3G IM2, Canada

Irina M. Landman

Department of Theoretical and Applied Mechanics, St. Petersburg State University, St. Petersburg, Russia, 198504
E-mail: ilandman@mail.ru, LandmanIM@corning.com

Andrei L. Smirnov

Department of Theoretical and Applied Mechanics, St. Petersburg State University, St. Petersburg, Russia, 198504
E-mail: smirnov@AS1245.spb.edu

This paper presents an algorithm for the solution of boundary value problems for the vibrations of thin cylindrical shells by means of symbolic computation. The equations describing the vibrations of a shell contain several parameters, the main of which being the small parameter of the shell thickness. The construction of the convex hull of point set allows one to build formal asymptotic solutions in different domains of the space of parameters. The constructed solutions are used for studying the free vibration spectra of the shells.

5.1. Introduction

In this paper we consider the vibrations of thin circular cylindrical shells by applying the method of asymptotic integration developed by Goldenveizer, Lidsky and Tovstik [Goldenveizer *et al.* (1978)][4]. A detailed review of their work as well as a reference list may be found in [Bauer *et al.* (1997)][1],

[Bauer *et al.* (1995)][2], [Bauer *et al.* (1993)][3], [Goldenveizer *et al.* (1978)][4]. The aim of this study is to develop an algorithm permitting symbolic integration of the governing equations for any range of values of the parameters appearing in these equations. This study is limited to the cases for which the asymptotic representation of the solution is the same in the entire domain of integration and the solutions are linearly independent (no turning points, no multiple roots). Some preliminary results of this work have been reported in [Landman *et al.* (1999)][5].

5.2. Problem Formulation

We consider a thin cylindrical shell having thickness t, length L, and radius R. We introduce the system of orthogonal coordinates, s, φ, that defines the position of a point on the neutral surface of the shell, where s is the length of the generatrix, $0 \leq s \leq L$, and φ is the longitudinal angle, $0 \leq \varphi \leq 2\pi$. The shell is bounded by two parallels $s = 0$ and $s = L$. The cylindrical shell is said to be thin if its relative thickness t/R is small. We introduce a local orthogonal system of coordinates $\boldsymbol{e}_1$, $\boldsymbol{e}_2$, $\boldsymbol{n}$, where $\boldsymbol{e}_1$ and $\boldsymbol{e}_2$ are unit vectors in the s and φ direction, respectively, and $\boldsymbol{n}$ is the normal unit vector ($\boldsymbol{n} = \boldsymbol{e}_1 \times \boldsymbol{e}_2$). Let u, v, and w be the components of the displacement U in the directions $\boldsymbol{e}_1$, $\boldsymbol{e}_2$, and $\boldsymbol{n}$. We use the shell equations of the 2D Kirchhoff–Love theory. After we separate the variables in the circumferential and axial directions the equations of vibrations for thin cylindrical shells have the form

$$\frac{d\boldsymbol{Y}}{ds} = \boldsymbol{A}(\mu, m, \lambda)\boldsymbol{Y}, \tag{1}$$

where $\boldsymbol{A}$ is an 8×8 matrix, $\boldsymbol{Y}(s) = \{y_1(s), \ldots, y_8(s)\}$ is an 8×1 vector function, μ is the main small parameter related to the relative thickness of the shell, m is the wavenumber in the circumferential direction, and λ is the frequency parameter. The boundary conditions are

$$\boldsymbol{B}_i\boldsymbol{Y}(s_i) = 0, \qquad i = 1, 2 \tag{2}$$

where $s_1 = 0$ and $s_2 = L$, and $\boldsymbol{B}_i$ are $[4 \times 8]$ matrices.

When employing the Kirchhoff–Love theory it is most convenient to use the following variables: $\boldsymbol{Y} = (u, v, w, T_1, S_{21}, N_1, M_1, \gamma_1)$, where T_1 and S_{21} are the stress resultants, N_1 is the transverse shear resultant, M_1 is the moment resultant, and γ_1 is the angle of rotation of the normal [Bauer *et al.* (1993)][3]. For such variables we consider boundary conditions of the

form: $u = 0$ or $T_1 = 0$, $v = 0$ or S_{12}, $w = 0$ or $N_1 = 0$, $\gamma_1 = 0$ or $M_1 = 0$ at $s = 0$ or $s = L$.

Sometimes it is more convenient to express the resultants and the angle of rotation as functions of the displacements, In this case, we get the system of equations for $\boldsymbol{U} = (u, v, w)$

$$\mu^4 L_\mu(\boldsymbol{U}, \mu, m) + L(\boldsymbol{U}, \mu, m) + \lambda \boldsymbol{U} = 0, \tag{3}$$

where L_μ and L are linear differential operators of the eighth order and of the fourth order, respectively. In this case, the boundary conditions must be formulated in terms of u, v, w and their derivatives.

To solve the boundary value problem (1)–(2) we apply the asymptotic integration method described in [Bauer *et al.* (1997)][1], [Bauer *et al.* (1995)][2], [Bauer *et al.* (1993)][3]. For this we need to construct the formal asymptotic solution of equation (1) and then require that the boundary conditions (2) are satisfied.

We seek the solution of equation (1) in the form

$$\boldsymbol{Y}(s, \mu) = \sum_{i=1}^{8} \sum_{k=0}^{\infty} C_i \boldsymbol{Y}_k^i \mu^{k\kappa_i} \exp p_i s, \tag{4}$$

where C_i are arbitrary constants, $\boldsymbol{Y}_k^i$ is the matrix of the amplitude vectors, and κ_i depends on the order of p_i with respect to μ. For example, if $p_i \sim \mu^{-1}$, then $\kappa_i = 1$.

Substituting solution (4) into equation (1) we obtain the characteristic equation for p_i

$$|\boldsymbol{A}(m, \mu, \lambda) - p\boldsymbol{I}| = 0, \tag{5}$$

where $\boldsymbol{I}$ is the identity matrix. In this study we consider only the cases where all p_i are simple roots of equation (5), i.e. $p_i \neq p_j$ for $i \neq j$. Under such assumptions, we can use the formal asymptotic solution (4). Then, all solutions are linearly independent and their linear combination provides the general solution of the initial equation.

For different relations between the parameters, solutions (4) have different forms. In this study we use symbolic computation to construct formal asymptotic solutions for different values of the parameters μ, λ, and m.

The order of the function $|p|$ in μ is called the *index of variation* of the solution. The solution is exponentially increasing away from the edge $s = 0$ if $\Re p_i > 0$. Such integral is called the integral of the edge effect near the end $s = L$. The solution is exponentially decreasing away from the edge $s = 0$ if $\Re p_i < 0$. Such integral is called the edge effect near the end $s = 0$.

The solution is oscillating if $\Re p_i = 0$ and $\Im p_i \neq 0$. If $p_i \equiv 0$, the solution is said to be slowly varying. In solving the boundary value problem with an error of order e^{-c/μ^d}, where c and d are some positive constants, we may take the value of the edge effect integrals to be equal to zero at the other end.

After the construction of the formal asymptotic solutions, the boundary conditions should be imposed to find the frequency parameter λ. Substituting (4) into (2) we obtain a system of linear equations in C_i that has nonzero solutions if its determinant vanishes,

$$\Delta(\lambda, \mu) = 0. \tag{6}$$

One can solve this eighth-degree equation numerically. In some cases this equation may be simplified.

Simultaneously with the problem for $\mu \neq 0$ (perturbed problem) we consider the same problem with $\mu = 0$ (unperturbed problem).

If all p_i are different from 0 and not pure imaginary, then

$$\lim_{\mu \to 0} \Delta(\lambda, \mu) = \Delta(\lambda, 0) \tag{7}$$

and

$$\lambda = \lambda_0 + \mu\lambda_1 + \cdots, \tag{8}$$

where λ_0 is the frequency for the unperturbed system, i.e. $\Delta(\lambda_0, 0) = 0$.

Of special interest are the cases of regular degeneracy [Vishik and Lyusternik (1957)][6]. Let the perturbed system have order n and the unperturbed system have order m. Let the perturbed system have $l = n - m$ additional roots such that l_1 of them have negative real parts and l_2 have positive real parts, where l_1 is the number of additional boundary conditions on the left edge and l_2 is the number of additional boundary conditions on the right edge. In this case the solution may be constructed by an iterative method.

The existence of pure imaginary roots makes the problem more difficult. As a rule, in this case, the function $\Delta(\lambda, \mu)$ has a limit point at $\mu = 0$ and $\lim_{\mu \to 0} \Delta(\lambda, \mu) \neq \Delta(\lambda, 0)$.

5.3. Formal Asymptotic Solutions of the Equations of Cylindrical Shells

We consider the equations describing the vibrations of thin cylindrical shells in terms of displacements [Goldenveizer *et al.* (1978)][4].

$$
\begin{aligned}
&-\frac{\partial^2 u}{\partial s^2}-\frac{1-\nu}{2}\frac{\partial^2 u}{\partial \varphi^2}-(1-\nu^2)\lambda u-\frac{1+\nu}{2}\frac{\partial^2 v}{\partial s\partial\varphi}+\nu\frac{\partial w}{\partial s}=0,\\
&-\frac{1+\nu}{2}\frac{\partial^2 u}{\partial s\partial\varphi}-\frac{1-\nu}{2}\frac{\partial^2 v}{\partial s^2}-\frac{\partial^2 v}{\partial\varphi^2}+\mu^4\left(-2(1-\nu)\frac{\partial^2 v}{\partial s^2}-\frac{\partial^2 v}{\partial\varphi^2}\right)-\\
&\quad(1-\nu^2)\lambda v+\frac{\partial w}{\partial\varphi}+\mu^4\left(-(2-\nu)\frac{\partial^3 w}{\partial s^2\partial\varphi}-\frac{\partial^3 w}{\partial\varphi^3}\right)=0,\\
&-\nu\frac{\partial u}{\partial s}-\frac{\partial v}{\partial\varphi}+\mu^4\left((2-\nu)\frac{\partial^3 v}{\partial s^2\partial\varphi}+\frac{\partial^3 v}{\partial\varphi^3}\right)\\
&\quad+w-(1-\nu^2)\lambda w+\mu^4\left(\frac{\partial^4 w}{\partial s^4}+2\frac{\partial^4 w}{\partial s^2\partial\varphi^2}+\frac{\partial^4 w}{\partial\varphi^4}\right)=0.
\end{aligned}
\tag{9}
$$

Here $\mu^4 = t^2/(12R^2)$ is the main small parameter, $\lambda = \rho\omega^2 R^2/E$ is the frequency parameter, E is Young's modulus, ν is Poisson's ratio, ρ is the shell mass density, and ω is the natural frequency.

Separating the variables s and φ in the expressions of the displacements

$$
\begin{aligned}
u(s,\varphi) &= U(s)\sin m\varphi,\\
v(s,\varphi) &= V(s)\cos m\varphi,\\
w(s,\varphi) &= W(s)\sin m\varphi,
\end{aligned}
\tag{10}
$$

and substituting them in (9) we obtain the system of ordinary differential equations

$$
\begin{aligned}
&-\frac{\partial^2 U}{\partial s^2}+\frac{1-\nu}{2}m^2U-(1-\nu^2)\lambda U+\frac{1+\nu}{2}m\frac{\partial V}{\partial s}+\nu\frac{\partial W}{\partial s}=0,\\
&-\frac{1+\nu}{2}m\frac{\partial U}{\partial s}-\frac{1-\nu}{2}\frac{\partial^2 V}{\partial s^2}+m^2V+\mu^4\left(-2(1-\nu)\frac{\partial^2 V}{\partial s^2}+m^2V\right)-\\
&\quad(1-\nu^2)\lambda V+mW+\mu^4\left(-(2-\nu)m\frac{\partial^2 W}{\partial s^2}+m^3W\right)=0,\\
&-\nu\frac{\partial U}{\partial s}+mV+\mu^4\left(-(2-\nu)m\frac{\partial^2 V}{\partial s^2}+m^3V\right)+\\
&\quad W-(1-\nu^2)\lambda W+\mu^4\left(\frac{\partial^4 W}{\partial s^4}-2m^2\frac{\partial^2 W}{\partial s^2}+m^4W\right)=0.
\end{aligned}
\tag{11}
$$

To determine the structure of the asymptotic expansions, we seek a solution in the form

$$U = U_0\, e^{ps}, \quad V = V_0\, e^{ps}, \quad W = W_0\, e^{ps}. \tag{12}$$

Substituting (12) in (11) we obtain the following linear system of three equations in U_0, V_0, and W_0:

$$\begin{aligned}
&\left[-p^2 + \frac{1-\nu}{2}\, m^2 - (1-\nu^2)\lambda\right] U_0 + \frac{1+\nu}{2}\, mpV_0 + \nu p W_0 = 0,\\
&-\frac{1+\nu}{2}\, mpU_0 - \left[\frac{1-\nu}{2}\, p^2 - m^2 + \mu^4\left(2(1-\nu)p^2 - m^2\right)\right.\\
&\qquad \left. + (1-\nu^2)\lambda\right] V_0 + \left[m - \mu^4\left((2-\nu)mp^2 - m^3\right)\right] W_0 = 0,\\
&-\nu p U_0 + \left[m - \mu^4\left((2-\nu)mp^2 - m^3\right)\right] V_0\\
&\qquad + \left[1 - (1-\nu^2)\lambda + \mu^4\left(p^2 - m^2\right)^2\right] W_0 = 0.
\end{aligned} \tag{13}$$

System (13) has nontrivial solutions if its determinant is equal to zero. This determinant is an eighth-degree polynomial in p. Thus, its eight zeros can be found.

5.4. Axisymmetric Vibrations

We start with the analysis of the axisymmetric case ($m = 0$). In this case, system (13) becomes

$$\begin{aligned}
&-\left[p^2 + (1-\nu^2)\lambda\right] U_0 + \nu p W_0 = 0,\\
&-\left[\frac{1-\nu}{2}\, p^2 + \mu^4 2(1-\nu)p^2 + (1-\nu^2)\lambda\right] V_0 = 0,\\
&-\nu p U_0 + \left[1 - (1-\nu^2)\lambda + \mu^4 p^4\right] W_0 = 0.
\end{aligned} \tag{14}$$

This system splits. The first and third equations in (14) define the transverse-axial vibrations, and the second equation defines the torsional vibrations. We consider only the transverse-axial vibrations.

The characteristic equations is

$$P(p; h, \lambda) = \begin{vmatrix} -p^2 - (1-\nu^2)\lambda & \nu p \\ -\nu p & 1 - (1-\nu^2)\lambda + \mu^4 p^4 \end{vmatrix} = 0, \tag{15}$$

which expands to

$$\lambda - \lambda^2 + \lambda^2\nu^2 + p^2 - \lambda p^2 + h^4\lambda p^4 - h^4\lambda\nu^2 p^4 + h^4 p^6 = 0, \tag{16}$$

where $h^4 = \mu^4/\left(1-\nu^2\right)$.

Now we must find the roots p_i of equation (16) for different values of the small parameter $h \ll 1$. We write (16) in the form

$$P(p; h, \lambda) = \sum_{i}^{6} a_i p^{k_i} h^{\alpha_i} \lambda^{\beta_i} = 0, \tag{17}$$

where the coefficients a_i do not depend on p, h and λ, and i is the number of the term in (16). The points $M_i = \{k_i, \alpha_i, \beta_i\}$ in the (p, h, λ) space are called the representative points. Each point is associated with a coefficient a_i, that is later called the weight of the point. For equation (16) we have $M_i = \{\{1, \{0, 0, 1\}\}, \{\{-1 + \nu^2, \{0, 0, 2\}\}, \{\{1, \{2, 0, 0\}\}, \{\{-1, \{2, 0, 1\}\}, \{\{1 - \nu^2, \{4, 4, 1\}\}, \{\{1, \{6, 4, 0\}\}$.

If the order of the parameter λ is given, i.e. $\lambda = \lambda_0 h^{\varkappa}$, where $\lambda_0 \sim 1$ and $\varkappa$ is known, then equation (16) contains only one small parameter h. Newton's diagram method may be used [Bauer *et al.* (1993)][3] to obtain the roots of such an equation. In this case, the representative points lie in the (p, h) plane and have the form $M_i = \{k_i, \alpha_i + \beta_i \varkappa\}$. The segments of the lower part of the convex hull of the set of the points M_i, i. e. the segments that are visible from the point $(p, h) = (0, -\infty)$, define the terms of equation (16) that should be kept to determine the main terms of the roots, p_i.

We consider three cases here, where $\varkappa$ is equal to 1, 0 and -1, respectively. We start with the case $\varkappa = 1$ for which Newton's diagram is plotted in Fig. 5.1.

In this case, the representative points for equation (16) are $M_1 = (0, 1)$, $M_2 = (0, 2)$, $M_3 = (2, 0)$, $M_4 = (2, 1)$, $M_5 = (4, 5)$, and $M_6 = (6, 4)$ and Newton's diagram consists of two segments. The first segment is determined by M_1 and M_3, and the second segment by M_3 and M_6. Therefore, equation (16) has two sets of roots, the first one being defined by the equation

$$\lambda + p^2 = 0, \tag{18}$$

while the second one may be found from the equation

$$p^2 + h^4 p^6 = 0. \tag{19}$$

Hence, the roots are

$$p_{1,2} = \pm i\sqrt{\lambda} \tag{20}$$

and

$$p_j = \frac{\varepsilon_j}{h}, \quad \varepsilon_j = \pm\frac{\sqrt{2}}{2} \pm i\frac{\sqrt{2}}{2} \qquad j = 3, 4, 5, 6. \tag{21}$$

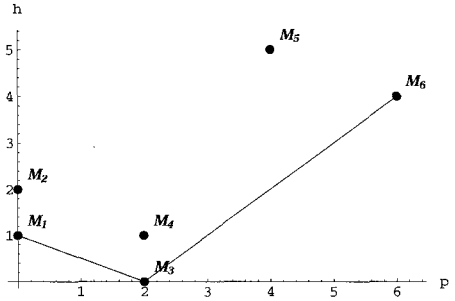

Fig. 5.1. Newton's diagram for $\varkappa = 1$, $m = 0$.

The order of the p_j may be determined by the angles between the segments and the p axis.

We also can determine the relative orders of the eigenvectors U_0^i and W_0^i. For this we keep only the main terms in equations (14) and substitute the expressions for the roots p_i into either the first or the third equation. The only limitation for this choice is that both coefficients of U_0^i and W_0^i are nonzero. The main terms for U_0^i and W_0^i are given in Table 5.1.

Table 5.1. Roots and eigenvectors for $m = 0$, $\varkappa = 1$.

	1	2	3	4	5	6
p	$\sqrt{\lambda}i$	$-\sqrt{\lambda}i$	$\frac{\varepsilon_1}{h}$	$\frac{\varepsilon_2}{h}$	$\frac{\varepsilon_3}{h}$	$\frac{\varepsilon_4}{h}$
U_0	p_1	p_2	ν	ν	ν	ν
W_0	$-\nu\lambda$	$-\nu\lambda$	p_3	p_4	p_5	p_6

In the second case, $\varkappa = 0$, the representative points for equation (16) are $M_1 = (0,1)$, $M_2 = (0,1)$, $M_3 = (2,0)$, $M_4 = (2,0)$, $M_5 = (4,4)$, and $M_6 = (6,4)$. In this case, Newton's diagram consists of 2 segments (Fig. 5.2).

The first segment is determined by the points M_1, M_2, M_3 and M_4, and the second one by the points M_3, M_4, and M_6. Therefore, equation (16) has two groups of roots, the first one being defined by the equation

$$\lambda - \lambda^2 + \lambda^2\nu^2 + p^2 - \lambda p^2 = 0, \tag{22}$$

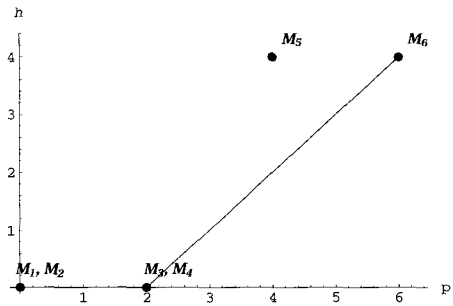

Fig. 5.2. Newton's diagram for $\varkappa = 1$, $m = 0$.

and the second one by the equation

$$p^2 - \lambda p^2 + h^4 p^6 = 0. \tag{23}$$

Hence

$$p_{1,2} = \pm F(\lambda), \quad F(\lambda) = \sqrt{\frac{\lambda - (1-\nu^2)\lambda^2}{\lambda - 1}}, \tag{24}$$

and

$$p_{3,4,5,6} = \frac{(\lambda - 1)^{1/4}}{h}. \tag{25}$$

For this case, the roots and the eigenvectors are shown in Table 5.2.

Table 5.2. Roots and eigenvectors for $m = 0$, $\varkappa = 0$.

	1	2	3	4	5	6
p	$F(\lambda)$	$-F(\lambda)$	$\frac{(\lambda-1)^{1/4}}{h}$	$-\frac{(\lambda-1)^{1/4}}{h}$	$\frac{(\lambda-1)^{1/4}i}{h}$	$-\frac{(\lambda-1)^{1/4}i}{h}$
U_0	p_1	p_2	ν	ν	ν	ν
W_0	$\frac{\lambda\nu}{\lambda-1}$	$\frac{\lambda\nu}{\lambda-1}$	p_3	p_4	p_5	p_6

Note that the above results for $\varkappa = 0$ are valid when λ is not too close to 1, otherwise the first negligible term for p has the same order as the main term [Bauer *et al.* (1995)]^2.

Finally, in the third case, $\varkappa = -1$ and the representative points are $M_1 = (0,-1)$, $M_2 = (0,-2)$, $M_3 = (2,0)$, $M_4 = (2,-1)$, $M_5 = (4,3)$, and $M_6 = (6,4)$.

In this case, Newton's diagram consists again of 2 segments. The first segment is determined by the points M_2, M_4, and the second one by the points M_4, and M_6. Therefore, equation (16) has two groups of roots, the first one being defined by the equation

$$-\lambda^2 + \lambda^2\nu^2 - \lambda p^2 = 0, \tag{26}$$

and the second one defined by

$$-\lambda p^2 + h^4 p^6 = 0.$$

For this case, the roots and the eigenvectors are given in Table 5.3. Note that, for the roots p_1 and p_2, the coefficient of U_0 in the first equation in (14) is equal to zero, and to determine U_0 and W_0 we must use the third equation in (14).

Table 5.3. Roots and eigenvectors for $m = 0$, $\varkappa = -1$.

	1	2	3	4	5	6
p	$\sqrt{(1-\nu^2)\lambda}\,i$	$-\sqrt{(1-\nu^2)\lambda}\,i$	$\frac{\lambda^{1/4}}{h}$	$-\frac{\lambda^{1/4}}{h}$	$\frac{\lambda^{1/4}i}{h}$	$-\frac{\lambda^{1/4}i}{h}$
U_0	p_1	p_2	ν	ν	ν	ν
W_0	ν	ν	p_3	p_4	p_5	p_6

As $\varkappa$ changes, the representative points move in the (p,h)-plane. We are interested in the cases (called separative) when the convex hull changes. These occur when one of the interior points reaches the convex hull, or two or more segments form a straight line. If we plot the representative points in the 3D-space (p,h,λ), then, the separative cases are determined by the 3D convex hull faces. For equation (16), the 3D convex hull is plotted in Fig. 5.3. Since we assume that the parameter h is small, we need only the faces that are visible from the point $h = -\infty$.

In the present case, the 3D convex hull consists of three faces: 1: (M_1, M_2, M_3, M_4); 2: (M_3, M_4, M_6); 3: (M_2, M_4, M_5, M_6). Imposing the orders of all terms forming a face to be equal to each other, we find the relations from which the orders of λ for the separative cases may be determined:

$$\begin{gathered} \lambda \sim \lambda^2 \sim p^2 \sim \lambda p^2, \\ \lambda p^2 \sim p^2 \sim h^4 p^6, \\ \lambda^2 \sim \lambda p^2 \sim \lambda h^4 p^4 \sim h^4 p^6. \end{gathered} \tag{27}$$

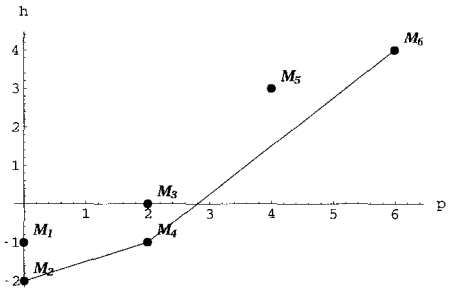

Fig. 5.3. Newton's diagram for $\varkappa = -1$, $m = 0$.

So, for the first and the second relations $\varkappa = 0$, and for the third $\varkappa = -4$.

Therefore, the entire range of the parameter λ is divided into three domains where the 2D convex hulls are essentially different. Each of these domains is defined as Domain I: $\varkappa > 0$, Domain II: $0 > \varkappa > -4$, and Domain III: $\varkappa < -4$, as well as the separative cases A: $\varkappa = 0$ and B: $\varkappa = -4$ must be considered separately. Since the initial equations are valid for $\lambda \ll h^{-4}$, cases III and B have no physical meaning. Case A is special since in this case the second term in the expansion for p is important [Bauer *et al.* (1995)]^2. So here, we consider only the solutions in Domains I and II. For any λ inside a domain, the structure of the convex hull and therefore the roots and the eigenvectors are similar. Thus, we can obtain the values of the roots and eigenvectors by considering only one value of λ for each domain. For Domains I and II we use the results for the considered cases $\varkappa = 1$ and $\varkappa = -1$, respectively.

5.5. Boundary Value Problem

The geometry of the point set and its convex hull for Domain I are shown in Fig. 5.4. In this case, the solution may be written as

$$u = \sum_{i=0}^{6} U_i \exp p_i s, \qquad w = \sum_{i=0}^{6} W_i \exp p_i s, \tag{28}$$

where p_i, U_i and W_i are determined from Table 5.1.

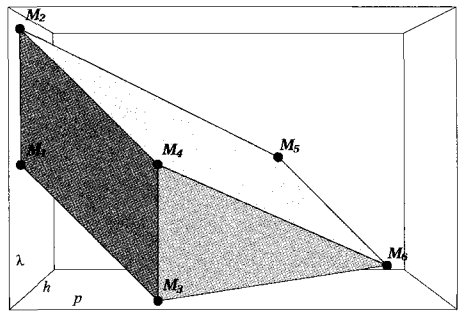

Fig. 5.4. 3D convex hull for $m = 0$.

We consider two types of boundary conditions: freely supported edges and clamped edges. For low frequency vibrations ($\lambda \ll 1, \varkappa > 0$) of a cylindrical shell with freely supported edges, the boundary conditions have the form

$$u' = w = w'' = 0 \qquad \text{at} \quad s = 0 \quad \text{and} \quad s = L. \tag{29}$$

Substituting solution (28) into the boundary conditions (29) we get the characteristic equation from which the first approximation for the frequency parameter λ may be found as the zeros of the determinant

$$D(\lambda) = \begin{vmatrix} p_1U_1 & p_2U_2 & p_3U_3 & p_4U_4 & p_5U_5 & p_6U_6 \\ W_1 & W_2 & W_3 & W_4 & W_5 & W_6 \\ p_1^2W_1 & p_2^2W_2 & p_3^2W_3 & p_4^2W_4 & p_5^2W_5 & p_6^2W_6 \\ p_1U_1e^{p_1L} & p_2U_2e^{p_1L} & p_3U_3e^{p_1L} & p_4U_4e^{p_1L} & p_5U_5e^{p_1L} & p_6U_6e^{p_1L} \\ W_1e^{p_1L} & W_2e^{p_2L} & W_3e^{p_3L} & W_4e^{p_4L} & W_5e^{p_5L} & W_6e^{p_6L} \\ p_1^2W_1e^{p_1L} & p_2^2W_2e^{p_2L} & p_3^2W_3e^{p_3L} & p_4^2W_4e^{p_4L} & p_5^2W_5e^{p_5L} & p_6^2W_6e^{p_6L} \end{vmatrix}. \tag{30}$$

The values of λ may me obtained numerically from this equation. But we may also try to simplify this determinant. We neglect the values of the third and fourth integrals on the left edge and the values of the fifth and the sixth integrals on the right edge. Then, after factorization, the determinant has the form

$$D(\lambda) = -\frac{4}{h^8}\, e^{(\sqrt{2}-ih\sqrt{\lambda})L/h} \left(-1 + e^{2iL\sqrt{\lambda}}\right) \lambda^2 \left(-1+\nu^2\right)^2 = 0. \tag{31}$$

So, we obtain one set for the natural frequency parameter

$$\lambda_k = \left(\frac{\pi k}{L}\right)^2, \qquad k = 0, 1, 2, \ldots. \tag{32}$$

This frequency coincides with that for the unperturbed (momentless) system. In this case two additional roots have negative real parts and two have positive parts. Since there are four additional boundary conditions (two on each edge) this is a case of regular degeneracy and the next corrections for λ may be constructed with an iterative method. Note that relation (32) is valid for $\lambda \ll 1$.

Similarly, for high frequency vibrations of a cylindrical shell with freely supported edges ($\lambda \gg 1$, $-4 < \varkappa < 0$), we use the same equation (30), but now p_i, U_i and W_i are determined from Table 5.3.

As usual, we neglect the values of the edge effect integrals on the other edge. Thus, after simplification, we get the following expression for $D(\lambda)$:

$$D(\lambda) = -\frac{4}{h^8}\, e^{iL\lambda^{1/4}((1+i)+h\lambda^{1/4}\sqrt{1-\nu^2})/h} \left(-1 + e^{2iL\lambda^{1/4}/h}\right) \times \left(-1 + e^{2iL\sqrt{\lambda(1-\nu^2)}}\right) \lambda^2 \left(\nu^2 + \lambda\left(1-\nu^2\right)\right)^2 = 0. \tag{33}$$

So, we obtain two sets for the natural frequency parameter,

$$\lambda_k = \frac{1}{1-\nu^2}\left(\frac{\pi k}{L}\right)^2, \qquad k = 0, 1, 2, \ldots \tag{34}$$

and

$$\lambda_k = \left(\frac{\pi k}{L}\, h\right)^4, \qquad k = 0, 1, 2, \ldots. \tag{35}$$

Here, there are four pure imaginary roots among the additional ones and this is not a case of regular degeneracy. Expressions (34) and (35) are valid for $\lambda \gg 1$.

For low frequency vibrations of a cylindrical shell with clamped edges ($\lambda \ll 1$, $\varkappa > 0$), the boundary conditions have the form

$$u = w = w' = 0 \qquad \text{at} \quad s = 0 \quad \text{and} \quad s = L. \tag{36}$$

So, we must find the zeros of the determinant $D(\lambda)$:

$$\begin{vmatrix} U_1 & U_2 & U_3 & U_4 & U_5 & U_6 \\ W_1 & W_2 & W_3 & W_4 & W_5 & W_6 \\ p_1W_1 & p_2W_2 & p_3W_3 & p_4W_4 & p_5W_5 & p_6W_6 \\ U_1e^{p_1L} & U_2e^{p_2L} & U_3e^{p_3L} & U_4e^{p_4L} & U_5e^{p_5L} & U_6e^{p_6L} \\ W_1e^{p_1L} & W_2e^{p_2L} & W_3e^{p_3L} & W_4e^{p_4L} & W_5e^{p_5L} & W_6e^{p_6L} \\ p_1W_1e^{p_1L} & p_2W_2e^{p_2L} & p_3W_3e^{p_3L} & p_4W_4e^{p_4L} & p_5W_5e^{p_5L} & p_6W_6e^{p_6L} \end{vmatrix}, \tag{37}$$

where p_i U_i, and W_i are determined from Table 5.1. After transformations, we keep only the main terms and obtain

$$D(\lambda) = 2\,e^{(\sqrt{2}-ih\sqrt{\lambda})L/h}\lambda\left(-1+e^{2iL\sqrt{\lambda}}+O(h)\right)=0. \tag{38}$$

This equation has only the set of roots

$$\lambda_k = \left(\frac{\pi k}{L}\right)^2, \qquad k=0,1,2,\ldots. \tag{39}$$

Again this is a case of regular degeneracy.

For the higher frequency vibrations ($\lambda \gg 1$, $-4 < \varkappa < 0$) the determinant (37) must be used, but p_i, U_i and W_i should be determined from Table 5.3.

After transformations, we keep only the main terms and obtain

$$D(\lambda) = -\frac{2}{h^6}\,e^{-(1+i+h\lambda^{1/4}\sqrt{1-\nu^2}iL\lambda^{1/4})/h} \times \lambda i\left[\left(-1+e^{2iL\sqrt{\lambda}\sqrt{1-\nu^2}}\right)\left(1+e^{2iL\lambda^{1/4}/h}\right)+O(h)\right]=0. \tag{40}$$

This equation has two sets of roots,

$$\lambda_1 = \frac{1}{1-\nu^2}\left(\frac{\pi k}{L}\right)^2, \qquad k=0,1,2,\ldots, \tag{41}$$

$$\lambda_2 = \left(\frac{\pi(2k+1)h}{2L}\right)^4, \qquad k=0,1,2,\ldots. \tag{42}$$

The second set has no analog for an unperturbed (momentless) system. Again this is a case of nonregular degeneracy. Note, again that the above expressions are obtained by assuming $\lambda \gg 1$.

5.6. Nonaxisymmetric Vibrations

The same approach may be used to study the nonaxisymmetric vibrations of cylindrical shells. Equation (13) now should be analyzed for $m \neq 0$. In this case, the system does not split, and one has to find the roots of the characteristic equation of order eight,

$$\begin{vmatrix} -p^2+\frac{1-\nu}{2}m^2-(1-\nu^2)\lambda & \frac{1+\nu}{2}mp & \nu p \\ -\frac{1+\nu}{2}mp & g(p,\mu,m)-(1-\nu^2)\lambda & f(p,\mu,m) \\ -\nu p & f(p,\mu,m) & q(p,\mu,m) \end{vmatrix} = 0, \tag{43}$$

where

$$f(p,\mu,m) = m + \mu^4\left(-(2-\nu)mp^2 + m^3\right).$$
$$g(p,\mu,m) = \mu^4\left(-2(1-\nu)p^2 + m^2\right) - \frac{1-\nu}{2}p^2 + m^2,$$
$$q(p,\mu,m) = 1 - (1-\nu^2)\lambda + \mu^4\left(p^2 - m^2\right)^2.$$

This equation is represented in the form

$$P(p;h,\lambda) = \sum_i a_i p^{k_i} h^{\alpha_i} \lambda^{\beta_i} m^{l_i}. \tag{44}$$

The representative points have four coordinates, $M_i = \{k_i, \alpha_i, \beta_i, l_i\}$ in the 4D space (p, h, λ, m). As in the previous axisymmetric case, we must construct a convex hull in 4D, the faces of which determine the lines that divide the (λ, m)-plane into domains with different structures of the roots of the characteristic equation.

In this paper we consider only the cases for which the order of m is known. This allows us to reduce the 4D problem to the 3D one discussed in the previous section.

We consider the case where $m = m_0 h^\tau$, $\tau = 0$, i.e. $M_i = \{k_i, \alpha_i, \beta_i\}$. Equation (43) for this case may be written as

$$P(p;h,\lambda) = \sum_i^{24} a_i p^{k_i} h_i^\alpha \lambda_i^\beta$$

where the 24 representative points $M_i = \{a_i, \{k_i, \alpha_i, \beta_i\}\}$, $i = 1, \ldots, 24$, with their weights a_i are listed below:

$\{-m^2(1+m^2), \{0,0,1\}\}$,
$\{-(1+\nu)(-2-3m^2+m^2\nu), \{0,0,2\}\}, \{2(-1+\nu)(1+\nu)^2, \{0,0,3\}\}$,
$\{(-1+m)^2m^4(1+m)^2, \{0,4,0\}\}$,
$\{m^2(1+\nu)(-2+3m^2-3m^4+m^2\nu+m^4\nu), \{0,4,1\}\}$,
$\{-2m^2(1+m^2)(-1+\nu)(1+\nu)^2, \{0,4,2\}\}, \{3+2m^2+2\nu, \{2,0,1\}\}$,
$\{(-3+\nu)(1+\nu), \{2,0,2\}\}, \{-4(-1+m)^2m^2(1+m)^2, \{2,4,0\}\}$,
$\{-(1+\nu)(-4+4m^2-9m^4+4\nu+3m^4\nu-2m^2\nu^2), \{2,4,1\}\}$,
$\{4(1+m^2-\nu)(-1+\nu)(1+\nu)^2, \{2,4,2\}\}$,
$\{1, \{4,0,0\}\}, \{-1, \{4,0,1\}\}$,
$\{2(2-4m^2+3m^4-2\nu^2+m^2\nu^2), \{4,4,0\}\}$,
$\{(1+\nu)(-4-9m^2+4\nu+3m^2\nu), \{4,4,1\}\}$,

$\{-2(-1+\nu)(1+\nu)^2, \{4,4,2\}\}, \{m^4(-1+\nu)^2(1+\nu)^2, \{4,8,0\}\},$
$\{-2m^2(-1+\nu)^2(1+\nu)^3, \{4,8,1\}\}, \{-4m^2, \{6,4,0\}\},$
$\{-(-3+\nu)(1+\nu), \{6,4,1\}\}, \{4m^2(-1+\nu)(1+\nu), \{6,8,0\}\},$
$\{4(-1+\nu)^2(1+\nu)^2, \{6,8,1\}\}, \{1, \{8,4,0\}\},$
$\{-4(-1+\nu)(1+\nu), \{8,8,0\}\}.$

The convex hull of these points is plotted in Fig. 5.5.

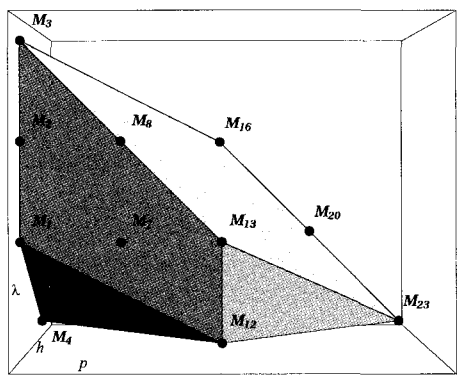

Fig. 5.5. 3D convex hull for $m \sim 1$.

The faces of the convex hull determine the separative points $\varkappa$ ($\lambda \sim h^{\varkappa}$). In the considered case, the 3D convex hull consists of four faces:

(1) (M_1, M_2, M_3, M_7, M_8, M_{12}, M_{13});
(2) (M_{12}, M_{13}, M_{23});
(3) (M_1, M_4, M_{12});
(4) (M_3, M_8, M_{13}, M_{16}, M_{20}, M_{23}).

Assuming that the orders of all terms forming a face to be equal to each other, we find the relations from which the orders of λ for the separative

cases may be determined:

$$\begin{gathered}\lambda \sim \lambda^2 \sim \lambda^3 \sim \lambda p^2 \sim \lambda^2 p^2 \sim p^4 \sim \lambda p^4, \\ p^4 \sim \lambda p^4 \sim h^4 p^8, \\ h^4 \sim \lambda \sim p^4, \\ \lambda^3 \sim \lambda^2 p^2 \sim \lambda p^4 \sim \lambda^2 h^4 p^4 \sim \lambda h^4 p^6 \sim h^4 p^8.\end{gathered} \tag{45}$$

So, for the first and the second relations $\varkappa = 0$, for the third one $\varkappa = 4$, and for the fourth one $\varkappa = -4$. Note that for $m = 1$, the representative points M_4 and M_9 are absent since their weights $a_i = 0$. For this specific case there is no face 3 and, therefore, no separative point $\varkappa = 4$. This case is similar to the case $m = 0$.

For the case $m \sim 1$ the convex hulls for the domains $-4 < \varkappa < 0$ and $0 < \varkappa < 4$ are plotted in Figs. 5.6 and 5.7.

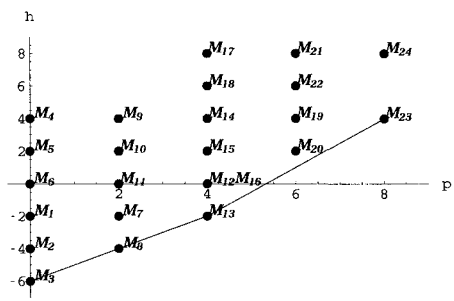

Fig. 5.6. Newton's diagram for $\varkappa = -1$, $m \sim 1$.

The most interesting case is $m \sim h^{-1/4}$. For such wavenumbers the natural frequency is the lowest [Goldenveizer *et al.* (1978)][4]. The 3D convex hull for this case is plotted in Fig. 5.8.

The asymptotic expansions of the integral have different structures in the four domains separated by the separative points:

$$\varkappa = 3, \quad \varkappa = 0, \quad \varkappa = -1/2, \quad \varkappa = -4.$$

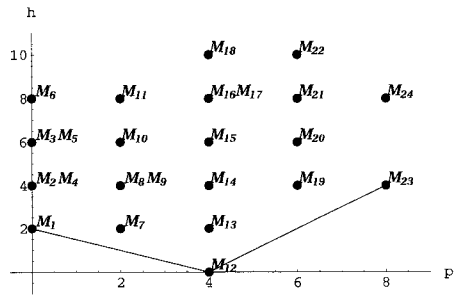

Fig. 5.7. Newton's diagram for $\varkappa = 1$, $m \sim 1$.

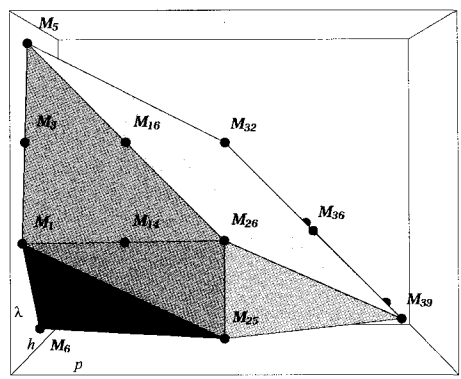

Fig. 5.8. 3D convex hull for $m \sim h^{-1/4}$.

5.7. Symbolic Computation

The Mathematica software has been used to perform the symbolic computation. The following functions have been built

(1) Construction of the representative points.
In the system of equations (9) or similar, after substitutions (10) and

(12) the characteristic polynomial of type (43) is constructed and written in the form of a list of representative points with their weights a_i.

(2) Construction of 3D convex hull.
For the representative points set, the part of the 3D convex hull visible from the point $(p, h, \lambda) = (0, -\infty, 0)$ is constructed. The vertices of the convex hull and its faces are listed. Initially, the algorithm based on the gift wrapping method and Graham scan was used to construct the convex hull. It is important that the weights of the points forming the convex hull not be equal to zero for any values of the parameters. For example, the weights of two points of the convex hull for $m \sim 1$ contain the multipliers $(m-1)$. This means that the case $m = 1$ must be considered separately.

(3) Construction of the domains with similar structures of solution.
Solving the systems of linear equations for each face, we find the orders of the corresponding λ (separative points). The entire area of the parameter λ splits into several domains by these separative points.

(4) Construction of the lower part of the 2D convex hull.
For each separative point and for each domain, the roots of the characteristic polynomial are found. For that purpose, λ is represented in the form $\lambda = \lambda h^{\varkappa}$, where the order of $\varkappa$ is known. For 2D point sets the convex hull is constructed using standard function from the package "Computational Geometry". As a result we get the list of the segments of the convex hull.

(5) Deletion of terms in equations of the type (18) and (19) and extraction of the roots and eigenvectors.
In some domain of the parameter space, we may neglect some of the terms of the initial equation to shorten an equation. Say, instead of one equation of the eighth degree we get two equations of the fourth degree with fewer terms. The main asymptotic terms of the roots of the initial and the transformed equations will be same. The points of a segment determine the terms of a shorter equation. Each equation is solved for the main terms of the roots p. Then, the eigenvectors are obtained. For this purpose, one equation of system (44) is excluded, and, in the remaining two, only the main terms are considered. The solution of the system

$$a_{11}u + a_{12}v + a_{13}w = 0, \tag{46}$$

$$a_{21}u + a_{22}v + a_{23}w = 0, \tag{47}$$

is represented in the form $w = \Delta$, $u = \Delta_u$, $v = \Delta_v$, where

$$\Delta = \begin{vmatrix} a_{11}, a_{12} \\ a_{21}, a_{22} \end{vmatrix}, \quad \Delta_u = -\begin{vmatrix} a_{13}, a_{12} \\ a_{23}, a_{22} \end{vmatrix}, \quad \Delta_v = -\begin{vmatrix} a_{11}, a_{13} \\ a_{21}, a_{23} \end{vmatrix}. \tag{48}$$

Δ, Δ_u and Δ_v should not be equal to zero. Similarly, we construct n integrals of the initial system. It is assumed that all its root are simple.

(6) Factorization of the characteristic equation of type (30) or (37). Substituting solutions into the boundary conditions, we find the characteristic equation for λ. Then, we try factorizing it to find the analytical expression for the roots. For some boundary conditions this can be done. Otherwise, we solve the equation numerically.

Acknowledgments

The authors gratefully acknowledge the partial support provided for this work by the Natural Sciences and Engineering Research Council of Canada through grant number OPG 0170338, by Concordia University through the Graduate Fellowship program, and by the Russian Foundation for Basic Research through grant number 04-01-00257.

References

1. Bauer, S. M., Smirnov, A. L., Tovstik, P. E., and Filippov, S. B., (1997), "Asymptotic methods in examples and problems", St. Petersburg University Press, (in Russian).
2. Bauer, S. M., Smirnov, A. L., Tovstik, P. E., and Filippov, S. B., (1995), "Asymptotic methods in mechanics of thin shell structures", St. Petersburg University Press, (in Russian).
3. Bauer, S. M., Smirnov, A. L., Tovstik, P. E., and Filippov, S. B., (1993), "Asymptotic methods in mechanics with applications to thin shells and plates", in Asymptotic Methods in Mechanics, CRM Proceedings and Lecture Notes, AMS, Providence RI.
4. Goldenveizer, A. L. , Lidsky, V. B., and Tovstik, P. E., (1978), "Free vibrations of thin shells", Nauka, Moscow, (in Russian).
5. Landman, I. M., Smirnov, A. L. and Haseganu, E. M., (1999), "Asymptotic integration of thin shell equations by means of computer algebra methods", in Proceedings of the 17th Canadian Congress of Applied Mechanics, McMaster University, Hamilton, ON, 37–38.
6. Vishik, M. I., and Lyusternik, L. A., (1957), "Regular degeneracy and boundary layer for linear differential equations with small parameter", Uspekhi Mat. Nauk (N.S.), vol. 12, no. 5(77), 3–122, (in Russian).

PART 2

Vibrations and Stability in Continuum Mechanics

This page is intentionally left blank

CHAPTER 6

THE MECHANICS OF PRE-STRESSED AND PRE-POLARIZED PIEZOELECTRIC CRYSTALS

Eveline Baesu

Department of Engineering Mechanics, University of Nebraska-Lincoln, Lincoln, NE 68505 USA
E-mail: ebaesu@unlserve.unl.edu

The basic theoretical framework to analyze the behavior of single crystal piezoelectric materials in the presence of pre-existing stresses and electric fields is discussed. The biasing fields are assumed to be static. The associated system of equations describing the behavior of single crystals with biasing fields under subsequent deformation and electric fields are self-adjoint. The static biasing fields appear explicitly in the final equations. This framework proves to be ideally suited for the study of material stability under superposed infinitesimal deformations and electric fields. Stability issues are discussed in the context of superposed infinitesimal plane harmonic waves; stability envelopes for the biasing fields are established through this analysis. The general solution in terms of complex potentials is obtained for antiplane problems. The influence of biasing fields on fracture phenomena is analyzed in this framework. In the context of this work, the biasing fields can be large, making it possible to obtain critical values of the biasing fields for resonance (in general, loss in stability). In particular, results are obtained for single crystal from the classes 23, 6mm, and 42m.

6.1. Introduction

Pre-stress and pre-polarization occur naturally in devices containing piezoelectric components. For example, residual stresses from manufacturing processes, poling, and the high stresses due to pressure lead to the presence of significant initial fields, which have a profound influence on the behavior of these materials. Indeed there is experimental evidence documenting the influence of such initial fields on the evolution of damage and fatigue. For example, by measuring the hysteresis loop in experiments on polycrys-

talline lead zirconate titanate stannate (PZST), it has been shown that pre-stress strongly affects its antiferroelectric-ferroelectric phase transformation (see [Essig *et al.* (1999)][1]). Another experimental investigation of the same phenomenon in lanthanum stannate zirconate titanate (PLSnZT) demonstrates a great sensitivity to pre-stress along the electric-field direction [Pan *et al.* (1996)][2]. Specifically, the displacement was observed to decrease by 50% from its pre-stress free value when a small pre-stress of 3 MPa was applied. Further, in the experiments presented in [Adachi *et al.* (1998)][3], the estimation of pre-stress was found to be indispensable to the design of BLT's (bolt-clamped Langevin-type transducers), due to the fact that pre-stress significantly reduces electromechanical coupling. The microscopic mechanism responsible for the reduction of the piezoelectric effect is not yet known. An example of the effects of pre-polarization is presented in [Lee and Ramesh (1996)][4], where it was found to play an important role in determining further imprint behavior in epitaxial PLZT thin-film capacitors. Also, experiments performed on one of the most frequently used bulk piezoelectrics, PZT (lead-zirconate-titanate), reveal the unusual effect that residual stresses have on microcracks: they migrate inside the body in a manner that depends on the orientation of the residual stresses and electric field.

The experimental results indicated above furnish a strong impetus for studying pre-existing mechanical and electromagnetic fields in deformable solids from a theoretical viewpoint. Moreover, an investigation of the effect of initial fields is particularly important as piezoelectric materials are gaining in importance for a variety of structural applications at both large and small scales (for a good survey of structural applications of piezoelectric materials, see [Sunar and Rao (1999)][5] and the references cited therein). There is a considerable body of work on the theory of piezoelectrics in the absence of initial fields; indeed a number of expository works are available in the literature (see for e.g. [Mindlin (1989)][6], [Tiersten (1969)][7], [Lee and Haines (1974)][8] and [Rogacheva (1994)][9]). Further, a comprehensive review of higher order theories of piezoelectric plates from the point of view of applications is contained in [Wang and Yang (2000)][10]. Initial (or biasing) fields have been treated from a theoretical point of view in the context of elastostatics; in particular, results for elastostatics plates under biasing fields involving second order theories can be found in [Yang and Jiang (2002)][11], [Yang and Jiang (2002)][12], and [Yang and Jiang (2002)][13]. Although special cases of biasing fields in piezoelectrics have been treated from a theoretical standpoint (for e.g. [Tiersten (1995)][14]), until recently,

a satisfactory general theoretical treatment of initial fields in piezoelectrics has been lacking in the literature. In a recent series of papers, the author, along with Professor Eugen Soos, has developed a theoretical framework for piezoelectricity in the presence of initial fields, and used it to study material stability and crack propagation [Soós (1996)][15], [Baesu *et al.* (2003)][16]–[Beasu][21].

This chapter is organized as follows. In section 6.2, I introduce notation and summarize the basic equations of elastic dielectrics under the quasi-electrostatic approximation. In section 6.3, I present the general theory of piezoelectric materials with initial fields and discuss the linearized incremental theory. The special case of antiplane incremental deformations is developed in section 6.4. Stability results in the presence of initial fields are presented in section 6.5. Finally, in section 6.6, I briefly discuss transverse wave propagation.

6.2. Background

In this section I present the basic equations describing the behavior of a non-magnetizable elastic dielectric which conducts neither heat nor electricity; in the following we adopt the quasi-electrostatic approximation. Let $\mathcal{B}$ be a deformable continuum moving in the 3-dimensional Euclidean space under the influence of external forces. Let X be a particle of $\mathcal{B}$, and let $\mathbf{X}$ and $\mathbf{x}$ be its position vectors in the reference and present configurations (at time t), B_R and B, respectively; Let V_R and V be the associated spatial domains. A motion χ of the body is any sufficiently smooth function

$$\mathbf{x} = \chi(\mathbf{X}, t). \tag{1}$$

The deformation gradient $\mathbf{F}$ relative to $\mathbf{X}$, and its determinant are defined by

$$\mathbf{F} = \frac{\partial \chi(\mathbf{X}, t)}{\partial \mathbf{X}}, \qquad J = \det \mathbf{F}. \tag{2}$$

Taking the reference configuration to be occupiable, we have $J > 0$. The right and left Cauchy-Green strain tensors are given by

$$\mathbf{C} = \mathbf{F}^T\mathbf{F}, \qquad \mathbf{B} = \mathbf{F}\mathbf{F}^T, \tag{3}$$

respectively, and the Lagrangian strain tensor $\mathbf{G}$ by

$$\mathbf{G} = \frac{1}{2}(\mathbf{C} - \mathbf{I}). \tag{4}$$

Let ρ_R and ρ denote the mass densities in the reference and present configurations, respectively. The local equation for conservation of mass can be written as

$$\rho_R = \rho J. \tag{5}$$

Let $\mathbf{T}$ denote the Cauchy mechanical stress tensor and $\mathbf{S}$ its symmetric part. The latter is derived from the Helmholtz free energy in accordance with conventional elasticity, with the proviso that the energy is now a function of the electromechanical variables. Let $\mathbf{E}$, $\mathbf{P}$ and $\mathbf{D}$ denote the electric field, the electric polarization and the electric displacement, respectively. These satisfy ([Eringen and Maugin (1990)][22]):

$$\mathbf{T} = \mathbf{S} - \mathbf{P} \otimes \mathbf{E}, \qquad \mathbf{D} = \mathbf{E} + \mathbf{P}. \tag{6}$$

The differential equations of balance in the quasi-electrostatic approximation (i.e. neglect of time derivatives in Maxwell's equations) are

$$\rho \dot{\mathbf{v}} = \operatorname{div} \mathbf{T} + \rho \mathbf{f} + q\mathbf{E} + (\mathbf{P} \cdot \nabla)\mathbf{E}, \tag{7}$$

$$\begin{aligned} \operatorname{div} \mathbf{D} &= q, \\ \operatorname{curl} \mathbf{E} &= \mathbf{0}, \end{aligned} \tag{8}$$

where $\mathbf{v}$ is the velocity field, the superposed dot denotes the material time derivative, $\mathbf{f}$ represents the mechanical body force, and q denotes the volumetric charge density. In equations (7) and (8), the spatial description is used, i.e. the various fields are functions of the spatial coordinate $\mathbf{x}$ and of the current time t. The fields $\mathbf{E}$, $\mathbf{P}$ and $\mathbf{D}$ are also defined in the domain exterior to V.

The jump conditions satisfied at the boundary ∂V of V are

$$\mathbf{n} \cdot [\mathbf{D}] = w, \qquad \mathbf{n} \times [\mathbf{E}] = \mathbf{0} \qquad \text{on} \quad \partial V, \tag{9}$$

where w represents the given surface charge density and $\mathbf{n}$ represents the exterior unit normal to the boundary. Here,

$$[\phi] = \phi^+ - \phi^- \tag{10}$$

is the jump of a generic field ϕ across ∂V, and ϕ^+ and ϕ^- are the limits of ϕ on ∂V from the outside and inside, respectively. For simplicity, the inside limit value ϕ^- will henceforth be denoted simply by ϕ.

From the momentum balance (7), the mechanical surface traction $\mathbf{t_n}$ acting on the boundary of the body is

$$\mathbf{t_n} = \mathbf{n} \cdot \mathbf{T} = \mathbf{n} \cdot (\mathbf{S} - \mathbf{P} \otimes \mathbf{E}) \qquad \text{on} \quad \partial V. \tag{11}$$

The local balance laws and associated jump conditions may be expressed in an equivalent form by introducing Piola–Kirchhoff type fields, related to the reference configuration B_R, and defined through the relations:

$$\begin{aligned} \mathbf{\Pi} &= J\mathbf{F}^{-1}\mathbf{S}\mathbf{F}^{-T}, \\ \mathbf{\Theta} &= J\mathbf{F}^{-1}\mathbf{S} = \mathbf{\Pi}\mathbf{F}^{T}, \end{aligned} \tag{12}$$

$$\mathcal{P} = J\mathbf{F}^{-1}\mathbf{P}, \qquad \mathfrak{E} = \mathbf{F}^{T}\mathbf{E}, \qquad \mathfrak{D} = J\mathbf{F}^{-1}\mathbf{D} = J\mathbf{F}^{-1}\mathbf{E} + \mathcal{P}, \tag{13}$$

$$\mathbf{T} = J\mathbf{F}^{-1}\mathbf{T} = \mathbf{\Theta} - \mathcal{P}\otimes\mathbf{E}, \tag{14}$$

$$q_R = Jq. \tag{15}$$

Here, $\mathbf{\Theta}$ and $\mathbf{\Pi}$ represent the nominal stress and the symmetric Piola–Kirchhoff stress corresponding to the symmetric part $\mathbf{S}$ of the Cauchy mechanical stress $\mathbf{T}$, and q_R is the referential volumetric charge density.

The referential forms of the local balance laws are:

$$\rho_R\ddot{\mathbf{u}} = \operatorname{div}\mathfrak{T} + \rho_R\mathbf{f} + q_R\mathbf{E} + (\mathcal{P}\cdot\nabla)\mathbf{E}, \tag{16}$$

$$\operatorname{div}\mathfrak{D} = q_R, \qquad \operatorname{curl}\mathfrak{E} = \mathbf{0}, \tag{17}$$

wherein $\mathbf{u}$ is the displacement vector from B_R to B,and the differential operators are associated with the reference configuration. In these balance laws the material description is used, i.e. all fields are functions of the independent material coordinates $\mathbf{X}$ and the time t.

The jump conditions (9) are equivalent to:

$$\mathbf{N}\cdot[\mathfrak{D}] = w_R, \qquad \mathbf{N}\times[\mathfrak{E}] = \mathbf{0} \qquad \text{on} \quad \partial V_{\mathbf{R}}, \tag{18}$$

where $\mathbf{N}$ is the exterior unit normal to the boundary ∂V_R of V_R and w_R is the surface charge density per unit material surface area in the reference configuration.

From the momentum balance (16), it follows that the mechanical surface traction $\mathbf{t_N}$, acting on the boundary of the body, is given by

$$\mathbf{t_N} = \mathbf{N}\cdot\mathfrak{T} = \mathbf{N}\cdot(\mathbf{\Theta} - \mathcal{P}\otimes\mathbf{E}). \tag{19}$$

The field equations and the jump conditions are supplemented by the constitutive equations:

$$\mathbf{\Pi} = \frac{\partial\mathcal{H}}{\partial\mathbf{G}}, \qquad \mathcal{P} = -\frac{\partial\mathcal{H}}{\partial\mathfrak{E}}, \tag{20}$$

where

$$\rho_R\psi = \mathcal{H}(\mathbf{G},\mathfrak{E}), \tag{21}$$

is the generalized Helmholtz free energy and $\mathbf{G}$ is the Green strain tensor.

6.3. General Theory of Piezoelectricity with Initial Fields

6.3.1. *Small deformation and electric fields superposed on large static fields*

The equations describing the behavior of the incremental fields are given by [Eringen and Maugin (1990)][22]. To obtain these equations, they use the field equations and jump conditions corresponding to the spatial description. In their work, the perturbed mechanical surface forces, together with the surface and volumetric charges, are referred to material surface and volume elements in the perturbed current configuration B. In the present work, these quantities will instead be referred to unit material surfaces and volumes in the initially deformed static configuration $\mathring{B}$, which is regarded as being known [Baesu *et al.* (2003)][16].

In the reference configuration B_R, the body is assumed to be free of all fields. Further at the time $t = 0$ the body is assumed to be deformed statically and carries static fields. $\mathring{B}$ is the initial equilibrium configuration. The static deformation of the body from B_R to $\mathring{B}$ is described by $\mathbf{x} = \mathbf{x}(\mathbf{X})$, the associated deformation gradient is $\mathring{\mathbf{F}} = \mathring{\mathbf{F}}(\mathbf{X})$, and $\mathring{J} = \mathring{J}(\mathbf{X}) = \det \mathring{\mathbf{F}}(\mathbf{X})$. The mechanical and electrostatic fields in $\mathring{B}$ are identified by a superposed "$\circ$", *i.e.*

$$\mathring{\mathbf{u}} = \mathring{\mathbf{u}}(\mathbf{X}), \quad \mathring{\mathbf{F}} = \mathring{\mathbf{F}}(\mathbf{X}), \quad \mathring{\mathbf{T}} = \mathring{\mathbf{T}}(\mathbf{x}), \ldots, \mathring{\mathbf{E}} = \mathring{\mathbf{E}}(\mathbf{x}), \quad \mathring{\mathbf{P}} = \mathring{\mathbf{P}}(\mathbf{x}), \ldots. \tag{22}$$

Thus,

$$\mathring{\rho}\mathring{J} = \rho_R, \qquad \text{with } \mathring{J} = \det \mathring{\mathbf{F}}. \tag{23}$$

Further, in view of the general relations (6),

$$\mathring{\mathbf{T}} = \mathring{\mathbf{S}} - \mathring{\mathbf{P}} \otimes \mathring{\mathbf{E}}, \quad \mathring{\mathbf{D}} = \mathring{\mathbf{E}} + \mathring{\mathbf{P}}. \tag{24}$$

According to (7) and (8), the field equations satisfied by these static fields are:

$$\begin{aligned} \operatorname{div} \mathring{\mathbf{T}} + \mathring{\rho}\mathring{\mathbf{f}} + \mathring{q}\mathring{\mathbf{E}} + (\mathring{\mathbf{P}} \cdot \nabla)\mathring{\mathbf{E}} &= \mathbf{0}, \\ \operatorname{div} \mathring{\mathbf{D}} &= \mathring{q}, \\ \operatorname{curl} \mathring{\mathbf{E}} &= \mathbf{0}. \end{aligned} \tag{25}$$

At the boundary $\partial\mathring{V}$ of $\mathring{V}$, the volume occupied by the reference configuration $\mathring{B}$, we have:

$$\mathbf{n} \cdot [\mathring{\mathbf{D}}] = \mathring{w}, \qquad \mathbf{n} \times [\mathring{\mathbf{E}}] = \mathbf{0}, \tag{26}$$

where $\mathbf{n}$ is the exterior unit normal to $\partial\mathring{V}$. Further, in view of $(24)_1$, the mechanical surface traction $\mathring{\mathbf{t}}_{\mathbf{n}}$ acting on $\partial\mathring{V}$ is

$$\mathring{\mathbf{t}}_{\mathbf{n}} = \mathbf{n}\cdot\mathring{\mathbf{T}} = \mathbf{n}\cdot(\mathring{\mathbf{S}} - \mathring{\mathbf{P}}\otimes\mathring{\mathbf{E}}). \tag{27}$$

The constitutive equations (20) for mechanical stress and electric polarization in the static equilibrium configuration $\mathring{B}$ are:

$$\mathbf{\Pi}^{\circ} = \frac{\partial\mathcal{H}}{\partial\mathbf{G}}(\mathring{\mathbf{G}},\overset{o}{\mathfrak{E}}), \quad \overset{o}{\mathcal{P}} = -\frac{\partial\mathcal{H}}{\partial\mathbf{E}}(\mathring{\mathbf{G}},\overset{o}{\mathfrak{E}}), \tag{28}$$

where

$$\mathring{\mathbf{G}} = \frac{1}{2}(\mathring{\mathbf{F}}^T\mathring{\mathbf{F}} - \mathbf{1}), \quad \overset{o}{\mathfrak{E}} = \mathring{\mathbf{F}}^T\mathring{\mathbf{E}}.$$

Time-dependent incremental deformations and fields are now assumed to be applied to the body in the initial configuration $\mathring{B}$, resulting in the current configuration $B_t = B$. Let $\mathbf{u}(\mathbf{x},t)$ be the small displacement from $\mathring{B}$ to B, and let $\mathbf{F}_0 = \mathbf{F}_0(\mathbf{x}, t)$ be the gradient of the deformation from $\mathring{B}$ to B, (i.e. $\mathring{B}$ is taken here as the reference configuration). The gradient of the displacement $\mathbf{u} = \mathbf{u}(\mathbf{x}, t)$ is $\mathbf{H}_0 = \mathbf{H}_0(\mathbf{x}, t)$, and $J_0(\mathbf{x}, t)$ is the determinant of $\mathbf{F}_0$

The fields referred to $\mathring{B}$ will be identified by the subscript "o" and will be regarded as functions of $\mathbf{x}$ and t. For simplicity, the argument $\mathbf{x}$ will be suppressed in the notation. Thus, we have:

$$\mathbf{F}_0(t) = \mathbf{1} + \mathbf{H}_0(t), \qquad \mathbf{H}_0(t) = \nabla\mathbf{u}(t), \qquad J_0 = \det\mathbf{F}_0(t), \tag{29}$$

and

$$\mathbf{F}(t) = \mathbf{F}_0(t)\mathring{\mathbf{F}}, \qquad J(t) = J_0(t)\mathring{J}, \qquad \mathring{J} = \det\mathring{\mathbf{F}}. \tag{30}$$

The Piola–Kirchhoff versions of the various fields are:

$$\mathbf{\Theta}_0(t) = J_0(t)\mathbf{F}_0^{-1}(t)\mathbf{S}(t) = \mathring{J}\mathring{\mathbf{F}}\mathbf{\Pi}(t)\mathring{\mathbf{F}}\mathbf{F}_0^{T}(t), \tag{31}$$

$$\mathcal{P}_0(t) = J_0(t)\mathbf{F}_0^{-1}(t)\mathbf{P}(t) = \mathring{J}^{-1}\mathring{\mathbf{F}}\mathcal{P}(t), \tag{32}$$

$$\mathbf{E}_0(t) = \mathbf{F}_0^T(t)\mathbf{E}(t), \tag{33}$$

$$\mathfrak{D}_0(t) = J_0(t)\mathbf{F}_0^{-1}(t)\mathbf{D}(t) = J_0(t)\mathbf{F}_0^{-1}(t)\mathbf{E}(t) + \mathcal{P}_0(t), \tag{34}$$

$$\mathfrak{T}_0(t) = \mathrm{J}_0(t)\mathbf{F}_0^{-1}(t)\mathbf{T}(t) = \mathbf{\Theta}_0(t) - \mathcal{P}_0(t)\otimes\mathbf{E}(t). \tag{35}$$

Further,

$$\mathbf{H}_0(0) = \mathbf{0}, \qquad \mathbf{F}_0(0) = \mathbf{1}, \qquad J_0(0) = 1, \tag{36}$$

and therefore,

$$\boldsymbol{\Theta}_0(0) = \mathring{\mathbf{S}}, \quad \mathcal{P}_0(0) = \mathring{\mathbf{P}}, \quad \mathfrak{E}_0(0) = \mathring{\mathbf{E}}, \quad \mathfrak{D}_0(0) = \mathring{\mathbf{D}}, \quad \mathfrak{T}_0(0) = \mathring{\mathbf{T}}. \tag{37}$$

Equations (15), (16) and (17) then yield the balance equations:

$$\rho(t)J_0(t) = \mathring{\rho}, \tag{38}$$

$$\mathring{\rho}\ddot{\mathbf{u}}(t) = \operatorname{div} \mathfrak{T}_0(t) + \mathring{\rho}\mathbf{f}(t) + q_0\mathbf{E}(t) + (\mathcal{P}_0 \cdot \nabla)\mathbf{E}(t), \tag{39}$$

$$\operatorname{div} \mathfrak{D}_0(t) = q_0(t), \qquad \operatorname{curl} \mathfrak{E}_0(t) = \mathbf{0}. \tag{40}$$

Here, $q_0 = q_0(t)$ is the current volumetric charge density per unit material volume in the initially deformed configuration $\mathring{B}$. The jump conditions satisfied at the boundary $\partial\mathring{V}$ of $\mathring{V}$ are:

$$\mathbf{n} \cdot [\mathfrak{D}_0(t)] = w_0(t), \qquad \mathbf{n} \times [\mathfrak{E}_0(t)] = \mathbf{0}, \tag{41}$$

where $w_0 = w_0(t)$ is the current surface charge density per unit material surface area in $\mathring{B}$.

From (39), we conclude that the Piola–Kirchhoff mechanical traction $\mathbf{t}_{o\mathbf{n}}(t)$ is given by

$$\mathbf{t}_{o\mathbf{n}}(t) = \mathbf{n}\cdot\mathfrak{T}_0(t) = \mathbf{n} \cdot (\boldsymbol{\Theta}_0(t) - \mathcal{P}_0(t) \otimes \mathbf{E}(t)) \qquad \text{on} \qquad \partial\mathring{V}. \tag{42}$$

Finally, according to (20), the constitutive equations are:

$$\boldsymbol{\Pi}(t) = \frac{\partial \mathcal{H}}{\partial \mathbf{G}}(\mathbf{G}(t), \mathfrak{E}(t)), \qquad \mathcal{P}(t) = -\frac{\partial \mathcal{H}}{\partial \mathfrak{E}}(\mathbf{G}(t), \mathfrak{E}(t)), \tag{43}$$

where

$$\mathbf{G}(t) = \frac{1}{2}(\mathbf{F}^T(t)\mathbf{F}(t) - \mathbf{1}), \qquad \mathfrak{E}(t) = \mathbf{F}^T(t)\mathbf{E}(t), \tag{44}$$

and

$$\mathbf{G}(0) = \mathring{\mathbf{G}} \qquad \mathbf{E}(0) = \mathring{\mathbf{F}}^T\mathring{\mathbf{E}}. \tag{45}$$

Small perturbations of the initial electric field are denoted by $\mathbf{e} = \mathbf{e}(\mathbf{x},t)$, *i.e.*:

$$\mathbf{E}(t) = \mathring{\mathbf{E}} + \mathbf{e}(t), \tag{46}$$

and the relation

$$\mathbf{F}(t) = \mathring{\mathbf{F}} + \mathbf{H}_0(t)\mathring{\mathbf{F}}, \tag{47}$$

which follows from $(29)_2$ and (25), will be used in the subsequent development. The perturbations $\mathbf{H}_0(t)$ and $\mathbf{e}(t)$ are considered to be small, such

that the products of all perturbations due to $\mathbf{H}_0(t)$ and $\mathbf{e}(t)$ may be neglected. In particular, we have

$$J_0(t) = 1 + tr\mathbf{H}_0(t), \qquad \mathbf{F}_0^{-1}(t) = \mathbf{1} - \mathbf{H}_0(t). \tag{48}$$

Henceforth, a superposed bar will be used to denote small perturbations of the various fields. For example, Green's strain tensor is approximated by

$$\mathbf{G}(t) = \mathring{\mathbf{G}} + \bar{\mathbf{G}}(t), \tag{49}$$

wherein

$$\bar{\mathbf{G}}(t) = \mathring{\mathbf{F}}^T \mathbf{g}(t) \mathring{\mathbf{F}}, \tag{50}$$

by virtue of (29) and (44), and

$$\mathbf{g}(t) = \frac{1}{2}(\mathbf{H}_0(t) + \mathbf{H}_0^T(t)) \tag{51}$$

is the associated infinitesimal strain tensor. In the same way, we have

$$\mathfrak{E}(t) = \overset{o}{\mathfrak{E}} + \bar{\mathfrak{E}}(t), \tag{52}$$

in which the perturbation $\bar{\mathfrak{E}}(t)$ is derived by using eqs. $(13)_1$, (46) and (47):

$$\bar{\mathfrak{E}}(t) = \mathring{\mathbf{F}}^T(\mathbf{e}(t) + \mathbf{H}_0^T(t)\mathring{\mathbf{E}}). \tag{53}$$

We also have

$$\mathbf{\Theta}_0(t) = \mathring{\mathbf{S}} + \bar{\mathbf{\Theta}}_0(t), \qquad \mathbf{\Pi}(t) = \mathbf{\Pi}^\circ + \bar{\mathbf{\Pi}}(t). \tag{54}$$

Equations $(29)_1$ and (31) then lead to a relation between the perturbations $\bar{\mathbf{\Theta}}_0(t)$ and $\bar{\mathbf{\Pi}}(t)$:

$$\bar{\mathbf{\Theta}}_0(t) = \mathring{J}^{-1}\mathring{\mathbf{F}}\bar{\mathbf{\Pi}}(t)\mathring{\mathbf{F}}^T + \mathring{\mathbf{S}}\mathbf{H}_0^T(t). \tag{55}$$

Next, consider

$$\mathcal{P}_0(t) = \mathring{\mathbf{P}} + \bar{\mathcal{P}}_0(t), \qquad \mathcal{P}(t) = \overset{o}{\mathcal{P}} + \bar{\mathcal{P}}(t), \tag{56}$$

and note that, from $(32)_2$,

$$\bar{\mathcal{P}}_0(t) = \mathring{J}^{-1}\mathring{\mathbf{F}}\bar{\mathcal{P}}(t). \tag{57}$$

Thus, the perturbation $\bar{\mathcal{P}}_0(t)$ is known if $\bar{\mathcal{P}}(t)$ is known. Similarly, if we take

$$\mathfrak{D}_0(t) = \mathring{\mathbf{D}} + \bar{\mathfrak{D}}_0(t), \tag{58}$$

then, from eqs. (29), (34), (46), (48) and (59), we derive

$$\bar{\mathfrak{D}}_0(t) = \mathbf{e}(t) + \bar{\mathcal{P}}_0(t) + \mathring{\mathbf{E}}\,\mathrm{tr}\,\mathbf{H}_0(t) - \mathbf{H}_0(t)\mathring{\mathbf{E}} \tag{59}$$

and observe that computation of the perturbation $\mathfrak{D}_0(t)$ requires knowledge of $\mathcal{P}_0(t)$. Continuing, we have

$$\mathfrak{E}_0(t) = \mathring{\mathbf{E}} + \bar{\mathfrak{E}}_0(t), \tag{60}$$

where, from eqs. (35), (50) and (51),

$$\bar{\mathfrak{E}}_0(t) = \mathbf{e}(t) + \mathbf{H}_0^T(t)\mathring{\mathbf{E}}. \tag{61}$$

Finally, if

$$\mathfrak{T}_0(t) = \mathring{\mathbf{T}} + \bar{\mathfrak{T}}(t), \tag{62}$$

then eqs. (35), (46), (54) and (56) yield the perturbation $\bar{\mathbf{T}}(t)$:

$$\bar{\mathbf{T}}_0(t) = \bar{\mathbf{\Theta}}_0(t) - \bar{\mathcal{P}}_0(t) \otimes \mathring{\mathbf{E}} - \mathring{\mathbf{P}} \otimes \mathbf{e}(t). \tag{63}$$

At this stage it is evident that all perturbations are known if the perturbations $\bar{\mathbf{\Pi}}(t)$ and $\bar{\mathcal{P}}(t)$ are known. To obtain the latter, the constitutive equations (43) are used. Thus, taking into account (49), (50), (52) and (53), together with (28), we derive

$$\bar{\mathbf{\Pi}}(t) = \frac{\partial^2 \mathcal{H}^\circ}{\partial \mathbf{G} \partial \mathbf{G}}\{\mathring{\mathbf{F}}^T \mathbf{g}(t) \mathring{\mathbf{F}}\} + \frac{\partial^2 \mathcal{H}^\circ}{\partial \mathfrak{E} \partial \mathbf{G}}\{\mathring{\mathbf{F}}^T(\mathbf{e}(t) + \mathbf{H}_0^T(t)\mathring{\mathbf{E}})\}, \tag{64}$$

$$\bar{\mathcal{P}}(t) = -\frac{\partial^2 \mathcal{H}^\circ}{\partial \mathfrak{E} \partial \mathbf{G}}\{\mathring{\mathbf{F}}^T \mathbf{g}(t) \mathring{\mathbf{F}}\} - \frac{\partial^2 \mathcal{H}^\circ}{\partial \mathfrak{E} \partial \mathfrak{E}}\{\mathring{\mathbf{F}}^T(\mathbf{e}(t) + \mathbf{H}_0^T(t)\mathring{\mathbf{E}})\}. \tag{65}$$

The superscript "$\circ$" on $\mathcal{H}$ indicates that the corresponding second-order derivatives of the generalized Helmholtz free energy are evaluated at $\mathring{\mathbf{G}}$ and $\mathbf{E}^\circ$.

The perturbations of the force and charge densities are introduced through:

$$\mathbf{f}(t) = \mathring{\mathbf{f}} + \bar{\mathbf{f}}(t), \qquad q_0(t) = \mathring{q} + \bar{q}(t), \qquad w_0(t) = \mathring{w} + \bar{w}(t). \tag{66}$$

Using the relations (25), (39), (40), (46), $(56)_1$, and (58)–(63), it may then be shown that the incremental fields satisfy the following balance equations:

$$\rho^\circ \ddot{\mathbf{u}}(t) = \mathrm{div}(\bar{\mathbf{\Theta}}_0(t) - \bar{\mathcal{P}}_0(t) \otimes \mathring{\mathbf{E}} - \mathring{\mathbf{P}} \otimes \mathbf{e}(t)) + \rho^\circ \bar{\mathbf{f}}(t) + \bar{q}(t)\mathring{\mathbf{E}} + \mathring{q}\mathbf{e}(t) + (\bar{\mathcal{P}}_0(t) \cdot \nabla)\mathring{\mathbf{E}} + (\mathring{\mathbf{P}} \cdot \nabla)\mathbf{e}(t), \tag{67}$$

$$\begin{aligned} \operatorname{div}\,(\mathbf{e}(t) + \bar{\mathcal{P}}_0(t) + \mathring{\mathbf{E}}\,\operatorname{tr}\mathbf{H}_0(t) - \mathbf{H}_0(t)\mathring{\mathbf{E}}) &= \bar{q}(t) \\ \operatorname{curl}(\mathbf{e}(t) + \mathbf{H}_0^T(t)\mathring{\mathbf{E}}) &= \mathbf{0}. \end{aligned} \tag{68}$$

From (41), the jump conditions for the incremental fields are:

$$\begin{aligned} \mathbf{n}\cdot[\mathbf{e}(t) + \bar{\mathcal{P}}_0(t) + \mathring{\mathbf{E}}\,\operatorname{tr}\mathring{\mathbf{H}}(t) - \mathbf{H}_0(t)\mathring{\mathbf{E}}] &= \bar{w}(t) \\ \mathbf{n}\times[\mathbf{e}(t) + \mathbf{H}_0^T(t)\mathring{\mathbf{E}}] &= \mathbf{0}. \end{aligned} \tag{69}$$

Finally, (42) may be used show that the incremental Piola–Kirchhoff mechanical traction $\bar{\mathbf{t}}_{on}(t)$ reduces to

$$\bar{\mathbf{t}}_{on}(t) = \mathbf{n}\cdot(\bar{\boldsymbol{\Theta}}_0(t) - \bar{\mathcal{P}}_0(t)\otimes\mathring{\mathbf{E}} - \mathring{\mathbf{P}}\otimes\mathbf{e}(t)) \qquad \text{on} \quad \partial\mathring{V}. \tag{70}$$

6.3.2. *Special case of homogeneous initial state and non-polarizable environment*

The following development is based on two further assumptions:

(H_1) The body is homogeneous, the initial deformation gradient $\mathring{\mathbf{F}}$ is constant in the domain V_R, and the initial electric field $\mathring{\mathbf{E}}$ is constant.
(H_2) The environment of the body (vacuum in our case) is not polarizable.

The second assumption is justified since the dielectric constants of the material are significantly larger than the dielectric constant of vacuum. Then, according to this assumption, we have $\mathring{\mathbf{P}} = \mathbf{0}$ and $\mathbf{e}(t) = \mathbf{0}$ in the whole space exterior to $\mathring{V}$. Consequently, the associated limit values satisfy the relation $\mathring{\mathbf{P}}^+ = \mathbf{0}$ and $\mathbf{e}^+(t) = \mathbf{0}$ on the boundary $\partial\mathring{V}$. Obviously, our second assumption leads to a significant simplification of the problem, since, by neglecting the surroundings of the body, our problem is transformed to one of a simple hyperelastic dielectric.

Returning to our assumption (H_1), we first observe that $\mathring{\mathbf{S}}$, $\mathring{\mathbf{P}}$, $\mathring{\mathbf{T}}$ and $\mathring{\mathbf{D}}$ will also be constant quantities in the domain $\mathring{V}$ occupied by the initially deformed and polarized body; and, as a consequence of the balance equations (25), the assumed homogeneous state can exist only if

$$\mathring{\mathbf{f}} = \mathbf{0}, \qquad \mathring{q} = 0 \qquad \text{in} \quad \mathring{V}. \tag{71}$$

Since the initial applied electric field is assumed to be spatially constant, the second jump condition (26) is identically satisfied, whereas the assumptions

(H_1) and (H_2) taken together show that $\mathring{\mathbf{P}}$ and $\mathring{w}$ are related by

$$\mathbf{n} \cdot \mathring{\mathbf{P}} = -\mathring{w} \qquad \text{on} \quad \partial \mathring{V}. \tag{72}$$

The mechanical traction $\mathring{\mathbf{t}}_{\mathbf{n}}$ acting on the boundary $\partial \mathring{V}$ is given by (27).

Our first assumption (H_1), its consequence (71), and (57) imply that the local balance equations are:

$$\mathring{\rho}\ddot{\mathbf{u}}(t) = \operatorname{div}\,(\bar{\mathbf{\Theta}}_0(t) - \bar{\mathcal{P}}_0(t) \otimes \mathring{\mathbf{E}}) + \mathring{\rho}\bar{\mathbf{f}}(t) + \bar{q}(t)\mathring{\mathbf{E}}, \tag{73}$$

$$\begin{aligned} \operatorname{div}\,(\mathbf{e}(t) + \bar{\mathcal{P}}_0(t)) &= \bar{q}(t), \\ \operatorname{curl}\,\mathbf{e}(t) &= \mathbf{0}, \end{aligned} \tag{74}$$

provided that the initial equilibrium state of the body is homogeneous. Moreover, our second assumption (H_2) implies that the boundary conditions (26) reduce to:

$$\mathbf{n} \cdot (\mathbf{e}(t) + \bar{\mathcal{P}}_0(t)) = -\bar{w}(t), \qquad \mathbf{n} \times \mathbf{e}(t) = \mathbf{0} \qquad \text{on} \quad \partial \mathring{V}, \tag{75}$$

which follow from the fact that $\mathring{\mathbf{E}}$ is constant and the environment of the body is not polarizable. Finally, from the momentum balance (73), it follows that the incremental Piola–Kirchhoff type mechanical traction $\bar{\mathbf{t}}_{\mathbf{on}}(t)$ is

$$\bar{\mathbf{t}}_{\mathbf{on}}(t) = \mathbf{n} \cdot (\bar{\mathbf{\Theta}}_0(t) - \bar{\mathcal{P}}_0(t) \times \mathring{\mathbf{E}}) \qquad \text{on} \quad \partial \mathring{V}, \tag{76}$$

whenever the initial state of the body is homogeneous.

To complete the system describing the incremental behavior of the body, we return to the constitutive equations (64) and (65) giving the perturbations $\bar{\mathbf{\Pi}}(t)$ and $\bar{\mathcal{P}}(t)$. We also use (55) and (57), expressing the perturbations $\bar{\mathbf{\Theta}}_0(t)$ and $\bar{\mathcal{P}}_0(t)$ in terms of $\bar{\mathbf{\Pi}}(t)$ and $\bar{\mathcal{P}}(t)$, to derive:

$$\bar{\Theta}_{okl} = (\mathring{c}_{klmn} + \mathring{S}_{kn}\delta_{lm} - \mathring{e}_{nkl}\mathring{E}_m)u_{m,n} - \mathring{e}_{mkl}e_m, \tag{77}$$

$$\bar{\mathcal{P}}_{ok} = (\mathring{e}_{kmn} + \overset{o}{\chi}_{km}\mathring{E}_n)u_{m,n} + \mathring{\chi}_{kl}e_l, \tag{78}$$

where

$$\begin{aligned} \mathring{c}_{klmn} &= \mathring{J}^{-1}\mathring{F}_{kp}\mathring{F}_{lq}\mathring{F}_{mr}\mathring{F}_{ns}\frac{\partial^2 \mathcal{H}^\circ}{\partial G_{pq}\partial G_{rs}}, \\ \overset{o}{e}_{mkl} &= \mathring{J}^{-1}\mathring{F}_{mp}\mathring{F}_{kq}\mathring{F}_{lr}\frac{\partial^2 \mathcal{H}^\circ}{\partial \mathfrak{E}_p \partial G_{qr}}, \\ \mathring{\chi}_{kl} &= -\mathring{J}^{-1}\mathring{F}_{km}\mathring{F}_{\ln}\frac{\partial^2 \mathcal{H}^\circ}{\partial \mathfrak{E}_m \partial \mathfrak{E}_n}. \end{aligned} \tag{79}$$

It is noteworthy that equations (78) and (79) are valid even if hypotheses (H_1) and (H_2) are not satisfied. The material moduli possess the following symmetry properties:

$$\mathring{c}_{klmn} = \mathring{c}_{lkmn} = \mathring{c}_{k\,\mathrm{ln}\,m} = \mathring{c}_{mnkl}, \qquad \mathring{e}_{mkl} = \mathring{e}_{mlk}, \qquad \mathring{\chi}_{kl} = \mathring{\chi}_{lk}. \tag{80}$$

Hence, in general, there exist 21 independent elastic moduli $\mathring{c}_{klmn}$, 18 independent coupling moduli $\mathring{e}_{mkl}$ and 6 independent dielectric moduli $\mathring{\chi}_{kl}$.

At this juncture I introduce the incremental mechanical stress tensor $\mathbf{\Sigma}$ and electric displacement vector $\mathbf{\Delta}$. We may conclude from the balance equations (73) and $(74)_1$ that, if (H_1) and (H_2) are applicable, then

$$\begin{aligned} \mathbf{\Sigma}(t) &= \mathbf{\Theta}_0(t) - \bar{\mathcal{P}}_0(t) \otimes \mathring{\mathbf{E}}, \\ \mathbf{\Delta}(t) &= \mathbf{e}(t) + \bar{\mathcal{P}}_0(t). \end{aligned} \tag{81}$$

Moreover, according to (77) and (78), the constitutive equations describing the behavior of the incremental fields are:

$$\begin{aligned} \Sigma_{kl} &= \mathring{\Omega}_{klmn} u_{m,n} - \mathring{\Lambda}_{mkl} e_m, \\ \Delta_k &= \mathring{\Lambda}_{kmn} u_{m,n} + \mathring{\varepsilon}_{kl} e_l \end{aligned} \tag{82}$$

where

$$\begin{aligned} \mathring{\Omega}_{klmn} &= \mathring{c}_{klmn} + \mathring{S}_{kn}\delta_{lm} - \mathring{e}_{kmn}\mathring{E}_l - \mathring{e}_{nkl}\mathring{E}_m - \mathring{\chi}_{kn}\mathring{E}_l\mathring{E}_m, \\ \Lambda^{\circ}_{mkl} &= \mathring{e}_{mkl} + \mathring{\chi}_{mk}\mathring{E}_l, \\ \mathring{\varepsilon}_{kl} &= \delta_{kl} + \mathring{\chi}_{kl}, \end{aligned} \tag{83}$$

and, from (80), the following symmetry relations are satisfied:

$$\mathring{\Omega}_{klmn} = \mathring{\Omega}_{nmlk}, \qquad \mathring{\varepsilon}_{kl} = \mathring{\varepsilon}_{lk}. \tag{84}$$

We observe that $\mathring{\Omega}_{klmn}$ are not symmetric relative to the indices (k,l) and (m,n), and that $\mathring{\Lambda}_{mkl}$ are not symmetric relative to (k,l). Hence, in general, there are 45 independent elastic moduli $\mathring{\Omega}_{klmn}$, 27 independent coupling moduli $\mathring{\Lambda}_{mkl}$, and 6 independent dielectric moduli $\mathring{\varepsilon}_{kl}$. These moduli are constant parameters which depend on the considered hyperelastic dielectric through the Helmholtz generalized free energy. They also depend on the initial deformation and electric field through $\mathring{S}_{kl}$ and $\mathring{E}_k$.

Using the incremental mechanical stress tensor $\mathbf{\Sigma}$ and the displacement vector $\mathbf{\Delta}$, we may cast the differential balance equations (73) and (74) in

the forms

$$\begin{aligned} \mathring{\rho}\ddot{\mathbf{u}} &= \mathrm{div}\boldsymbol{\Sigma} + \mathring{\rho}\,\bar{\mathbf{f}} + \bar{q}\,\mathring{\mathbf{E}}, \\ \mathrm{div}\boldsymbol{\Delta} &= \bar{q}, \\ \mathrm{curl}\mathbf{e} &= 0. \end{aligned} \tag{85}$$

The associated boundary conditions are

$$\mathbf{n}\cdot\boldsymbol{\Delta} = -\bar{w}, \qquad \mathbf{n}\times\mathbf{e} = 0 \qquad \text{on} \quad \partial\mathring{V}, \tag{86}$$

and the incremental mechanical traction $\bar{\mathbf{t}}_{o\mathbf{n}}$ satisfies

$$\bar{\mathbf{t}}_{o\mathbf{n}} = \mathbf{n}\cdot\boldsymbol{\Sigma} \qquad \text{on} \quad \partial\mathring{V}. \tag{87}$$

6.4. Special Case of Antiplane Deformation

The special case of antiplane deformation was explored in a series of papers by Baesu and Soos ([Baesu and Soós (2001)][17], [Baesu and Soós (2001)][18], [Baesu and Soós][19]). In the following, the body is assumed to be prismatic with cross-sectional geometry independent of x_3. In particular, the exterior unit normal, $\mathbf{n}$, to the boundary of the cross-section depends only on x_1, x_2, and $n_3 = 0$. We also assume that

$$\bar{f}_\alpha = 0 \quad \text{in } \mathcal{V}, \qquad \text{and} \qquad \bar{g}_\alpha = 0 \quad \text{on } \partial\mathcal{V}; \qquad \alpha = 1,2, \tag{88}$$

and that $\bar{f}_3$, $\bar{q}$, $\bar{w}$, $\bar{g}_3$ depend only on x_1, x_2, and t. We have an *antiplane!incremental state* relative to the (x_1, x_2)-plane if

$$u_\alpha = 0, \quad u_3 = u_3(x_\beta, t), \quad \varphi = \varphi(x_\beta, t); \quad \alpha,\beta = 1,2. \tag{89}$$

In particular, from (25),

$$e_\alpha = e_\alpha(x_\beta, t), \quad e_3 = 0. \tag{90}$$

Next, sufficient conditions for the existence of an antiplane state in a piezoelectric crystal are obtained. To this end we observe that all fields depend only on x_1, x_2, and t; hence, (85) implies that

$$\Sigma_{\alpha\beta,\alpha} + \bar{q}\mathring{E}_\beta = 0; \quad \alpha,\beta = 1,2, \tag{91}$$

where, according to (82),

$$\Sigma_{\alpha\beta} = \mathring{\Omega}_{\alpha\beta3\gamma}u_{3,\gamma} + \mathring{\Lambda}_{\gamma\alpha\beta}\varphi_{,\gamma}; \quad \alpha,\beta,\gamma = 1,2. \tag{92}$$

Equation (91) then becomes

$$\mathring{\Omega}_{\alpha\beta3\gamma}u_{3,\gamma\alpha} + \mathring{\Lambda}_{\gamma\alpha\beta}\varphi_{,\gamma\alpha} + \bar{q}\mathring{E}_\beta = 0; \quad \alpha,\beta,\gamma = 1,2, \tag{93}$$

and for this to be satisfied it is sufficient that

$$\mathring{\Omega}_{\alpha\beta 3\gamma} = 0, \quad \mathring{\Lambda}_{\gamma\alpha\beta} = 0, \quad \mathring{E}_\beta = 0; \quad \alpha, \beta, \gamma = 1, 2. \tag{94}$$

These conditions, together with $(83\dot{)}_{1,2}$ lead to further restrictions on the components of the elastic moduli $\mathbf{c}$ and the coupling moduli $\mathbf{e}$:

$$c_{\alpha\beta 3\gamma} = 0, \quad e_{\gamma\alpha\beta} = 0. \tag{95}$$

Using the Voigt notation, these are equivalent to

$$\begin{aligned} &c_{14} = c_{15} = c_{24} = c_{25} = c_{46} = c_{16} = 0, \\ &e_{11} = e_{21} = e_{12} = e_{16} = e_{22} = e_{26} = 0, \end{aligned} \tag{96}$$

which are satisfied for the crystal classes: 222, $mm2$, 4, 6, ∞, $\bar{4}$, and $\bar{4}2m$ ([Sirotin and Shaskolskaya (1975)][23]). We conclude that, under hypotheses (H_1)–(H_5), the antiplane state is always possible in these crystals. Then, (94) and (95) yield

$$\Sigma_{\alpha\beta} = 0; \quad \alpha, \beta = 1, 2. \tag{97}$$

We also observe that for the crystal classes in question, the existence of the antiplane state is not contingent upon any restrictions involving $\mathring{\mathbf{S}}$.

For antiplane states, the field equations (85) simplify to

$$\begin{aligned} \mathring{\rho}\ddot{u}_3 &= \mathbf{\Sigma}_{\alpha 3,\alpha} + \mathring{\rho}\bar{f}_3 + \bar{q}\mathring{E}_3, \\ \Delta_{\alpha,\alpha} &= \bar{q}, \end{aligned} \tag{98}$$

where

$$\begin{aligned} \Sigma_{\alpha 3} &= \mathring{\Omega}_{\alpha 33\beta} u_{3,\beta} + \mathring{\Lambda}_{\beta\alpha 3}\varphi_{,\beta}, \\ \Delta_\alpha &= \mathring{\Lambda}_{\alpha\beta 3} u_{3,\beta} - \mathring{\varepsilon}_{\alpha\beta}\varphi_{,\beta}; \quad \alpha, \beta = 1, 2. \end{aligned} \tag{99}$$

The moduli involved in these equations may be obtained by using the general results given in $(83)_{1,2}$:

$$\begin{aligned} \mathring{\Omega}_{1331} &= c_{55} + \mathring{S}_{11} - 2e_{15}\mathring{E}_3 - \chi_{11}^2\mathring{E}_3^2, \\ \mathring{\Omega}_{1332} &= c_{45} + \mathring{S}_{12} - (e_{14} + e_{25})\mathring{E}_3 - \chi_{12}^2\mathring{E}_3^2, \\ \mathring{\Omega}_{2331} &= c_{45} + \mathring{S}_{12} - (e_{14} + e_{25})\mathring{E}_3 - \chi_{12}\mathring{E}_3^2, \\ \mathring{\Omega}_{2332} &= c_{44} + \mathring{S}_{22} - 2e_{24}\mathring{E}_3 - \chi_{22}\mathring{E}_3^2, \\ \mathring{\Lambda}_{113} &= e_{15} + \chi_{11}\mathring{E}_3, \\ \mathring{\Lambda}_{213} &= e_{25} + \chi_{12}\mathring{E}_3, \\ \mathring{\Lambda}_{123} &= e_{14} + \chi_{12}\mathring{E}_3, \\ \mathring{\Lambda}_{223} &= e_{24} + \chi_{22}\mathring{E}_3. \end{aligned} \tag{100}$$

Consequently, the incremental constitutive equations become

$$\begin{aligned}\Sigma_{13} &= \left(c_{55} + \mathring{S}_{11} - 2e_{15}\mathring{E}_3 - \chi_{11}\mathring{E}_3^2\right) u_{3,1} \\ &+ \left(c_{45} + \mathring{S}_{12} - (e_{14}+e_{25})\mathring{E}_3 - \chi_{12}\mathring{E}_3^2\right) u_{3,2} \\ &+ \left(e_{15} + \chi_{11}\mathring{E}_3\right)\varphi_{,1} + \left(e_{25} + \chi_{12}\mathring{E}_3\right)\varphi_{,2},\end{aligned} \tag{101}$$

$$\begin{aligned}\Sigma_{23} &= \left(c_{45} + \mathring{S}_{12} - (e_{14}+e_{25})\mathring{E}_3 - \chi_{12}\mathring{E}_3^2\right) u_{3,1} \\ &+ \left(c_{44} + \mathring{S}_{22} - 2e_{24}\mathring{E}_3 - \chi_{22}\mathring{E}_3^2\right) u_{3,2} \\ &+ \left(e_{14} + \chi_{12}\mathring{E}_3\right)\varphi_{,1} + \left(e_{24} + \chi_{22}\mathring{E}_3\right)\varphi_{,2},\end{aligned} \tag{102}$$

and

$$\begin{aligned}\Delta_1 &= \left(e_{15} + \chi_{11}\mathring{E}\right) u_{3,1} + \left(e_{14} + \chi_{12}\mathring{E}_3\right) u_{3,2} - \varepsilon_{11}\varphi_{,1} - \varepsilon_{12}\varphi_{,2} \\ \Delta_2 &= \left(e_{25} + \chi_{12}\mathring{E}_3\right) u_{3,1} + \left(e_{24} + \chi_{22}\mathring{E}_3\right) u_{3,2} - \varepsilon_{12}\varphi_{,1} - \varepsilon_{22}\varphi_{,2}.\end{aligned}$$

For the crystal class $\bar{4}2m$, the matrices of the associated elastic, coupling and dielectric moduli take the forms:

$$\begin{bmatrix} \varepsilon_{11} & 0 & 0 \\ 0 & \varepsilon_{11} & 0 \\ 0 & 0 & \varepsilon_{33} \end{bmatrix}, \quad \begin{bmatrix} \chi_{11} & 0 & 0 \\ 0 & \chi_{11} & 0 \\ 0 & 0 & \chi_{33} \end{bmatrix},$$

$$\begin{bmatrix} 0 & 0 & 0 & e_{14} & 0 & 0 \\ 0 & 0 & 0 & 0 & e_{14} & 0 \\ 0 & 0 & 0 & 0 & 0 & e_{36} \end{bmatrix}, \begin{bmatrix} c_{11} & c_{12} & c_{13} & 0 & 0 & c_{16} \\ 0 & c_{11} & c_{13} & 0 & 0 & -c_{16} \\ 0 & 0 & c_{33} & 0 & 0 & 0 \\ 0 & 0 & 0 & c_{44} & 0 & 0 \\ 0 & 0 & 0 & 0 & c_{44} & 0 \\ 0 & 0 & 0 & 0 & 0 & c_{66} \end{bmatrix}. \tag{103}$$

Then, the constitutive equations (101) reduce to

$$\begin{aligned}\Sigma_{13} &= \left(c_{44} + \mathring{S}_{11} - \chi_{11}\mathring{E}_3^2\right) u_{3,1} + \left(\mathring{S}_{12} - 2e_{14}\mathring{E}_3\right) u_{3,2} + \chi_{11}\mathring{E}_3\varphi_{,1} + e_{14}\varphi_{,2}, \\ \Sigma_{23} &= \left(\mathring{S}_{12} - 2e_{14}\mathring{E}_3\right) u_{3,1} + \left(c_{44} + \mathring{S}_{22} - \chi_{11}\mathring{E}_3^2\right) u_{3,2} + e_{14}\varphi_{,1} + \\ &\quad \chi_{11}\mathring{E}_3\varphi_{,2},\end{aligned} \tag{104}$$

$$\Delta_1 = \chi_{11}\mathring{E}_3 u_{3,1} + e_{14}u_{3,2} - \varepsilon_{11}\varphi_{,1}, \quad \Delta_2 = e_{14}u_{3,1} + \chi_{11}\mathring{E}_3 u_{3,2} - \varepsilon_{11}\varphi_{,2}.$$

We simplify the equations for incremental antiplane strain states in a piezoelectric crystal belonging to the class $\bar{4}2m$. To ensure the homogeneity

of the initially stressed and polarized state, the initial stresses and electric displacement must satisfy the restrictions

$$\mathring{S}_{21} = \mathring{S}_{22} = \mathring{S}_{23} = 0, \quad \mathring{D}_2 = 0. \tag{105}$$

The resulting infinitesimal strain $\mathring{\mathbf{g}}$ and polarization $\mathring{\mathbf{P}}$ may be determined, provided that $\mathring{E}_3$, $\mathring{S}_{11}$, $\mathring{S}_{33}$, and $\mathring{S}_{13}$ are known, and assuming that $\mathbf{c}$ and ε are positive definite (which implies that the reference state of the body is locally stable).

For simplicity, we use the notation:

$$u_3 = u,\ c_{44} = c,\ \mathring{S}_{11} = \mathring{\sigma},\ \chi_{11} = \chi,\ \varepsilon_{11} = \varepsilon,\ \mathring{E}_3 = \mathring{E},\ e_{14} = e,$$

and note that

$$\varepsilon = 1 + \chi. \tag{106}$$

The constitutive equations (104) are

$$\begin{aligned}
\Sigma_{13} &= \left(c + \overset{o}{\sigma} - \chi\mathring{E}^2\right) u_{,1} - 2e\mathring{E}u_{,2} + \chi\mathring{E}\varphi_{,1} + e\varphi_{,2},\\
\Sigma_{23} &= -2e\mathring{E}u_{,1} + \left(c - \chi\mathring{E}^2\right) u_{,2} + e\varphi_{,1} + \chi\mathring{E}\varphi_{,2},\\
\Delta_1 &= \chi\mathring{E}u_{,1} + eu_{,2} - \varepsilon\varphi_{,1},\\
\Delta_2 &= eu_{,1} + \chi\mathring{E}u_{,2} - \varepsilon\varphi_{,2}.
\end{aligned} \tag{107}$$

We also assume that

$$\bar{f}_3 = 0 \qquad \text{and} \qquad \bar{q} = 0. \tag{108}$$

The field equations (98) then reduce to

$$\begin{aligned}
\overset{o}{\rho}\ddot{u} &= (c + \overset{o}{\sigma} - \chi\mathring{E}^2)\ u_{,11} - 4e\mathring{E}u_{,12} + (c - \chi\mathring{E}^2)u_{,22} + \chi\mathring{E}\varphi_{,11}\\
&\quad +2e\varphi_{,12} + \chi\mathring{E}\varphi_{,22},\\
0 &= \chi\mathring{E}u_{,11} + 2eu_{,12} + \chi\mathring{E}u_{,22} - \varepsilon\varphi_{,22} - \varepsilon\varphi_{,11}.
\end{aligned} \tag{109}$$

6.5. Stability Considerations

6.5.1. *Static and dynamic local stability*

In the following, dynamic and static energy balance laws are formulated as consequences of the incremental field equations given in the previous section and show that the associated differential operators are self-adjoint ([Soós (1996)][15]–[Beasu][21]). This property, in turn, follows directly from the structure of the incremental constitutive laws (82), and from the symmetry properties (84) of the moduli $\mathring{\mathbf{\Omega}}$ and $\mathring{\varepsilon}$. These energetic balance laws

generalize similar results known in the theory of prestressed hyperelastic solids [Balakirev and Gilinskii (1982)][24] and the classical theory of linear piezoelectric crystals [Dieulesaint and Roger (1974)][25].

To obtain the dynamic incremental energy balance law, we first consider the scalar product of the velocity $\dot{\mathbf{u}}$ with the momentum balance $(85)_1$. Integrating the resulting expression over $\overset{\circ}{V}$, and using the divergence theorem, we obtain:

$$\frac{d}{dt}\int_{\overset{\circ}{V}} \frac{1}{2}\overset{\circ}{\rho}\dot{\mathbf{u}}\cdot\dot{\mathbf{u}}dv = \int_{\partial\overset{\circ}{V}} \dot{\mathbf{u}}\cdot(\mathbf{n}\cdot\boldsymbol{\Sigma})ds + \int_{\overset{\circ}{V}} (\overset{\circ}{\rho}\bar{\mathbf{f}}\cdot\dot{\mathbf{u}} + \bar{q}\overset{\circ}{\mathbf{E}}\cdot\dot{\mathbf{u}})dv - \int_{\overset{\circ}{V}} \left(\nabla\dot{\mathbf{u}}\bullet\boldsymbol{\Sigma}\right)dv. \tag{110}$$

Further, from the balance law $(85)_3$, we conclude that the incremental electric field $\mathbf{e}$ is the gradient of a scalar electric potential $\phi = \phi(\mathbf{x},t)$, *i.e.*

$$\mathbf{e} = -\nabla\phi. \tag{111}$$

Multiplying ϕ by the time derivative of $(85)_2$, integrating the resulting equation on $\overset{\circ}{V}$ and using the divergence theorem once more, we derive

$$0 = -\int_{\partial\overset{\circ}{V}} \phi\mathbf{n}\cdot\dot{\boldsymbol{\Delta}}ds + \int_{\overset{\circ}{V}} \phi\dot{\bar{q}}dv - \int_{\overset{\circ}{V}} \left(\dot{\boldsymbol{\Delta}}\cdot\mathbf{e}\right)dv. \tag{112}$$

The addition of (110) and (112) then results in

$$\frac{d}{dt}\int_{\mathring{V}} \frac{1}{2}\mathring{\rho}\dot{\mathbf{u}}\cdot\dot{\mathbf{u}}dv = \int_{\mathring{V}} \mathbf{n}\cdot(\boldsymbol{\Sigma}\dot{\mathbf{u}} - \phi\dot{\boldsymbol{\Delta}})ds + \int_{\mathring{V}} (\mathring{\rho}\bar{\mathbf{f}}\cdot\dot{\mathbf{u}} + \bar{q}\mathring{\mathbf{E}}\cdot\dot{\mathbf{u}} + \phi\dot{\bar{q}})dv - \int_{\mathring{V}} \left(\nabla\dot{\mathbf{u}}\bullet\boldsymbol{\Sigma} + \dot{\boldsymbol{\Delta}}\cdot\mathbf{e}\right)dv. \tag{113}$$

Using the constitutive laws (82) and the symmetry properties (84) of the moduli $\mathring{\boldsymbol{\Omega}}$ and $\mathring{\varepsilon}$, we reduce the last term in (113) to

$$\nabla\dot{\mathbf{u}}\bullet\boldsymbol{\Sigma} + \dot{\boldsymbol{\Delta}}\cdot\mathbf{e} = \frac{d}{dt}\left(\frac{1}{2}\nabla\mathbf{u}\cdot\mathring{\boldsymbol{\Omega}}\nabla\mathbf{u} + \frac{1}{2}\mathbf{e}\cdot\mathring{\varepsilon}\mathbf{e}\right). \tag{114}$$

This allows us to rewrite (113) in the form:

$$\frac{1}{2}\frac{d}{dt}\int_{\mathring{V}} (\mathring{\rho}\dot{\mathbf{u}}\cdot\dot{\mathbf{u}} + \nabla\mathbf{u}\cdot\mathring{\boldsymbol{\Omega}}\nabla\mathbf{u} + \mathbf{e}\cdot\mathring{\varepsilon}\mathbf{e})dv = \int_{\partial\mathring{V}} \mathbf{n}\cdot(\boldsymbol{\Sigma}\dot{\mathbf{u}} - \phi\dot{\boldsymbol{\Delta}})ds + \int_{\mathring{V}} (\mathring{\rho}\bar{\mathbf{f}}\cdot\dot{\mathbf{u}} + \bar{q}\mathring{\mathbf{E}}\cdot\dot{\mathbf{u}} + \phi\dot{\bar{q}})dv. \tag{115}$$

The right-hand side the first integral represents the incremental kinetic energy of the body; the second, the incremental strain energy of the dielectric material; and the last, the energy of the incremental electric field. The mechanical and electrical significance of the various terms in the second integral of the right-hand side is obvious, these being similar to terms

appearing in the classical theory of linear piezoelectric bodies. It is evident that the vector

$$\phi = -\boldsymbol{\Sigma}\dot{\mathbf{u}} + \phi\dot{\boldsymbol{\Delta}}, \tag{116}$$

appearing in the surface integral of eq. (115), is the incremental electromechanical energy flux vector, characterizing the electromechanical energy gained or lost by the body through its boundary. This vector plays a fundamental role in the analysis of reflection and refraction of electromechanical waves.

Let W be the sum of the specific incremental strain energy and the energy density of the incremental electric field, *i.e.*

$$2W = \nabla\mathbf{u} \cdot \mathring{\boldsymbol{\Omega}}\nabla\mathbf{u} + \mathbf{e} \cdot \overset{\circ}{\varepsilon}\mathbf{e}. \tag{117}$$

This enables us to rewrite the energy balance law (115) in the following useful form:

$$\begin{aligned} &\frac{d}{dt}\int_{\mathring{V}} (\frac{1}{2}\mathring{\rho}\dot{\mathbf{u}} \cdot \dot{\mathbf{u}} + W)dv \\ &= \int_{\partial\mathring{V}} \mathbf{n} \cdot \boldsymbol{\Sigma}\dot{\mathbf{u}}ds - \int_{\partial\mathring{V}} \phi\mathbf{n} \cdot \dot{\boldsymbol{\Delta}}ds + \int_{\mathring{V}} (\mathring{\rho}\bar{\mathbf{f}} \cdot \dot{\mathbf{u}} + \bar{q}\mathring{\mathbf{E}} \cdot \dot{\mathbf{u}} + \phi\dot{q})dv, \end{aligned} \tag{118}$$

which may be used to identify those well-posed incremental initial- and boundary- value problems having unique solutions, provided that the energy density W is a positive-definite quadratic form. In turn, the latter property holds if and only if the moduli $\mathring{\boldsymbol{\Omega}}$ and $\mathring{\varepsilon}$ are positive definite. As in the classical linear theory of piezoelectric crystals, the foregoing uniqueness conditions do not impose any restrictions on the coupling moduli $\mathring{\boldsymbol{\Lambda}}$.

Using the same procedure for static problems, it may be demonstrated that

$$\int_{\mathring{V}} W dv = \int_{\partial\mathring{V}} \mathbf{n} \cdot \boldsymbol{\Sigma}\mathbf{u}ds - \int_{\partial\mathring{V}} \mathbf{n} \cdot \boldsymbol{\Delta}\phi ds + \int_{\mathring{V}} (\mathring{\rho}\bar{\mathbf{f}} \cdot \mathbf{u} + \bar{q}\mathring{\mathbf{E}} \cdot \mathbf{u} + \phi\bar{q})dv. \tag{119}$$

As in the foregoing, this equation may be used to identify those well-posed equilibrium boundary- value problems for which uniqueness of classical regular solutions may be proved. Moreover, as in the dynamical case, uniqueness is assured if W is positive definite; that is, if $\mathring{\boldsymbol{\Omega}}$ and $\mathring{\varepsilon}$ are positive definite. Thus, we may conclude that bifurcation, or local instability, of the initially deformed and polarized equilibrium state $\mathring{B}$ may occur only if the moduli $\mathring{\boldsymbol{\Omega}}$ and/or $\mathring{\varepsilon}$ cease to be positive definite. Hence, there exists a strong connection between uniqueness and local stability according to Euler's criterion of adjacent equilibrium.

In the following, we assume time-independent fields. We further suppose that only dead mechanical and electrical loads act on the body, *i.e.* loads which are not altered by changes of configuration. Under these assumptions, we consider the following homogeneous boundary value problem:

$$\begin{aligned} &\operatorname{div}\mathring{\boldsymbol{\Sigma}} = \mathbf{0} \quad \text{in } \mathring{V}, \quad \mathbf{n}\cdot\mathring{\boldsymbol{\Sigma}} = 0 \quad \text{on } \partial\mathring{V}_1, \quad \mathbf{u} = \mathbf{0} \quad \text{on } \partial\mathring{V}_2, \\ &\operatorname{div}\mathring{\boldsymbol{\Delta}} = \mathbf{0} \quad \text{in } \mathring{V}, \mathbf{e} = -\nabla\phi, \\ &\mathbf{n}\cdot\mathring{\boldsymbol{\Delta}} = 0 \quad \text{on } \partial\mathring{V}_3, \quad \phi = 0 \quad \text{on } \partial\mathring{V}_4, \end{aligned} \tag{120}$$

where $\partial\mathring{V}_1$, $\partial\mathring{V}_2$ and $\partial\mathring{V}_3$, $\partial\mathring{V}_4$ are sets with disjoint interior parts, and $\partial\mathring{V}_1 \cup \partial\mathring{V}_2 = \partial\mathring{V}_3 \cup \partial\mathring{V}_4 = \partial\mathring{V}$.

Adapting ideas from the classical linear stability theory of elastic solids ([Ogden (1984)][26], [Guz (1976)][27], [Guz (1986)][28]), we invoke the following static stability criterion:

Criterion 1 *The initially deformed and polarized equilibrium state $\mathring{B}$ is locally stable if and only if the homogeneous incremental boundary value problem (120) has only the null solution. If this condition is not fulfilled, we say that $\mathring{B}$ is locally unstable or neutrally stable.*

It is apparent that there exists a strong connection between incremental uniqueness and local stability: If, for a loaded configuration $\mathring{B}$, the incremental boundary value problem has unique solutions, then $\mathring{B}$ is locally stable; and if, for $\mathring{B}$, the incremental boundary value problem has non-unique solutions for the given incremental electromechanical loadings, then $\mathring{B}$ is locally unstable. In particular, we may assert that if the moduli $\mathring{\boldsymbol{\Omega}}$ and $\mathring{\varepsilon}$ are positive definite, then the initially deformed and polarized state $\mathring{B}$ is locally stable. Hence, local instability on a given loading path may occur only if, for some critical values of the external electromechanical dead loads, either of these moduli ceases to be positive definite.

The foregoing stability criterion is applicable only to static problems. Dynamical stability criteria involving the time evolution of the system are more general, and may be used to solve both dynamic and static stability problems. Generally, the equilibrium configuration $\mathring{B}$ is locally stable, from the dynamical point of view, if small time-dependent perturbations of $\mathring{B}$ remain small for all time. Specifically, we shall assume the following standard space-time decompositions for the incremental displacement $\mathbf{u}(\mathbf{x},t)$ and the electric potential $\phi(\mathbf{x},t)$:

$$\mathbf{u}(\mathbf{x},t) = e^{i\omega t}\tilde{\mathbf{u}}(\mathbf{x}), \qquad \phi(\mathbf{x},t) = e^{i\omega t}\tilde{\phi}(\mathbf{x}), \tag{121}$$

where ω is a complex number and $\tilde{\mathbf{u}}(\mathbf{x})$, $\tilde{\phi}(\mathbf{x})$ are time-independent fields.

The homogeneous dynamical incremental boundary-value problem to be solved is:

$$\begin{aligned} &\mathring{\rho}\ddot{\mathbf{u}} = \operatorname{div}\boldsymbol{\Sigma} \quad \text{in } \mathring{V}, \quad \mathbf{n}\cdot\boldsymbol{\Sigma} = 0 \quad \text{on } \partial\mathring{V}_1, \quad \mathbf{u} = \mathbf{0} \quad \text{on } \partial\mathring{V}_2, \\ &\operatorname{div}\boldsymbol{\Delta} = 0, \quad \mathbf{e} = -\nabla\phi \quad \text{in } \mathring{V}, \\ &\mathbf{n}\cdot\boldsymbol{\Delta} = 0 \quad \text{on } \partial\mathring{V}_3, \quad \phi = 0 \quad \text{on } \partial\mathring{V}_4. \end{aligned} \tag{122}$$

The incremental constitutive equations imply that $\boldsymbol{\Sigma}$, $\boldsymbol{\Delta}$ and $\mathbf{e}$ may be written in the form

$$\boldsymbol{\Sigma}(\mathbf{x},t) = e^{i\omega t}\tilde{\boldsymbol{\Sigma}}(\mathbf{x}), \quad \boldsymbol{\Delta}(\mathbf{x},t) = e^{i\omega t}\tilde{\boldsymbol{\Delta}}(\mathbf{x}), \quad \mathbf{e}(\mathbf{x},t) = e^{i\omega t}\tilde{\mathbf{e}}(\mathbf{x}), \tag{123}$$

which, when combined with (121)–(123), generate a proper-value problem for ω:

$$\operatorname{div}\tilde{\boldsymbol{\Sigma}} = \mathring{\rho}\omega^2\tilde{\mathbf{u}}, \quad \operatorname{div}\tilde{\boldsymbol{\Delta}} = 0, \quad \tilde{\mathbf{e}} = -\nabla\tilde{\phi} \text{ in } \mathring{V}, \tag{124}$$

with boundary conditions

$$\begin{aligned} &\mathbf{n}\cdot\tilde{\boldsymbol{\Sigma}} = 0 \quad \text{on } \partial\mathring{V}_1, \qquad \tilde{\mathbf{u}} = \mathbf{0} \quad \text{on } \partial\mathring{V}_2, \\ &\mathbf{n}\cdot\tilde{\boldsymbol{\Delta}} = 0 \quad \text{on } \partial\mathring{V}_3, \qquad \tilde{\phi} = 0 \quad \text{on } \partial\mathring{V}_4. \end{aligned}$$

We note that $\tilde{\boldsymbol{\Sigma}}$ and $\tilde{\boldsymbol{\Delta}}$ may be expressed in terms of $\nabla\tilde{\mathbf{u}}$ and $\tilde{\mathbf{e}}$ via the constitutive equations (82).

The following dynamic local stability criterion is assumed in respect of the incremental fields: We say that the initially deformed and polarized equilibrium configuration $\mathring{B}$ is locally stable if the possible eigenvalues ω of the proper-value problem (124) have non-negative imaginary part; *i.e.*, if

$$\operatorname{Im}\omega \geq 0. \tag{125}$$

More precisely, dynamic local stability obtains if small perturbations of $\mathring{B}$, corresponding to small initial oscillations, decay to zero in time, or remain small for all time. Configuration $\mathring{B}$ is locally unstable if the small oscillation becomes unbounded in time. Such a situation cannot occur if and only if (125) applies. Evidently ω depends on the initial deformation (or stress) and electric field through the moduli. Hence, assuming a locally stable reference configuration, the critical loads producing dynamic instability correspond to those values for which, for the first time on the loading path, the condition

$$\operatorname{Im}\omega = 0 \tag{126}$$

is satisfied, this relation determining the boundary of the stability domain.

To establish the relationship between the critical electromechanical loads corresponding to impending local instability, we shall first demonstrate that all eigenvalues ω^2 are real numbers. To do this, we assume that ω^2 may be complex. In this case, all incremental fields will also be complex, and we denote their complex conjugates by a superposed star. We note that, if $\{\mathbf{u},\ \phi,\ \omega^2\}$ is a solution of the proper-value problem (124), then $\{\mathbf{u}^*,\ \phi^*,\ \omega^{*2}\}$ also solves the same problem. Hence, we have

$$\begin{aligned}
&\operatorname{div}\boldsymbol{\Sigma} = \overset{o}{\rho}\omega^2\mathbf{u}, \quad \operatorname{div}\boldsymbol{\Sigma}^* = \overset{o}{\rho}\omega^{*2}\mathbf{u}^*, \quad \operatorname{div}\boldsymbol{\Delta} = 0, \quad \operatorname{div}\boldsymbol{\Delta}^* = 0,\\
&\qquad \mathbf{e} = -\nabla\phi, \quad \mathbf{e}^* = -\nabla\phi^*,\\
&\mathbf{n}\cdot\boldsymbol{\Sigma} = \mathbf{n}\cdot\boldsymbol{\Sigma}^* = 0 \quad \text{on } \partial\overset{o}{V}_1, \quad \mathbf{u} = \mathbf{u}^* = \mathbf{0} \quad \text{on } \partial\overset{o}{V}_2,\\
&\mathbf{n}\cdot\boldsymbol{\Delta} = \mathbf{n}\cdot\boldsymbol{\Delta}^* = 0 \quad \text{on } \partial\overset{o}{V}_3, \quad \phi = \phi^* = 0 \quad \text{on}\partial\overset{o}{V}_4.
\end{aligned} \tag{127}$$

After some manipulation, we are lead to the following result [Baesu *et al.* (2003)][16]

$$\overset{o}{\rho}(\omega^2-\omega^{*2})\int_{\overset{o}{V}}\mathbf{u}\cdot\mathbf{u}^*dv = -\int_{\overset{o}{V}}(\nabla\mathbf{u}^*\bullet\boldsymbol{\Sigma}+\boldsymbol{\Delta}\cdot\mathbf{e}^*-\nabla\mathbf{u}\bullet\boldsymbol{\Sigma}^*-\boldsymbol{\Delta}^*\cdot\mathbf{e})dv. \tag{128}$$

If we take the symmetry properties (84) into account, we conclude that the integrand on the right-hand side of (128) vanishes. Thus,

$$\overset{o}{\rho}(\omega^2-\omega^{*2})\int_{\overset{o}{V}}\mathbf{u}\cdot\mathbf{u}^*dv = 0. \tag{129}$$

Now, $(\mathbf{u},\phi)$ is a proper vector corresponding to the proper value ω, and so the integral in (129) is non-vanishing. Consequently,

$$\omega^2 = \omega^{*2} \quad \text{or} \quad \operatorname{Im}\omega^2 = 0, \tag{130}$$

from which it follows that ω is either purely real or purely imaginary.

As we have seen, the assumed dynamic stability criterion indicates loss of stability at those critical values of the loading parameters for which $\operatorname{Im}\omega$ just passes from positive to negative values. Since, according to (130), $\omega(\neq 0)$ cannot be a complex number, then assuming continuous dependence of ω on the loading parameters, we conclude that ω must vanish when stability is lost:

$$\omega = 0. \tag{131}$$

Hence, the boundary of the stability domain is determined by those critical values of the loading parameters at which (131) is satisfied for the first time on a given loading path. Said differently, the equilibrium configuration $\overset{o}{B}$ becomes locally unstable when the eigenvalue problem (124) has

a non-zero solution corresponding to a zero eigenvalue. However, in this case, the eigenvalue problems (124) and (120) corresponding to the dynamic and static criteria become identical. The two criteria therefore yield the same critical value of the loading parameters for a given dead-loading path. This result extends to hyperelastic dielectrics a similar conclusion demonstrated by Guz for prestressed hyperelastic solids ([Ogden (1984)][26], [Guz (1976)][27]). We observe that this equivalence is a direct consequence of the self-adjointness of the differential operator describing the incremental behaviour of the body.

An important time-dependent perturbation frequently used in stability analysis is the progressive or harmonic wave, defined in our electromechanical context by

$$\mathbf{u} = \mathbf{a}e^{i(\mathbf{p}\cdot\mathbf{x}-\omega t)}, \qquad \phi = ae^{i(\mathbf{p}\cdot\mathbf{x}-\omega t)}, \tag{132}$$

where $\mathbf{a}$ and a are constant quantities characterizing the amplitude of the wave, ω is the frequency, $\mathbf{p} = p\mathbf{n}$ $(\mathbf{n}\cdot\mathbf{n}=1)$ is a constant vector, p representing the wave number and $\mathbf{n}$ is the direction of propagation. Such waves may exist for all time only in an unbounded domain. It is easily seen that the fields (132) satisfy the homogeneous incremental balance equations (85) only if $\mathbf{a}$, $\mathbf{p}$ and ω satisfy the following equations:

$$\mathring{\mathrm{A}}_{lm}a_m + \mathring{\Gamma}_l a = \mathring{\rho}\omega^2 a_l, \qquad -\mathring{\Gamma}_m a_m + \mathring{\Gamma} a = 0, \tag{133}$$

with

$$\mathring{\mathrm{A}}_{lm}(\mathbf{p}) = \mathring{\Omega}_{klmn}p_k p_n, \quad \mathring{\Gamma}_l(\mathbf{p}) = \mathring{\mathrm{A}}_{mkl}p_m p_k, \quad \mathring{\Gamma}(\mathbf{p}) = \mathring{\varepsilon}_{kl}p_k p_l, \tag{134}$$

and, from $(84)_1$,

$$\mathring{\mathrm{A}}_{lm}(\mathbf{p}) = \mathring{\mathrm{A}}_{ml}(\mathbf{p}). \tag{135}$$

We assume the moduli $\mathring{\mathbf{\Omega}}$ and $\mathring{\varepsilon}$ are positive definite so that the initially deformed and polarized configuration is locally stable. In this case, from $(133)_2$, we may express a through a_m and conclude, using (133), that (132) is an admissible incremental solution only if

$$(\mathring{\mathrm{A}}_{lm} + \mathring{\Gamma}_l\mathring{\Gamma}_m/\mathring{\Gamma})a_m = \mathring{\rho}\omega^2 a_l. \tag{136}$$

Thus, the incremental acoustic tensor $\mathring{\mathbf{Q}}(\mathbf{p})$ is

$$\mathring{Q}_{lm}(\mathbf{p}) = \mathring{\mathrm{A}}_{lm}(\mathbf{p}) + \mathring{\Gamma}_l(\mathbf{p})\mathring{\Gamma}_m(\mathbf{p})/\mathring{\Gamma}(\mathbf{p}), \tag{137}$$

which, together with (135), implies that

$$\mathring{\mathbf{Q}}^T(\mathbf{p}) = \mathring{\mathbf{Q}}(\mathbf{p}) \qquad \text{for any } \mathbf{p}. \tag{138}$$

Consequently, the propagation condition corresponding to our harmonic plane-wave problem is

$$\mathring{\mathbf{Q}}(\mathbf{p})\mathbf{a} = \mathring{\rho}\omega^2\mathbf{a}, \tag{139}$$

and this furnishes the frequencies and wave amplitudes corresponding to the wave vector $\mathbf{p}$.

Since the acoustic tensor is symmetric, we once again conclude that the eigenvalues $\mathring{\rho}\omega^2(\mathbf{p})$ are real. Moreover, since we have assumed positive definiteness of the instantaneous moduli, we may use (137) to deduce that the acoustic tensor $\mathring{\mathbf{Q}}(\mathbf{p})$ is positive definite for any $\mathbf{p}$. Consequently, the eigenvalues $\mathring{\rho}\omega^2(\mathbf{p})$ are positive. We then infer that, to each $\mathbf{p}$, there corresponds a triad of mutually orthogonal eigenvectors $\mathbf{a}_1$, $\mathbf{a}_2$, $\mathbf{a}_3$, provided that the initially deformed and polarized equilibrium state is locally stable. This, in turn, leads us to conclude that the incremental behaviour of the body in its initially deformed and polarized state $\mathring{B}$ is similar to that of a classical linear piezoelectric crystal ([Balakirev and Gilinskii (1982)][24], [Dieulesaint and Roger (1974)][25]). Moreover, as in the classical case, all of our conclusions remain valid if we retain the assumption that $\mathring{\varepsilon}(\mathbf{p})$ is positive definite, but relax the restriction on $\mathring{\mathbf{\Omega}}(\mathbf{p})$ and require that it be merely strongly elliptic:

$$(\mathbf{b}\otimes\mathbf{c})^T\cdot\mathring{\mathbf{\Omega}}(\mathbf{p})(\mathbf{b}\otimes\mathbf{c}) > 0 \tag{140}$$

for any $\mathbf{p}$ and any $\mathbf{b}\otimes\mathbf{c}\neq\mathbf{0}$.

If $\mathring{\varepsilon}(\mathbf{p})$ and $\mathring{\mathbf{\Omega}}(\mathbf{p})$ are so restricted, then harmonic plane waves may propagate in any direction in a prestressed and pre-polarized hyperelastic material. The direction of propagation $\mathbf{n}$, the wave number $\mathbf{p}$, and the associated frequency ω satisfy the dispersion relation:

$$\det(\mathring{\mathbf{Q}}(\mathbf{p}) - \mathring{\rho}\omega^2(\mathbf{p})\mathbf{1}) = 0. \tag{141}$$

The velocity of propagation $V(\mathbf{p})$ of the wave is then given by

$$\mathrm{V}^2(\mathbf{p}) = \omega^2(\mathbf{p})/p \tag{142}$$

for any given $\mathbf{p}$.

We close by recalling that the instantaneous moduli depend on the material properties through Helmholtz' generalized free energy $\mathcal{H}$, as well as on the initial deformation and electric field. Considerable simplification of the constitutive laws may be achieved if we invoke three additional hypotheses:

(H_3) The initial applied static deformation $\mathring{\mathbf{F}}$ is infinitesimal (geometric linearity).

(H_4) The initial applied static electric field $\mathring{\mathbf{E}}$ is weak (electrical linearity).
(H_5) Helmholtz' generalized free energy $\mathcal{H}$ is a quadratic function of the infinitesimal strain $\mathbf{g}$ and of the electric field $\mathbf{E}$ (physical linearity).

In accordance with (H_5), we have

$$\mathcal{H} = \mathcal{H}(\mathbf{g}, \mathbf{E}) = \frac{1}{2} g_{kl} c_{klmn} g_{mn} - E_m e_{mkl} g_{kl} - \frac{1}{2} E_k \chi_{kl} E_l, \tag{143}$$

where c_{klmn}, e_{mkl} and χ_{kl} are the classical material constants of the hyperelastic material or piezoelectric crystal, possessing the well-known symmetry properties:

$$c_{klmn} = c_{lkmn} = c_{k\,l\,n\,m} = c_{mnkl}, \qquad e_{mkl} = e_{mlk}, \qquad \chi_{kl} = \chi_{lk}. \tag{144}$$

If (H_3) is satisfied, we may set $\mathring{\mathbf{F}} \approx \mathbf{1}$ in eqs. (79) for the instantaneous moduli. Thus, taking (143) and (83) into consideration, we derive

$$\begin{aligned} \mathring{\Omega}_{klmn} &= c_{klmn} + \mathring{S}_{kn}\delta_{lm} - e_{kmn}\mathring{E}_l - \mathring{\chi}_{kn}\mathring{E}_l\mathring{E}_m, \\ \mathring{\Lambda}_{mkl} &= e_{mkl} + \chi_{mk}\mathring{E}_l, \quad \text{and} \qquad \mathring{\varepsilon}_{kl} = \delta_{kl} + \chi_{kl}, \end{aligned} \tag{145}$$

where

$$\mathring{S}_{kn} = c_{knlm}\mathring{g}_{lm} - e_{mkn}\mathring{E}_n, \qquad \mathring{g}_{lm} = \frac{1}{2}(\mathring{u}_{l,m} + \mathring{u}_{m,l}). \tag{146}$$

Hypothesis (H_4) further implies that the last term in $(145)_1$ may be neglected.

We stress the fact that these equations are applicable only if the considered material is linear and only if the initial deformation and electric field are infinitesimal. Further reductions may be achieved for particular types of material symmetry and for particular forms of the initial perturbations. These issues will be addressed in a forthcoming work concerned with applications of the general theory.

6.5.2. *Local stability against antitplane perturbations*

In the course of obtaining sufficient conditions for the local stability of the configuration $\mathring{B}$, we first investigate the reference configuration B_R. From [Eringen and Maugin (1990)][22], the incremental specific energy W is

$$2W = u_{l,k}\mathring{\Omega}_{klmn}u_{m,n} + e_k\mathring{\varepsilon}_{kl}e_l, \tag{147}$$

which may also be written, relative to B_R, as

$$2W = \mathring{g}_{kl}c_{klmn}\mathring{g}_{mn} + \mathring{e}_k\varepsilon_{kl}\mathring{e}_l. \tag{148}$$

From the last expression it is clear that B_R is stable if the elasticity tensor, $\mathbf{c}$, and the dielectric tensor, ε, are positive definite - conditions which we assume to hold in what follows. Similarly, from (147), the local stability of $\mathring{B}$ is guaranteed by the positive definiteness of $\mathring{\Omega}$ - the instantaneous elasticity tensor, and of $\mathring{\varepsilon}$ - the dielectric tensor. If we assume that $\mathring{\varepsilon} = \varepsilon$, the second requirement is satisfied if B_R is stable.

We now investigate the requirements for the positive definiteness of $\mathring{\Omega}$. In the special case of an antiplane incremental state, W reduces to

$$2W = u_{3,1}\mathring{\Omega}_{1331}u_{3,1} + u_{3,1}\mathring{\Omega}_{1332}u_{3,2} + u_{3,2}\mathring{\Omega}_{2331}u_{3,1} + u_{3,2}\mathring{\Omega}_{2332}u_{3,2} + e_1\mathring{\varepsilon}_{11}e_1 + e_1\mathring{\varepsilon}_{12}e_2 + e_2\mathring{\varepsilon}_{21}e_1 + e_2\mathring{\varepsilon}_{22}e_2, \quad (149)$$

where, in consequence of the symmetries possessed by $\mathring{\mathbf{\Omega}}$,

$$\mathring{\Omega}_{1332} = \mathring{\Omega}_{2331}. \quad (150)$$

Hence, from (149), sufficient conditions for the local stability of $\mathring{B}$ against antiplane displacements are

$$\mathring{\Omega}_{1331} > 0, \quad \mathring{\Omega}_{1331}\mathring{\Omega}_{2332} - \mathring{\Omega}_{1332}^2 > 0, \quad \mathring{\Omega}_{2332} > 0. \quad (151)$$

For the crystal class $\bar{4}2m$, these are equivalent to

$$c - \chi\mathring{E}^2 > 0, \quad \left(c - \chi\mathring{E}^2\right)\left(c + \overset{o}{\sigma} - \chi\mathring{E}^2\right) - 4e^2\mathring{E}^2 > 0, \quad c + \overset{o}{\sigma} - \chi\mathring{E}^2 > 0. \quad (152)$$

Moreover, the positive definiteness of ε implies that

$$\varepsilon = 1 + \chi > 0. \quad (153)$$

Henceforth we assume the initial stress $\mathring{\sigma}$ and electric field $\mathring{E}$ to be such as to satisfy the sufficient conditions (152) and (153) for the local stability of $\mathring{B}$.

6.6. Transverse Electro-Acoustic Waves

To illustrate the foregoing theory, in this section we consider propagation of antiplane waves in class-23 piezoelectric crystals subject to initial deformations and electric fields. We suppose that the body is unbounded, that the initial applied stress is zero, *i.e.*,

$$\mathring{S}_{kn} = 0, \quad (154)$$

that only the $\mathring{E}_2$ component of the electric field is non-zero, and that the piezoelectric crystal under consideration has cubic symmetry and belongs

to the symmetry class 23. Under these assumptions as was shown in [Baesu and Soós (2001)][20] the constitutive equations take the form

$$\begin{aligned}
\Sigma_{12} &= \left(c - \chi \mathring{E}^2\right) u_{,1} - 2e\mathring{E}u_{,3} + \chi \mathring{E}\varphi_{,1} + e\varphi_{,3}, \\
\Sigma_{23} &= -2e\mathring{E}u_{,1} + \left(c - \chi \mathring{E}^2\right) u_{,3} + e\varphi_{,1} + \chi \mathring{E}\varphi_{,3}, \\
\Delta_1 &= \chi \mathring{E}u_{,1} + eu_{,3} - \varepsilon\varphi_{,1}; \qquad \Delta_2 = \chi \mathring{E}u_{,3} + eu_{,1} - \varepsilon\varphi_{,3},
\end{aligned} \tag{155}$$

where for the sake of simplicity we have used the notation

$$u = u_2, \quad c = c_{44}, \quad e = e_{14}, \quad \chi = \chi_{11}, \quad \varepsilon = 1 + \chi, \quad \mathring{E} = \mathring{E}_2. \tag{156}$$

The field equations take the form

$$\rho\, \ddot{u} = \left(c - \chi \mathring{E}^2\right) \Delta u - 4\, e\mathring{E}u_{,13} + \chi \mathring{E}\Delta\varphi + 2e\varphi_{,13}, \tag{157}$$

$$\chi \mathring{E}\Delta u + 2eu_{,13} - \varepsilon\Delta\varphi = 0. \tag{158}$$

We also note that the density of specific incremental energy W (see [Baesu *et al.* (2003)][16] takes the form

$$\begin{aligned}
2W = {} & u_{,1}\Omega_{1221}u_{,1} + u_{,1}\Omega_{1223}u_{,3} + u_{,3}\Omega_{3221}u_{,1} + u_{,3}\Omega_{3223}u_{,3} \\
& + \varphi_{,1}\varepsilon_{11}\varphi_{,1} + \varphi_{,1}\varepsilon_{13}\varphi_{,3} + \varphi_{,3}\varepsilon_{31}\varphi_{,1} + \varphi_{,3}\varepsilon_{33}\varphi_{,3},
\end{aligned} \tag{159}$$

which, for the case under consideration, may be reduced to [Baesu and Soós (2001)][20]

$$2W = \left(c - \chi \mathring{\mathrm{E}}^2\right) u_{,1}^2 - 4e\mathring{\mathrm{E}}^2 u_{,3}u_{,1} + \left(c - \chi \mathring{\mathrm{E}}^2\right) u_{,3}^2 + \varepsilon\varphi_{,1}^2 + \varepsilon\varphi_{,3}^2. \tag{160}$$

From (160) we observe that the specific energy W is positive if and only if c, e, ε, and the applied electric field $\mathring{E}$ satisfy the conditions

$$c - \chi \mathring{E}^2 > 0, \quad \left(c - \chi \mathring{E}^2\right)^2 - 4e^2\mathring{E}^2 > 0, \quad \varepsilon > 0. \tag{161}$$

These conditions guarantee that the pre-strained and pre-polarized configuration is locally stable with respect to antiplane perturbations. Note also that the assumption that the reference configuration of the body is locally stable translates as

$$c > 0, \quad \varepsilon > 0. \tag{162}$$

We are interested next in conditions for propagation of a plane transverse homogenous wave which is polarized parallel to the symmetry axis x_2 and its direction of propagation is parallel to (x_1, x_3). We assume that

$$u = ae^{i(k_1x_1 + k_3x_3 - \omega t)}, \quad \varphi = be^{i(k_1x_1 + k_3x_3 - \omega t)}. \tag{163}$$

Here, k_1 and k_3 are the components of the wave vector $\mathbf{k}$, ω is the constant frequency of the wave, a and b are constant amplitudes of the incremental displacement u, and φ is the incremental potential. With (163) the system (157)–(158) becomes

$$\rho\omega^2 a = \left[\left(c - \chi\mathring{E}^2\right)k^2 - 4\,e\mathring{E}k_1k_3\right]a + \left[\chi\mathring{E}k^2 + 2ek_1k_3\right]b \tag{164}$$

$$\left[\chi\mathring{E}k^2 + 2ek_1k_3\right]a - \varepsilon k^2 b = 0, \tag{165}$$

with

$$k^2 = k_1^2 + k_3^2.$$

Solving for b in (165) we get

$$b = \frac{\chi\mathring{E}k^2 + 2ek_1k_3}{\varepsilon k^2}a, \tag{166}$$

and substituting the result in (164) we obtain

$$\rho\omega^2 a = \left[\left(c - \chi\mathring{E}^2\right)k^2 - 4\,e\mathring{E}k_1k_3 + \frac{\left(\chi\mathring{E}k^2 + 2ek_1k_3\right)^2}{\varepsilon k^2}\right]a. \tag{167}$$

Equation (167) shows that the wave under consideration exists if and only if the following *dispersion equation* is satisfied

$$\rho\omega^2 = \frac{1}{\varepsilon}\left(\varepsilon\left(c - \mathring{E}^2\right) + \left(e\sin 2\theta - \mathring{E}\right)^2\right)k^2, \tag{168}$$

where we used the relations

$$k_1 = k\cos\theta, \quad k_3 = k\sin\theta, \quad \text{with } \theta \in [0, 2\pi], \tag{169}$$

and θ is the angle between the symmetry axis x_1 and the wave vector $\mathbf{k}$.

To analyze the dispersion (168) let first assume that the wave vector k is given and try to obtain conditions to be satisfied such that ω is real. Note that that the right hand side of (168) is positive for all $k > 0$ and all directions of propagation $\theta \in [0, 2\pi]$, if (161) are satisfied. Under these conditions we conclude that plane transverse incremental, homogenous waves can propagate in all directions and for all wavelengths $\lambda = 2\pi/k > 0$. The amplitude of such a wave is indeterminate (i.e. a remains arbitrary). These particular results are in agreement with the general results in [Baesu *et al.* (2003)][16], except that in reference, W positive is only a sufficient condition (not necessary and sufficient as in this particular case) for these results to hold.

We can rewrite the dispersion relation (168) in the following manner

$$\omega^2 = v_0^2 \left(1 - \alpha^2 + \kappa^2 \left(\sin 2\theta - \beta\right)^2\right) k^2, \tag{170}$$

where

$$v_0^2 = \frac{c}{\rho}, \quad \kappa^2 = \frac{e^2}{\varepsilon c}, \tag{171}$$

and

$$\alpha^2 = \mathring{\mathrm{E}}^2/c, \quad \beta = \mathring{\mathrm{E}}/e. \tag{172}$$

Note that v_0 is the speed of propagation for the case of a weak electromechanic coupling ($e \approx 0$), and zero initial electric field. Also note that for $e \neq 0$, but for $\mathring{E} = 0$, the dispersion relation (168) has the classical form

$$\omega^2 = v_0^2 \left(1 + \kappa^2 \left(\sin 2\theta\right)\right) k^2. \tag{173}$$

This shows that in the case of $e \neq 0$ the phase velocity $v = \omega/k$ becomes dependent on the direction, and the group velocity $v_g = \partial\omega\left(k\right)/\partial k$ does not coincide with the phase velocity (as in the case $e = 0$). In conclusion, even in the absence of an initially applied electric field, we have the dispersion of the acousto-electric waves, which is due to the the electromechanic coupling that occurs.

We now introduce in the dispersion equation the function

$$f(\theta) = 1 - \alpha^2 + \kappa^2 \left(\sin 2\theta - \beta\right)^2, \quad \theta \in [0, 2\pi]. \tag{174}$$

It is easy to see that this function has the following properties

$$\text{if } \beta > 1, \text{ then } f(\theta) > 0, \quad \text{for } \theta \in [0, 2\pi], \tag{175}$$

if and only if

$$1 - \alpha^2 + \kappa^2 \left(1 - \beta\right)^2 > 0; \tag{176}$$

$$\text{if } \beta < -1, \text{ then } f(\theta) > 0, \quad \text{for } \theta \in [0, 2\pi], \tag{177}$$

if and only if

$$1 - \alpha^2 + \kappa^2 \left(1 + \beta\right)^2 > 0; \tag{178}$$

$$\text{if } -1 < \beta < 1, \text{ then } f(\theta) > 0, \quad \text{for } \theta \in [0, 2\pi], \tag{179}$$

and if and only if

$$1 - \alpha^2 > 0. \tag{180}$$

To sum up, if the material constants $c > 0$, $\varepsilon > 0$, e and the initial applied field $\mathring{E}$ satisfy (175)–(180), then in the piezoelectric crystal under consideration, pre-strained and pre-polarized transverse homogeneous incremental waves can propagate with any wavelength; the real and positive frequency is determined by the dispersion relation (170). If the above conditions (175)–(180) are violated, there may be directions for which $f(\theta) < 0$. In this case the solution of the dispersion equation can be purely imaginary, which leads to exponential growth of the corresponding amplitude and ultimately to the loss of stability.

In [Baesu and Soós (2001)][20] it was verified that the assumptions of the infinitesimal model are in fact satisfied for typical values of material constants, *i.e.* that the initial electric field produces only infinitesimal initial deformations. This leads us to the conclusion that an initial electric field which produces initial infinitesimal deformations in a piezoelectric crystal from the class 23 for typical values of material constants *cannot produce the loss of local stability* with respect to incremental antiplane states. However, we remark that the loss of stability may still happen with respect to other states, like plane states with respect to (x_1, x_2), for example.

Acknowledgment

I wish to thank the North Atlantic Treaty Organization, which supported portions of the work presented here through a Collaborative Research Grant (#975687).

References

1. Essig, O., Wang, P., Hartweg, M., and Janker, P., (1999), "Uniaxial stress and temperature dependence of field induced strains in antiferroelectric lead zirconate titanate stannate ceramics", J. European Ceramic Society, **19**, 1223–8.
2. Pan, M.J., Park, S.E., Markowski, K.A., and Yoshikawa, S., (1996), "Antiferroelectric-to-ferroelectric phase switching PLSnZT ceramics II. The effect of pre-stress conditions on the strain behavior", Proc. of the 10th IEEE Symposium on Applications of Ferroelectrics, East Brunswick, N.J., Aug. 1996, 18–21.
3. Adachi, K., Tsuji, M., and Kato, H., (1998), "Influence of static pre-stress on the characteristics of bolt-clamped Langevin-type transducers", Japanese J. Appl. Phys., **37**, 2982–2987.
4. Lee, J., and Ramesh, R., (1996), "Imprint of (Pb, La)(Zr, Ti) O_3 thin films with various crystalline qualities", Appl. Phys. Lett., **68**, 484–6.
5. Sunar, M., and Rao, S. S., (1999), "Recent advances in sensing and control of flexible structures via piezoelectric materials technology", Appl. Mech. Rev., **52**, 1–16.

6. Mindlin, R. D., (1989), "The collected papers of Raymond D. Mindlin", Editor H. Deresiewicz, et. al., Springer-Verlag, New York.
7. Tiersten, H. F., (1969), "Linear Piezoelectric Plate Vibrations", Plenum Press, New York.
8. Lee, P.C.Y., and Haines, D. W., (1974) "Piezoelectric crystals and electroelasticity", R. D. Mindlin and Applied Mechanics, G. Hermann (ed.), Pergamon, New York, 149–196.
9. Rogacheva, N. N., (1994), "The Theory of Piezoelectric Shells and Plates", CRC Press, Boca Raton.
10. Wang, J., and Yang, J. S., (2000), "Higher order theories for piezoelectric plates and applications", Appl. Mech. Rev., **53**, April 2000.
11. Yang, J. S., and Jiang, Q., (2002), "A model for electroelastic plates under biasing fields with applications to bucking analysis", Int. J. Solids Structures, **39**, 2629–2642.
12. Yang, J. S., and Jiang, Q., (2002), "On modeling of extension and flexure response of electroelastic shells under biasing fields", Acta Mechanica, **156**, 163–178.
13. Yang, J. S., and Jiang, Q., (2002), "Characterization of electroelastic beams under biasing fields with applications in buckling analysis", Arch. of Appl. Mech., **72**, 439–450.
14. Tiersten, H. F., (1995), "On the accurate description of piezoelectric resonators subject to biasing deformations", Int. J. Engineering Science, **33**, 2239–2259.
15. Soós, E., (1996), "Stability, resonance and stress concentration in prestressed piezoelectric crystals containing a crack", Int. J. Engng. Sci., **34**, 1647–1673.
16. Baesu, E., Fortune, D., and Soós, E., (2003), "Incremental behavior of piezoelectric crystals under initial mechanical and electric fields", J. Appl. Math. Phys. (ZAMP), **54**, 160–178.
17. Baesu, E., and Soós, E., (2001), "Antiplane piezoelectricity in the presence of initial mechanical and electrical fields", Mathematics and Mechanics of Solids, **6**, 409–422.
18. Baesu, E., and Soós, E., (2001), "Antiplane fracture in a prestressed and prepolarized piezoelectric crystal", IMA J. of Appl. Math., **66**, 499–508.
19. Baesu, E., and Soós, E., "Fracture criteria for prestressed and prepolarized piezoelectric crystals", Mathematics and Mechanics of Solids, in press.
20. Baesu, E., and Soós, E., (2001), "Transverse acousto-electric waves in prestrained and pre-polarized piezoelectrics", Mathematical Reports, **3**, 75–82.
21. Baesu, E., "On electroacoustic flux", J. Appl. Math. Phys. (ZAMP), in press.
22. Eringen, A. C., and Maugin, G. A., (1990), "Electrodynamics of Continua", Vol. 1, Foundations and Solid Media, Springer, New York.
23. Sirotin, I. I., and Shaskolskaya, M. P., (1975), Crystal Physics, Naukova, Moscow, (in Russian).
24. Balakirev, M. K., and Gilinskii, I. A., (1982), "Waves in Piezoelectric Crystals", Nauka, Moscow, (in Russian).
25. Dieulesaint, E., and Roger, D., (1974), "Ondes élastiques dans les solides", Masson, Paris.

26. Ogden, R. W., (1984), "Non-linear Elastic Deformations", John Wiley & Sons, New York.
27. Guz, A. N., (1976), "Stability of Elastic Bodies Acted Upon by Hydrostatic Pressure", Naukova Dumka, Kiev, (in Russian).
28. Guz, A. N., (1986), "Fundamentals of the Three-Dimensional Theory of Stability of Deformable Bodies", Viska Schola, Kiev, (in Russian).

CHAPTER 7

ON THE STABILITY OF TRANSIENT VISCOUS FLOW IN AN ANNULUS

Andrei A. Kolyshkin

Department of Engineering Mathematics, Riga Technical University, Riga, Latvia LV 1048
E-mail: andrejs.koliskins@rbs.lv

Rémi Vaillancourt

Department of Mathematics and Statistics, University of Ottawa, Ottawa, Ontario, Canada K1N 6N5
E-mail: remi@uottawa.ca

Inta Volodko

Department of Engineering Mathematics, Riga Technical University, Riga, Latvia LV 1048
E-mail: inta@cs.rtu.lv

Linear stability theory is applied to the analysis of transient viscous flow in an annulus. The transient phase is generated by a sudden closure of the annulus. The velocity profiles used for linear stability calculations are obtained by the method of matched asymptotic expansions. A quasi-steady assumption is used in the analysis of the flow linear stability. Calculations are done for the first two non–axisymmetric modes. The results show that the critical Reynolds numbers decrease considerably during a short time interval after the sudden closure of the annulus.

7.1. Introduction

Transient fluid flows often occur in applications, examples of which include the design and analysis of water supply systems, oil and gas pipelines and the analysis of blood flow in arteries. Fast changes in the characteristics of the flow (for example, velocity and pressure) are known to cause damage

to pipelines and other hydraulic devices (in hydraulics such an event is usually referred to as waterhammer). The pressure in unsteady flow can also lead to cavitation. Blood flow unsteadiness induced by cardiac cycle can result in atherosclerosis plaque development in regions where the shear stress changes direction [Waters and Pedley (1999)][1].

Recent experimental and theoretical studies of transient flows in pipes and channels indicate that transition from one flow regime to another can lead to essential changes in the characteristics of the flow. For example, the measurements of waterhammer velocity profiles in [Brunone *et al.* (2000)][2] showed strong flow asymmetry with respect to the axis of the pipe. The transition in accelerated and decelerated pipe flows was studied in [Das and Arakeri (1998)][3], where the fluid motion was induced by a piston. It is shown that for some set sof experimental conditions flow instabilities result in the formation of helical vortices with rapid transition to turbulence.

One of the effective means for the theoretical study of the transition from one flow regime to another is the linear stability theory which can be used in order to predict when a particular flow becomes unstable. The theory has been applied to many problems where the basic flow is usually assumed to be steady [Drazin and Reid (1981)][4]. Linear stability of time-dependent flows is not a well-developed topic in hydrodynamic stability theory. It has been pointed out in [Drazin and Reid (1981)][4] that even the terms "stable flow" and "unstable flow" may become unclear in the case of time-dependent basic flows which change substantially with time. Rigorous linear stability analysis of unsteady flows is possible only for periodic base flows, where the Floquet theory can be used [Yang and Yih (1977)][5], [von Kerczek and Davis (1974)][6], [Davis (1976)][7]. Strictly speaking, the method of normal modes used in the linear stability analysis of steady flows cannot be applied to arbitrary unsteady basic flows. However, in some cases a quasi-steady assumption can be used. In this case, time is treated as a parameter and not as an independent variable. Examples of the use of the quasi-steady assumption are given in [Garg (1981)][8], [Gad-el-Hak *et al* (1984)][9], [Ghidaoui and Kolyshkin (2001)][10], [Moss and da Silva (1993)][11]. It is argued in [Hall and Parker (1976)][12] that the quasi-steady assumption is justifiable if there exists a fast (convective) time scale on which a perturbation can grow before significant changes in the base flow can be observed. It is shown in [Hall and Parker (1976)][12] that the quasi-steady approach represents the first term of an asymptotic expansion of the WKB type.

In order to perform linear stability calculations calculations, one needs to specify the base flow. We are mainly interested in the velocity distribu-

tion under conditions of rapid change of the flow rate in a short time. A theoretical investigation of laminar flow in a channel or a pipe caused by a rapid closure of a valve is performed in [Weinbaum and Parker (1975)][13], where it is shown that the flow is essentially two-dimensional only in a region whose length, measured from the end wall, is of the order of the channel height. Outside this region, the flow can be considered as one dimensional. An approximate solution for the velocity distribution outside the above mentioned region is found in [Weinbaum and Parker (1975)][13] by a Pohlhausen type technique used in boundary layer theory provided the flow before deceleration was a steady Poiseuille flow. Recently, an asymptotic solution for the velocity distribution in a pipe is found in [Ghidaoui and Kolyshkin (2002)][14]. Similar solutions for the case of a plane channel and an annulus are found in [Kolyshkin and Vaillancourt (2001)][15] and [Kolyshkin and Volodko (2002)][16]. The solutions found in [Ghidaoui and Kolyshkin (2002)][14] and [Kolyshkin and Volodko (2002)][16] are valid for short times and the flow, before deceleration, can be represented by an arbitrary smooth function of the radial coordinate and time (assuming that only the longitudinal velocity component is not equal to zero).

Linear stability theory is used in the present paper to analyze unsteady laminar flow in an annulus. The base flow is assumed to be of the form given in [Kolyshkin and Volodko (2002)][16]. A quasi-steady assumption is used for the linear stability calculations. The stability problem is solved by a pseudospectral collocation method for both symmetric and non-symmetric modes. Critical Reynolds numbers are calculated. It is shown that there is a sharp decrease in the critical Reynolds number right after deceleration.

7.2. Mathematical Formulation of the Problem

Consider an infinitely long annulus of inner and outer radii R_1 and R_2, respectively, filled with a viscous incompressible fluid. At time $t = 0$, the flow is suddenly blocked so that the total fluid flux through the cross section of the annulus is zero. The flow, before and after deceleration, is unidirectional, that is, the velocity vector has only one nonzero (longitudinal) component which is a function of the radial coordinate and time. The method of matched asymptotic expansions [Ghidaoui and Kolyshkin (2002)][14], [Kolyshkin and Volodko (2002)][16] is used to derive an approximate velocity distribution valid for short times. It is shown in [Kolyshkin and Volodko (2002)][16] that the velocity distribution shortly after sudden

blockage has the form

$$U(r,t) = g(r) - G + \frac{G}{2R(1-R)}\,(R^2+3R-3Rr-r)\operatorname{erfc}\frac{r-R}{2\sqrt{\varepsilon t}} + \frac{G}{2(1-R)}\,(-3-R+5r-Rr)\operatorname{erfc}\frac{1-r}{2\sqrt{\varepsilon t}} + \frac{4G}{1-R}\sqrt{\frac{\varepsilon t}{\pi}}\left\{\exp\left[-\frac{(r-R)^2}{4\varepsilon t}\right] + \exp\left[-\frac{(1-r)^2}{4\varepsilon t}\right] - 1\right\} + O(\varepsilon), \tag{1}$$

where r and t are dimensionless radial coordinate and time, respectively, $\varepsilon = \nu T/R_2^2$, T is the characteristic time, ν is the kinematic viscosity of the fluid, $R = R_1/R_2$ is the radius ratio, $g(r)$ is the initial velocity distribution prior to deceleration, that is, $u|_{t=0} = g(r)$, and G is the average velocity of the flow prior to deceleration which is given by the integral

$$G = \frac{2}{1-R^2}\int_R^1 rg(r)\,dr. \tag{2}$$

The velocity profiles (1) contain inflection points. Hence, these profiles are potentially highly unstable. We shall consider conditions under which the flow (1) becomes linearly unstable.

We assume that $u(r,\theta,z,t)$, $v(r,\theta,z,t)$ and $w(r,\theta,z,t)$ denote the radial, azimuthal and longitudinal velocity components, respectively, and $p(r,\theta,z,t)$ represents the pressure. We consider normal perturbations of the form

$$\begin{aligned} u(r,z,t) &= u'(r)\,e^{in\theta+i\alpha z-\gamma t},\\ v(r,z,t) &= v'(r)\,e^{in\theta+i\alpha z-\gamma t},\\ w(r,z,t) &= U(r,t) + w'(r)\,e^{in\theta+i\alpha z-\gamma t},\\ p(r,z,t) &= P(t) + p'(r)\,e^{in\theta+i\alpha z-\gamma t}, \end{aligned} \tag{3}$$

where α is the axial wavenumber, n is the azimuthal wavenumber, u', v', w' and p' are small amplitudes of the normal perturbations. Substituting (3) into the Navier–Stokes equations and linearizing the equations in a neighborhood of the base flow, we obtain the following dimensionless linearized stability equations:

$$-\gamma u' + i\alpha u' U = -\frac{dp'}{dr} + \frac{1}{Re}\left[Nu' - \frac{u'}{r^2} - 2in\frac{v'}{r^2}\right], \tag{4}$$

$$-\gamma v' + i\alpha v' U = -in\frac{p'}{r} + \frac{1}{Re}\left[Nv' - \frac{v'}{r^2} + 2in\frac{u'}{r^2}\right], \tag{5}$$

$$-\gamma w' + i\alpha w' U + u'\frac{\partial U}{\partial r} = -i\alpha p' + \frac{1}{Re}Nw', \tag{6}$$

$$\frac{du'}{dr} + \frac{u'}{r} + in\frac{v'}{r} + i\alpha w' = 0, \tag{7}$$

where

$$N = \frac{d^2}{dr^2} + \frac{1}{r}\frac{d}{dr} - \frac{n^2}{r^2} - \alpha^2.$$

The Reynolds number is defined by the formula $Re = U_* R_2/\nu$, where U_* is some characteristic velocity scale. Note that a quasi-steady approximation is used in deriving equations (4)–(7), that is, the variable t in $U(r,t)$ is treated as a parameter. The quasi-steady assumption is justified if the rate of change of the growth rate of perturbations is larger than the rate of change of the base flow with respect to time. Calculations performed in [Ghidaoui and Kolyshkin (2001)][10] and [Ghidaoui and Kolyshkin (2002)][14] show that this condition is satisfied for similar transient flow in a pipe.

The boundary conditions are

$$u' = 0, \quad v' = 0, \quad w' = 0, \qquad \text{at } r = R \text{ and } r = 1. \tag{8}$$

Equations (4)–(7) together with the boundary conditions (8) form an eigenvalue problem. The eigenvalues, $\gamma_m = \gamma_{rm} + i\gamma_{im}$, $m = 1, 2, \ldots$, determine the stability of the base flow $U(r,t)$. The flow is stable if $\gamma_{rm} > 0$ for all m and unstable if $\gamma_{rm} < 0$ for at least one value of m. The real part of γ is proportional to the growth rate of perturbations while the imaginary part of γ is proportional to the phase speed.

System (4)–(7) and the boundary conditions (8) depend on several parameters, namely, Re, t, α and n. For fixed values of t and n, the set of numbers $Re = Re(\alpha)$ is determined as a function of α in the case only one eigenvalue has zero real part, while the others have positive real parts. Then the critical Reynolds numbers are found by setting $Re^c = \min\limits_{\alpha} Re(\alpha)$. This procedure is repeated for other sets of values of t and n.

The details of the numerical procedure are briefly summarized below. In order to simplify system (4)–(7), we eliminate the functions p' and w' from the system. As a result, we obtain a system of two ordinary differential

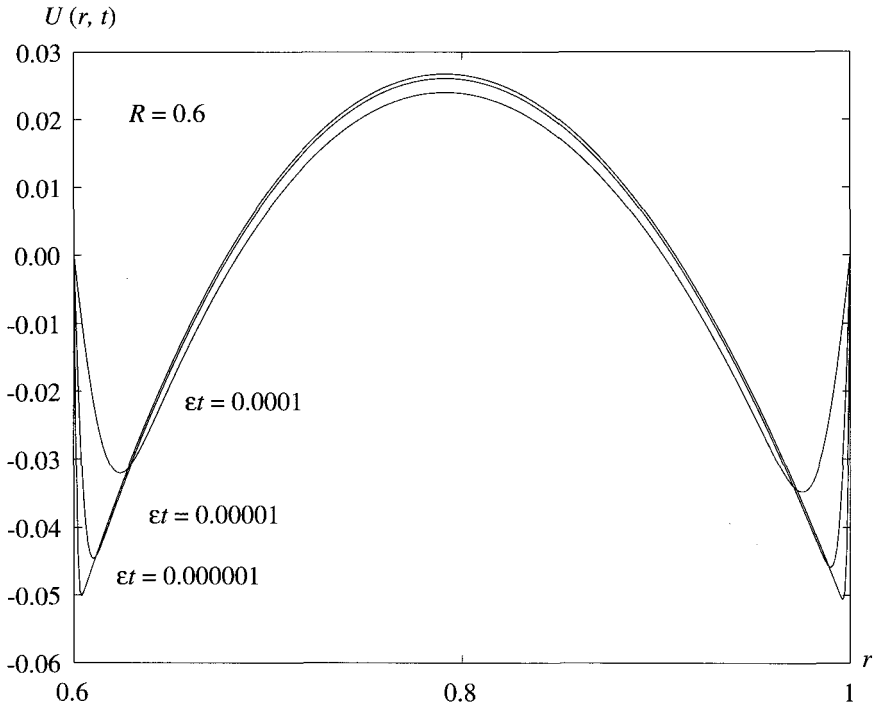

Fig. 7.1. Base flow velocity profiles, $U(r,t)$, for different values of εt and $R = 0.6$.

equations for u' and v'. Since the equation for u' is of order four, additional boundary conditions are needed. These conditions are found from the continuity equation (7) and have the form

$$\frac{du'}{dr} = 0, \qquad \text{at } r = R \text{ and } r = 1. \tag{9}$$

A collocation method based on Chebyshev polynomials is used to solve problem (4)–(9). The interval $(R, 1)$ is mapped onto the interval $(-1, 1)$ by means of the transformation

$$\tau = \frac{2}{1-R} r - \frac{1+R}{1-R}. \tag{10}$$

A solution to (4)–(9) in terms of the coordinate τ is sought in the following

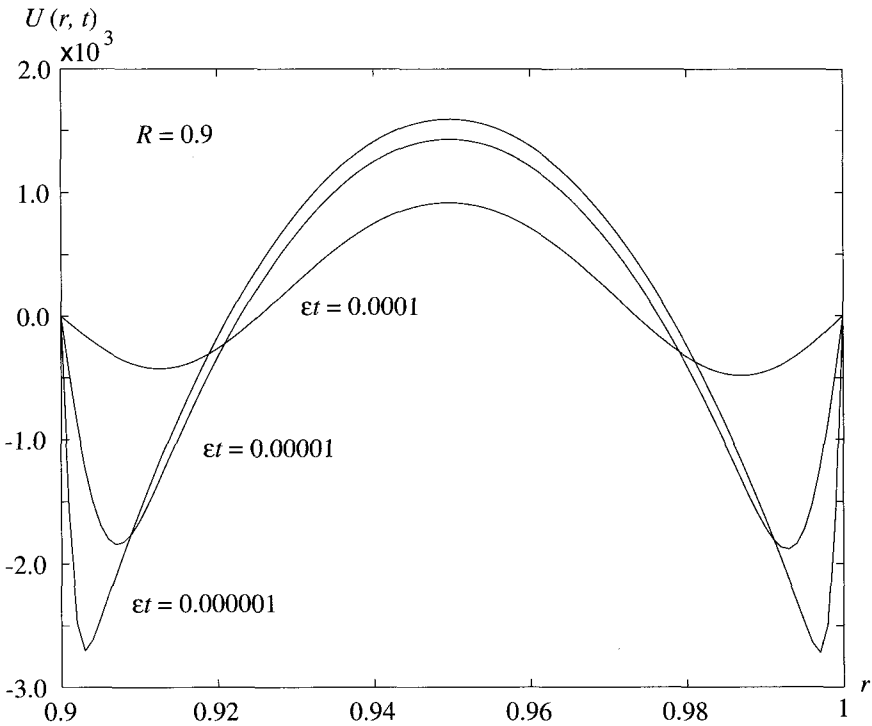

Fig. 7.2. Base flow velocity profiles, $U(r,t)$, for different values of εt and $R = 0.9$.

form:

$$u'(\tau) = \sum_{j=1}^{m} a_j p_{mj}(\tau), \tag{11}$$

$$v'(\tau) = \sum_{j=1}^{m} b_j q_{mj}(\tau), \tag{12}$$

where a_j and b_j are arbitrary (complex) constants, and $p_{mj}(\tau)$ and $q_{mj}(\tau)$ are the fundamental interpolation polynomials:

$$\begin{aligned} p_{mj}(\tau) &= \frac{(1-\tau^2)^2}{(1-\tau_j^2)^2} \frac{T_m(\tau)}{(\tau-\tau_j)T'_m(\tau_j)}, \\ q_{mj}(\tau) &= \frac{(1-\tau^2)}{(1-\tau_j^2)} \frac{T_m(\tau)}{(\tau-\tau_j)T'_m(\tau_j)}. \end{aligned} \tag{13}$$

Here $T_m(\tau)$ denotes Chebyshev's polynomial of the first kind of degree m

whose zeros are

$$\tau_j = \cos\frac{(2j-1)\pi}{2m}, \qquad j = 1, 2, \ldots, m. \tag{14}$$

The form of the polynomials $p_{mj}(\tau)$ and $q_{mj}(\tau)$ ensures that the boundary conditions for the functions u' and v' are satisfied automatically. The points τ_j in (14) are chosen as the collocation points. Therefore, the problem reduces to the generalized eigenvalue problem

$$(A - \gamma B)\psi = 0. \tag{15}$$

Equation (15) is solved by the IMSL routine DGVLCG. Note that solutions of the form (11) and (12) are more convenient than those obtained by traditional collocation methods [Canuto *et al* (1988)][17] for two reasons: first, in the present case the matrix B in (15) is nonsingular, and second, the use of basis functions of the form (11) and (12), which satisfy the given boundary conditions, considerably reduces the condition number of the matrices in this method (see [Heinrichs (1989)][18]).

7.3. Numerical Results

All calculations correspond to the case of fully developed Poiseuille flow in the annulus before sudden blockage. The function $g(r)$ and the average velocity G, in this case, have the form

$$g(r) = 1 - r^2 - \frac{1 - R^2}{\ln R}\ln r, \tag{16}$$

and

$$G = \frac{1 + R^2}{2} + \frac{1 - R^2}{2\ln R}. \tag{17}$$

Only nonaxisymmetric modes with azimuthal wave numbers $n = 1$ and $n = 2$ are considered. The results in [Ghidaoui and Kolyshkin (2001)][10] and [Ghidaoui and Kolyshkin (2002)][14] indicate that these two modes are the most unstable ones for transient flows in a pipe.

Figures 7.1 and 7.2 show the velocity distribution given by (1), (16) and (17) for different values of the dimensionless time εt for the cases $R = 0.6$ and $R = 0.9$, respectively. Both graphs indicate that the velocity profile rapidly changes in the boundary layers near the walls while the core region is characterized by relatively slow variation of the velocity. Note that, if $R_2 = 10$ cm and the fluid inside the annulus is water, then $\varepsilon t = 0.0001$ corresponds to 1 sec.

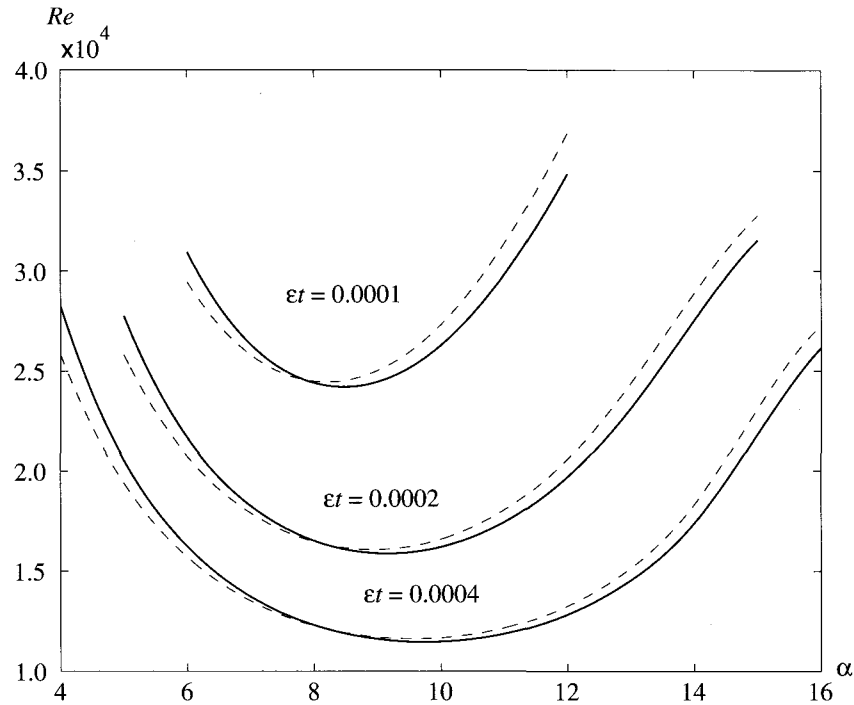

Fig. 7.3. Critical Reynolds numbers, Re^c, versus α for different values of εt. The graphs for the modes with $n = 1$ and $n = 2$ are shown by solid and dashed lines, respectively.

In waterhammer analysis, the time scale is of the order of a few seconds; therefore we restrict attention to values of the dimensionless parameter εt in the range [0.0001, 0.001]. The graphs in Figs. 7.1 and 7.2 show that the velocity profiles for all times contain inflection points.

The stability curves for the first two nonaxisymmetric modes with $n = 1$ and $n = 2$ versus the wavenumber α are shown on Fig. 7.3 for three values of the time εt. It is seen from the figure that the modes with $n = 1$ and $n = 2$ intersect. However, the most unstable mode is the first nonaxisymmetric mode with $n = 1$. The critical Reynolds numbers and the critical wavenumbers for $n = 1$ and $n = 2$ for all three values of time are very close to each other. For example, for $\varepsilon t = 0.0002$ and the mode with $n = 1$, we have $Re^c = 15880$ and $\alpha^c = 9.16$, while, for the case $n = 2$, one has $Re^c = 16071$ and $\alpha^c = 8.93$.

Critical Reynolds numbers versus time are shown in Fig. 7.4. The graph

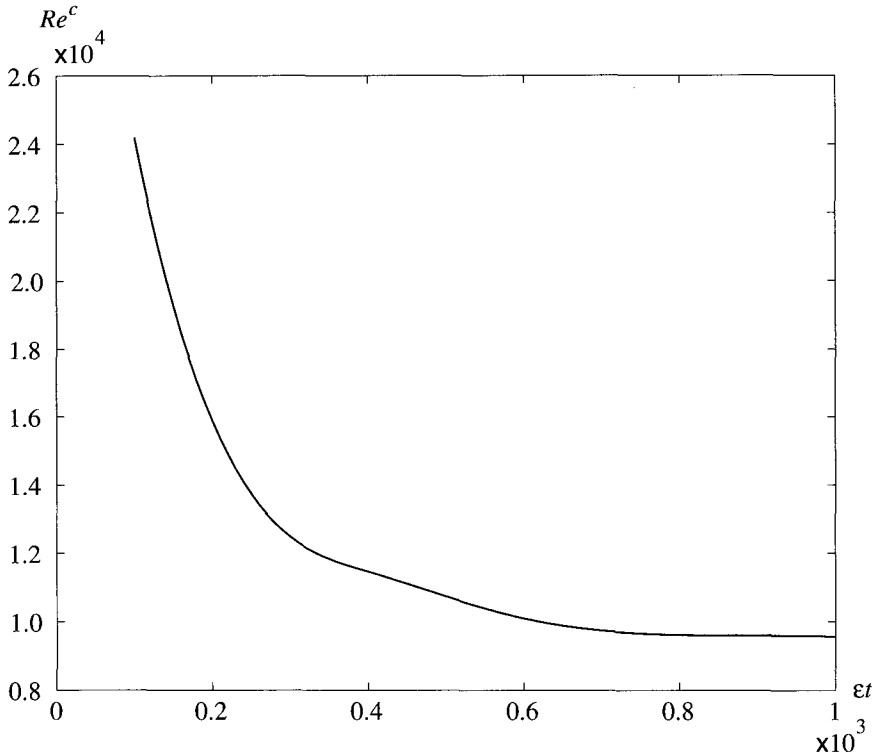

Fig. 7.4. Critical Reynolds numbers, Re^c, versus εt.

indicates that there is a sharp decrease in the critical Reynolds numbers in the interval $[0.0001, 0.003]$. Note that as $t \to +0$ the flow is linearly stable so that $Re^c = \infty$ at $t = 0$ (see [Drazin and Reid (1981)][4]).

Figure 7.5 shows the dependence of the critical wavenumbers upon time. As can be seen from the graph, the critical wavenumbers increase as time increases.

7.4. Conclusion

Linear stability analysis of unsteady flow in an annulus is performed in the present paper. The unsteadiness of the flow results from a sudden closure of the annulus. The velocity profiles are obtained by the method of matched asymptotic expansions. The existence of inflection points in base velocity profiles suggests that these profiles can be highly unstable. A quasi-steady

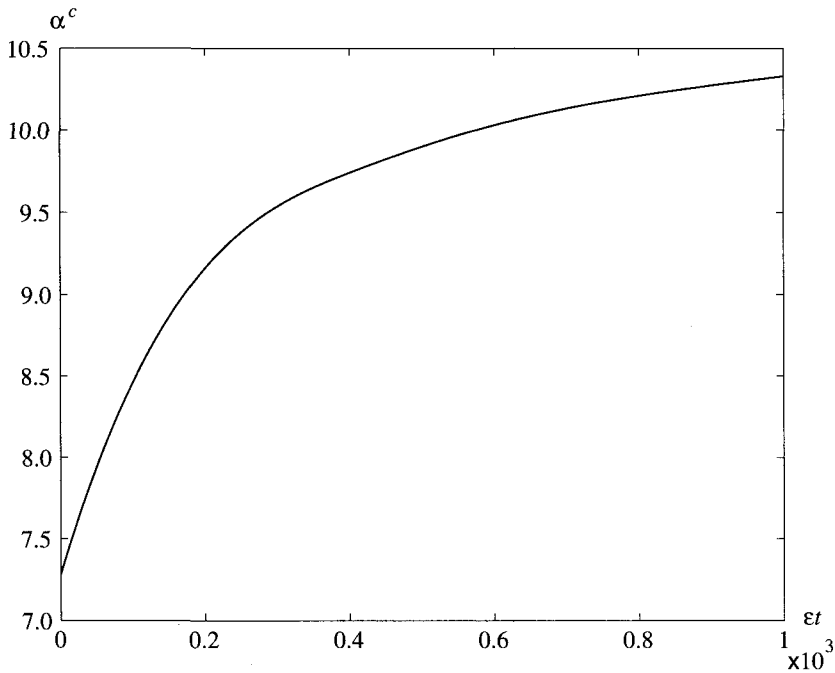

Fig. 7.5. Critical wavenumbers numbers, α^c, versus εt.

assumption is used for the numerical solution of the linear stability problem. The results show a sharp decrease in the critical Reynolds numbers during the short time interval after sudden closure.

Acknowledgments

The authors gratefully acknowledge the partial support provided for this work by the Latvian Council of Science, project 04.1239, and the Natural Sciences and Engineering Research Council of Canada.

References

1. Waters, S. L., and Pedley, T. J., (1999), "Oscillatory flow in a tube of time-dependent curvature. Part 1: Perturbation to flow in a stationary curved tube." J. Fluid Mech., 383, 327–352.
2. Brunone, B., Karney, B. W., Micarelli, M., and Ferrante, M., (2000), "Velocity profiles and unsteady pipe friction in transient flow", J. Water Resources Planning and Management, 126, 236–244.

3. Das, D., and Arakeri, J. H., (1998), "Transition of unsteady velocity profiles with reverse flow". J. Fluid Mech., 374, 251–283.
4. Drazin, P., and Reid, W., (1981), "Hydrodynamic stability". Cambridge University Press, Cambridge.
5. Yang, W. H., and Yih, C.-S., (1977), "Stability of time-periodic flows in a circular pipe". J. Fluid Mech., 82, 497–505.
6. von Kerczek, C., and Davis, S. H, (1974), "Linear stability theory of oscillatory Stokes layers". J. Fluid Mech., 62, 753–773.
7. Davis, S. H., (1976), "The stability of time-periodic flows". Ann. Rev. Fluid Mech., 8, 57–74.
8. Garg, V. K., (1981), "Stability of developing flow in a pipe: non-axisymmetric disturbances". J. Fluid Mech., 110, 209–216.
9. Gad-el-Hak, M., Davis, S. H., McMurray, J. T., and Orszag, S. A., (1984), "On the stability of decelerating laminar boundary layer". J. Fluid Mech., 138, 297–323.
10. Ghidaoui, M. S., and Kolyshkin, A. A., (2001), "Stability analysis of velocity profiles in water-hammer flows", J. Hydraulic Engineering, 127, 499–512.
11. Moss, E. A., and da Silva, D. F., (1993), "The evolution of unstable regions in impulsively started pipe entrance flows". Phys. Fluids, A5, 2721–2724.
12. Hall, P., and Parker, K. H., (1976), "The stability of the decaying flow in a suddenly blocked channel flow". J. Fluid Mech., 75, 305–314.
13. Weinbaum, S., and Parker, K. H., (1975), "The laminar decay of suddenly blocked channel and pipe flows". J. Fluid Mech., 69, 729–752.
14. Ghidaoui, M. S., and Kolyshkin, A. A., (2002), "A quasi-steady approach to the instability of time dependent flows in pipes", J. Fluid Mech., 465, 301–330.
15. Kolyshkin, A. A., and Vaillancourt, R., (2001), "Asymptotic solution for unsteady viscous flow in a plane channel", Latvian J. of Physics and Technical Sciences, no. 3, 12–19.
16. Kolyshkin, A. A., and Volodko, I., (2002), "Transient viscous flow in an annulus", 7th International Conference on Mathematical Modelling and Analysis MMA2002, May 31 – June 2, 2002, Kaäriku, Estonia.
17. Canuto, C., Hussaini, M. Y., Quarteroni, A., and Zang, T. A., (1988), "Spectral methods in fluid dynamics", Springer, New York.
18. Heinrichs, W., (1989), "Improved condition number for spectral methods". Math. of Computations, 53, 103–119.

PART 3

Biomechanics

This page is intentionally left blank

CHAPTER 8

MECHANICAL MODELS OF THE DEVELOPMENT OF GLAUCOMA

Svetlana M. Bauer

Department of Hydroelasticity, St. Petersburg State University, St. Petersburg, Russia, 198504
E-mail: s_bauer@mail.ru

The different mechanical aspects of the development of glaucomatous atrophy of the optic nerve fibres are considered. It is known that the site of damage of nerve fibres under glaucoma is the scleral lamina cribrosa (LC). From the mechanical point of view the LC is a circular perforated plate, which is weakened by many pores.

In the first case, the LC is modelled as a continuous nonuniform anisotropic plate. The calculations of the stresses and deformations in the LC show that the shear deformation of the vertical element of the LC could cause the atrophy of the optic nerve fibres. The solutions for LC with different degrees of nonuniformity can help reveal the structure of the LC, for which the glaucomatous damage is most probable to develop.

The LC consists of a few parallel layers of connective tissue. In the second model, large axisymmetric deformations of multilayer momentless (membrane) shell of revolution with elastic ties between the layers are considered. The numerical solution of this problem reveals that, if the intraocular pressure increases, the essential shear of the layers occurs at the periphery of the LC. This phenomenon may also leads to the atrophy of the optic nerve fibres.

Buckling in the nonaxisymmetric state in the neighborhood of the edge could also cause edemas at the periphery of the LC and the atrophy of the optic nerve fibres.

8.1. Introduction

What exactly causes optic nerve damage in glaucoma is still an open problem. From the points of view of some scholars, after A. von Graefe (1857), mechanical genesis of this atrophy should be generally admitted. Among the

adherents to this conception there are such scholars as J. Emery, D. Minckler and V. V. Volkov [Volkov (2001)][12]. However, other scientists, namely E. Jaeger and his followers, think that the disease is of a sciatical (vascular) nature. D. O. Harington, A. P. Nesterov [Nesterov (1995)][6] also agree with the conception of vascular glaucoma genesis. Both conceptions are currently held. In fact, the adherents to the sciatical nature of glaucoma also admit the "role of mechanical factor" [Nesterov (1995)][6]. This is why it is important to consider the mechanical models of the development of glaucoma.

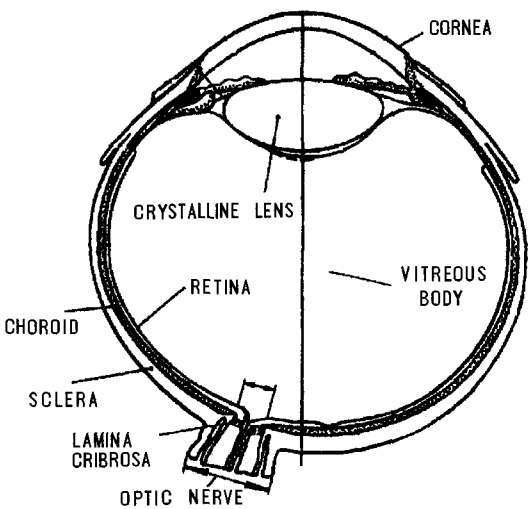

Fig. 8.1. Meridional section of the eye

The form of the eye is determined by the outer shell, the sclera. The Lamina Cribrosa (LC) is a part of sclera, where the optic nerve fibers pass through (Fig. 8.1) and where the layer of sclera becomes thinner and many (more than 400) little pores appear. LC plays an important role in the balance of intraocular and intraskull pressure. In normal conditions, the pressure on LC from the inside (intraocular pressure) is higher than the intraskull pressure. And it is known that under glaucoma the visual field changes due to dystrophy and then atrophy of the optic nerve fibres, which are deformed just at the level of LC [Nesterov (1995)][6], [Quigley and Ad-

dicks (1981)][10], [Quigley and Addicks (1982)][11], [Volkov (2001)][12]. In 1996, in Canada a new method of glaucoma treatment was proposed. It is based on the synthesis of biopolymers, which strengthen LC [Kanagalingam and Shoichet (1996)][7]. The polymer is introduced into the bottom of the optic nerve. After the final polymerization it solidifies and keeps the nerve safe from mechanical influences of increased pressure.

For ophthalmologists it is important to know how to predict if a patient is at risk of developing a damage before the damage occurs. That is why it is essential to understand the mechanical response of the LC to elevate intraocular pressure and this makes the analysis of the deformations of the LC important. The deformation of the LC was addressed in [Dongi and Zeqin (1999)][4], where the LC is considered to be uniform and isotropic. The authors attempted to take the influence of the tensile forces into account since these forces affect the LC from the scleral shell of the eye. This effect is not essential, because the LC is much softer ($E/E_1 \simeq 10$) and 4 to 5 times thinner than the sclera. Beside this, in [Dongi and Zeqin (1999)][4] it was supposed that at the edge the stress in the LC is equal to the stress in the scleral shell. In fact we should make equal not the stresses, but the resultants, since the problem is considered to be 2D. Experimental research has revealed that an increased pressure [Yan *et al.* (1994)][13] does not cause an increase in the size of the scleral canal through which the optic nerve passes (diameter of the LC). Beside this, in [Bauer *et al.* (2001)][2] the deformations obtained with two models: the shell structure (sclera and LC) and the LC alone was compared. In both models the structures were subjected to normal pressure. The effect of the increase of the scleral ring and also the effect of the deformations of the scleral eye shell on the deflections of the LC were studied. The comparison of the results obtained for the combined shells and for the simplified structures, where the effect of the scleral shell on the LC is neglected, shows that the difference in the maximal deflection values of the LC is not more than 2%. So, presumably, the deformation of the LC may be analyzed separately from the deformation of the scleral shell. Such approach helps to take the peculiarities of the structure of the LC into account.

LC has a circular or, in some eyes, a slightly oval form. The average diameter of the LC is 1.5–2 mm [Nesterov (1995)][6], [Volkov (2001)][12]. Experimental research shows that the variations in the disc size of the LC is correlated with the variations in the diameters of the eyes and that the size of the LC has no influence on the risk of glaucomatous damage [Papastathopoulous *et al.* (1995)][9].

The eyes of most people have LCs with density of the pores increasing at the periphery of LC, but in some eyes these pores are arranged uniformly. Besides that, the investigation made by ophthalmologists shows that the superior and inferior parts of the LC often contain larger pores and thinner tissue support for the passage of nerve-fiber bundles than the nasal-temporal parts of the LC [Quigley and Addicks (1981)][10], [Quigley and Addicks (1982)][11], [Yan *et al.* (1994)][13], [Yan *et al.* (1998)][14]. LC is modelled as a continuous transversal isotropic plate with clamped edges. The equations for such plate contain reduced parameters [Grigolyuk and Filshtinskii (1970)][5]. The main problem in the analytical evaluations of the deformations of the LC is the lack of precise data on the mechanical nature of the LC. Some research data on the average depth of the optic disk cupping under fixed values of the intraocular pressure [Quigley and Addicks (1982)][11], and experimental data of special research [Yan *et al.* (1994)][13], [Yan *et al.* (1998)][14], permit to estimate the reduced modulus of elasticity for the LC. If microtubuli (pores) uniformly cover the entire plate, then we can assume the modulus of elasticity to be constant. In the general case, we consider a nonuniform plate and suppose that in the plane of the plate the modulus of elasticity is determined as

$$E(r,\theta) = E_1(r) + E_2(r)\cos 2\theta, \tag{1}$$

where r, θ are polar coordinates. The functions $E_1(r)$ and $E_2(r)$ decrease away from the center.

Below, the deflection of the LC under a uniform normal pressure is studied by means of the linear and nonlinear Ambartsumyan theory of plate [Ambartsumian (1987)][1].

8.2. Deformations of LC. Linear Theory

We suppose that the LC is a transversal isotropic plate [Ambartsumian (1987)][1]:

$$\begin{aligned}
e_r &= \frac{1}{E_1}\sigma_r - \frac{\nu}{E_1}\sigma_\theta - \frac{\nu'}{E_2}\sigma_z, \qquad e_{rz} = \frac{\tau_{rz}}{G'},\\
e_\theta &= \frac{1}{E_1}\sigma_\theta - \frac{\nu}{E_1}\sigma_r - \frac{\nu'}{E_2}\sigma_z, \qquad e_{\theta z} = \frac{\tau_{\theta z}}{G'},\\
e_z &= \frac{1}{E_2}\sigma_z - \frac{\nu''}{E_1}\sigma_r - \frac{\nu''}{E_1}\sigma_\theta, \qquad e_{r\theta} = \frac{\tau_{r\theta}}{G},\\
\nu'' E_2 &= \nu' E_1, \qquad G = \frac{E_1}{2(1+\nu)},
\end{aligned} \tag{2}$$

where σ_r, σ_θ, σ_z, τ_{rz}, $\tau_{\theta z}$, and $\tau_{r\theta}$ are the stresses and e_r, e_{rz}, e_θ, $e_{\theta z}$ e_z, and $e_{r\theta}$ are the deformations in the polar coordinates.

The lower and upper surfaces of the plate are loaded by the uniform intraocular, p^-, and intraskull, p^+, pressures:

$$\sigma_z = -p^- \quad \tau_{rz} = \tau_{\theta z} = 0 \quad \text{for} \quad z = -\frac{h}{2},$$
$$\sigma_z = -p^+ \quad \tau_{rz} = \tau_{\theta z} = 0 \quad \text{for} \quad z = \frac{h}{2}.$$

According to Ambartsumyan's theory, we assume

$$e_z = 0, \quad \tau_{rz} = \frac{1}{2}\left(\frac{h^2}{4} - z^2\right)\varphi(r), \quad \tau_{\theta z} = \frac{1}{2}\left(\frac{h^2}{4} - z^2\right)\psi(r), \tag{3}$$

where h is the thickness of LC, $\varphi(r,\theta)$ and $\psi(r,\theta)$ are the force functions in r, θ, and

$$u_z = w(r),$$
$$u_r = u - z\frac{\partial w}{\partial r} + \frac{z}{2}\left(\frac{h^2}{4} - \frac{z^2}{3}\right)\frac{\varphi(r,\theta)}{G'},$$
$$u_\theta = v - z\frac{\partial w}{r\partial\theta} + \frac{z}{2}\left(\frac{h^2}{4} - \frac{z^2}{3}\right)\frac{\psi(r,\theta)}{G'}.$$

Substituting these expressions into the elasticity relations and then into the equilibrium equations we obtain the system of differential equations for the functions u and v in the form

$$\begin{aligned}
&C(r,\theta)\left[\frac{\partial^2 u}{\partial r^2} + \frac{1}{r}\frac{\partial u}{\partial r} - \frac{u}{r^2} + \frac{(1-\nu)}{2r^2}\frac{\partial^2 u}{\partial\theta^2} + \frac{(1+\nu)}{2r}\frac{\partial^2 v}{\partial r\partial\theta} - \frac{(3-\nu)}{2r^2}\frac{\partial v}{\partial\theta}\right] \\
&\quad + \frac{\partial C}{\partial r}\left[\frac{\partial u}{\partial r} + \frac{\nu}{r}\left(\frac{\partial v}{\partial\theta} + u\right)\right] + \frac{(1-\nu)}{2r}\frac{\partial C}{\partial\theta}\left[\frac{1}{r}\frac{\partial u}{\partial\theta} + \frac{\partial v}{\partial r} - \frac{v}{r}\right] = 0, \\
&C(r,\theta)\left[\frac{(1+\nu)}{2r}\frac{\partial^2 u}{\partial r\partial\theta} + \frac{(3-\nu)}{2r^2}\frac{\partial u}{\partial\theta} + \frac{1}{r^2}\frac{\partial^2 v}{\partial\theta^2}\right] \\
&\quad + C(r,\theta)\left[\frac{(1-\nu)}{2}\left(\frac{\partial^2 v}{\partial r^2} + \frac{1}{r}\frac{\partial v}{\partial r} - \frac{v}{r^2}\right)\right] + (1-\nu)\frac{\partial C}{\partial r}\left[\frac{1}{r}\frac{\partial u}{\partial\theta} + \frac{\partial v}{\partial r} - \frac{v}{r}\right] \\
&\quad + \frac{1}{r}\frac{\partial C}{\partial\theta}\left[\frac{1}{r}\left(\frac{\partial v}{\partial\theta} + u\right) + \nu\frac{\partial u}{\partial r}\right] = 0,
\end{aligned} \tag{4}$$

where

$$C = \frac{E_1 h}{1-\nu^2}.$$

Similarly we obtain the system of differential equations for the functions w, φ and ψ,

$$
\begin{aligned}
&D(r,\theta)\left[\frac{\partial^3 w}{\partial r^3}+\frac{1}{r}\frac{\partial^2 w}{\partial r^2}+\frac{1}{r^2}\frac{\partial^3 w}{\partial r\partial\theta^2}-\frac{2}{r^3}\frac{\partial^2 w}{\partial\theta^2}-\frac{1}{r^2}\frac{\partial w}{\partial r}\right]\\
&\quad+\frac{\partial D}{\partial r}\left[\frac{\partial^2 w}{\partial r^2}+\frac{\nu}{r}\left(\frac{1}{r}\frac{\partial^2 w}{\partial\theta^2}+\frac{\partial w}{\partial r}\right)\right]+\frac{(1-\nu)}{r^2}\frac{\partial D}{\partial\theta}\left[\frac{\partial^2 w}{\partial r\partial\theta}-\frac{1}{r}\frac{\partial w}{\partial\theta}\right]\\
&\quad-\frac{Dh^2}{10G'}\left[\frac{\partial^2\varphi}{\partial r^2}+\frac{1+\nu}{2r}\frac{\partial^2\psi}{\partial r\partial\theta}+\frac{1-\nu}{2r^2}\frac{\partial^2\varphi}{\partial\theta^2}-\frac{3-\nu}{2r^2}\frac{\partial\psi}{\partial\theta}+\frac{1}{r}\frac{\partial\varphi}{\partial r}-\frac{\varphi}{r^2}\right]\\
&\quad-\frac{\partial}{\partial r}\left(\frac{D}{G'}\right)\frac{h^2}{10}\left[\frac{\partial\varphi}{\partial r}+\frac{\nu}{r}\left(\varphi+\frac{\partial\psi}{\partial\theta}\right)\right]+\frac{\partial}{\partial r}\left[\frac{Dh^2}{10G'^2}\left(\frac{\partial G'}{\partial r}\varphi+\frac{\partial G'}{\partial\theta}\frac{\nu\psi}{r}\right)\right]\\
&\quad+\frac{1}{r}\frac{\partial}{\partial\theta}\left[\frac{Dh^2(1-\nu)}{20G'^2}\left(\frac{\partial G'}{\partial r}\psi+\frac{\partial G'}{\partial\theta}\frac{\varphi}{r}\right)\right]+\frac{Dh^2(1-\nu)}{10rG'^2}\left[\frac{\partial G'}{\partial r}\varphi-\frac{\psi}{r}\frac{\partial G'}{\partial\theta}\right]\\
&\quad-\frac{\partial}{\partial\theta}\left(\frac{D}{G'}\right)\frac{h^2(1-\nu)}{20r^2}\left[\frac{\partial\varphi}{\partial\theta}+r\frac{\partial\psi}{\partial r}-\psi\right]+\frac{h^3\varphi}{12}=0,\\
&\frac{\partial\varphi}{\partial r}+\frac{\varphi}{r}+\frac{1}{r}\frac{\partial\psi}{\partial\theta}=-\frac{12P}{h^3},\qquad(5)\\
&D(r,\theta)\left[\frac{1}{r^2}\frac{\partial^2 w}{\partial r\partial\theta}+\frac{1}{r}\frac{\partial^3 w}{\partial r^2\partial\theta}+\frac{1}{r^3}\frac{\partial^3 w}{\partial\theta^3}\right]+\frac{\partial D}{\partial r}\frac{(1-\nu)}{r}\left[\frac{\partial^2 w}{\partial r\partial\theta}-\frac{1}{r}\frac{\partial w}{\partial\theta}\right]\\
&\quad+\frac{1}{r}\frac{\partial D}{\partial\theta}\left[\frac{1}{r^2}\frac{\partial^2 w}{\partial\theta^2}+\frac{1}{r}\frac{\partial w}{\partial r}+\nu\frac{\partial^2 w}{\partial r^2}\right]+\frac{1}{r}\frac{\partial}{\partial\theta}\left[\frac{Dh^2}{10G'^2}\left(\frac{\partial G'}{\partial\theta}\frac{\psi}{r}+\nu\varphi\frac{\partial G'}{\partial r}\right)\right]\\
&\quad-\frac{Dh^2}{10G'}\left[\frac{1+\nu}{2r}\frac{\partial^2\varphi}{\partial r\partial\theta}+\frac{3-\nu}{2r^2}\frac{\partial\varphi}{\partial\theta}+\frac{1}{r^2}\frac{\partial^2\psi}{\partial\theta^2}+\frac{1-\nu}{2}\left(\frac{1}{r}\frac{\partial\psi}{\partial r}-\frac{\psi}{r^2}+\frac{\partial^2\psi}{\partial r^2}\right)\right]\\
&\quad+\frac{\partial}{\partial r}\left[\frac{Dh^2(1-\nu)}{20G'^2}\left(\frac{\partial G'}{\partial\theta}\frac{\varphi}{r}+\psi\frac{\partial G'}{\partial r}\right)\right]+\frac{Dh^2(1-\nu)}{10G'^2}\left(\frac{\varphi}{r}\frac{\partial G'}{\partial\theta}+\psi\frac{\partial G'}{\partial r}\right)\\
&\quad-\frac{\partial}{\partial r}\left(\frac{D}{G'}\right)\frac{h^2(1-\nu)}{10}\left[\frac{1}{2r}\frac{\partial\varphi}{\partial\theta}+\frac{1}{2}\frac{\partial\psi}{\partial r}-\frac{\psi}{2r}\right]\\
&\quad-\frac{\partial}{\partial\theta}\left(\frac{D}{G'}\right)\frac{h^2}{10r}\left[\frac{1}{r}\frac{\partial\psi}{\partial\theta}+\frac{\varphi}{r}+\nu\frac{\partial\varphi}{\partial r}\right]+\frac{h^3\psi}{12}=0
\end{aligned}
$$

where

$$D=\frac{E_1h^3}{12(1-\nu^2)},\qquad D_k=\frac{h^3G}{12}.$$

For a clamped circular plate, the following boundary conditions are imposed [Ambartsumian (1987)][1]:

$$u=0,\quad v=0,\quad w=0,\quad \frac{\partial w}{\partial r}=-\frac{h^2\varphi}{8G'},\quad \psi=0,\quad \text{at}\quad r=R.\qquad(6)$$

If the microtubuli uniformly cover the entire LC, then we can take the modulus of elasticity as constant. If $E_1 = \text{const}$ (and $D = \text{const}$) then systems (4)–(5) coincide with the systems for uniform transversal isotropic plate found in [Ambartsumian (1987)][1] and has the following solutions:

$$\begin{aligned} w = w_0(r) &= \frac{P}{64D}(r^2 - R^2)^2 + \frac{3P}{8G'h}(R^2 - r^2), \\ \varphi = \varphi_0 &= -\frac{6Pr}{h^3}, \quad u = u_0 = 0, \qquad (v \equiv 0, \qquad \psi \equiv 0). \end{aligned} \tag{7}$$

When the system of equations is linear one can separately evaluate the effect of the radial and angular non-uniformity and small deflections in the form of the plate.

8.2.1. *Axisymmetric deformation of the LC*

If the number of microtubuli (or their total area) increases radially towards the edge of the plate, then the modulus of elasticity decreases away from the center of the plate and it can be assumed, for example, that

$$E_1 = E\left(1 - \varepsilon_1 \frac{r}{R}\right). \tag{8}$$

If ε_1 is small, then one can use a perturbation method and seek the solution of the systems (4)–(5) in the following form:

$$\begin{aligned} u(r) &= u_0(r) + \varepsilon_1 u_1(r), \\ w(r) &= w_0(r) + \varepsilon_1 w_1(r), \\ \varphi(r) &= \varphi_0(r) + \varepsilon_1 \varphi_1(r). \end{aligned} \tag{9}$$

Substituting these expressions into the equilibrium equations and equating the coefficients of ε_1, we obtain a system of equations for u_1, w_1, and φ_1.

$$\begin{aligned} &\frac{d^2u_1}{dr^2} + \frac{1}{r}\frac{du_1}{dr} - \frac{u_1}{r^2} = 0, \\ &\frac{d\varphi_1}{dr} + \frac{\varphi_1}{r} = 0, \\ &\frac{d^3w_1}{dr^3} + \frac{1}{r}\frac{d^2w_1}{dr^2} - \frac{1}{r^2}\frac{dw_1}{dr} = r\left(\frac{d^3w_0}{dr^3} + \frac{1}{r}\frac{d^2w_0}{dr^2} - \frac{1}{r^2}\frac{dw_0}{dr}\right) \\ &\frac{d^2w_0}{dr^2} + \frac{\nu}{r}\frac{dw_0}{dr} - \left(\frac{h^2}{10G'}\right)\left[\frac{d\varphi_0}{dr} + \frac{\nu\varphi_0}{r}\right] - \frac{\varphi_1(1-\nu^2)}{E}. \end{aligned} \tag{10}$$

Taking boundary conditions into account, we may obtain the solution of system (10):

$$
\begin{aligned}
&u_1 = 0,\\
&\varphi_1 = 0,\\
&w_1(r) = \frac{P(1-\nu^2)(11+\nu)}{200Eh^3}(2r^5 - 5r^2R^3 + 3R^5)\\
&-\frac{P(1+\nu)}{24Eh^3}\left[1-\nu^2+\frac{Eh^2}{5G'}\left(1-\frac{5z_0^2}{3}\right)\right](2r^3 - 3r^2R + R^3).
\end{aligned}
\tag{11}
$$

Thus the solution of systems (4)–(5) has a form

$$
\begin{aligned}
&u(r) = O(\varepsilon_1^2);\\
&w(r) = w_0(r) + \varepsilon_1 w_1(r) + O(\varepsilon_1^2);\\
&\varphi(r) = -\frac{6Pr}{h^3} + O(\varepsilon_1^2);\\
&v(r) \equiv 0;\\
&\psi(r) \equiv 0.
\end{aligned}
\tag{12}
$$

We recall that $O(\varepsilon_1^2)$ means that the order of this term is not larger than ε_1^2.

It is convenient to introduce dimensionless variables by the following formulas

$$
\rho = \frac{r}{R}, \quad \hat{w} = \frac{w}{h}\frac{E_{\text{av}}}{P(1-\nu^2)}\frac{h^4}{R^4}, \quad K = \frac{E_{\text{av}}}{G'}\frac{h^2}{R^2(1-\nu^2)}, \tag{13}
$$

where E_{av} is the constant average value of the modulus of elasticity. Then for a uniform plate

$$
\hat{w}_0 = \frac{3}{16}\left[(1-\rho^2)^2 + 2K(1-\rho^2)\right] \tag{14}
$$

and for small value ε_1 for a nonuniform plate of the same average elasticity

$$
\int_0^1 E(r) r dr = \text{const}, \quad E = \frac{E_{1av}}{1 - 2/3\varepsilon_1}
$$

and

$$
\begin{aligned}
\hat{w}_{\text{nonun}} &= \frac{3}{16}\left[(1-\rho^2)^2 + 2K(1-\rho^2)\right]\\
&+ \frac{\varepsilon_1}{8}\left[\frac{11+\nu}{25}(2\rho^5 - 5\rho^2 + 3) - \frac{1+\nu}{3}\left(1+\frac{K}{5}\right)(2\rho^3 - 3\rho^2 + 1)\right].
\end{aligned}
$$

For ε_1 small, the value of the deflection of the uniform and nonuniform plates are close to each other, but in the neighborhood of the edge (for $\rho > \rho_*$) the deflection of the nonuniform plate is larger. For example, for $K = 0.6$ and $\nu = 0.4$, the value ρ_*=0.491.

Real LC usually has significantly more pores in the neighborhood of the edge then in the center (see [Quigley and Addicks (1981)][10], [Quigley and Addicks (1982)][11]). To examine the effect of the non-uniformity of the LC on the shape of the deflection of the plate we suppose that

$$E = \hat{E}e^{-q\rho}.$$

We have solved the corresponding problems numerically for different values of $\hat{E}$ and q but for the constant average value of the modulus of elasticity E_{av}, i.e.

$$\hat{E} = \frac{q^2 E_{\text{av}}}{2\,(1 - e^{-q}(1+q))}.$$

Since the modulus of elasticity in the middle of the plate could not be larger than the modulus of elasticity of the sclera for real material, $\hat{E} < 10E_{\text{av}}$ and $q < 4.31$.

The equation for the non-dimensional deflection in this case is

$$\frac{d^3\hat{w}}{d\rho^3} + \frac{1}{\rho}\frac{d^2\hat{w}}{d\rho^2} - \frac{1}{\rho^2}\frac{d\hat{w}}{d\rho} - q\left[\frac{d^2\hat{w}}{d\rho^2} + \frac{\nu}{\rho}\frac{d\hat{w}}{d\rho}\right] = \frac{12\rho e^{q\rho}(1 - e^{-q}(1+q))}{q^2} + \frac{3qK(1+\nu)}{5}.$$

The boundary conditions in non-dimensional variables has the form

$$\rho = 1, \qquad \hat{w} = 0, \qquad \frac{d\hat{w}}{dr} = -\frac{3}{4}K.$$

Estimates show that, for small q (similar when ε_1 is small), the deflection in the middle of the plate is less than the deflection of the equivalent uniform plate, but in the neighborhood of the edge (for $\rho > \rho_*$) the deflection of the nonuniform plate becomes larger. In Fig. 8.2 the displacements $\hat{w}$ for the uniform plate (1) and the nonuniform plate (2) with $q = 2$ are shown. In this case $\rho_* = 0.45$.

If the parameter of non-uniformity, q, increases, then the value of ρ_* decreases and $\rho_* = 0$ for $q = 3.95$. For $q > 3.95$ the deflection of the nonuniform plate is larger than the deflection of the equivalent uniform plate for all ρ.

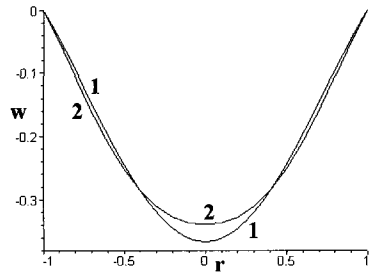

Fig. 8.2. The deflections of uniform plate and nonuniform plate with $q = 2$

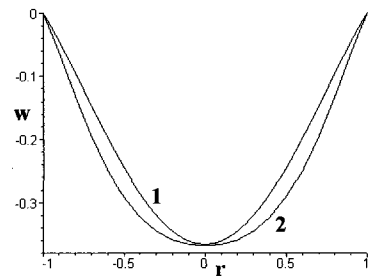

Fig. 8.3. The deflections of uniform and nonuniform plates with $q = 4$

In Fig. 8.3 the displacement $\hat{w}$ of the uniform plate (1) and the nonuniform plate (2) with $q = 4$ are shown.

Thus, one can see, that increasing the parameter of non-uniformity leads to an increase in the deflection of the plate.

8.2.2. *Nonaxisymmetric deformation of the LC*

If we take into account that the superior and inferior parts of the LC contain larger pores [Quigley and Addicks (1981)][10], [Quigley and Addicks (1982)][11], we can suppose that

$$E_1 = E(1 + \varepsilon_2 \cos 2\theta)$$

If ε_2 is small, then using a perturbation method, we can seek the solution of systems (4)–(5) in the form

$$\begin{aligned} u(r,\theta) &= \varepsilon_2 u_2(r)\cos 2\theta, \\ v(r,\theta) &= \varepsilon_2 v_2(r)\sin 2\theta, \\ w(r,\theta) &= w_0(r) + \varepsilon_2 w_2(r)\cos 2\theta, \\ \varphi(r,\theta) &= \varphi_0(r) + \varepsilon_2 \varphi_2(r)\cos 2\theta, \\ \psi(r,\theta) &= \varepsilon_2 \psi_2(r)\sin 2\theta. \end{aligned} \tag{15}$$

Substituting these expressions into the equilibrium equations (4) and equating the coefficients of ε_2 we obtain a system of equations for u_2 and v_2. Taking the boundary conditions into account, the solution of this system appears to be $u_2 = 0$ and $v_2 = 0$.

Substituting expressions (15) into the equilibrium equations (5) and equating the coefficients of ε_2, we obtain a system of equations. From the second equation

$$\frac{d\varphi_2}{dr} + \frac{\varphi_2}{r} + \frac{2\psi_2}{r} = 0,$$

we obtain

$$\psi_2 = -\frac{1}{2}\left(\frac{d\varphi_2}{dr}r + \varphi_2\right). \tag{16}$$

By (16) two other equations in dimensionless form similar to (13),

$$\hat{w}_2 = \frac{\bar{w}_2 E_{\mathrm{av}} \bar{h}^3}{P(1-\nu^2)}, \quad \hat{\varphi}_2 = \frac{\bar{\varphi}_2 \bar{h}^3}{\bar{P}}, \quad \hat{\psi}_2 = \frac{\bar{\psi}_2 \bar{h}^3}{\bar{P}}$$

yield

$$\begin{aligned} &\frac{d^3\hat{w}_2}{d\rho^3} + \frac{1}{\rho}\frac{d^2\hat{w}_2}{d\rho^2} - \frac{5}{\rho^2}\frac{d\hat{w}_2}{d\rho} + \frac{8\hat{w}_2}{\rho^3} + 6\rho \\ &\qquad + \hat{\varphi}_2 - \frac{K(1-\nu)}{20}\left[\frac{d^2\hat{\varphi}_2}{d\rho^2} + \frac{3}{\rho}\frac{d\hat{\varphi}_2}{d\rho} - \frac{3\hat{\varphi}_2}{\rho^2}\right] = 0, \\ &\frac{d^2\hat{w}_2}{d\rho^2} + \frac{1}{\rho}\frac{d\hat{w}_2}{d\rho} - \frac{4\hat{w}_2}{\rho^2} + \frac{1}{\rho}\frac{d\hat{w}_0}{d\rho} + \nu\frac{d^2\hat{w}_0}{d\rho^2} \\ &\qquad + \frac{3}{5}(1+\nu)K + \frac{\rho}{4}\left(\frac{d\hat{\varphi}_2}{d\rho}\rho + \hat{\varphi}_2\right) \\ &\qquad - \frac{K(1-\nu)}{80}\left[\frac{d^3\hat{\varphi}_2}{d\rho^3}r^2 + 4\frac{d^2\hat{\varphi}_2}{d\rho^2}\rho - 3\frac{d\hat{\varphi}_2}{d\rho} + \frac{3\hat{\varphi}_2}{\rho}\right] = 0. \end{aligned} \tag{17}$$

The boundary conditions for $\hat{\varphi}_2$ and $\hat{w}_2$ are

$$\frac{d\hat{\varphi}_2}{d\rho}(1) + \hat{\varphi}_2(1) = 0, \quad \hat{w}_2(1) = 0, \quad \frac{d\hat{w}_2}{d\rho}(1) = \frac{K}{8}\hat{\varphi}_2(1). \tag{18}$$

Here we introduce the new variables

$$\begin{aligned} F_1 &= \frac{d^2\hat{w}_2}{d\rho^2} + \frac{1}{\rho}\frac{d\hat{w}_2}{d\rho} - \frac{4\hat{w}_2}{\rho^2} \\ F_2 &= \hat{\varphi}_2 - \frac{K(1-\nu)}{20}\left[\frac{d^2\hat{\varphi}_2}{d\rho^2} + \frac{3}{\rho}\frac{d\hat{\varphi}_2}{d\rho} - \frac{3\hat{\varphi}_2}{\rho^2}\right], \end{aligned} \tag{19}$$

and system (17) transforms to

$$\frac{dF_1}{d\rho} + 6\rho + F_2 = 0,$$

$$F_1 + \frac{\rho^2}{4}\left(\frac{dF_2}{d\rho} + \frac{F_2}{\rho}\right) = -\frac{1}{\rho}\frac{d\hat{w}_0}{d\rho} - \nu\frac{d^2\hat{w}_0}{d\rho^2} - \frac{3(1+\nu)K}{5}.$$

Substituting $\hat{w}_0$ from (14) in the above equations we find

$$F_1 = -\frac{9(1-\nu)}{4}\rho^2 \ln r + \frac{3(1+\nu)}{4}\left(1 + \frac{K}{5}\right) + \hat{C}_1\rho^2 + \frac{\hat{C}_2}{\rho^2},$$

where $\hat{C}_1$ and $\hat{C}_2$ are arbitrary constants and

$$\begin{aligned} \hat{w}_2 = -\frac{3P(1-\nu)}{16}\rho^4 \ln\rho + \frac{3(1+\nu)}{16}\left(1 + \frac{K}{5}\right)\rho^2 \ln\rho \\ + C_1\rho^4 + C_2\rho^2 + C_3 + \frac{C_4}{\rho^2}. \end{aligned} \tag{20}$$

Here C_1, C_2, C_3, C_4 are constants to be determined from the boundary conditions. The function $\hat{w}_2$ must be bounded and, therefore, $C_4 = 0$. Since $w_2(0) = 0$ then $C_3 = 0$. Taking the equality $w_2(1) = 0$ into account, we obtain

$$\hat{w}_2 = -\frac{3(1-\nu)}{16}\rho^4 \ln\rho + \frac{3(1+\nu)}{16}\left(1 + \frac{K}{5}\right)\rho^2 \ln\rho + C_1\rho^2(\rho^2 - 1). \tag{21}$$

The constant C_1 may be determined after we find the function $\hat{\varphi}_2$. By equations (19)

$$F_2 = \frac{9}{2}(1-\nu)\rho \ln\rho - 3\rho\left(\frac{1+7\nu}{4} + 8C_1\right).$$

Then, by (18)

$$\hat{\varphi}_2 = \frac{9(1-\nu)}{2}\left[\rho\ln\rho + \frac{K(1-\nu)}{5\rho} - \frac{K^2(1-\nu)^2}{25\rho^3}\right] 3\rho\left(\frac{1+7\nu}{4} + 8C_1\right)$$
$$+ \frac{\tilde{C}_2}{\rho} I_2(\alpha\rho) + \frac{\tilde{C}_3}{\rho} K_2(\alpha\rho), \qquad \alpha = \sqrt{\frac{20}{K(1-\nu)}},$$

where $\tilde{C}_2$ and $\tilde{C}_3$ are arbitrary constants, $I_2(z)$ and $K_2(z)$ are modified Bessel functions, which are solutions of the equation

$$z^2\frac{d^2y}{dz^2} + z\frac{dy}{dz} - (z^2+4)y = 0.$$

In the neighborhood of zero, the functions $I_2(z)$ and $K_2(z)$ have the expansions:

$$K_2(z) = \frac{2}{z^2} - \frac{1}{2} - I_2(z)\ln\frac{\gamma z}{2} + \frac{1}{2}\sum_{i=0}^{\infty}\frac{1}{i!(i+2)!}\left(\frac{z}{2}\right)^{2(i+1)}\left(\sum_{l=1}^{i}\frac{1}{l} + \sum_{l=1}^{i+2}\frac{1}{l}\right)$$

$$I_2(z) = \left(\frac{z}{2}\right)^2\sum_{i=0}^{\infty}\frac{1}{i!(i+2)!}\left(\frac{z}{2}\right)^{2i}, \quad \gamma = 1.781.$$

Hence in the neighborhood of zero, the function $\dfrac{K_2(\alpha\rho)}{\rho}$ may be represented as

$$\frac{K_2(\alpha\rho)}{\rho} = \frac{1}{2\rho}\left[\frac{K(1-\nu)}{5\rho^2} - 1\right] + O(\rho).$$

Since the function $\varphi_2(\rho)$ is bounded at zero, then

$$\tilde{C}_3 = \frac{9(1-\nu)^2K}{5}.$$

The constants C_1 and $\tilde{C}_2$ should be determined from the boundary conditions (18).

Figure 8.4 shows the displacements of the transversal isotropic (a) ($K = 0.6$) and isotropic nonuniform (b) plates ($\varepsilon_2 = 0.4$) under normal pressure. The transversal isotropic plates have smoother surfaces in a neighborhood of the clamped edges.

The results obtained with the asymptotic relations have been compared with those obtained with FEM ADINA (900 nodes). Calculations were made for plates with real parameters [Nesterov (1995)][6], [Quigley and Addicks (1981)][10], [Quigley and Addicks (1982)][11], $h = 0.24\,\text{mm}$, $R = 1\,\text{mm}$, $E = 1.4\,\text{MPa}$, and $E/G' = 5$. The difference in results is less than 2%.

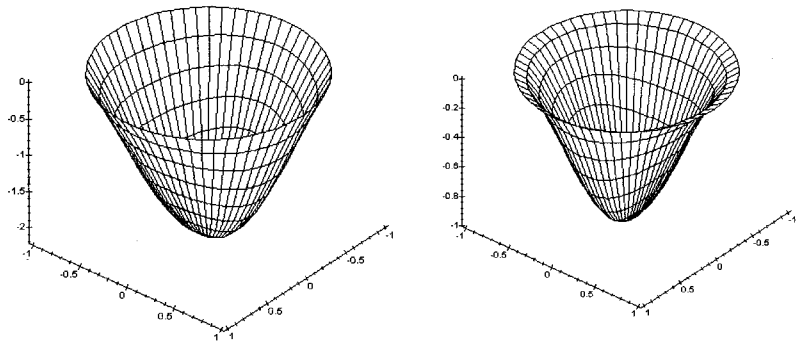

Fig. 8.4.

In Figs. 8.5 and 8.6, the cross-section area of the deformed plate obtained with FEM ADINA for $\theta = 0$ and $\theta = \pi/2$ is plotted.

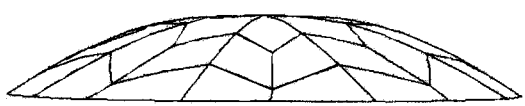

Fig. 8.5. The section $\theta = 0$ of the deformed plate.

Fig. 8.6. The section $\theta = \pi/2$ of the deformed plate.

In Fig. 8.7, the lines $\varphi = \text{const}$ for $\varepsilon_2 = 0.5$ are shown. These results agree well with the ophthalmological data [Nesterov (1995)][6], [Volkov (2001)][12]. In Fig. 8.8 there is a picture from a medical textbook showing the effect of the narrowing of the field of vision under glaucoma.

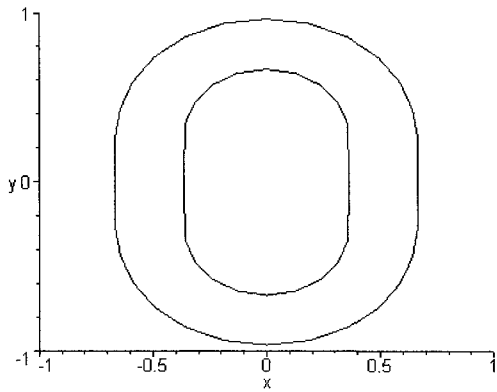

Fig. 8.7. $\varphi = const$ for $\varepsilon_2 = 0.5$

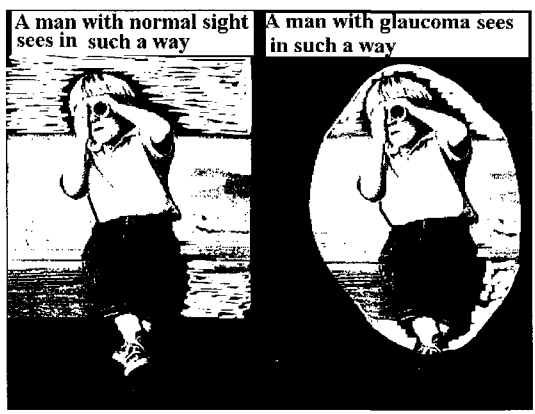

Fig. 8.8. Narrowing of the field of vision under glaucoma

Comparing Fig. 8.7 and Fig. 8.8, one sees that, apparently, the atrophy of the optic nerve takes place when the tangent stresses reach some critical values. This relates to the change in the field of vision under glaucoma. It confirms the mechanical genesis of glaucoma and shows that a larger non-uniformity of the LC leads to a stronger predisposition to glaucomatous damage.

8.2.3. *Deformation of the oval LC*

According to ophthalmologic data, the LC in some eyes could have an oval form. The difference between the vertical and horizontal diameters may reach 10% of the average value of the radius. Modelling the LCs of different forms but constant area can help reveal the shape of the LC, for which glaucomatous damage is most probable.

If the boundary of the LC has the form

$$\rho_e = 1 - \varepsilon_3 \cos 2\theta, \tag{22}$$

where ε_3 is a small parameter, then in the boundary conditions one should replace $\dfrac{\partial}{\partial \rho}$ with $\dfrac{\partial}{\partial n}$. Here n is the normal to the boundary. By (22), in non-dimensional variables,

$$\frac{\partial}{\partial n} = \frac{\partial}{\partial \rho} - \varepsilon_3 \cos 2\theta \frac{\partial}{\partial \rho} - \frac{2\varepsilon_3 \sin 2\theta}{\rho} \frac{\partial}{\partial \theta},$$

and the solution of equations (4)–(5) may be represented in the form of (15) where ε_2 is replaced with ε_3. Again we introduce new variables similar to (19) and obtain

$$\frac{dF_1}{d\rho} + F_2 = 0,$$

$$F_1 + \frac{\rho^2}{4}\left(\frac{dF_2}{d\rho} + \frac{F_2}{\rho}\right) = 0.$$

From the first of these equations, we can evaluate F_2 and then, from the second equation,

$$F_1 = \hat{C}_1 \rho^2 + \frac{\hat{C}_2}{\rho^2},$$

or

$$\hat{w}_2 = C_1 \rho^4 + C_2 \rho^2 + C_3 + \frac{C_4}{\rho^2},$$

where C_1, C_2, C_3, and C_4 are arbitrary constants.

Since the function $\hat{w}_2$ should be bounded and $w_3(0) = 0$, then $C_4 = C_3 = 0$. From the condition $\hat{w}(1 - \varepsilon_3 \cos 2\theta) = 0$ we get

$$C_2 = -\frac{3}{4}K - C_1.$$

The constant C_1 could be obtained as soon as one knows the function $\hat{\varphi}_2$. By (19) $F_2 = -4C_1\rho$ and hence

$$\hat{\varphi}_3 = -24C_1\rho + \frac{\tilde{C}_2}{\rho} I_2(\alpha\rho) + \frac{\tilde{C}_3}{\rho} K_2(\alpha\rho), \quad \alpha = \sqrt{\frac{20}{K(1-\nu)}},$$

where $\tilde{C}_2$ and $\tilde{C}_3$ are arbitrary constants. The function $\varphi_2(\rho)$ is bounded at zero; therefore, $\tilde{C}_3 = 0$. The constants C_1 and $\tilde{C}_2$ can be evaluated from the boundary conditions, which in this case have the forms

$$4w_2(1) = \frac{K}{8}\left(\varphi_2(1) + \varphi_2'(1)\right) \quad \text{or} \quad -48C_1 + \tilde{C}_2\alpha I_2'(\alpha) = -24,$$

$$\frac{\partial w}{\partial n}|_{\rho_g} = \frac{K\varphi}{8} \quad \text{or} \quad C_1(2+3K) = \frac{3}{2} + \frac{3K}{2} + \tilde{C}_2 I_2(\alpha)\frac{K}{8}.$$

Figure 8.9 shows the displacements of transversal isotropic: (a) ($K = 0.6$) and isotropic nonuniform, (b) plates ($\varepsilon_3 = 0.1$) under normal pressure.

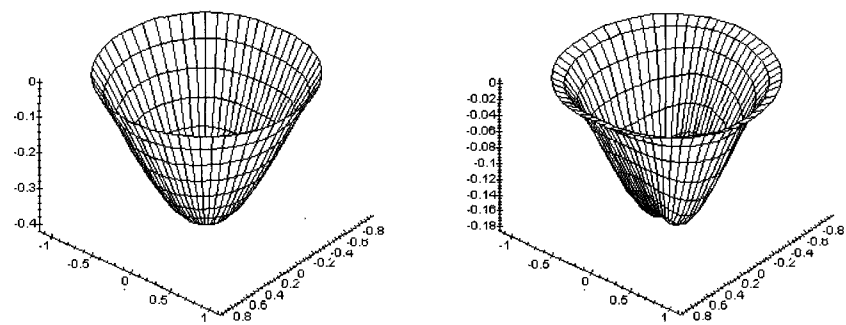

Fig. 8.9. Displacements of transversal isotropic: (a) ($K = 0.6$) and isotropic nonuniform, (b) plates ($\varepsilon_3 = 0.1$) under normal pressure

Calculations show that the influence of the shape of the LC (parameter ε_3) is less than the influence of the parameter ε_2 (provided $\varepsilon_2 = \varepsilon_3$), which characterizes the angular non-uniformity of the plate. As it was noted for the real LC parameter, ε_3 is smaller than the parameter ε_2. If the LC is oval (22), then the maximal displacements of the LC is $w(0) \approx W_r\left(1 - 6\varepsilon_3^2\right)$, where W_r is the maximal displacement of the corresponding circular LC. If the LC is oval, then the shear deformations of the LC are smaller. It seems that the eyes with an oval LC have a lower risk of developing glaucoma under ocular hypertension.

8.3. Shear of the Layers

According to ophthalmologic data [Nesterov (1995)][6], [Yan *et al.* (1994)][13], the LC consists of a few parallel layers of connective tissue. The number of layers varies widely from eye to eye. The holes in the layers form little channels for the nerve fibres. The outer layer is the thickest one. We analyze the large axisymmetric deformations of multilayer momentless (membrane) shell of revolution with elastic ties between the layers [Bauer *et al.* (2000)][3]. It is assumed that the shape of the LC before deformation is given by the functions $r_0(s_0)$, $z(s_0)$, and $\varphi_0(s_0)$, where s_0 is the arclength from the shell apex, r_0 is the distance between the shell surface and the axis of revolution, z_0 is the vertical coordinate, φ_0 is the angle between the normal to the shell and the axis of revolution, and

$$r_0' = \cos\varphi_0, \quad z_0' = \sin\varphi_0, \quad (\cdot)' \equiv \frac{d(\cdot)}{ds_0}.$$

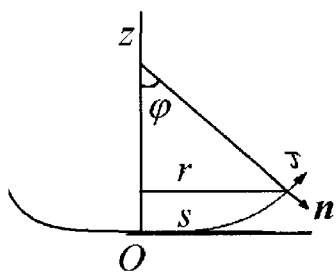

Fig. 8.10. Deformed LC.

After deformation the form of the LC is described by the functions (Fig. 8.10) $r(s)$, $z(s)$, and $\varphi(s)$, where

$$\frac{dr}{ds} = \cos\varphi, \quad \frac{dz}{ds} = \sin\varphi.$$

It is assumed that the layers can slide over each other. The functions $s_0^k(s)$ and $k = 1, 2, \ldots, n$ represent the arc coordinate of the point s on the k-th layer before the deformation. Then,

$$s_0^k(s) = \int_0^s \frac{ds}{\lambda_1^k}, \quad \lambda_2^k = \frac{r}{r_0^k}, \quad r_0^k = r_0(s_0^k), \quad k = 1, 2, \ldots, n,$$

where λ_1^k and λ_2^k are the tensile strains in the middle surface of the k-th layer in the meridional and circular directions.

The equilibrium equations for the k-th layer are

$$\begin{aligned} &\frac{d(rT_1^k)}{ds} - T_2^k \cos\varphi + r\left(q_1^{k-1} - q_1^k\right) = 0, \\ &\qquad\qquad\qquad\qquad\qquad\qquad\qquad\qquad k = 1, 2, \ldots, n, \\ &rT_1^k \frac{d\varphi}{ds} + T_2^k \sin\varphi - r\left(q_3^{k-1} - q_3^k\right) = 0, \end{aligned} \tag{23}$$

where T_1^k and T_2^k are the stress-resultants in the k-th layer measured per unit of length after deformation, q_1^i and q_3^i are the intensity of the external load on the deformed k-th layer measured per unit of area acting from the inner (q_1^{k-1} and q_3^{k-1}) and outer (q_1^k and q_3^k) surfaces of the layer (Fig. 8.11).

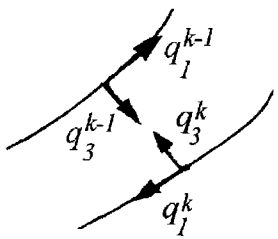

Fig. 8.11. The stress-resultants in the k-th layer

The functions q_1^0, q_3^0, q_1^n, and q_3^n are defined by the loads which act on the shell. We assume that the eye shell is under the intraocular (p_1) and retrolamina tissue (p_2) pressure. Then

$$q_1^0 = 0, \quad q_3^0 = p_1, \quad q_1^n = 0, \quad q_3^n = p_2.$$

The functions q_1^k, q_3^k, $k = 1, 2, \ldots, n-1$, are the tangential and normal interaction stresses in the shell layers, respectively. Tangential stresses are supposed to be functions of the relative displacements of the layers:

$$q_1^k = q_1^k(s, \Delta_k), \quad \Delta_k = s_0^{k+1} - s_0^k, \qquad k = 1, 2, \ldots, n-1.$$

The normal stresses q_3^k are obtained from the equilibrium equations.

Here we use the following elasticity relations for the eye shell material

$$T_1^k = \frac{E_p h_k}{1-\mu^2}\left(\varepsilon_1^k + \mu\varepsilon_2^k\right), \qquad \varepsilon_i^k = \lambda_i^k - 1, \quad i = 1,2;\ k = 1,2,\ldots,n, \tag{24}$$
$$T_2^k = \frac{E_p h_k}{1-\mu^2}\left(\varepsilon_2^k + \mu\varepsilon_1^k\right),$$

where h_k is the thickness of the k-th layer of the LC, E_p is the reduced Young's modulus of perforated layers of the LC.

Summarizing the equilibrium equations for each layer we write the equilibrium equations for the entire eye shell as

$$\begin{gathered} \frac{d(rT_1)}{ds} - T_2\cos\varphi = 0, \\ rT_1\frac{d\varphi}{ds} + T_2\sin\varphi - r\left(p_1 - p_2\right) = 0, \\ T_j = \sum_{k=1}^{n} T_j^k,\ j = 1,2, \end{gathered} \tag{25}$$

where T_j are the total stress-resultants. So, we get a system of $2n+2$ differential equations for the unknowns $T_1^k(s)$, $s_0^k(s)$, $\varphi(s)$, and $r(s)$.

Using dimensionless variables,

$$y_k = \frac{T_1^k(\bar{s})}{E_p h_k}, \quad y_{n+k} = \frac{s_0^k(\bar{s})}{r_*}, \quad y_{2n+1} = \varphi(\bar{s}), \quad y_{2n+2} = \frac{r(\bar{s})}{r_*},$$

we get the system

$$\begin{aligned} y_k' &= \left(\frac{y_k(\mu-1)}{y_{2n+2}} + \frac{1}{y_{n+k}} - \frac{1}{y_{2n+2}}\right)\cos y_{2n+1} + \left(\bar{q}_1^k - \bar{q}_1^{k-1}\right), \\ y_{n+k}' &= \left(1 + y_k(1-\mu^2) - \mu\left(\frac{y_{2n+2}}{y_{n+k}} - 1\right)\right)^{-1}, \\ y_{2n+1}' &= -\frac{\sin y_{2n+1}}{y_{2n+2}}\frac{T_2}{T_1} + \Delta\bar{p}, \\ y_{2n+2}' &= \cos y_{2n+1}, \qquad k = 1,2,\ldots,n, \end{aligned} \tag{26}$$

where $\bar{s} = \dfrac{s}{r_*}$, r_* is the radius of the edge parallel and

$$(\cdot)' \equiv \frac{d(\cdot)}{d\bar{s}}, \quad \bar{q}_1^k = \frac{q_1^k}{E_p h_k} \quad T_1 = E_p\sum_{k=1}^{n} h_k y_k,$$

$$T_2 = \mu T_1 + E_p\sum_{k=1}^{n} h_k\left(\frac{y_{2n+2}}{y_{n+k}} - 1\right), \quad \Delta\bar{p} = \frac{p_1 - p_2}{T_1}r_*.$$

The following boundary conditions are introduced in the dome apex:

$$s_0^k = r = \varphi = z = 0, \quad T_1^k = T_2^k \quad \text{at} \quad s = 0,$$

or, in dimensionless variables,

$$y_{k+n} = y_{2n+2} = y_{2n+1} = 0, \quad y'_{n+k} = \frac{1}{1 + y_k(1-\mu)} \text{ at } \bar{s} = 0.$$

The solution is bounded at the shell apex if the necessary condition $T_1^k = T_2^k$ holds.

The asymptotic analysis of the $(2n+1)$-st equation of the system shows that

$$y'_{2n+1} \to \Delta\bar{p}/2 \quad \text{as} \quad \bar{s} \to 0.$$

At the edge of the plate, conditions of elastic support are introduced for each layer,

$$T_1^k = c_k(s - s_0^k) \quad \text{at} \quad r = r_*.$$

The elastic moduli c_k may be different for different layers.

According to some ophthalmologic data [Nesterov (1995)][6], [Yan *et al.* (1994)][13], on the edge "outer" layer of lamina cribrosa, the boundary conditions are the strongest, i.e. $c_N > c_k$ for $k < N$. The stresses corresponding to the tangential displacements of the layers can be expressed in the form

$$q_1^k = \alpha_k(s_0^{k+1} - s_0^k)(r - r_*).$$

We solved the boundary problem numerically for shells with two and three layers with different values of the parameters c_k and α_k taking into account that the "outer" layer is the thickest one, i.e. $h_N > h_k$ for $k < N$.

The non-dimensional displacement of the LC is shown in Fig. 8.12 for $c_k/E_p = 0.03, k = 1, 2; c_3/E_p = 0.04$.

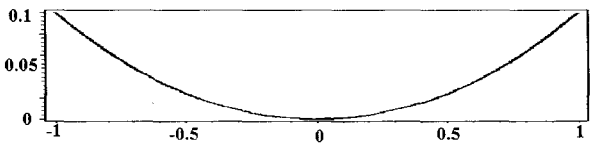

Fig. 8.12. Displacement of the LC

The results show that, if the intraocular pressure increases (or the retrolamina tissue pressure decreases), the essential shear of the layers occurs

at the periphery of the LC. And the largest shear is at the level of the last layer, as was observed by ophthalmologists [Nesterov (1995)][6], [Yan *et al.* (1994)][13]. This phenomenon may lead to the atrophy of the optic nerve fibres [Nesterov (1995)][6].

8.4. Buckling of the LC

Large deformation and buckling of the thin circular isotropic plates under normal pressure are considered in [Panov and Feodos'ev (1948)][8]. It was noted that under some critical load the buckling of the plate takes place near the edge of the plate. The buckling mode has eight waves (folds).

In fact, sometimes, in the case of glaucoma, the formation of small folds, oedemata, is observed near the edge of the LC [Nesterov (1995)][6], [Volkov (2001)][12]. This phenomenon also could be explained by the local buckling of the LC.

If we assume that LC is axisymmetric, then the large deformations of the LC are described by the following equations [Bauer *et al.* (2000)][3], [Ambartsumian (1987)][1], [Volkov (2001)][12],

$$
\begin{aligned}
&\frac{d}{dr}(\varphi r) + \frac{12}{h^3}\frac{d}{dr}\left(\frac{dw}{dr}\frac{dF}{dr}\right) = -\frac{12pr}{h^3},\\
&\frac{d^3F}{dr^3} + \frac{1}{r}\frac{d^2F}{dr^2} - \frac{1}{r^2}\frac{dF}{dr} = -\frac{E_1 h}{2r}\left(\frac{dw}{dr}\right)^2 - \frac{1}{E_1}\frac{dE_1}{dr}\left(\frac{d^2F}{dr^2} - \frac{\nu}{r}\frac{dF}{dr}\right),\\
&E_1(r)\left[\frac{d^3w}{dr^3} + \frac{1}{r}\frac{d^2w}{dr^2} - \frac{1}{r^2}\frac{dw}{dr}\right] + \frac{dE_1}{dr}\left[\frac{d^2w}{dr^2} + \frac{\nu}{r}\frac{dw}{dr}\right] \qquad (27)\\
&\quad = \frac{dE_1}{dr}\frac{h^2}{10G'}\left(\frac{d\varphi}{dr} + \frac{\nu\varphi}{r}\right) + \frac{h^2E_1}{10G'}\frac{d}{dr}\left(\frac{1}{r}\frac{d}{dr}(r\varphi)\right) - (1-\nu^2)\varphi(r),
\end{aligned}
$$

where $F = F(r)$ is the force function. The stress-resultants are expressed by means of the first and second derivatives of F:

$$T_r = \frac{1}{r}\frac{dF}{dr}, \qquad T_\theta = \frac{d^2F}{dr^2}.$$

The boundary conditions for the system of equations (27) has the form (6) similar to those for the linear system

$$r = R, \qquad w = 0, \quad \frac{dw}{dr} = \frac{h^2\varphi}{8G'},$$

and an additional condition is needed. This condition connects the stress-resultant T_r and the displacement in the radial direction u. We suppose

that the edge moves freely; therefore

$$T_r = \frac{1}{r}\frac{dF}{dr} = 0.$$

This boundary problem was analyzed by a perturbation method in [Ambartsumian (1987)][1].

To examine if a bifurcation of the LC is possible or not one should use nonlinear nonaxisymmetric equations [Ambartsumian (1987)][1]. If the buckling mode is localized near the edge of the LC, we write the equations for the uniform nonaxisymmetric plates [Ambartsumian (1987)][1] and seek the solution of these equations in the form

$$\begin{aligned} w &= w_0(r) + w_m(r)\cos m\theta, \\ F &= F_0(r) + F_m(r)\cos m\theta, \\ \varphi &= \varphi_0(r) + \varphi_m(r)\cos m\theta, \\ \psi &= \psi_m(r)\sin m\theta, \end{aligned}$$

where the prebuckling state of a plate w_0, F_0, φ_0 is obtained from the solution of system (27). After separation of variables, we get a linear system for the additional non-symmetrical components $w_m(r)$, $F_m(r)$, $\varphi_m(r)$, and $\psi_m(r)$. Taking

$$m^2 \gg 1, \quad \frac{d\varphi_m}{d\rho} \gg \varphi_m, \quad \frac{dw_m}{d\rho} \gg w_m, \quad \ldots,$$

into account, this system can be rewritten in dimensionless variables in the form

$$\begin{aligned} &\frac{1}{12}\left[\rho\frac{d\varphi_m^*}{d\rho} + m\psi_m^*\right] + \frac{dF_0^*}{d\rho}\frac{d^2w_m^*}{d\rho^2} - \frac{m^2w_m^*}{\rho}\frac{d^2F_0^*}{d\rho^2} \\ &\quad - \frac{m^2F_m^*}{\rho}\frac{d^2w_0^*}{d\rho^2} + \frac{dw_0^*}{d\rho}\frac{d^2F_m^*}{d\rho^2} = 0, \\ &\rho\frac{d^3w_m^*}{d\rho^3} - \frac{m^2}{\rho}\frac{dw_m^*}{d\rho} + (1-\nu^2)\varphi_m^*\rho \\ &\quad - \frac{h^*}{10}\left[\rho\frac{d^2\varphi_m^*}{d\rho^2} - \frac{m^2(1-\nu)\varphi_m^*}{2\rho} + \frac{m(1+\nu)}{2}\frac{d\psi_m^*}{d\rho}\right] = 0, \\ &\frac{m^3w_m^*}{\rho^2} - m\frac{d^2w_m^*}{d\rho^2} + (1-\nu^2)\psi_m^*\rho \\ &\quad + \frac{h^*}{10}\left[\frac{m^2\psi_m^*}{\rho} - \frac{1-\nu}{2}\rho\frac{d^2\psi_m^*}{d\rho^2} + \frac{(1+\nu)m}{2}\frac{d\varphi_m^*}{d\rho}\right] = 0, \\ &\frac{d^4F_m^*}{d\rho^4} - \frac{2m^2}{\rho^2}\frac{d^2F_m^*}{d\rho^2} + \frac{m^4F_m^*}{\rho^4} \end{aligned} \tag{28}$$

$$+\frac{1}{\rho}\left(\frac{dw_0^*}{d\rho}\frac{d^2w_m^*}{d\rho^2}-\frac{m^2}{\rho}\frac{d^2w_0^*}{d\rho^2}w_m^*\right)=0.$$

Here

$$\rho=\frac{r}{R},\quad w^*=\frac{w}{h},\quad F^*=\frac{F}{Eh^3},\quad h^*=\frac{Eh^2}{G'R^2},\quad \varphi^*=\frac{\varphi R^3}{Eh},\quad \psi^*=\frac{\psi R^3}{Eh}.$$

The boundary conditions for this system are

$$\begin{gathered}\rho=1 \qquad w_m^*=0,\quad \frac{dw_m^*}{d\rho}=\frac{h^*\varphi_m^*}{8},\\ T_{r_m}=\frac{1}{\rho}\frac{dF_m^*}{d\rho}-\frac{m^2}{\rho^2}F_m^*=0,\quad S_{r\theta_m}=\frac{m}{\rho^2}F_m^*-\frac{m}{\rho}\frac{dF_m^*}{d\rho}=0\end{gathered}\tag{29}$$

After the change of variables $x=\dfrac{1}{\rho}$, we finally get the system

$$\begin{aligned}&\frac{1}{12}\left[m\psi_m^*-x\frac{d\varphi_m^*}{dx}\right]+x^4f_1\frac{d^2w_m^*}{dx^2}-m^2xf_2w_m^*\\&\quad-m^2xf_4F_m^*+x^4f_3\frac{d^2F_m^*}{dx^2}=0,\\&\quad-x^6\frac{d^3w_m^*}{dx^3}+m^2x^4\frac{dw_m^*}{dx}+(1-\nu^2)\varphi_m^*\\&\quad-\frac{h^*x^2}{10}\left[x^2\frac{d^2\varphi_m^*}{dx^2}-\frac{m^2(1-\nu)}{2}\varphi_m^*-\frac{m(1+\nu)x}{2}\frac{d\psi_m^*}{dx}\right]=0,\\&mx^3\left(m^2w_m^*-x^2\frac{d^2w_m^*}{dx^2}\right)+(1-\nu^2)\psi_m^*\\&\quad+\frac{h^*x^2}{10}\left[m^2\psi_m^*-\frac{1-\nu}{2}x^2\frac{d^2\psi_m^*}{dx^2}-\frac{(1+\nu)mx}{2}\frac{d\varphi_m^*}{dx}\right]=0,\\&x^4\left(x^2\frac{d^2}{dx^2}-m^2\right)F_m^*+x^2\left[x^3f_3\frac{d^2w_m^*}{dx^2}-m^2f_4w_m^*\right]=0,\end{aligned}\tag{30}$$

where

$$\begin{aligned}f_1(x)&=\frac{dF_0^*}{d\rho}|_{\rho=1/x},\quad f_2(x)=\frac{d^2F_0^*}{d\rho^2}|_{\rho=1/x},\\f_3(x)&=\frac{dw_0^*}{d\rho}|_{\rho=1/x},\quad f_4(x)=\frac{d^2w_0^*}{d\rho^2}|_{\rho=1/x},\end{aligned}$$

and $f_i(x)$ are determined from the solution of system (27).

The functions ψ_m^*, φ_m^*, w_m^*, F_m^* should exist in the interval $[1,\infty)$ and quickly decrease as x moves away from the edge $x=1$.

Supposing that

$$w_m^* = C_1 e^{\int_1^x \lambda(t)dt}, \quad F_m^* = C_2 e^{\int_1^x \lambda(t)dt},$$
$$\varphi_m = C_3 e^{\int_1^x \lambda(t)dt}, \quad \psi_m = C_4 e^{\int_1^x \lambda(t)dt},$$

the existence condition for the solution of system (30) has the form

$$\left[x^2(x^2\lambda^2 - m^2)^2(f_1 x^3\lambda^2 - m^2 f_2) - (f_3\lambda^2 x^3 - m^2 f_4)^2\right] \times \left[1 - \nu^2 - \frac{h^* x^2}{10}(\lambda^2 x^2 - m^2)\right] - \frac{x^2}{12}(m^2 - \lambda^2 x^2)^4 = 0.$$

This characteristic equation has four roots $\lambda^2(x)$. Since the solution decreases as x moves away from the edge $x = 1$, we select only the roots with a negative real part and substitute them in (30) and (29). Finally, after a minimization in x and with wave number m we obtain the buckling load.

The numerical analysis shows that under some critical load the buckling of the plate takes place near the edge of the plate. The buckling mode has eight waves (folds) similar to the isotropic case, but the value of the critical load for the non-homogeneous transversal isotropic LC could be considerably less than the critical load for the isotropic plate. For thin LC (h=0.1mm) the buckling occurs under pressure equals about 60 mm Hg.

Thus, the buckling in the nonaxisymmetric state in the neighborhood of the edge could also cause the atrophy of the optic nerve fibres.

8.5. Conclusion

The different mechanical models of the LC are considered. All these models confirm the mechanical genesis of glaucoma.

It is shown that the shear deformation of the vertical element (or essential shear of the layers) at the periphery of the LC could cause the atrophy of the optic nerve fibres. The solutions for LC with different degrees of nonuniformity can help reveal the structure of the LC, for which the glaucomatous damage is most probable to develop.

It is shown also that the buckling in the nonaxisymmetric state in the neighborhood of the edge could also cause edemas at the periphery of the LC and the atrophy of the optic nerve fibres.

Acknowledgment

The research described in this publication was made possible in part by Grant 04-01-00258 from Russian Foundation for Fundamental Research.

References

1. Ambartsumian, S. A., (1987), "Theory of anisotropic plates", Moscow, (in Russian).
2. Bauer, S. M., Romanova, A. A., and Smirnov, A. L., (2001), "On formulation of the problem on deformation of the lamina cribrosa", Russian J. of Biomechanics, Vol. 5, **3**, 18–22.
3. Bauer S. M., Zimin, B. A., and Tovstik, P. E., (2000), "The simplest analytical models of shells and plates in ophthalmology", St. Petersburg University Press, (in Russian).
4. Dongi, H., and Zeqin, R., (1999), "A biomathematical model for pressure-dependent lamina cribrosa behavior", J. of Biomechanics, **32**, 579–584.
5. Grigolyuk E. I., and Filshtinskii, L. A., (1970), "Perforated plates and shells, Moscow, (in Russian).
6. Nesterov, A. G., (1995), "Glaucoma", Moscow, (in Russian).
7. Kanagalingam, S., and Shoichet, M. S., (1996), "Biopolymer synthesis for use in the treatment of glaucoma", Abstr. Annu. Fall Meet. Biomed. Eng. Soc., University Park, PA, Oct. 3–6, 24, Suppl. No.!1, p. 7.
8. Panov, D. Yu., and Feodos'ev, V. I., (1948), "On equilibrium and loss of stability of shallow shells under large deflections", PMM, **XII**, 389–406, (in Russian).
9. Papastathopoulous, K. I., Jonas, J. B., and Panda-Jonas, S., (1995), "Large optic discs in large eyes, small optic discs in small eyes", Exp. Eye Res., **60**, 459–462.
10. Quigley H. A., and Addicks, E. M., (1981), "Regional differences in the structure of the lamina cribrosa and their relation to glaucomatous optic nerve damage", Arch. Ophthalmol., **99**, 137–143.
11. Quigley, H. A., and Addicks, E. M., (1982), "Quantitative studies of retinal nerve fiber layer d efects", Arch. Ophthalmol., **100**, 807–814.
12. Volkov, V. V., (2001), "Pseudonormal Pressure Glaucoma: Guide for Physicians", Moscow, (in Russian).
13. Yan, D. B., Coloma, F. M., Metheetrairut, A., Trope, G. E., Heathcote, J.G., and Ethier, C.R., (1994), "Deformation of the lamina cribrosa by elevated intraocular pressure", British J. of Ophthalmology., **78**, 643–648.
14. Yan, D. B., Flanagan, J. G., Farra, T., Trope G. E., and Ethier C. R., (1998), "Study of regional deformation of the optic nerve head using scanning laser tomography", Current Eye Research, **17**, 903–916.

CHAPTER 9

A MICROMECHANICAL MODEL FOR PREDICTING MICROCRACKING INDUCED MATERIAL DEGRADATION IN HUMAN CORTICAL BONE TISSUE

Ozan Akkus

Department of Bioengineering, The University of Toledo, OH 43606-3390, USA
E-mail: ozan.akkus@utoledo.edu

Clare Marie Rimnac

Department of Mechanics and Aerospace Engineering, Case Western Reserve University, Cleveland, OH 44106, USA
E-mail: Clare.Rimnac@case.edu

Ardéshir Guran

School of Mechanical Engineering, Sharif University of Technology, P.O. Box 11365-9567, Azadi Ave., Tehran, IRAN
E-mail: arde'guran@yahoo.com

The purpose of this study was to investigate the contribution of linear microcracks to material property degradation in human cortical bone tissue in quantifiable terms. To achieve this purpose, damage that was induced in cortical bone tensile specimens was examined. The number of linear microcracks, their length and their orientation to the loading axis were determined histologically. The volume fraction of damage was then calculated by using histologically determined parameters. A micromechanical damage model was developed to estimate the amount of degradation corresponding to the experimentally determined volume fraction of damage due to linear microcracks. The degradation observed experimentally was compared to the degradation predicted by the model to determine the contribution of linear microcracks to the observed material property degradation.

9.1. Introduction

Since Frost's [Frost (1960)][8] observation of *in vivo* microcracks nearly 40 years ago, a relationship between *damage* and *degradation* in bone tissue was expected but was not investigated until recently ([Burr *et al.* (1998)][5], [Jepsen and Davy (1997)][10]). Burr *et al.* [Burr *et al.* (1998)][5] investigated the relationship between area fraction of damage and degradation in secant modulus, while [Jepsen *et al.* (1999)][12] investigated the relationship between numerical crack density and degradation of viscous and elastic properties. These studies demonstrated that there is a relationship between the damage process and degradation of material properties in cortical bone tissue. Further, Griffin *et al.* [Griffin *et al.* (1997)][9] developed a model that successfully simulated an experimentally observed modulus degradation in cortical bone [Pattin *et al.* (1996)][17] by assuming that the loss of modulus was completely due to cracks assumed to be present in the interstitial matrix. That is, the amount of damage modeled was an outcome of the fit of the model, but was not validated by histological observation. Thus, the contribution of histologically observable damage to material property degradation is not completely known in quantifiable terms. In the case the histologically observable damage does not degrade the mechanical properties of bone then its presence or absence may not be relevant to skeletal fragility. Histologically observed damage appears in the form of diffuse damage and linear microcracks ([Boyce *et al.* (1998)][3], [Burr and Stafford (1990)][4]). Since the morphology of linear microcracks [Taylor and Lee (1998)][23] and their relation to the microstructure ([Norman and Wang (1997)][16], [Schaffler *et al.*(1995)][19]) are better known in comparison to diffuse damage, it may be possible to use the knowledge of linear microcracks to develop a quantifiable and mechanistic relationship between linear microcracks and degradation processes.

The purpose of this study was to investigate the contribution of linear microcracks to material property degradation in human cortical bone tissue in quantifiable terms. To achieve this purpose, damage that was induced in cortical bone tensile specimens [Knott (2000)][13] was examined. The number of linear microcracks, their length and their orientation to the loading axis were determined histologically. The volume fraction of damage was then calculated by using histologically determined parameters. A micromechanical damage model was developed to estimate the amount of degradation corresponding to the experimentally determined volume fraction of damage due to linear microcracks. The degradation observed experimentally

was compared to the degradation predicted by the model to determine the contribution of linear microcracks to the observed material property degradation.

9.2. Experimental Materials and Methods

The micromechanical model was conducted on the experimental data provided [Knott (2000)][13]. The left femur was obtained from a 24 year-old male and a 72 year-old male with no known skeletal pathologies. Following the removal of soft tissue, the bone was rough cut transversely into rings 50 mm in length using a band saw. Each ring was cut into four pegs, one for each anatomical quadrant, i.e. anterior, posterior, lateral and medial. The pegs were cut into 1.5 mm thick wafers using a Buehler Isomet 1000 low-speed precision circular saw. The wafers were machined to the final dimensions shown in Fig. 9.1. The number of specimens for the mechanical tests was 18 for the younger femur and 19 for the older femur.

Damage accumulation tests in monotonic tension were conducted to different levels of strain. All mechanical testing was performed on an Instron 8501M servohydraulic testing machine. The top grip was connected to the actuator through a ball and socket joint that provided proper alignment for pure tension. The lower grip was attached to a 500 lb load cell (Eaton). A 10% strain gage extensometer (Instron) was used to measure strain. All testing was performed in an environmental chamber that was kept at 37°C. The specimen was kept wet by a drip of Ringer's solution at 37°C.

Specimens were subjected to a three-cycle damage protocol where the first diagnostic cycle quantified the material properties within the elastic range, the second cycle induced damage to the specimen and the third diagnostic cycle, identical to the first one, quantified the material properties after the induction of damage (Fig. 9.2) [Jepsen and Davy (1997)][10]. The pre-damage and post-damage diagnostic cycles were trapezoidal-shaped with a hold strain of 0.25% for 30 seconds and with loading and unloading rates of 1%/s.

The damage cycle was triangular shaped with ramp-up and ramp-down rates of 1%/s to one of five peak strain levels. These peak strain levels were determined based on monotonic tensile tests conducted on separate sets of specimens ($n = 6$) from each donor. The tests were conducted at a rate of 1%/s to fracture. The five damage levels were chosen to cover the entire monotonic stress-strain curve such that there were two pre-yield, one yield and two post-yield damage levels. The first four damage levels were 0.25%

($n = 3$, pre-yield), 0.60% ($n = 4$, pre-yield), 0.75% ($n = 4$, yield), and 1.00% ($n = 4$, post-yield) for both subjects. The fifth damage level was set at 1.50% ($n = 4$, post-yield) for the 24 year-old femur and 1.25% for the 72 year-old femur ($n = 4$, post-yield). The fifth damage level for the 72 year old specimens was reduced to a strain level of 1.25% since monotonic tests of several specimens from the same donor experienced failure at a level of 1.50% strain. A 240 sec relaxation period at zero strain followed the unloading of the damage cycle to allow time for anelastic effects to dissipate. Elastic moduli were calculated from the slopes of the pre-damage and the post-damage diagnostic cycles by linear regression within the strain range of 0-0.2%. The degradation parameter, ϕ, was calculated as the ratio of the elastic modulus of the post-damage diagnostic cycle (E_3) and the elastic modulus of the pre-damage diagnostic cycle (E_1) such that $\phi = E_3/E_1$:

$$\phi = \frac{E_3}{E_1} \quad \text{and} \quad D = 1 - \phi. \tag{1}$$

Following mechanical testing, the gage region of each specimen was isolated by removing the grip regions with a low speed saw, fixed in 70% ethanol overnight and bulk stained in 1% basic fuchsin. The gage region specimens were embedded in poly(methylmethacrylate) and sectioned to 250 μm thickness using a diamond coated saw. Two sections were taken in the longitudinal circumferential plane (parallel to the flat face of the specimen) of the cortical bone tissue. The sections were glued to acrylic plates and ground to 150 μm thickness. Final polishing was performed with 1 μm diamond suspension.

The following is the histological analyses employed on the specimens obtained from [Knott (2000)][13]. The length of the microcracks, L_i, was measured in transmission mode using a video microscopy system attached to a Nikon Optiphot 2 microscope (Nikon Inc., New York). The horizontal axis of the monitor was aligned with the width and the vertical axis of the monitor was aligned with the tensile loading axis of the specimen.

Only linear microcracks having a sharp appearance with stain uptake along their length and that were traceable through the section thickness with changing depth of focus were quantified in this study [Burr and Stafford (1990)][4]. The angle, β_i, between the microcracks and the horizontal axis of the monitor was measured using a transparent goniometer (Fig. 9.3). For each specimen, a mean crack orientation, β_M, and a mean crack length L_M were determined using β_i and L_i, respectively. The number of linear microcracks, $Cr\ \#$, and the sum of the crack lengths, ΣL_i, were also determined for each specimen.

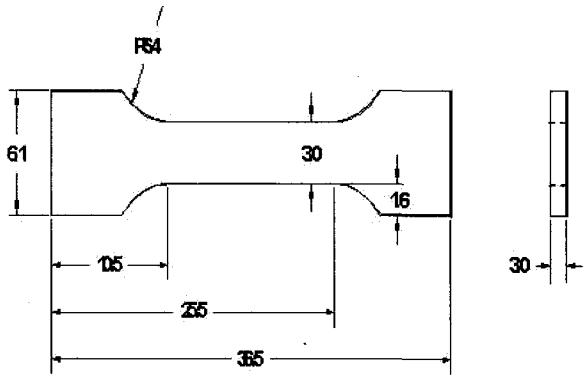

Fig. 9.1. All dimensions are in millimeters. The front view is in the longitudinal-circumferential plane and the side view is in the radial-circumferential plane of the cortical diaphysis.

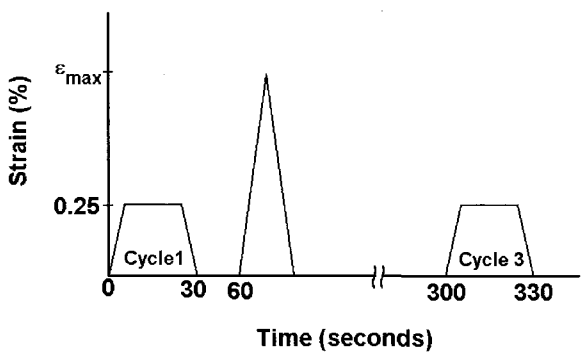

Fig. 9.2. Damage accumulation protocol.

According to the tensor nature of damage it was assumed that the degradation of Young's modulus along the longitudinal direction would be better explained by the projection of the microcracks on the radial-circumferential plane rather than by their actual orientation (Fig. 9.3). Therefore, the cracks observed in the longitudinal sections were projected on the radial-circumferential plane and they were idealized as oblate ellipsoids. The diameter of an oblate ellipsoid shaped microcrack, L_{Pi}, was calculated by taking the product of L_i and $\cos\beta_i$ for each crack. A mean

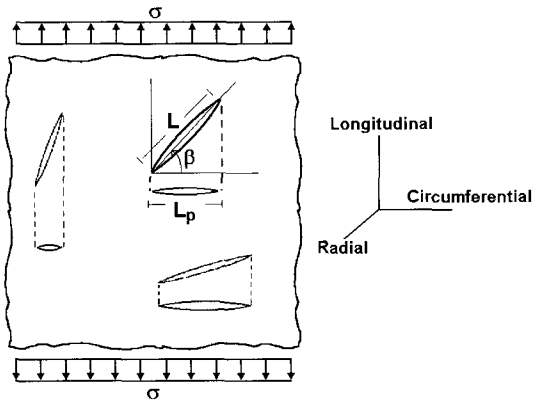

Fig. 9.3. Projection of cracks on the radial-circumferential plane. The specimen is loaded under uniaxial tension with stress σ. L is the length of the crack and L_P is the projected length of the crack in the radial-circumferential plane. β is the angle between the crack and the radial-circumferential plane.

projected crack length, L_{PM}, and sum of the projected crack lengths, ΣL_{Pi}, were determined for each specimen.

The section taken through an idealized oblate ellipsoid shaped crack will be at a certain distance, h, and orientation, θ, to the actual diameter of an oblate ellipsoid shaped crack, $2c$ (Fig. 9.4) [Taylor and Lee (1998)][23]; [Underwood(1970)][24]. Therefore, the mean projected length of the measured crack, L_{PM}, will be less than the actual length. The crack diameter, $2c$, was estimated from L_{PM} by using methods of quantitative stereology [Underwood(1970)][24]. In that analysis, h and θ were assumed to be random variables. In the radial-circumferential plane, the oblate ellipsoid shaped cracks were expressed as:

$$x^2 + y^2 = c^2, \tag{2}$$

where the origin of x and y coordinates are at the center of the oblate ellipsoid shaped crack. For $\theta = 0$ and constant c, the mean value, L_{PM}, will be:

$$L_{PM} = \frac{2}{c} \int_0^c x \, dy. \tag{3}$$

This leads to $c = 0.637 L_{PM}$. In this manner, the diameter of an average sized oblate ellipsoid shaped crack for each specimen was obtained using

the mean projected crack length L_{PM}. The volume of the average sized oblate ellipsoid shaped crack, V_{PM}, was determined using the formula:

$$V_{PM} = \frac{4}{3}\pi\ (c)^2\, a. \tag{4}$$

The half thickness of the crack, a, along the longitudinal direction (or half of the crack opening displacement along the longitudinal direction) and was taken as $c/10$. That is, the crack aspect ratio, γ, was assumed to be $c/a = 10$. The following rationale was used to arrive at this assumption. For experiment, the Young's modulus was determined from the linear fit to the stress-strain curve up to 0.15% strain. A strain of 0.15% corresponds to a far field (global) displacement of 15μm along the gage length. The crack opening displacement, $2a$, is an unknown function of global displacement for cortical bone tissue. However, it is known for composite materials [Krasnikovs and Varna (1997)][14] and titanium alloys [Sharpe *et al.* (1992)][20] that the crack opening displacement is less than the global displacement. Assuming then that the crack opening displacement 2a is half of the applied global strain, a can be estimated as 4 μm at a global strain level of 0.15%. If a typical value of 45 μm is taken for L_{PM} (Tables 6.2 and 6.3), the corresponding c value is determined to be 30 μm using eqn. (3). Thus, the aspect ratio c/a can be estimated to be 30/4=7.5 (which was rounded to an aspect ratio of $\gamma = 10$ for the purpose of this analysis). In addition, the estimated crack opening displacement was in agreement with qualitative observations of crack opening displacements of the microcracks observed during cyclic loading [Akkus and Rimnac (2001)][1].

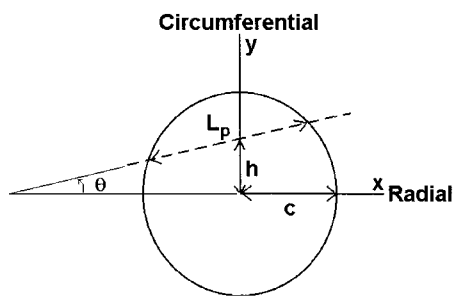

Fig. 9.4. Schema of an oblate ellipsoid shaped microcrack in the radial circumferential plane. A crack length of LP at height h and angle θ will be observed instead of the actual length of the crack, 2c. (Adapted from [Taylor and Lee (1998)][23]).

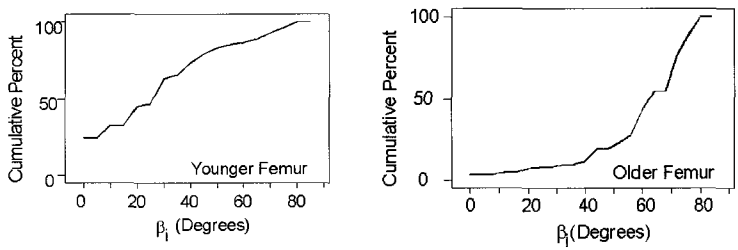

Fig. 9.5. Cumulative percent distribution of angular orientation, β_i, of microcracks for the specimen sections from the younger femur and from the older femur. Sample size was 380 for the specimen sections from the younger femur and 529 for the older femur. β_i values within the younger femur and the older femur were pooled to obtain the cumulative percent distributions.

The total volume of damage within a specimen, V_D, was calculated by taking the product of V_{PM} and Cr # for that specimen. V_D was normalized by the total observation volume (i.e., volume of the histological sections) so as to obtain the volume fraction of damage, F, for each specimen. F was, thus, calculated for the total volume of the two histological sections taken from each specimen. If one assumes that the cracks are randomly distributed within the volume of the gage length, the volume fraction$F$ obtained from the sections would also reflect the volume fraction of damage for the specimen. The width, length and the thickness of the sections were determined from which the volume of the histological sections (two per specimen) was calculated. The width of the sections was taken to be equal to the width ($\cong$ 3 mm) of the specimen from which they came. The length of the sections was taken to be equal to the gage length (15mm) for each specimen. The thickness of the sections was measured using a dial indicator ($\pm$0.01mm accuracy). The volume of the two sections, V_S, was calculated by taking the product of length, width and the total thickness of the two sections from each specimen. Finally, the volume fraction of damage, F, was calculated for each specimen by dividing the total volume of damage for that specimen, V_D, by the volume of the histological sections, V_S ($F = V_D/V_S$).

A statistical analysis was conducted using Minitab (Minitab, Inc., State College, PA). Differences between the mean values for the younger and the older femora were determined by Mann Whitney test at a significance level of $p < 0.05$. The variation in E_3/E_1 (y: response) as a function of ΣL_i, ΣL_{Pi}, V_D, F and Cr# (x: predictors) was investigated using linear regression analysis and the coefficient of variation, R^2, was determined. The

outliers were determined by checking the Cook's distance value. The observations which had a Cook's distance value greater than 1 were excluded from the regression analysis ([Cook (1977)][7]). Cook's distance combines leverage and standardized residual into one overall measure of how unusual is an observation ([Weisberg (1980)][25]). Leverage indicates if an observation has unusual predictors (x variable), and standardized residual indicates if an observation has an unusual response (y variable). A $p < 0.05$ was taken as significant for the results of the regression analyses.

The statistical distribution of the observations was confirmed by probability plotting. Probability plotting is a graphical method for determining whether sample data conform to a hypothesized distribution based on a subjective visual examination of the data. To construct the plot, the observations are ranked from smallest to largest. The ordered observations are then plotted against their observed cumulative frequency. If the hypothesized distribution adequately describes the data, the plotted points will fall approximately on a straight line and will lie within the 95% confidence interval.

9.3. Prediction of Material Property Degradation by a Micromechanical Damage Model

It was of interest to determine the degradation in Young's modulus along the longitudinal direction by a micromechanical model. The model employs an analytical technique that is a combination of Eshelby's equivalent inclusion method and the mean field theory ([Pedersen (1983)][18]). In this model, microcracks are introduced as ellipsoidal inclusions with a zero stiffness tensor, C_I, that are embedded in the transversely isotropic cortical bone medium, C_M. The following coordinate axes will be used in this model: the x_3 axis is along the direction of osteonal orientation (longitudinal axis); and, the x_1 and x_2 axes define the plane of isotropy (radial-circumferential plane) in cortical bone. The geometry of a microcrack is defined as, $(x_1/c)^2 + (x_2/c)^2 + (x_3/a)^2 = 1$, where the half length of the ellipsoid along the x_1 and x_2 axes is c and along the x_3 axis is a. As noted in section 10.2, the aspect ratio, $\gamma = c/a$, was taken as 10 for the oblate ellipsoid approximation of linear microcracks during experimental analysis. However, the model was also utilized to examine the effect of other aspect ratios, so that different microcrack morphologies could be examined.

The derivation of the formulation for the prediction of damaged elastic constants is adopted from the textbook by Clyne and Withers [Clyne and

Withers (1993)][6]. The composite material is loaded by an applied stress σ^A which generates an overall strain of ε^A that is averaged across the composite. As the initial step a homogenization scheme is carried out to convert the elastic properties of microcracks to those of bone tissue. The homogenization requires the representation of the microcrack (i.e. real inclusion) with a *ghost inclusion* that has the elastic properties of bone. Due to a appropriate transformation strain, ε^T, imposed on the ghost inclusion, the shape of the resulting inclusion is the same with the real inclusion, making it possible to homogenize the problem without changing the stress field in the matrix. Following the homogenization scheme a *mean field stress*, $< \sigma >_M$, is introduced to account for high volume fraction of inclusions. The mean field stress is a perturbation on the stress state of an inclusion due to all other inclusions; thus, it represents the average over the volume of the composite.

States of strain and stress for the ghost inclusion after the application of the external load are:

$$\varepsilon^A + \varepsilon^C + < \varepsilon >_M, \tag{5}$$

$$\sigma_I + \sigma^A + < \sigma >_M = C_M \left(\varepsilon^A + \varepsilon^C + < \varepsilon >_M - \varepsilon^T\right), \tag{6}$$

where ε^C is the constrained strain in the ghost inclusion before the external stress is applied and the stress corresponding to the constrained strain is σ_I. Eshelby has proven that the constrained strain is related to the transformation strain through the Eshelby tensor, S:

$$\varepsilon^C = S\varepsilon^T. \tag{7}$$

The mean average stress acting on the inclusion after accounting for the effects of other inclusions is $< \sigma >_I = \sigma_I + < \sigma >_M$. The mean field partitions between the inclusion and the matrix akin to an externally applied load and when averaged throughout the volume of the composite it vanishes:

$$(1 - f) < \sigma >_M + f < \sigma >_I = 0. \tag{8}$$

States of strain and stress for the real inclusion after the application of the external load are:

$$\varepsilon^A + \varepsilon^C + < \varepsilon >_M, \tag{9}$$

$$\sigma_I + \sigma^A + < \sigma >_M = < \sigma >_I + \sigma^A = C_I \left(\varepsilon^A + \varepsilon^C + < \varepsilon >_M\right) \tag{10}$$

The transformation strain is obtained by using eqns. (7) and (8), and by combining the equivalent stress states in the ghost and real inclusions

(eqns. (6) and (10)):

$$\varepsilon^T = -\{(C_M - C_I)[S - f(S - I)] - C_M\}^{-1}(C_M - C_I)\varepsilon^A. \tag{11}$$

Knowing the transformation strain, substituting eqn. (6) in eqn. (8) and making use of $< \sigma >_I = \sigma_I + < \sigma >_M$ and $\varepsilon^C = S\varepsilon^T$ the perturbation on the stress acting on the matrix becomes:

$$< \sigma >_M = -fC_M(S - I)\varepsilon^T. \tag{12}$$

Using eqn. (8) the stress perturbation acting on the inclusion becomes:

$$< \sigma >_I = (1 - f)C_M(S - I)\varepsilon^T. \tag{13}$$

The overall stiffness matrix of the composite, C_C, is related to the volume averaged composite strain, $\bar{\varepsilon}_C^A$:

$$\sigma^A = C_M\varepsilon^A = C_C\bar{\varepsilon}_C^A = C_C(\varepsilon^A + < \varepsilon >_C), \tag{14}$$

where $< \varepsilon >_C$ is the perturbation in the overall strain of the composite due to the presence of inclusions. This perturbation is the summation of the perturbed strain, $< \varepsilon >_M$, acting on the matrix and the inclusion (over the total volume) and the constrained strain ε^C acting on the inclusions only:

$$< \varepsilon >_C = < \varepsilon >_M + f\varepsilon^C \tag{15}$$

The mean matrix strain $< \varepsilon >_M$ can be obtained using eqns. (7) and (13):

$$\begin{aligned} &< \sigma >_M = C_M \quad < \varepsilon >_M = -fC_M(S - I)\varepsilon^T, \\ &< \varepsilon >_M = -f(\varepsilon^C - \varepsilon^T). \end{aligned} \tag{16}$$

Substituting eqn. (16) in eqn. (15):

$$< \varepsilon >_C = f\varepsilon^T \tag{17}$$

Therefore, the overall composite strain $\bar{\varepsilon}_C^A$ becomes:

$$\bar{\varepsilon}_C^A = \varepsilon^A + f\varepsilon^T \tag{18}$$

The stiffness matrix of the composite can be determined by substituting for the transformation strain (eqn. (11)) in eqn. (18) and substituting the resulting in eqn. (14):

$$C_C = \left[C_M^{-1} - f\{(C_I - C_M)[S - f(S - I)] + C_M\}^{-1}(C_I - C_M)C_M^{-1}\right]^{-1}. \tag{19}$$

Equation (19) is used to determine the changes in the elastic stiffness tensor of bone tissue with increasing volume fraction of penny-shaped microcracks.

$$C_C = \left[C_M^{-1} + fC_M[S - f(S - I)] + C_M^{-1}\right]^{-1}. \tag{20}$$

The undamaged stiffness C_M for human cortical bone was obtained from experimentally determined technical constants by ultrasonic testing [Yoon and Katz (1976)][26]:

$$E_1 = E_2 = 18.80\text{GPa}, \quad E_3 = 27.40\text{GPa}, \quad (E_i\text{: Young's moduli}),$$
$$G_{13} = G_{23} = 8.71\text{GPa}, \quad G_{12} = 7.17\text{GPa}, \quad (G_{ij}\text{: shear moduli}),$$
$$\nu_{12} = \nu_{21} = 0.312, \quad \nu_{13} = \nu_{23} = 0.193,$$
$$\nu_{31} = \nu_{32} = 0.281, \quad (\nu_{ij}\text{: Poisson's ratio}).$$

A property ratio was represented as the ratio of the damaged technical constants obtained from C_C to the undamaged technical constants obtained from C_M.

9.4. Experimental Results

Almost 75% of the cracks observed in the younger femur sections had a $\beta_i < 45°$ while about 20% of the microcracks observed in the older femur sections had a $\beta_i < 45°$ (Fig. 9.5). About 25% of the microcracks were oriented perpendicular ($\beta = 0°$) to the longitudinal axis of the younger femur while the older femur had few such microcracks. The mean crack orientation, β_M, for the younger femur was significantly smaller than that of the older ($p < 0.01$). The mean crack length, L_M, increased significantly with increasing mean crack orientation, β_M, for the younger femur ($R^2 = 0.383$, $p < 0.01$) but not for the older femur ($R^2 = 0.109$, $p = 0.168$). L_M increased significantly with increasing β_M, when the observations for the younger and the older femora were pooled together ($R^2 = 0.300$, $p < 0.01$). The mean crack length, L_M, for the younger femur was also significantly smaller than that of the older femur $p < 0.05$). In contrast, the mean projected crack length, L_{PM}, for the younger femur was significantly greater than that of the old femur ($p < 0.05$). The physical damage parameters ΣL_i and Cr# for the older femur were significantly greater than for the younger femur (p < 0.05). There was no significant difference in ΣL_{Pi}, V_D and F between the younger and older femurs.

The physical damage parameter values covered several orders of magnitude as the degradation increased. Specifically, the maximum values of ΣL_i,

Table 9.1. Statistical results for the regression analysis between the Young's modulus degradation (E_3/E_1) and the logarithm of the damage parameters.

Damage Parameters	Younger		Older		Combined	
	R^2	p	R^2	p	R^2	p
Log $\Sigma L_i(\mu\text{m})$	0.132	0.139	0.327	0.011	0.149	0.018
Log $\Sigma L_{P|i}(\mu\text{m})$	0.211	0.055	0.352	0.007	0.239	0.002
Log V_D	0.207	0.058	0.335	0.009	0.251	0.002
Log F	0.244	0.037	0.353	0.007	0.283	0.001
Log Cr #	0.173	0.086	0.280	0.020	0.180	0.009

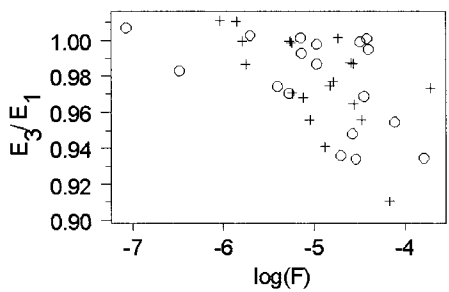

Fig. 9.6. The variation in degradation of Young's modulus (E_3/E_1) with the logarithm of the damage volume fraction F. The open circle and plus symbols refer to the specimens from the younger and older femora, respectively.

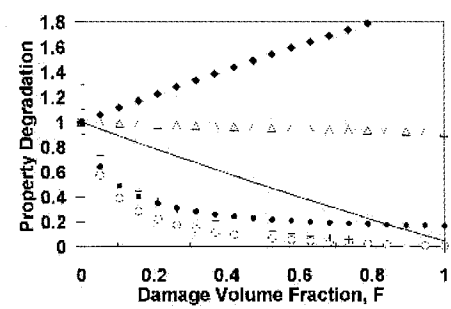

Fig. 9.7. Prediction of property degradation for an oblate ellipsoid with an aspect ratio of $c/a = 10$. (— E_1 and G_{12}; ○ E_3; + G_{13}; Δ ν_{12} and ν_{21}; ◇ ν_{13} and ν_{23}; • ν_{31} and ν_{32}.

ΣL_{Pi}, V_D, F and Cr. # were approximately 500, 250, 2000, 2000 and 150 times greater than the minimum value (for observations pooled over age), respectively. The span of the data raised the possibility that a lognormal

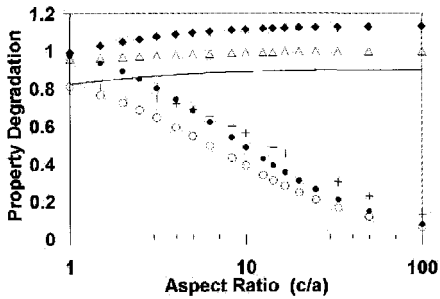

Fig. 9.8. Prediction of property degradation for changing aspect ratio at a constant volume fraction of 0.1. (— E_1 and G_{12}; ○ E_3; + G_{13}; Δ ν_{12} and ν_{21}; ◇ ν_{13} and ν_{23}; • ν_{31} and ν_{32}). An aspect ratio of 1 represents spherical voids whereas an aspect ratio of 100 represents a penny shaped crack.

distribution would better represent the data than a normal distribution. Therefore, normal and lognormal probability plots for each of the physical damage parameters were examined. Probability plots of the physical damage parameters showed that the lognormal distribution described the data better than a normal distribution.

Because the lognormal distribution better represented the physical damage parameters, the logarithms of the damage parameters were taken and their relation to the degradation parameter (E_3/E_1) was investigated by linear regression (Table 9.1 and Fig. 9.6). No outliers were detected during the regression analysis between the modulus degradation and the logarithm of damage parameters. For the younger femur Log F was the only damage parameter which was significantly related to modulus degradation (Table 9.1). For the older femur, all parameters were significantly related to modulus degradation. All of the logarithm damage parameter values had a significant relationship to modulus degradation when they were pooled over age. The damage volume fraction, F, had the smallest p values and the greatest R^2 values for all regressions of the logarithm damage parameter values. In all of the regressions of logarithm damage parameters described above, the sum of the projected crack lengths, ΣL_{P_i}, consistently had greater R^2 values than the sum of the crack lengths, ΣL_i.

9.5. Results of the Micromechanical Damage Model

The degradation in the technical constants was modeled for increasing damage volume fraction (F) of microcracks having oblate ellipsoid geometry

(Fig. 9.7). As expected, the moduli values approached 0 as the damage volume fraction approached 1. The model predicted that E_3, ν_{31}, ν_{32} and G_{13} were the most sensitive material properties to accumulation of oblate shaped cracks. The Poisson's ratio in the plane of transverse isotropy, ν_{12} $(= \nu_{21})$, was insensitive to increasing damage volume fraction. Interestingly, the model predicted that ν_{13} $(= \nu_{23})$ should increase with damage accumulation. This was expected since the increase in strain (ε_3) along the x_3 direction would be greater than the increase in strain (ε_3) along the x_1 direction with the accumulation of oblate ellipsoid shaped microcracks. This would be expected to increase ν_{13} $(= -\varepsilon_3/\varepsilon_1)$ with an increase in damage volume fraction.

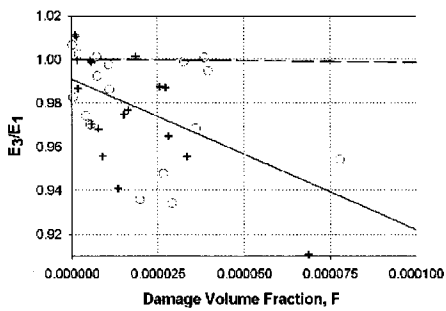

Fig. 9.9. Linear regression (solid line) for the experimentally observed degradation and the degradation predicted by the model (dashed line). For the experimentally observed degradation: $E_3/E_1 = -690.7F + 0.9911$, with $R^2 = 0.265$ and $p < 0.05$. For the model prediction: $E_3/E_1 = -14.05F + 1.0000$, with $R^2 = 0.9988$ and $p < 0.05$. The dashed line was obtained from the regression to the model results within the range of $0 < F < 0.0001$. The open circle (○) and the plus (+) symbols refer to data from the specimens of the younger and older femora, respectively.

The effect of microcrack morphology on the technical constants was also examined at a constant damage volume fraction $(F = 0.1)$ while increasing the aspect ratio c/a (Fig. 9.8). An aspect ratio of 1 represents spherical voids whereas an aspect ratio of 100 represents a penny shaped crack. The modulus in the radial circumferential plane, E_1, and ν_{12} $(= \nu_{21})$ were insensitive to increasing aspect ratio of the microcracks. The most sensitive parameters to increasing aspect ratio were ν_{31}, G_{13} and E_3. Microcracks that had an aspect ratio of 100 predicted 6 times more degradation than the microcracks that had an aspect ratio of 10 at the assumed constant

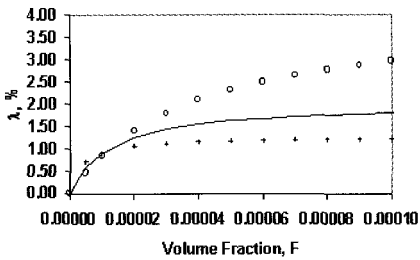

Fig. 9.10. Percent contribution of histologically observed linear microcracks to the degradation in Young's modulus, λ, versus damage volume fraction, F, for the younger femur (o), older femur (+) and combination of the two femora (solid line). $\lambda = D_{\mathrm{MOD/DEXP}}$, where DMOD and DEXP are the damage parameters defined by (1) for the experiment and the prediction, respectively.

damage volume fraction of 0.1.

9.6. Comparison of Experimental Results to the Micromechanical Damage Model

The relation between the degradation in longitudinal Young's modulus, E_3, and damage volume fraction was experimentally determined in the previous section. It was of interest to compare this experimentally determined relation with that predicted by the micromechanical model. For this purpose, the equation of the regression line (E_3/E_1 vs F) fitted to the combined experimental data was determined and compared to model predictions within the experimentally observed range of $0 < F < 0.0001$ (Fig. 9.9). Similarly, a line was fitted to the model prediction of the relationship between E_3/E_1 and F within the range of $0 < F < 0.0001$.

The model predicted much less degradation than the experimental results at a given damage volume fraction (Fig. 9.9). The slope of the regression line fitted to the experimental data was much greater than the slope of the regression line that was fitted to the model predictions (-690.7 vs -14.05, respectively, Fig. 9.9).

It is important to note that the experimentally observed degradation occurred due to accumulation of linear microcracks, diffuse damage and possibly other forms of damage that are not known or yet measurable. However, the degradation predicted by the model is only due to linear microcracks. Thus, it is possible to find the contribution of the linear microcracks (pre-

dicted degradation) to the total degradation (experimental degradation). For this purpose, the damage parameter that was defined in eqn. (1) was obtained for the experiment, D_{EXP}, and for the prediction, D_{MOD}:

$$D_{\mathrm{EXP}} = 1 - \left(\frac{E_3}{E_1}\right)_{\mathrm{EXP}} = 1 - a_{\mathrm{EXP}}F - b_{\mathrm{EXP}}, \tag{21}$$

$$D_{\mathrm{MOD}} = 1 - \left(\frac{E_3}{E_1}\right)_{\mathrm{MOD}} = 1 - a_{\mathrm{MOD}}F - b_{\mathrm{MOD}}. \tag{22}$$

Where $(E_3/E_1)_{\mathrm{EXP}}$ is the equation of the line obtained by regression of the experimental data (younger, older, and combined), $(E_3/E_1)_{\mathrm{MOD}}$ is the equation of the line obtained by regression of the predicted data, and a_{EXP} and a_{MOD} are the slopes of the regression lines for the experimental and predicted data, respectively. The slopes, a_{EXP}, for the experimentally determined regression lines were -338.6, -1113.7, and -690.7 for the younger femur, older femur and for the combination of the two femora, respectively. The slope for the model prediction, a_{MOD}, was -14.052.

The intercepts of the regression lines for the experimental data for the model prediction were $\mathrm{b_{EXP}}$ and $\mathrm{b_{MOD}}$, respectively. The intercept, $\mathrm{b_{EXP}}$, for the experimentally determined regression lines were 0.9866, 0.9955, and 0.9911 for the younger femur, older femur and for the combination of the two femora, respectively. The intercept for the model prediction, b_{MOD}, was 1.0000.

Using these slope and intercept values, the percent contribution of the histologically observed linear microcracks to the total (observed) degradation, λ, can then be calculated as:

$$\lambda = \left(\frac{D_{\mathrm{MOD}}}{D_{\mathrm{EXP}}}\right) x\,100 = \left(\frac{1 - a_{\mathrm{MOD}}\,F - b_{\mathrm{MOD}}}{1 - a_{\mathrm{EXP}}\,F - b_{\mathrm{EXP}}}\right) x\,100. \tag{23}$$

Using eqn. (23), λ was determined (Fig. 9.10) as a function of volume fraction F for the younger femur, older femur and for the combination of the two femora. Interestingly, the model predicts that only 2.97% (younger femur), 1.21% (older femur), and 1.80% (combination of the two femora) of the observed degradation is due to the accumulation of histologically observed linear microcracks at $F = 0.0001$.

Ideally, the intercepts of the regression lines should be unity since, at $F = 0$, the degradation, E_3/E_1, is equal to 1. The intercepts of the experimental regression lines are close to unity but still differ from unity due to experimental scatter. If b_{EXP} is assumed to be 1, eqn. (23) becomes $\lambda_1 = (a_{\mathrm{MOD}}/a_{\mathrm{EXP}}) \times 100$ (where λ_1 is the value of λ when $b_{\mathrm{EXP}} = 1$). The percent contribution of histologically observed linear microcracks to the

total degradation, λ_1, becomes 4.15%, 1.26%, and 2.03% for the younger femur, the older femur and the combination of the two femora, respectively.

The damage volume fraction, F, was calculated using the apparent volume, V_S, of the histological sections. However, cortical bone tissue has an inherent porosity. The volume fraction of damage would increase if it were calculated by accounting for the inherent porosity in the bone tissue:

$$F_P = \frac{V_D}{V_S - P V_S} = \frac{V_D}{V_S} \frac{1}{1-P} = \frac{F}{1-P}, \tag{24}$$

where F_P is the damage volume fraction when the inherent porosity is accounted for, V_D is the total volume of damage within a specimen, and P is the inherent porosity of the bone tissue. Knott [Knott (2000)][13] reported the porosity of the younger femur and the older femur used in this study as 3.9% and 7.9%, respectively. Using these porosity values, the damage volume fraction was recalculated using eqn. (24). The increase in the damage volume fraction by accounting for the porosity did not affect the results greatly. The percent contribution of linear microcracks, λ_1, becomes 4.32%, 1.37% and 2.12% when the inherent porosity is taken into consideration.

9.7. Discussion

In this study, human cortical bone tissue was damaged under tension and the degradation in the Young's modulus along the longitudinal axis was monitored. Other material properties have been used to monitor the process of degradation and the choice of these parameters affects the results. For example, [Jepsen *et al.* (1999)][12] have showed that the degradation in torsional relaxation is not significantly related to numerical crack density while the degradation in torsional stiffness is significantly related to numerical crack density for human cortical bone. Young's modulus is a reasonable material property to monitor as an indicator of damage, as opposed to a secant modulus, because Young's modulus is likely not as influenced by anelastic effects in cortical bone [Jepsen *et al.* (2000)][11].

A limitation of this study was that the specimens were obtained from a single younger femur and a single older femur. Thus, it is difficult to draw rigorous conclusions with respect to age effects on the observed differences in the microcracks. However, it is still interesting to compare the younger and older femora results.

It was found that the mean crack length, L_M, increased as the mean crack orientation, β_M, approached the longitudinal axis of the bone. This result is expected since crack growth becomes easier for orientations closer

to the longitudinal axis of bone tissue ([Behiri and Bonfield (1989)][2]). In addition, cracks that are propagating at closer angles to the longitudinal axis of the bone would be expected to grow longer before encountering a microstructural barrier as compared to cracks that grow in the radial circumferential plane.

In this study, the objective was to develop a damage parameter that would be more mechanistic in comparison with damage parameters like crack number ([Jepsen *et al.* (1999)][12]) or area fraction of damage ([Burr *et al.* (1998)][5]). For this purpose, microcrack morphology was partially accounted for by measuring the crack length and the crack orientation. The crack orientation was of additional interest since it was hypothesized that the degradation of Young's modulus along the longitudinal direction would be better explained by the projection of the microcrack lengths, L_{P_i} on the radial-circumferential plane rather than by the measured lengths, L_i (Fig. 9.3). In this analysis, damage was treated as a vector ([Talreja (1985)][21]), such that, if a crack does not have a component along a plane, then it will not lead to property degradation along the direction perpendicular to that plane. Vectorial consideration of damage has been successfully used to model the stiffness reduction in graphite fiber-epoxy matrix composites due to accumulation of transverse cracks ([Talreja *et al.*(1992)][22]). In support of the hypothesis, the regression analyses showed that the R^2 values for the sum of the projected crack lengths, ΣL_{Pi}, were always higher than the R^2 values for the sum of the crack lengths, ΣL_i (Table 9.1). The volume fraction of damage, F, was obtained by normalizing the total volume of damage by the volume of the histological sections. This modification further improved the relationship between damage and degradation processes such that, for every regression analysis, F had the best R^2 value for both the younger femur and the older femur as well for their combination.

The projections of the microcracks on the radial-circumferential plane were approximated as oblate ellipsoids. Taylor and Lee ([Taylor and Lee (1998)][23]) previously predicted that a linear microcrack could be represented as an ellipse whose major axis is lying close to the longitudinal axis. The projection of this ellipse on the radial-circumferential plane would also be an ellipse. However, no Eshelby's tensor solution for this shape was found. Thus, in this study, the projection of the ellipse on the radial-circumferential plane was idealized as a circle, for which the Eshelby's tensor exists.

Approximation of the projected crack as an oblate ellipsoid (that appears circular in the section taken along the radial circumferential plane)

allowed for determination of the microcrack volume, V_i. As noted previously, this calculation depended on the c/a ratio, which was assumed to be 10. Ideally, the c/a ratio would have been obtained experimentally. The total volume of damage, V_D, and the damage volume fraction, F, is inversely proportional to the aspect ratio, i.e. a tenfold increase in aspect ratio would lead to a ten fold decrease in V_D and F. Consequently, for a tenfold increase in aspect ratio, the slopes of the regression lines would increase ten fold while the intercepts would be unchanged. However, a tenfold increase in the aspect ratio does not alter the significance of the regression analyses. A tenfold increase in the aspect ratio increases the slope of the regression line predicted by the model by 9.3 times, which compensates the ten fold increase in the slopes of the regression lines obtained experimentally. Therefore, the contribution of histologically observable linear microcracks to property degradation (see eqn. (23)) is not altered significantly due to increasing aspect ratio. This argument is also valid for the decreasing aspect ratio.

As opposed to phenomenological models ([Griffin *et al.* (1997)][9]), the proposed micromechanical model accounts for both microcrack morphology and anisotropy of damage using a tensorial approach. However, only oblate ellipsoid shaped cracks perpendicular to the longitudinal axis can be modeled. This is due to the lack of an Eshelby's Tensor solution for an oblate ellipsoid shaped crack that is inclined to the plane of transverse isotropy. In the future, the model will be developed further in this respect by determining the Eshelby's tensor that would also account for the orientation of the microcracks. Nonetheless, the model provided insight into the approximate contribution of histologically observable linear microcracks to the observed degradation in Young's modulus.

An important limitation of this study was that it was not possible to separate damage that was formed *in vivo* and damage that occurred during specimen machining from the damage induced during tensile loading. This could have been achieved by labeling the damage with a stain that has a different color than basic fuchsin prior to mechanical loading ([Lee *et al.* (2000)][15]). If the background damage was isolated in this fashion, the observed damage volume fraction would be lowered, though the amount is unknown.

The results suggested that linear microcracks accounted for less than 5% of the observed degradation (Fig. 9.9). Had the background damage been accounted for, the contribution of the linear microcracks to degradation would have been even lower. The remaining degradation is likely due in part

to diffuse damage that is formed by arrays of submicroscopic cracks ([Boyce *et al.* (1998)][3]). Like the cracks at the microscale, these submicroscopic cracks will also contribute to the damage volume fraction. However, not much is known about the morphology and density of these submicroscopic cracks. Gaining insight into these aspects of submicroscopic cracks is crucial to more fully explaining material property degradation. Finally, it is also possible that an, as of yet, unidentified or undetectable mode of damage contributes to material property degradation in cortical bone tissue.

Acknowledgments

The experimental data and the histological sections used in the micromechanical were kindly provided by David. F. Knott, Dr. Dwight T. Davy and Dr. Karl J. Jepsen. The finalization of the manuscript was possible with the help of Dr. Rémi Vaillancourt. The authors gratefully acknowledge the funding from the U.S. Army Medical Research and Materiel Command (OA), the Whitaker Foundation (OA), the Musculoskeletal Transplant Foundation (CMR) and National Institutes of Health (NIH AG-17171, CMR).

References

1. Akkus, O., and Rimnac, C. M., (2001). Cortical bone tissue resists fatigue fracture by deceleration and arrest of microcrack growth. J Biomech, 34, pp. 757–64.
2. Behiri, J. C., and Bonfield, W., (1989). Orientation dependence of the fracture mechanics of cortical bone. J. Biomech., 22, pp. 863–72.
3. Boyce, T. M., Fyhrie, D. P., Glotkowski, M. C., Radin, E. R., and Schaffler, M. B., (1998). Damage type and strain mode associations in human compact bone bending fatigue. J. Orthop. Res., 16, pp. 322–329.
4. Burr, D. B., and Stafford, T., (1990). Validity of the bulk-staining technique to separate artifactual from in vivo bone microdamage. Clin. Orthop., 260, pp. 305–308.
5. Burr, D. B., Turner, C. H., Naick, P., Forwood, M. R., Ambrosius, W., Hasan, M. S. and Pidaparti, R., (1998). Does microdamage accumulation affect the mechanical properties of bone? J. Biomech., 31, pp. 337–45.
6. Clyne, T. W., and Withers, P. J., (1993): An Introduction to Metal Matrix Composites. Cambridge University Press, Cambridge.
7. Cook, R. D., (1977). Detection of influential observations in linear regression. Technometrics, 19, pp. 15–18.
8. Frost, H. L., (1960). Presence of microscopic cracks in vivo in bone. Henry Ford Hosp. Med. Bull., 8, pp. 25–35.
9. Griffin, L. V., Gibeling, J. C., Martin, R. B., Gibson, V. A., and Stover, S. M., (1997). Model of flexural fatigue damage accumulation for cortical bone. J. Orthop. Res., 15, pp. 607–14.

10. Jepsen, K. J., and Davy, D. T., (1997). Comparison of damage accumulation measures in human cortical bone. J. Biomech., 30, pp. 891–4.
11. Jepsen, K. J.,, Davy, D. T., and Akkus, O., (2000): Observations of Damage in Bone, in Bone Mechanics (Cowin SC ed), CRC Press.
12. Jepsen KJ, Davy DT and Krzypow DJ (1999). The role of the lamellar interface during torsional yielding of human cortical bone. J. Biomech., 32, pp. 303–10.
13. Knott, D. F. (2000): Age-related differences in the tensile damage accumulation behavior of adult human cortical bone, in Master of Science Thesis, Department of Mechanical and Aerospace Engineering pp 146, Case Western Reserve University, Cleveland.
14. Krasnikovs, A., and Varna, J., (1997). Transverse cracks in cross-ply laminates. I. Stress analysis. Mech. Compos. Mater. (in Russian), 33, pp. 565–582.
15. Lee, T. C.,, Arthur, T. L.,, Gibson, L. J., and Hayes, W. C., (2000). Sequential labelling of microdamage in bone using chelating agents. J. Orthop. Res., 18, pp. 322–325.
16. Norman, T. L., and Wang, Z., (1997). Microdamage of human cortical bone: incidence and morphology in long bones. Bone, 20, pp. 375–9.
17. Pattin, C. A., Caler, W. E., and Carter, D. R., (1996). Cyclic mechanical property degradation during fatigue loading of cortical bone. J. Biomech., 29, pp. 69–79.
18. Pedersen, O. B., (1983). Thermoelasticity and plasticity of composites -I. Mean field theory. Acta Metall., 31, pp. 1795–1808.
19. Schaffler, M. B.,, Choi, K., and Milgrom, C., (1995). Aging and matrix microdamage accumulation in human compact bone. Bone, 17, pp. 521–25.
20. Sharpe, W. N.,, Jira, J. R. and Larsen, J. M., (1992): Real-time measurements of small-crack opening behavior using an interferometric strain/displacement gage, in Small-Crack Test Methods (Allison JE ed) pp 92–115, ASTM, Philadelphia.
21. Talreja, R., (1985). A Continuum mechanics characterization of damage in composite materials. Proc. R. Soc. Lond., A399, pp. 195–216.
22. Talreja, R., Yalvac, S., Yats, L. D., and Wetters, D. G., (1992). Transverse cracking and stiffness reduction in cross ply laminates of different matrix toughness. J. Compos. Mater., 26, pp. 1644–1663.
23. Taylor, D., and Lee, T. C., (1998). Measuring the shape and size of microcracks in bone. J. Biomech., 31, pp. 1177–80.
24. Underwood, E. E., (1970): Quantitative Stereology. Addison-Wesley, Reading, MA.
25. Weisberg, S., (1980): Applied Linear Regression. John Wiley & Sons, Inc.
26. Yoon, H. S., and Katz, J. L., (1976). Ultrasonic wave propagation in human cortical bone–II. Measurements of elastic properties and microhardness. J. Biomech., 9, pp. 459–64.

PART 4

Experimental and Computational Mechanics of Solids

This page is intentionally left blank

CHAPTER 10

AN EVOLUTION OF SOLID ELEMENTS FOR THERMAL-MECHANICAL FINITE ELEMENT ANALYSIS

J. Moyra J. McDill

Mechanical and Aerospace Engineering, Carleton University, 1125 Colonel By Drive, Ottawa, Canada, K1S 5B68
E-mail: mmcdill@mae.carleton.ca

An evolution of three solid elements for thermal-mechanical finite element analysis (FEA) is presented. The elements were developed for a research-based FEA code for which the principal application was three-dimensional FEA of manufacturing processes such as welding. The evolution began with the 8-to 26-node hexahedron which permitted rapid grading from a fine mesh in the area of interest, typically the fusion zone, to a coarse mesh in the far field. A nonconforming 8-to 26-node hexahedron and an 8- to 16-node solid shell followed. The nonconforming element provided superior performance especially in areas involving bending and quickly became the preferred element. The evolution of the hexahedron to the solid shell then permitted the use of thinner elements in the far field. A further step to a nonconforming shell is proposed for the continued evolution of this element group.

10.1. Introduction

The finite element method is one of the most widely available numerical analysis techniques. It can be used in a variety of thermal, stress, thermal-stress, dynamic and other problems. In recent years, a number of familiar commercial finite element packages and CAD/CAM products have appeared. New elements appear only rarely in such commercially available codes and only after substantial testing.

Finite element analysis (FEA) of manufacturing processes such as welding is handled by few commercial FEA products as advanced computational techniques and complex material models are required for these thermal-mechanical processes. Research-based FEA codes are an appropriate av-

enue for the examination of such processes and elements which address the particular concerns of the developer may evolve to address the developers' concerns. Here, the evolution of three solid elements for a research-based FEA algorithm is presented. The 8- to 26-node linear hexahedron intended primarily for hexahedral mesh grading without the use of tetrahedrons was developed from a two-dimensional (2-D) 4- to 8-node linear quadrilateral. A nonconforming version of the same hexahedron which provided better response in areas with bending followed, as did an 8- to 16-node solid shell element for use in areas of the structure requiring a thinner element.

In the case of the thermal-mechanical FEA algorithm for which the elements were developed, an updated Lagrangian formulation in which thermal histories are used to compute thermal expansion, stresses and strains is employed. Good agreement with experiment has been established; e.g., [McDill *et al.* (1990)][16], [Oddy *et al.* (1990)][23], [McDill *et al.* (1992)][18]. The constitutive model embedded in the stress analysis includes elastic, plastic and thermal strains as well as strains, due to volume changes and the transformation plasticity, which occur during phase changes. The large strains and rotations that may take place are accommodated in a finite deformation algorithm which uses the Green-Naghdi stress and centred strain. A direct frontal solver and an iterative conjugate gradient solver are available.

10.2. 8- to 26-Node Linear Hexahedron

The need for three-dimensional (3-D) thermal-mechanical FEA analysis for welding, and similar processes, was known early in the development of the algorithm; e.g., [Goldak *et al.* (1986)][6]. At the time, mesh grading was essential to reduce computational costs. The 8- to 26-node hexahedron allowed the required grading to occur while, at the same time, eliminating the need for implementation of tetrahedral elements.

The 8- to 26-node linear hexahedron (Figs. 10.1(a) and 10.1(b)) is formulated [McDill *et al.* (1987)][15] much like the familiar 8-node linear brick using a standard isoparametric approach; i.e.,

$$N_i(\xi_j, \eta_j) = \delta_{ij}. \tag{1}$$

This 3-D element evolved from a 2-D 4- to 8-node linear quadrilateral [McDill *et al.* (1987)][15], [MacNeal and Harder (1985)][14]. In the 3-D element, nodes 1 to 8 are mandatory vertex nodes. Additional, but optional, nodes facilitate grading. Nodes 9 to 20 are optional midedge nodes and nodes 21 to 26 are optional midface nodes. These optional nodes may be used in any desired combination and create smooth (C^∞ continuous) subelements

within the element. Within each subelement the basis functions are linear. However, the basis functions for the midface nodes and midedge nodes as well as their adjacent corner nodes, are creased at the junction of the subelements and are, therefore, C^0 continuous. No irregular nodes [Rheinbolt and Meszenteyi (1980)][27] or external constraint equations [Somervaille (1972)][30], are needed for the optional nodes, since compatibility is inherent in the basis functions.

The presence of a midface node alters the basis functions of those midedge nodes present on that face as well as the corner nodes on that face. Similarly, a midedge node, alters the basis functions of the corner nodes on that edge. Basis functions (Table 10.1) should be evaluated, in decreasing order, from N_{26} to N_1. When a node is not present all references to it are removed from Table 10.1.

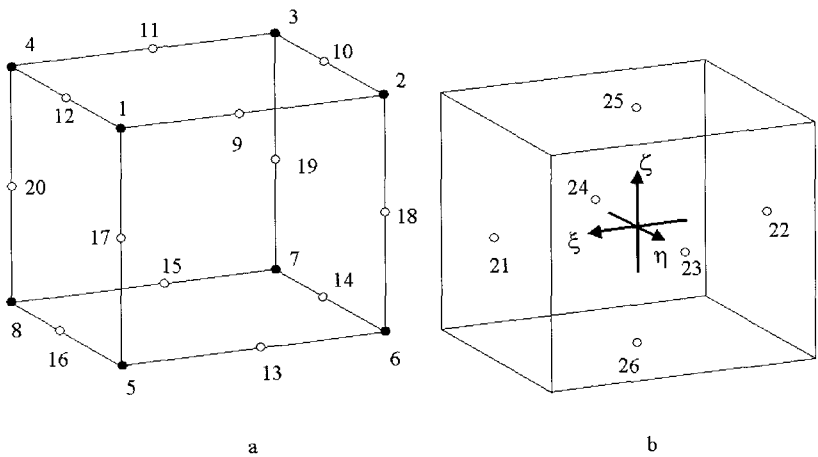

Fig. 10.1. Nodal positions for the 8- to 26-node linear hexahedron; (a) corner and optional midedge nodes; (b) optional midface nodes

Factoring the stiffness matrix is the most costly portion of FEA when using a direct solver. This cost, C_f, is proportional to the number of degrees

of freedom in the problem d_f, and to the square of the frontwidth f_w (or bandwidth):

$$C_f \propto d_f \times (f_w)^2. \tag{2}$$

With the 8- to 26-node hexahedron, grading can be done so that the characteristic dimension, h, doubles in the neighbouring element (2:1 grading). The cost ratio, C_r for an equivalent uniform mesh with m elements on an edge will approach the limit:

$$C_r \propto \frac{O(m)^7}{O(\log_2 m)}. \tag{3}$$

Naturally, the cost advantage of binary grading seen with C_r is not as easily exploited in an indirect solver; e.g., conjugate gradient, nevertheless it provided a useful point of comparison.

Table 10.1. Basis functions N_i for the 8- to 26-node hexahedron.

Node	$N(\xi,\eta,\zeta$
26	$\frac{1}{2}(1-\lvert\xi\rvert)(1-\lvert\eta\rvert)(1-\zeta)$
25	$\frac{1}{2}(1-\lvert\xi\rvert)(1-\lvert\eta\rvert)(1+\zeta)$
24	$\frac{1}{2}(1-\lvert\xi\rvert)(1-\eta)(1-\lvert\zeta\rvert)$
23	$\frac{1}{2}(1-\lvert\xi\rvert)(1+\eta)(1-\lvert\zeta\rvert)$
22	$\frac{1}{2}(1-\xi)(1-\lvert\eta\rvert)(1-\lvert\zeta\rvert)$
21	$\frac{1}{2}(1+\xi)(1-\lvert\eta\rvert)(1-\lvert\zeta\rvert)$
20	$\frac{1}{4}(1+\xi)(1-\eta)(1-\lvert\zeta\rvert)-\frac{1}{2}(N_{21}+N_{24})$
19	$\frac{1}{4}(1-\xi)(1-\eta)(1-\lvert\zeta\rvert)-\frac{1}{2}(N_{22}+N_{24})$
18	$\frac{1}{4}(1-\xi)(1+\eta)(1-\lvert\zeta\rvert)-\frac{1}{2}(N_{22}+N_{23})$
17	$\frac{1}{4}(1+\xi)(1+\eta)(1-\lvert\zeta\rvert)-\frac{1}{2}(N_{21}+N_{23})$
16	$\frac{1}{4}(1+\xi)(1-\lvert\eta\rvert)(1-\zeta)-\frac{1}{2}(N_{21}+N_{26})$
15	$\frac{1}{4}(1-\lvert\xi\rvert)(1-\eta)(1-\zeta)-\frac{1}{2}(N_{24}+N_{26})$
14	$\frac{1}{4}(1-\xi)(1-\lvert\eta\rvert)(1-\zeta)-\frac{1}{2}(N_{22}+N_{26})$
13	$\frac{1}{4}(1-\lvert\xi\rvert)(1+\eta)(1-\zeta)-\frac{1}{2}(N_{23}+N_{26})$
12	$\frac{1}{4}(1+\xi)(1-\lvert\eta\rvert)(1+\zeta)-\frac{1}{2}(N_{21}+N_{25})$
11	$\frac{1}{4}(1-\lvert\xi\rvert)(1-\eta)(1+\zeta)-\frac{1}{2}(N_{24}+N_{25})$
10	$\frac{1}{4}(1-\xi)(1-\lvert\eta\rvert)(1+\zeta)-\frac{1}{2}(N_{22}+N_{25})$
9	$\frac{1}{4}(1-\lvert\xi\rvert)(1+\eta)(1+\zeta)-\frac{1}{2}(N_{23}+N_{25})$
8	$\frac{1}{8}(1+\xi)(1-\eta)(1-\zeta)-\frac{1}{2}(N_{15}+N_{16}+N_{20})-\frac{1}{4}(N_{21}+N_{24}+N_{26})$
7	$\frac{1}{8}(1-\xi)(1-\eta)(1-\zeta)-\frac{1}{2}(N_{14}+N_{15}+N_{19})-\frac{1}{4}(N_{22}+N_{24}+N_{26})$
6	$\frac{1}{8}(1-\xi)(1+\eta)(1-\zeta)-\frac{1}{2}(N_{13}+N_{14}+N_{18})-\frac{1}{4}(N_{22}+N_{23}+N_{26})$
5	$\frac{1}{8}(1+\xi)(1+\eta)(1-\zeta)-\frac{1}{2}(N_{13}+N_{16}+N_{17})-\frac{1}{4}(N_{21}+N_{23}+N_{26})$
4	$\frac{1}{8}(1+\xi)(1-\eta)(1+\zeta)-\frac{1}{2}(N_{11}+N_{12}+N_{20})-\frac{1}{4}(N_{21}+N_{24}+N_{25})$
3	$\frac{1}{8}(1-\xi)(1-\eta)(1+\zeta)-\frac{1}{2}(N_{10}+N_{11}+N_{19})-\frac{1}{4}(N_{22}+N_{24}+N_{25})$
2	$\frac{1}{8}(1-\xi)(1+\eta)(1+\zeta)-\frac{1}{2}(N_{9}+N_{10}+N_{18})-\frac{1}{4}(N_{22}+N_{23}+N_{25})$
1	$\frac{1}{8}(1+\xi)(1+\eta)(1+\zeta)-\frac{1}{2}(N_{9}+N_{12}+N_{17})-\frac{1}{4}(N_{21}+N_{23}+N_{25})$

The 8- to 26-node hexahedron very quickly became the mainstay of

thermal, stress and thermal-stress analyses and was essential in demonstrating the feasibility of early 3-D thermal-mechanical analysis of welds; e.g., [Goldak *et al.* (1986)][6]. The use of other types of elements such as the 20-node quadratic hexahedron was discontinued, simplifying continued development of the FEA code. However, selective reduced integration [Hughes (1987)][8] was introduced for the 8- to 26-node hexahedron to deal with concerns during plastic deformation. The element, like other elements which utilize low order polynomials to model the displacement field, can be unsuitable for plasticity [Nagtegal *et al.* (1974)][22]. For a typical mesh, the incremental incompressibility condition may create too many constraints. When there are insufficient degrees of freedom to accommodate the incompressibility constraints, a form of locking occurs. This can be avoided through the application of reduced integration (quadrature) on the hydrostatic terms and normal integration of the deviatoric terms of the stiffness matrix.

The introduction of selective reduced integration, however, came at a price. Hughes [Hughes (1987)][8] noted that continuous pressure elements; i.e., those possessing identical displacement and pressure interpolations, may exhibit spurious pressure modes. A well-known example of this situation is seen in the failure of the 8-node linear brick, using selective reduced integration, in the patch test [MacNeal and Harder (1985)][14]. A cube composed of 7 distorted 8-node elements subjected to uniform strain, should develop a uniform stress field. With selective reduced integration, there is a variation in the hydrostatic stress although the deviatoric stresses are uniform as expected.

Another concern with the 8- to 26-node hexahedron was noted in thermal-elasto-plastic analysis. The element produces temperature or displacement fields which are linear functions of the three Cartesian coordinates. The use of selective reduced integration alone is insufficient in a thermal-elasto-plastic analysis if the thermal and transformation strains vary over the element [Oddy *et al.* (1990)][24]. For this reason, isothermal elements were typically employed in the stress analyses to produce consistent strain fields.

10.3. A Nonconforming 8- to 26-Node Hexahedron

The next step in the evolutionary process was to enhance the behaviour of the 8- to 26-node hexahedron in the stress portion of the thermal-mechanical analysis, eliminating the disadvantages discussed above. The

nonconforming 8- to 26-node hexahedron was chosen over higher order elements or p-refinement, since the grading capability of the 8- to 26-node hexahedron was essential. Typically, to minimize computing costs and still achieve reasonable accuracy, the mesh is graded so that small elements are used in the vicinity of some localized effect, such as a heat source, and larger elements are used further away.

The 8- to 26-node hexahedron was modified through the introduction of nodeless quadratic modes sometimes referred to as bending modes. Three nodeless modes, each with three degrees of freedom were associated with the centroid of each subelement [McDill and Oddy (1994)][20]. The resulting element is nonconforming (subparametric); i.e., the displacements are not continuous between the elements.

The geometry of the nonconforming element is described with the standard basis functions presented in Table 10.1; e.g.,

$$y = \sum_{i=1}^{n} N_i \, y_i, \quad 8 \leq n \leq 26. \tag{4}$$

It is well known that a single linear element, when subject to bending, responds in shear. This parasitic shear can be corrected if quadratic modes of deformation; i.e., pure bending, are incorporated in the element formulation [Hughes (1987)][8], [Chandra and Prathap (1989)][3].

For the nonconforming hexahedron the displacements are modified to include the necessary quadratic modes. In equations (5), (6) and (7), ϕ_i are the new basis functions for bending modes; α_i, β_i, and γ_i are their coefficients and the new degrees of freedom.

$$u = \sum_{i=1}^{n} N_i \, u_i + \sum_{i=1}^{3} \phi_i \alpha_i, \quad 8 \leq n \leq 26, \tag{5}$$

$$v = \sum_{i=1}^{n} N_i \, v_i + \sum_{i=1}^{3} \phi_i \beta_i; \quad 8 \leq n \leq 26, \tag{6}$$

$$w = \sum_{i=1}^{n} N_i \, w_i + \sum_{i=1}^{3} \phi_i \gamma_i \quad 8 \leq n \leq 26. \tag{7}$$

If there are no optional nodes then

$$\phi_1 = 1 - \xi^2, \quad \phi_2 = 1 - \eta^2, \quad \phi_3 = 1 - \zeta^2. \tag{8}$$

In practice, optional nodes are essential. Accordingly, a convenient general formulation was adopted to avoid dealing with the many possible combinations of optional nodes. As optional nodes are added each sublement becomes nonconforming and the basis functions become double-humped; e.g., $\phi_1 = 4|\xi|(1-|\xi|)$ expands to $\phi_1 = 4(|\xi|-1)+4(1-|\xi|^2)$. The double-humped basis function is used only for the Gauss point in the subelement of interest and is zero elsewhere. Table 10.2 summarizes the new additional basis functions required to convert the regular 8- to 26-node hexahedron to a nonconforming 8- to 26-node hexahedron.

Table 10.2. Additional basis functions – Nonconforming hexahedron.

Nodes present	ϕ
1,2,3,4,5,6,7,8	$\phi_1 = 1 - \xi^2$
1,2,3,4,5,6,7,8	$\phi_2 = 1 - \eta^2$
1,2,3,4,5,6,7,8	$\phi_3 = 1 - \zeta^2$
9,11,13,15,23,24,25,26	$\phi_1 = 4(\|\xi\| - 1) + 4\phi_1$
10,12,14,16,21,22,25,26	$\phi_2 = 4(\|\eta\| - 1) + 4\phi_2$
17,18,19,20,21,22,23,24	$\phi_3 = 4(\|\zeta\| - 1) + 4\phi_3$

To allow a distorted nonconforming hexahedron to satisfy the patch test, the appropriate strain-displacement matrix terms for the nodeless modes for each subelement were modified so that derivatives of x, y, and z with respect to ξ, η, and ζ were replaced by their values determined at the subelement centroid. The portion of the B matrix associated with the bending degrees of freedom for the first nodeless mode, $\hat{B}_1$, is:

$$\hat{B}_1 = \begin{bmatrix} \frac{\partial \phi_1}{\partial x} & 0 & 0 \\ 0 & \frac{\partial \phi_1}{\partial y} & 0 \\ 0 & 0 & \frac{\partial \phi_1}{\partial z} \\ \frac{\partial \phi_1}{\partial y} & \frac{\partial \phi_1}{\partial x} & 0 \\ 0 & \frac{\partial \phi_1}{\partial z} & \frac{\partial \phi_1}{\partial y} \\ \frac{\partial \phi_1}{\partial z} & 0 & \frac{\partial \phi_1}{\partial x} \end{bmatrix}. \tag{9}$$

Terms in $\hat{B}_1$ are replaced as follows:

$$\begin{bmatrix} \frac{\partial \phi_1}{\partial x} \\ \frac{\partial \phi_1}{\partial y} \\ \frac{\partial \phi_1}{\partial z} \end{bmatrix} = \frac{[J_{000}]^{-1} \det [J_{gp}]}{\det [J_{000}]} \times \begin{bmatrix} \frac{\partial \phi_1}{\partial \xi} \\ \frac{\partial \phi_1}{\partial \eta} \\ \frac{\partial \phi_1}{\partial \zeta} \end{bmatrix} \tag{10}$$

where $[J_{000}]^{-1}$, the inverse of the Jacobian matrix, is evaluated at the centroid of a subelement. The determinants $\det [J_{000}]$ and $\det [J_{gp}]$ refer to the

determinant of the Jacobian matrix evaluated at the subelement centroid and the Gauss point of interest, respectively.

The displacements associated with the nodeless modes are clearly specific to each element and are eliminated at the element level using static condensation and recovery [Cook (1981)][4]. Additional costs are incurred with the condensation of the stiffness matrix and recovery of the displacements associated with the nodeless modes. However, integration over the volume is less costly for a nonconforming 8-node hexahedron than for a 20-node quadratic brick since there are fewer Gauss points. Also, with the nodeless modes used, the cost of factoring the global stiffness matrix, when using a direct solver, does not increase.

In linear elastic FEA, the basis functions for the nodeless modes should not be included when integrating over surfaces or volumes in the calculation of consistent force vectors [Hughes (1987)][8]. The stress divergence is zero for the nodeless modes because no external forces or reactions are permitted on these degrees of freedom.

$$\int_{\Omega} \hat{B}^T \sigma \, d\Omega = F_{ext} = 0. \tag{11}$$

In a materially nonlinear FEA the stress state, σ, is modified for plasticity [Schreyer *et al.* (1979)][28] requiring an iterative solution. The modification of the stress field means the integral of the stress divergence associated with the nodeless modes is nonzero; i.e., there is a residual R.

$$\int_{\Omega} \hat{B}^T \sigma' \, d\Omega = R, \tag{12}$$

R was included in the force vector for the nodeless modes during condensation and recovery in all iterations. So, although external forces cannot directly excite the nodeless modes, thermal strains and residuals in nonlinear analyses may do so.

10.4. Nonconforming Elements in Thermal-Mechanical Analysis

The use of nonconforming 8- to 26-node hexahedrons was found to be approximately 20% more expensive than the use of selective reduced integration. This is a modest increase when it is considered that replacing all the linear hexahedrons with their nonconforming counterparts actually increases the number of degrees of freedom by about two and a half times. However, if need be, adaptive techniques; e.g., [McDill *et al.* (1991)][17]

[McDill and Oddy (1993)][19] can be modified so that nonconforming elements are used only in the areas of the mesh in which they would be of most benefit.

The nonconforming element provided a significant improvement in thermal-mechanical FEA. It quickly superseded the regular 8- to 26-node hexahedron. For example, it was used in the combined experimental and FEA investigation of a weaved repair weld on a 2.25Cr-1.0Mo steel. The investigation [Oddy *et al.* (1999)][25] provided an opportunity to validate numerical predictions against experimental measurements for a demanding case including complex 3-D thermal fields and stress fields caused by the oscillating path of the arc, phase transformations including transformation plasticity, temperature-dependent material properties and surface convection.

Neutron diffraction measurements of residual stresses for a sampling volume of 0.3 cm x 0.3 cm x 0.3 cm were made for three, identical welds on plates 25.4 cm x 25.4 cm x 1.9 cm. A fourth welded plate was used as a reference for the unstrained lattice parameters for the base metal, heat-affected zone and the fusion zone. All plates were taken from a single larger plate. The weaved patch was restricted to a rectangle 5 cm long with oscillations of 2.5 cm. The arc was on for 60 s with an average welding speed of 1.03 cm/s. Measurements of the three normal stress components were made on two traverses on the top and bottom surfaces as well as one through the thickness at the weld centre.

FEA of a weaved repair weld on a 2.25Cr-1.0Mo steel plate was then performed to compare the FEA residual stress predictions with those determined experimentally by neutron diffraction. In the FEA, creep strains were neglected since the time spent at high temperatures was small. Figure 10.2 shows the 5724-element mesh used for both the thermal and stress analyses. The 8- to 26-node hexahedron allowed a rapid transition from one element through the thickness at the edge of the plate to four elements through the thickness at the center of the plate. The thermal analysis allowed surface convection through 2740 surface elements. The stress analysis used nonconforming 8- to 26-node hexahedrons with the equivalent of over 30,000 nodes. Temperature-dependent thermal and mechanical properties were taken from a variety of sources; e.g. [BISRA (1953)][BISRA (1953)][2], [Alberry and Jones (1977)][1] as well as from dilatometric measurements [Oddy *et al.* (1999)][25].

Fig. 10.3 shows the longitudinal stress distribution computed from the top surface on a longitudinal scan along the weld centerline. It includes

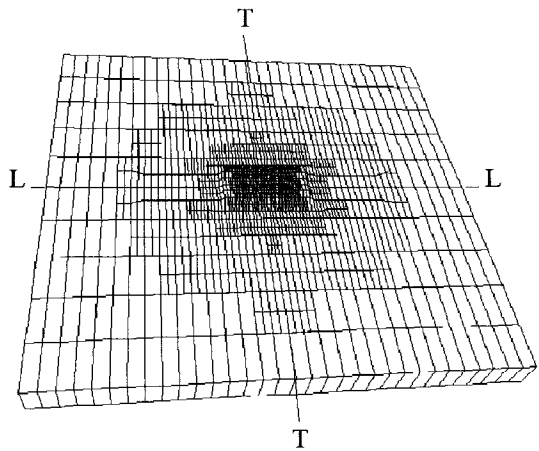

Fig. 10.2. Mesh used in the thermal and stress analyses of the weaved weld (L - longitudinal direction, T - transverse direction)

experimental average from three plates with a measurement precision error bar of 30 MPa equal to plus or minus one standard deviation [Oddy *et al.* (1999)][25]. The agreement between the FEA predictions and experimental measurements was found to be good with essential features found experimentally, reproduced in the FEA predictions although in the fusion zone the magnitude of the predicted stresses differed somewhat from experiment. Concerns raised in the project included the difficulty in finding suitable material properties as well as the size of the variations typically found in welds made in laboratory conditions. Field welds would presumably be subject to even larger variations.

10.5. 8- to 16-Node Solid Shell

The 8-to 26-node hexahedron was noted early on to have limitations in applications in which the elements were required to be thin (even just a little thin). The through-thickness behaviour of a linear hexahedron when used as a shell-like element contributes to a vastly overstiff $[K]$ and leads

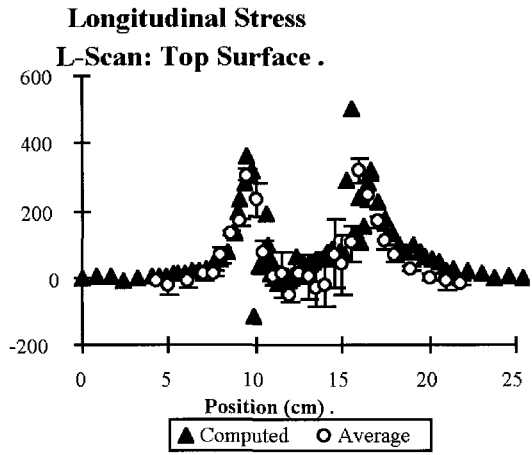

Fig. 10.3. Longitudinal stress distribution at the weld centerline, top surface

to results which are near-zero. Linear elements used in this way also have problems related to transverse shear and bending. The limitations of linear hexahedral elements in applications where thinness is needed are well understood; e.g., [Hughes *et al.* (1977)][10], [Parisch (1995)][26]. An analyst, unfamiliar with this issue using an element aspect ratio, $\mathcal{AR}$, of even 5 for example, may produce meaningless results in analyses involving bending.

These problems were less severe when the nonconforming elements were used. Nevertheless, it was clear that a solid shell was needed for modelling in the far field, away for example, from the severe thermal and stress gradients associated with the weld pool. In keeping with the original goals of limiting the number of different element types, special special shell-to-brick transition elements were not developed. Instead, solid shell and hexahedral elements were to co-exist within the mesh using the optional nodes to make a natural transition. A survey of past thermal-mechanical analyses suggested the solid shell required an $\mathcal{AR}$ of up to about 100.

Cumbersome rotational degrees of freedom seen in the degenerate Hughes and Liu shell [Hughes and Liu (1981)][9] were avoided by using

displacement degrees of freedom similar to that of [Parisch (1995)][26] and [Kanok-Nukulchai *et al.* (1981)][11]. Displacement degrees of freedom were more practical from an implementation point of view. With the selection of displacement degrees of freedom, an 8- to 16-node shell as shown in Fig. 10.4 was developed from the original 8- to 26-node hexahedron. Eight mandatory vertex nodes are accompanied by pairs of midedge nodes on the upper and lower surfaces of the shell; e.g., 9 and 13. The optional node pairs permit mesh grading and may be used in any combination. As with the original hexahedron, a pair of midedge nodes alters the basis functions of the corner nodes on two edges and creates smooth (C^∞ continuous) subelements within the element.

The solid shell is incrementally objective (rigid body rotations do not generate strains), it includes finite transverse shear strains, and has a through-thickness thinning capability [Gallbraith and Hallquist (1995)][5].

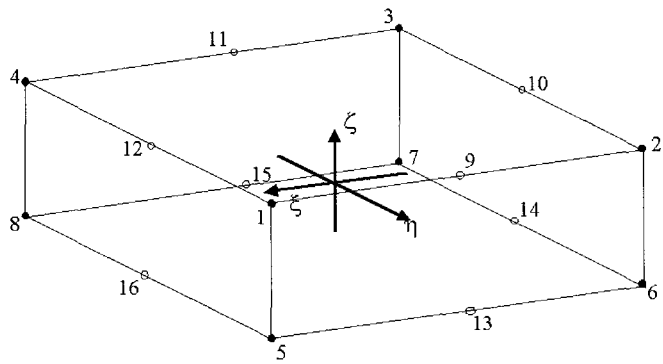

Fig. 10.4. Nodal positions in the 8- to 16-node solid shell

In a degenerated shell, the static constraints are usually those of zero-

normal stress and zero-normal stress rate [Stanley *et al.* (1986)][31]. To accommodate the static constraint in the formation of the stiffness matrix, it was decided to use a modified plane stress D matrix similar to that of [Kanok-Nukulchai *et al.* (1981)][11]. Compatibilty with the effective stress function [Kogic and Bathe (1987)][13] was critical for the analysis of creep and other similar phenomena seen in thermal-mechanical FEA; e.g., [Svobda *et al.* (1998)][33].

The kinematic constraints [Stanley *et al.* (1986)][31] are those of straight normals and incrementally-rigid normals. A fictitious coefficient applied to through-thickness term in the elastic stress-strain matrix, D was used by [Kanok-Nukulchai *et al.* (1981)][11]. Here, a through-thickness degradation factor, df, based on $\mathcal{AR}$ is applied to the strain-displacement matrix, B. This allows the element to be thinner without ill-conditioning of the stiffness matrix. Transverse shear locking and membrane locking that also seen in thin hexahedral elements, are eliminated by reduced integration.

The evolution of the solid shell required a smooth integration in the existing FEA software. For this reason the element was developed in the isoparametric style with the normal global (x, y, z) to isoparametric (ξ, η, ζ) relationship preserved through the Jacobian matrix. The shell is initially defined by a reference surface at $\zeta = 0$. Laminae are established at the planes of the Gauss points parallel to the reference surface. The isoparametric style is limited slightly in that ζ must be oriented in the thin through-thickness direction of the element.

A local lamina coordinate system is established at each Gauss point. The transformation from the global coordinate system to the local (and vice versa) is constructed from two base vectors tangent to the lamina and the normal. The lamina surface base vectors are as close as possible to the ξ and η directions [Hallquist and Benson (1986)][7], [Hughes (1987)][8]. The stress and strain are evaluated in the lamina system and rotated back to the global system as required.

A fibre coordinate system [Hallquist and Benson (1986)][7], [Hughes (1987)][8] is also required for the application of df. A fibre is a line in the ζ direction for a fixed ξ and η. At each node pair a unique local coordinate system is constructed in which one direction coincides directly with the fibre direction.

The displacement of a point is simply the displacement of the reference surface plus the displacement relative to the reference surface [Surana (1980)][32], [Kanok-Nukulchai *et al.* (1981)][11]. Modified relative displace-

ments $[\overline{U}_i{}']$ improve the through-thickness behaviour of the element:

$$[U] = \sum_{i=1}^{n} N_i(\xi, \eta, 0)\ [U_i] + \sum_{i=1}^{n} N_i(\xi, \eta, 0)\zeta[\overline{U}_i{}']. \tag{13}$$

$N_i (i = 1$ to n, for $8 \leq n \leq 16)$ extracted from Table 10.1 for nodes 1 through 16 are evaluated at the reference surface ($\zeta = 0$).

The degradation factor is applied in the fibre direction to the relative displacement, $\overline{U}_i$. There is a rotation using $[\Re]$, a 3×3 rotation matrix, into the fibre system, followed by the application of the degradation factor using $\mathcal{I}$, followed by a a rotation back to the global system [Hallquist and Benson (1986)][7], [Hughes (1987)][8].

$$[\overline{U}_i{}'] = \mathcal{I}_i[\overline{U}_i], \tag{14}$$

where:

$$[\overline{U}_i] = \frac{1}{2}\left[(U_i^{\text{top}} - U_i^{\text{bot}})\right], \quad \mathcal{I}_i = [\Re]^T \begin{bmatrix} 1 & 0 & 0 \\ 0 & 1 & 0 \\ 0 & 0 & df \end{bmatrix} [\Re]. \tag{15}$$

The value of df is based on $\mathcal{AR}$ which depends on the characteristic dimension, h, and the thickness, t. The latter are extracted from the Jacobian, evaluated at the element centroid [Kerlick and Klopfer (1982)][12]. Standard tests [MacNeal and Harder (1985)][14] provided the relationship between df and $\mathcal{AR}$ [McDill *et al.* (2001)][21]. It is helpful to note that a well-formed element with the fibre coordinate system aligned with the global axes will have $df = 1$ and $\mathcal{I}_i = I$, the identity matrix.

$$df = 2500 \times \mathcal{AR}^{-2} \quad (0 < df \leq 1). \tag{16}$$

Therefore,

$$[U] = \sum_{i=1}^{n} N_i(\xi, \eta, 0)\ [U_i] + \sum_{i=1}^{n} N_i(\xi, \eta, 0)\frac{\zeta}{2}\mathcal{I}_i[(U_i^{\text{top}} - U_i^{\text{bot}})]. \tag{17}$$

The next step is the development of the strain-displacement relationship. For a linear 8-node brick, $[B]$ for node 1 for strain as a vector with $[\epsilon_{xx}\ \epsilon_{yy}\ \epsilon_{zz}\ \gamma_{xy}\ \gamma_{yz}\ \gamma_{zx}]^T$ is:

$$B_1 = \begin{bmatrix} \frac{\partial N_1}{\partial x} & 0 & 0 \\ 0 & \frac{\partial N_1}{\partial y} & 0 \\ 0 & 0 & \frac{\partial N_1}{\partial z} \\ \frac{\partial N_1}{\partial y} & \frac{\partial N_1}{\partial x} & 0 \\ 0 & \frac{\partial N_1}{\partial z} & \frac{\partial N_1}{\partial y} \\ \partial N_1 \partial z & 0 & \frac{\partial N_1}{\partial x} \end{bmatrix}. \tag{18}$$

Collecting all relevant terms from nodal pairs; e.g., nodes 1 (top) and 5 (bottom), and those contributed by $\mathcal{I}$ gives B for the 8- to 16-node solid shell: e.g., the first column in B_1 is:

$$\begin{bmatrix} \frac{\partial N_1}{\partial x} + \frac{\partial (N_1\zeta)}{\partial x}\mathcal{I}_{11} \\ \frac{\partial (N_1\zeta)}{\partial y}\mathcal{I}_{21} \\ \frac{\partial (N_1\zeta)}{\partial z}\mathcal{I}_{31} \\ \frac{\partial N_1}{\partial y} + \frac{\partial (N_1\zeta)}{\partial y}\mathcal{I}_{11} + \frac{\partial (N_1\zeta)}{\partial x}\mathcal{I}_{21} \\ \frac{\partial (N_1\zeta)}{\partial y}\mathcal{I}_{31} + \frac{\partial (N_1\zeta)}{\partial z}\mathcal{I}_{21} \\ \frac{\partial N_1}{\partial z} + \frac{\partial (N_1\zeta)}{\partial z}\mathcal{I}_{11} + \frac{\partial (N_1\zeta)}{\partial x}\mathcal{I}_{31} \end{bmatrix}. \tag{19a}$$

Similarly the second and third columns in B_1 are:

$$\begin{bmatrix} \frac{\partial (N_1\zeta)}{\partial x}\mathcal{I}_{12} \\ \frac{\partial N_1}{\partial y} + \frac{\partial (N_1\zeta)}{\partial y}\mathcal{I}_{22} \\ \frac{\partial (N_1\zeta)}{\partial z}\mathcal{I}_{32} \\ \frac{\partial N_1}{\partial x} + \frac{\partial (N_1\zeta)}{\partial x}\mathcal{I}_{22} + \frac{\partial (N_1\zeta)}{\partial y}\mathcal{I}_{12} \\ \frac{\partial N_1}{\partial z} + \frac{\partial (N_1\zeta)}{\partial z}\mathcal{I}_{22} + \frac{\partial (N_1\zeta)}{\partial y}\mathcal{I}_{32} \\ \frac{\partial (N_1\zeta)}{\partial z}\mathcal{I}_{12} + \frac{\partial (N_1\zeta)}{\partial x}\mathcal{I}_{32} \end{bmatrix}, \begin{bmatrix} \frac{\partial (N_1\zeta)}{\partial x}\mathcal{I}_{13} \\ \frac{\partial (N_1\zeta)}{\partial y}\mathcal{I}_{23} \\ \frac{\partial N_1}{\partial z} + \frac{\partial (N_1\zeta)}{\partial z}\mathcal{I}_{33} \\ \frac{\partial (N_1\zeta)}{\partial y}\mathcal{I}_{13} + \frac{\partial (N_1\zeta)}{\partial x}\mathcal{I}_{23} \\ \frac{\partial N_1}{\partial y} + \frac{\partial (N_1\zeta)}{\partial y}\mathcal{I}_{33} + \frac{\partial (N_1\zeta)}{\partial z}\mathcal{I}_{23} \\ \frac{\partial N_1}{\partial x} + \frac{\partial (N_1\zeta)}{\partial x}\mathcal{I}_{33} + \frac{\partial (N_1\zeta)}{\partial z}\mathcal{I}_{13} \end{bmatrix}. \tag{19b}$$

The modified plane stress D matrix is in the lamina system. Since B is in the global system, D is rotated from the lamina coordinate system to the global coordinate system when the stiffness matrix is calculated:

$$D = \begin{bmatrix} \frac{E}{1-\nu^2} & \frac{E\nu}{1-\nu^2} & 0 & 0 & 0 & 0 \\ & \frac{E}{1-\nu^2} & 0 & 0 & 0 & 0 \\ & & \frac{E}{1-\nu^2} & 0 & 0 & 0 \\ & & & \frac{E}{2(1+\nu)} & 0 & 0 \\ & \text{symmetric} & & & \frac{E}{2(1+\nu)} & 0 \\ & & & & & \frac{E}{2(1+\nu)} \end{bmatrix}. \tag{20}$$

Selective reduced integration [Hallquist and Benson (1986)][7] alleviates any transverse shear and membrane locking. Unlike typical shell formulations, here B is in the global system. Hence only those terms in the lamina which require reduced integration are considered. The transverse shear and membrane strains in the lamina system are treated as components of the strains in the global system.

A local *abc* system is established in each lamina so that γ_{ac} and γ_{bc} are transverse shear strains and γ_{ab} is the membrane strain. Consider a lamina transverse shear strain of interest; e.g., γ_{bc}.

In the $\overline{B}$ approach this strain is replaced by $\gamma_{bc}^{00\zeta}$ where 00ζ refers to the lamina centroid.

The global strain tensor is converted to find the tensor shear strain in abc. Consider the scalar ϵ_{bc}.

$$\epsilon_{bc} = [P] : [\epsilon_{xyz}], \tag{21}$$

where: $[P]$ and $[\epsilon_{xyz}]$ are 3×3 tensors and : is the scalar product notation. Since $[P]$ involves $[b]$ and $[c]$, it describes the direction of ϵ_{bc} in the strain space.

$$[P] = \frac{1}{2}\left([c_1\ c_2\ c_3]^T[b_1\ b_2\ b_3] + [b_1\ b_2\ b_3]^T[c_1\ c_2\ c_3]\right), \tag{22}$$

where, e.g, c_1 is the x component of [c], $\epsilon_{xz} = \gamma_{xz}/2$ and

$$[\epsilon_{xyz}] = \begin{bmatrix} \epsilon_{xx} & \epsilon_{xy} & \epsilon_{xz} \\ \epsilon_{xy} & \epsilon_{yy} & \epsilon_{yz} \\ \epsilon_{xz} & \epsilon_{yz} & \epsilon_{zz} \end{bmatrix}. \tag{23}$$

After expansion it can be shown that:

$$\gamma_{bc} = 2[P_{11}\ P_{22}\ P_{33}\ P_{12}\ P_{23}\ P_{31}][\epsilon_{xx}\ \epsilon_{yy}\ \epsilon_{zz}\ \gamma_{xy}\ \gamma_{yz}\ \gamma_{zx}]^T. \tag{24}$$

γ_{bc} is the magnitude of the component of the global strain in the bc direction and should be removed from $[\epsilon]$ and replaced by $\gamma_{bc}^{00\zeta}$.

The tensor (or direction) of γ_{bc} is now required,

$$[\epsilon_{xyz}] = [P]\gamma_{bc}. \tag{25}$$

A further expansion gives:

$$[\epsilon_{xx}\ \epsilon_{yy}\ \epsilon_{zz}\ \gamma_{xy}\ \gamma_{yz}\ \gamma_{zx}]^T = [\mathcal{S}_{bc}][B][U]. \tag{26}$$

$\mathcal{S}_{bc}$ is a 6×6 matrix which takes the strain in xyz, finds the magnitude of the component of the global strain ϵ in the γ_{bc} direction; i.e., the direction of γ_{bc} in the strain space, and then creates the tensor for the strain component that should be removed from the global strain ϵ.

From the Gauss point strain in xyz; i.e., $[B][U]$, remove the local contribution of γ_{bc} and add $\gamma_{bc}^{00\zeta}$:

$$[\epsilon] = [B][U] - [\mathcal{S}_{bc}][B][U] + [\mathcal{S}_{bc}^{00\zeta}][B^{00\zeta}][U], \tag{27}$$

$$[\epsilon] = \left[[I] - [\mathcal{S}_{bc}][B] + [\mathcal{S}_{bc}^{00\zeta}][B^{00\zeta}]\right][U]. \tag{28}$$

In effect $[\epsilon] = [\overline{B}][U]$. This approach is repeated for the other transverse shear strain and the membrane strain.

For the FEA implementation, $[a]$, $[b]$ and $[c]$ are constructed at the lamina centroids and $[\mathcal{S}_{bc}^{00\zeta}]$, $[\mathcal{S}_{ac}^{00\zeta}]$, $[\mathcal{S}_{ab}^{00\zeta}]$ and $[B^{00\zeta}]$ are evaluated. $[\mathcal{S}_{bc}]$, $[\mathcal{S}_{ac}]$, $[\mathcal{S}_{ab}]$ and $[B]$ are evaluated at each Gauss point.

The final step in the development of the solid shell was its incorporation with the effective stress function (EFS) [Kogic and Bathe (1987)][13]. Given a set of displacements calculated by a frontal solver or the conjugate gradient solver, strains, stress, internal loads and residual loads can be determined. In this case the algorithm uses a temperature-dependent yield criterion (von-Mises) with isotropic-kinematic work hardening. From an estimate of the deviatoric total strain increment, the deviatoric stress is found using the ESF for standard elasto-plasticity and creep. For finite deformation, all plasticity correction is done in the initial orientation and then transformed to the final orientation. For the 8- to 16-node shell, there is an iteration [Hallquist and Benson (1986)][7] around the ESF routine to satisfy the static constraint related to plane stress. The strains are determined in the laminae and the stresses are calculated. These stresses are then rotated back to the global system. Then, finally, the stress, incremental strain, and plastic strain are rotated forward onto the final orientation.

An addition to the ESF detects whether the problem is materially linear or materially nonlinear. In a linear problem; e.g., when there is no plasticity or creep, the through-thickness stress from the ESF is modified using the D matrix (eq. 20) and the through-thickness strain. This stress is then used in the calculation of the stress divergence (see eq. (11)) and in the convergence of the increment. If the problem is materially nonlinear, the stress is based on guesses of strain which are bounded by the through-thickness strain, ϵ_{33}, for a fully elastic step and a strain based on a fully plastic step. Iterations, j, around the ESF proceed with convergence checked using a strain-based limit similar to that of Hallquist [Hallquist and Benson (1986)][7].

$$\frac{|(\Delta\epsilon_{33}^{j} - \Delta\epsilon_{33}^{j-1}|}{|\Delta\epsilon_{33}^{j+1}|} < 10^{-5}. \tag{29}$$

In a strict shell, the normal stress must be zero but in a thermal-mechanical problem this may not be the case if material is restrained by adjacent material. For this reason an additional check based on the change in stress, σ_{33}, is also implemented and is placed just before the strain-based check.

$$\frac{|\sigma_{33}^{j} - \sigma_{33}^{j-1}|}{E} \leq 10^{-8}. \tag{30}$$

10.6. Solid Shell Elements in Thermal-Mechanical Analysis

The solid shell element has been useful in linear, geometrically nonlinear and material nonlinear problems. The plate patch and rectangular plate tests [MacNeal and Harder (1985)][14] have been successfully tested to aspect ratios of 1000 or more. However, the solid shell will be used most frequently in applications requiring $\mathcal{AR}$ of up about 100. The Sordelis-Lo Roof and a uniaxial tensile test are used here to illustrate the capability of the element for use in the far field with aspect ratios in this range.

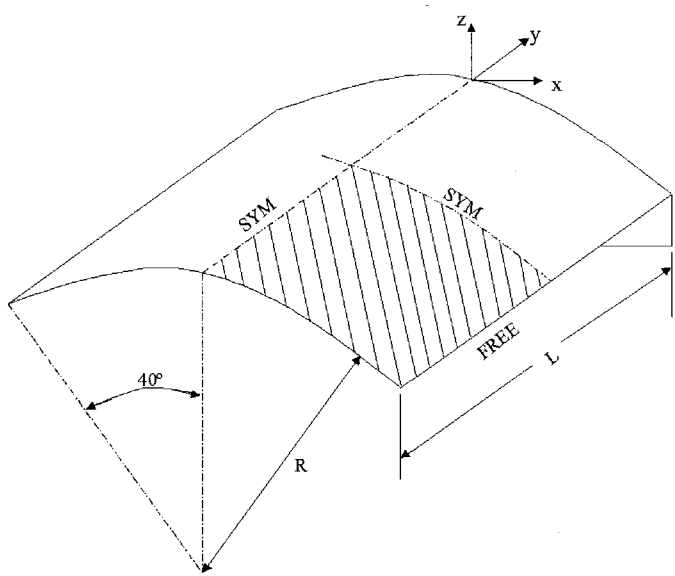

Fig. 10.5. Characteristics of the Sordelis-Lo Roof

The Scordelis-Lo Roof is a challenging problem which incorporates aspects of extension, in-plane and out-of-plane shear, twist, bending and higher order stress gradients [MacNeal and Harder (1985)][14] and involves complex states of membrane stress [Simo *et al.* (1990)][29]. Fig. 10.5 shows some of the conditions for the test. The radius of curvature, R, and the length, L, are 25.0 and 50.0 respectively. The angle from the apex of the roof to the free edge is 40° while t is 0.25. One quarter of the roof is mod-

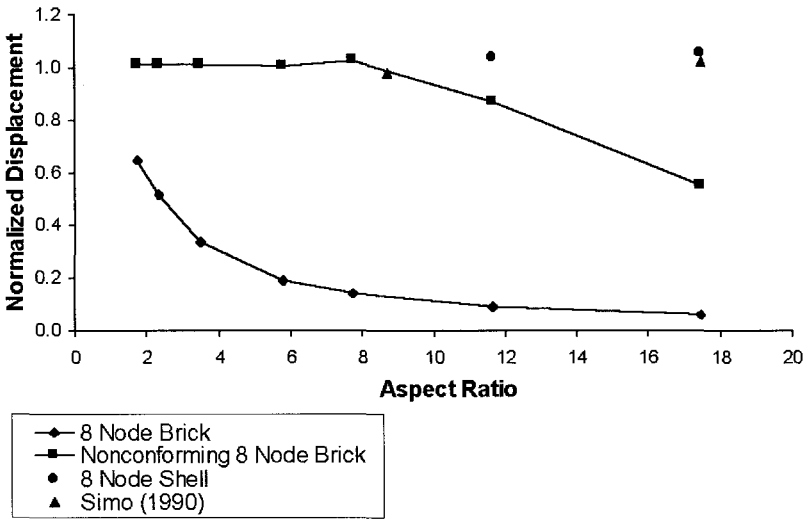

Fig. 10.6. Normalized displacement vs. AR - geometrically linear

elled with 8-node elements (linear hexahedron, nonconforming hexahedron and solid shell). The elastic modulus is 4.32×10^8 while Poisson's ratio is 0.

A downward load of 90/unit area was applied. Mesh densities of 4×4, 6×6, 9×9 and 30×30 are used for meshes one element thick.

The accuracy of the solution is based on the displacement at the midside node on the free edge. Fig. 10.6 shows the results normalized by 0.3086, the classic linear solution. Normalization by 0.3024 is common [MacNeal and Harder (1985)][14]. Results reported by Simo [Simo *et al.* (1990)][29] are shown for comparison. Locking of simple 8-node bricks is clearly evident at even small aspect ratios (less than 5). The nonconforming elements perform well to an $\mathcal{AR}$ of about 10. The new shell does not lock for $\mathcal{AR}$ less than 20 which is associated with a 4×4 mesh. The geometry of the problem cannot be captured by fewer elements.

The Scordelis-Lo Roof can also be treated as a geometrically nonlinear (large deformation) problem [Kanok-Nukulchai *et al.* (1981)][11]. In the

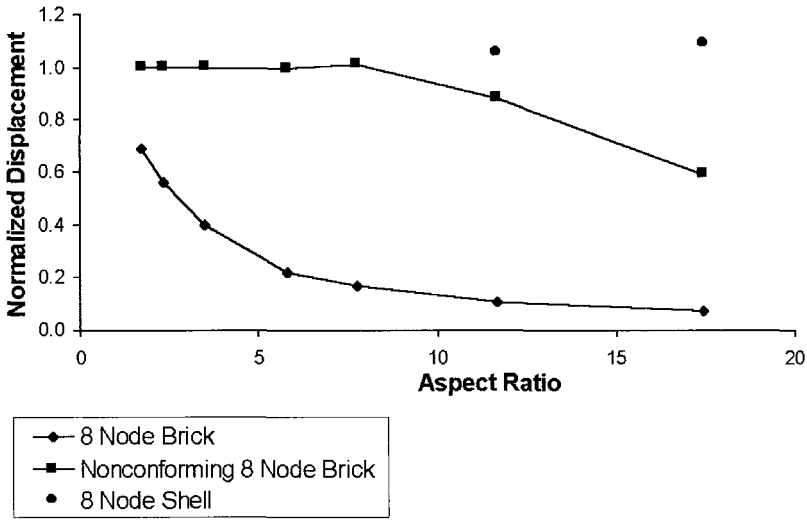

Fig. 10.7. Normalized displacement vs. AR - geometrically nonlinear

FEA, the regular hexahedrons and the nonconforming hexahedrons used a full Newton–Raphson technique while the solid shell elements required a modified Newton–Raphson approach in combination with line search. Fig. 10.7 shows locking of regular bricks while nonconforming elements perform well for $\mathcal{AR}$ less than 10. In this case, the results were normalized to a displacement of 0.2613, the solution obtained by a very dense mesh of nonconforming elements with $\mathcal{AR}$ less than 2. The new shell element did not exhibit locking for $\mathcal{AR}$ less than 20.

A simple bar fixed at one end with either prescribed loads or prescribed displacement applied to the free end in the plane of the shell illustrates the use of the shell in a materially nonlinear problem. Several cases including low and high hardening modulus, with and without mesh grading and with various aspect ratios were all tested with good results. For cases with low hardening modulus, Considère's condition, or plastic collapse, was observed for $\mathcal{AR}$ of about 25. In this condition, thinning reduces the load capacity more rapidly than strain hardening increases the load capacity.

Figure 10. 8 shows the results for the case with a high hardening modulus

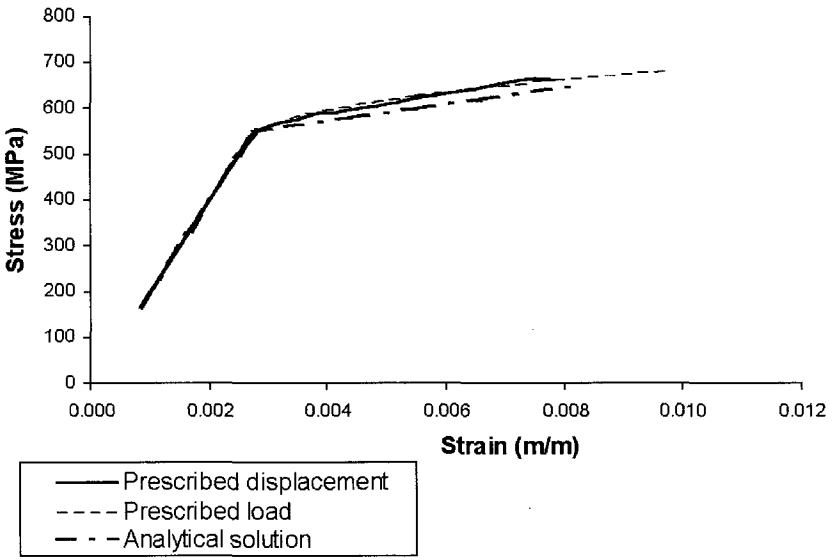

Fig. 10.8. Stress vs strain for uniaxial loading - materially nonlinear

and $\mathcal{AR}$ of about 15. It uses an elastic modulus, E, of 0.2×10^{12}; Poisson's ratio of 0.3; a uniaxial yield strength of 5.5×10^8 and a hardening modulus; i.e., $\frac{E \times E_t}{E - E_t}$ where the tangent modulus, $E_t = 0.1E$.

The prescribed load of 750 MPa was applied over 12 increments. Alternatively, the total prescribed displacement was 0.025 applied over 20 increments. A modified Newton–Raphson technique (without line search) was used. The analytical solution is $\epsilon = \frac{\sigma}{E}$, for $\sigma \leq \sigma_y$ and $\epsilon = \frac{\sigma}{E} + \frac{\sigma - \sigma_y}{E_t}$, for $\sigma > \sigma_y$ where σ_y is the yield strength. The three cases show excellent agreement.

In the thermal-mechanical analysis of large structures, the principal benefit of the 8- to 16-node shell will be in the far field in combined hexahedral-solid shell meshes. The solid shell elements have been used in tandem with the hexahedral elements in complex thermal-mechanical fields particularly in the far field; e.g., [McDill *et al.* (2001)][21]. The 8- to 16-node shell is computationally as expensive as a nonconforming hexahedral element; i.e., about 20% more expensive than a regular linear hexahedron. However, there

is a substantial improvement in performance. In geometrically and materially nonlinear problems, the shell is more expensive, requiring more iterations but converging to a superior answer justifying the increased costs for high aspect ratio areas of the mesh. In the future, the development of a nonconforming 8- to 16-node shell is expected to further improve the behaviour of these elements when they are used in the far field.

10.7. Contributions

An evolution of solid elements for use in 3-D thermal-mechanical FEA of manufacturing processes such as welding has been illustrated. The first element, an 8- to 26-node linear hexahedron, was initially developed to allow rapid mesh grading in both thermal and stress analyses. This element was essential in early analysis although selective reduced integration was needed in the stress portion for plasticity as was the use of isothermal elements to provide consistent strain fields. Limitations in the element particularly those just mentioned, combined with a problem of parasitic shear in linear elements subject to bending, led to the evolution of the 8- to 26-node nonconforming hexahedron. This element removed the need for selective reduced integration and allowed the full thermal field to be used in some cases. The nonconforming version was computationally more expensive that original element but provided nearly two and a half times the number of degrees of freedom. The 8- to 26-node linear hexahedron was also subject to locking and ill-conditioning of the stiffness matrix when used in applications requiring thinness. The nonconforming version was less sensitive to these problems but it was clear that a solid shell element with the capability to grade without the need for special transition elements would be beneficial. The evolution of the original hexahedron to an 8- to 16-node solid shell element followed. This element has been shown to perform very well in difficult tests and integrates smoothly with both the original and nonconforming hexahedrons. The next stage in the evolutionary process is the extension of the solid shell to a nonconforming version that may offer advantages in problems with applications in which a higher order thin element might be beneficial in the far field.

Acknowledgments

Over the period of the evolution of these elements a number of colleagues have been helpful. In particular, the author is indebted to Dr. J.A. Goldak, principal co-developer of the 8- to 26-node linear hexahedron, and Dr. H.R.

Runnemalm, principal co-developer of the 8- to 16-node solid shell. Also, the careful attentiveness of the late Dr. Alan Oddy P.Eng. must be mentioned. Alan assisted in the implementation of all three elements in the FEA algorithm. His contribution to the nonlinear aspects of the nonconforming hexahedron and in the rotations required for the solid shell were especially valuable. The financial support of the Natural Sciences and Engineering Research Council (NSERC) of Canada (Operating Grant 41745) is also gratefully acknowledged.

References

1. Alberry, P. J. and Jones, W. K. C. (1977). Structure and hardness of 0.5Cr-Mo-V and 2Cr-Mo simulated heat affected zones, *Metals Technology.* **4**, pp. 557–566.
2. British Iron and Steel Research Institute (1953). *Physical Constants of Some Commercial Steels at Elevated Temperatures.* Butterworths, London.
3. Chandra, S. and Prathap, G. (1989). A field-consistent formulation for the eight-noded solid finite element, *Comp. and Struct.* **33**, pp. 345–355.
4. Cook, R. D. (1981). *Concepts and Applications of Finite Element Analysis.* Department of Engineering Mechanics University of Wisconsin, Madison.
5. Gallbraith, P. C. and Hallquist, J. O. (1995). Shell-element formulations in LS-DYNA3D: their use in the modelling of sheet forming, *J. Materials Processing Technology.* **50**, pp. 158–167.
6. Goldak, J. A., McDill, M. J., Oddy, A. S., Bibby, M. J., House, R., Chakravarti, A. P., (1986). Progress in computing residual stress and strain in welds, *Proc. Int. Conf. on Trends in Welding Research.* Gatlinburg, TN.
7. Hallquist, J. O. and Benson, D. J. (1986). A comparison of an implicit and explicit implementation of the Hughes-Liu shell, *Finite Element Methods for Plate and Shell Structures.* ed. Hughes, T. R. J. and Hinton, E., Pineridge Press, Swansea. **1**, pp. 395-431.
8. Hughes, T. J. R. (1987). *The Finite Element Method, Linear Static and Dynamic Finite Element Analysis.* Prentice Hall N. J., pp. 383–417.
9. Hughes, T. J. R and Liu, W. K. (1981). Nonlinear finite element analysis of shells: part I, three-dimensional shells, *Comm. Appl. Num.* **26**, pp. 331–362.
10. Hughes, T. J. R., Taylor. R. L. and Kanok-Nukulchai, W. (1977). A simple and efficient finite element for plate bending, *Int. J. Numer. Meth. Engng.* **11**, pp. 1529–1547.
11. Kanok-Nukulchai, W., Taylor, R. L. and Hughes, T. J. R. (1981). A large deformation formulation for shell analysis by the finite element method, *Comp. and Stuct.* **13**, pp. 19–27.
12. Kerlick, G. and Klopfer, G. (1982). Assessing the quality of curvilinear coordinate meshes by decomposing the jacobian matrix, *Numerical Grid Generation.* ed. Thompson, J. F., Applied Mathematics and Computation, North-Holland, pp. 787–807.
13. Kogic, M. and Bathe K.-J. (1987). The effective-stress-function algorithm

for thermo-elasticity and creep, *Int. J. Numer. Meths. Engng.* **24**, pp. 1509–1532.

14. MacNeal, R. H. and Harder, R. L. (1985). A proposed standard set of problems to test finite element accuracy, *Finite Element Anal. Design.* **I**, pp. 3–20.
15. McDill, J. M., Goldak, J. A., Oddy, A. S. and Bibby, M. J. (1987). Isoparametric quadrilaterals and hexahedrons for mesh-grading algorithms, *Comm. Appl. Num. Meth.* **3**, pp. 155–163.
16. McDill, J. M., Oddy, A. S., Goldak, J. A. and Bennisson, S. (1990). Finite element analysis of weld distortion in carbon and stainless steels, *Strain Analysis for Eng. Des.* **25**, pp. 51–53.
17. McDill, J. M., Oddy, A. S. and Goldak, J. A. (1991). An adaptive mesh-management algorithm for three-dimensional automatic finite element analysis, *Trans. CSME.* **15**, pp. 57–70.
18. McDill, J. M., Oddy A. S. and Goldak, J. A. (1992). Comparing 2-D plane strain and 3-D analysis of residual stresses in welds, *Proc. 3rd Int. Conf. on Trends in Welding Research.* Gatlinburg, TN.
19. McDill, J. M. and Oddy, A. S. (1993). Arbitrary coarsening for adaptive mesh management in automatic finite element analysis, *J. Math. Model. and Sci. Computg.* **2**, pp. 1072–1077.
20. McDill, J. M. and Oddy, A. S. (1994). A nonconforming eight to 26-node hexahedron for three-dimensional thermal-elasto-plastic finite element analysis, *Comp. and Struct.* **54**, pp. 183–189.
21. McDill, J. M., Runnemalm, K. H. and Oddy, A. S. (2001). An 8- to 16-node solid graded shell element for far-field applications in thermal-mechanical FEA, *J. Math. Model. and Sci. Computg.* **13**, pp. 177–190.
22. Nagtegaal, J. C., Parks, D. M. and Rice, J. R. (1974). On numerically accurate finite element solutions in the fully plastic range, *Comp. Meth. App. Mech. and Engng.* **4**, pp. 153–177.
23. Oddy, A. S., Goldak, J. A. and McDill, J. M. (1990). A general relation for transformation plasticity relation in 3D finite element analysis of welds, *European J. of Mechanics, A/Solids* **9**, pp. 253–263.
24. Oddy, A. S., McDill, J. M. and Goldak, J. A. (1990). Consistent strain fields in 3D finite element analysis of welds, *J. Press. V. Tech., Trans. ASME.* pp. 309–311.
25. Oddy, A. S., McDill, J. M., Root, J. H., Braid, J. E. M. and Marsiglio, F. (1999). Measurement, variability and prediction of residual stresses in weaved repair welds, *Proc. 5th Int. Seminar on Numerical Analysis of Weldability.* Graz, Austria. ed. H. Cerjak, pp. 529-548.
26. Parisch, H. (1995). A continuum-based shell theory for non-linear applications, *Int. J. Numer. Meth. Engng.* **50**, pp. 1855–1883.
27. Rheinbolt, W. C. and Meszenteyi, F. H. (1980). On a data structure for adaptive finite element mesh refinements, *ACM Trans on Math. Software.* **6**, pp. 2, 166–187.
28. Schreyer, H. L., Kulak, R. F. and Kramer, J. M. (1979). Accurate solutions for elastic-plastic models, *Trans. ASME, J. Pres. V. Tech.* **101**, pp. 226–234.

29. Simo, J. C., Rifai, M. S. and Fox, D. D. (1990). On a stress resultant geometrically exact shell model, Part IV: Variable thickness shells with through-the-thickness stretching, *Comp. Meths. in Appl. Mech. Engng.* **81**, pp. 91–126.
30. Somervaille, I. J. (1972). A technique for mesh grading applied to conforming plate bending finite elements, *Int. J. Numer. Meth. in Engng.* **6**, pp. 310–312.
31. Stanley, G. M., Park, K. C. and Hughes, T. J. R. (1986). Continuum-based resultant shell elements, *Finite Element Methods for Plate and Shell Structures.* ed. Hughes, T. J. R and Hinton E., Pineridge Press, Swansea. **1**, pp. 1–45.
32. Surana, K. S. (1980). Transitional finite elements for three-dimensional stress analysis, *Int. J. Numer. Meth. Engng.* **15**, pp. 991–1020.
33. Svobda, A., Lindgren, L.-E., and Oddy, A. S. (1998). The effective-stress-function approach for pressure-dependent plasticity applied to hot isostatic pressing, *Int. J. Numer. Meth. Engng.* **43**, pp. 587–606.

Nomenclature

a, b, c	local axes
$\mathcal{AR}$	the aspect ratio; e.g, h/t of the element
B	maps the nodal displacement vector into strain at a given point
$\hat{B}_1$	portion of the B matrix associated with the bending degrees of freedom for the first nodeless node
C^0	the function is continuous, its first derivative is not
C^∞	the function and all its derivatives are continuous
C_f	cost of factoring (reduction and back-substitution) of K
C_r	cost ratio of uniform to graded mesh
d_f	number of degrees of freedom in the problem
df	the degradation factor applied to the through-thickness direction of the element
D	the stress-strain (elastic) matrix used in the determination of the stiffness matrix on the first iteration
E	elastic modulus
E_t	the tangent modulus
h	the characteristic dimension of the element
f_w	frontwidth of the problem
F_{ext}	external forces
gp	subscript for the evaluation of a quantity at the Gauss point
i	subscript for a Gauss point, node or nodeless mode
I	the identity matrix

$\mathcal{I}$	a 3×3 matrix which incorporates the degradation factor
j	coordinate subscript associated with node j or superscript for ESF iterations
J	Jacobian matrix
K	stiffness matrix
L	longitudinal direction or length
m	number of elements on an edge of a uniform mesh
n	the number of nodes in the element
N_i	basis function for node i
P	3×3 tensor which describes the direction of ϵ in the strain space
R	residual or stress divergence
R	radius
$\Re$	a 3×3 rotation matrix
$\mathcal{S}$	a 6×6 matrix used to find the magnitude of a component of the global strain
t	the thickness of the element
T	transverse direction
u, v, w	the x, y, and z displacements, respectively
U	the global displacement vector $[u\ v\ w]^T$
$\overline{U}_i$	the relative displacement vector
$\overline{U}_i{}'$	the modified relative displacement vector
x, y, z	coordinates in the physical domain
α, β, γ	coefficients of and new degrees of freedom for ϕ_i
γ	shear strain
ϵ	direct strain
δ	Kronecker delta
ζ, ζ'	coordinate in the computational domain
$\eta,\ \eta'$	coordinate in the computational domain
$\xi,\ \xi'$	coordinate in the computational domain
ϕ_i	basis functions for the nodeless modes
σ	stress state
σ'	modified
σ_y	uniaxial yield strength
ν	Poisson's ratio
Ω	the domain for integration over the volume
000	subscript for the evaluation of a quantity at the subelement centroid
00ζ	subscript for the lamina centroid

CHAPTER 11

QUANTIZATION EFFECTS IN SHALLOW POWDER BED VIBRATIONS

Joseph Pegna

Freeform Fabrication Laboratories, Department of Mechanical Engineering, École Polytechnique de Montréal, Montréal (Québec), Canada H3C 3A
E-mail: joseph.pegna@polymtl.ca

Jun Zhu

Freeform Fabrication Laboratories, Department of Mechanical Engineering, École Polytechnique de Montréal, Montréal (Québec), Canada H3C 3A
E-mail: jun.zhu@polymtl.ca

Few researches have characterized the vibrational behavior of shallow powder beds by analysis and simulation. Even fewer have pursued an experimental approach. Simulations of vertical vibrations to date describe a phenomenon that is mostly chaotic in nature, though a few periodic, yet unstable, modes have been identified. Experimental results mostly agree, but also point out some unexplained singular modes with remarkable stability that our experiments confirmed. These modes can be explained if we assume that the laws of elastic collisions do not hold at very low impact velocities so that a minimum "quantum" of kinetic energy be exchanged between the particle and the vibrating plate. A new impact model that matches classical laws except when approaching minimum impact velocity is introduced. This minor chink in the laws of elastic rebound has a profound effect on simulated behavior. It forces particle motion from a chaotic state into discrete, yet complex, but finite "allowed states". Transition between states is akin to a random walk.

11.1. Introduction

Vibrations of bulk material are a poorly understood, yet often used empirical mechanism to induce fluidization or flow of powders when fluid transport is not indicated. For analytical purposes, the rather sparse literature on the

subject often relies on the similarity between the vertical oscillations of a shallow granular bed and that of a single particle bouncing elastically off a sinusoidally oscillating rigid plate. This apparently simple model can be quite deceptive, as it exhibits an amazingly rich variety of behaviors presumed to be chaotic with occasional bifurcations, interspersed with families of periodic motions. Periodic motions identified in the literature consist of repeated patterns of one or more parabolic trajectories. The number n of successive parabolic trajectories before a pattern is repeated is used as a qualifier to characterize the motion, thus called *period-n motion.* When needed, the number k of plate periods needed to account for one period of the ball motion will be used as a subscript. For example in [Holmes (1982)][1] (figure 1.b) one sees a *period* - 2_2 motion consisting of a periodic succession of 2 parabolic trajectories over 2 plate periods. If multiple *period-*n_k motions are presumed to exist on the same k plate periods interval, we may have to refer to the order m of the motion as the order in which the first bounce occurs. If needed, this order will be indicated by a superscript *period-*n_k^m motion. For the most part, these period-n motions are surmised to be unstable.

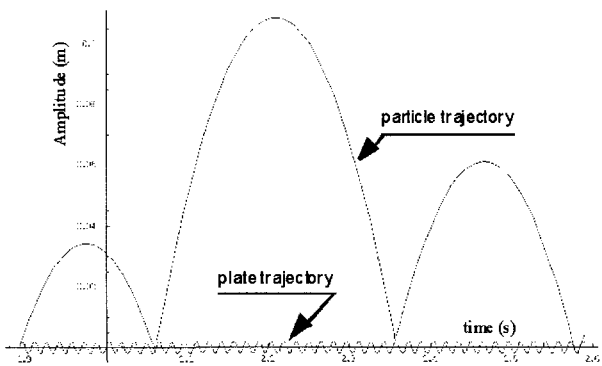

Fig. 11.1. Example of a *period*$-_s 4_{45}$ motion corresponding to the pattern detailed in Figure 11.13 (Amplitude: 2mm, frequency: 65 Hz, coefficient of restitution: 0.5.) After 3 rebounds, the particulate lands on the plate with matching velocity, is caught, and ejected again to repeat the pattern.

Following a synopsis of published research, and a discussion of methods and results in light of our discoveries, this article[a] identifies a new class of

[a]JP: This manuscript is a labor of love dedicated by the first author to the memory of

period-n motions where the last impact happens with zero relative velocity. To our knowledge, this class of phenomena has never been investigated, let alone identified in the literature. Yet they appear to constitute a fundamental pattern of behavior, which is at the core of our research on powder bed vibrations. We shall refer to these motions as *period-*$_s n$ motions, with appropriate subscripts and superscripts as needed to explicitly describe a *period-*$_s n_m^k$ motion. The prefix subscript "s" is meant to indicate *"soft-landing"*, In a *period-*$_s n$ motion, the particle exhibits a series of zero or more elastic bounces before landing on the plate with matching velocity. The particle then rides on the plate until it is thrown off again and the pattern repeats. To illustrate the difference between period-n and *period-*$_s n$ one should compare Figure 11.1 to [Holmes (1982), figure 1.b][1].

The defining characteristic of *period-*$_s n$ motions is their terminal zero relative velocity landing before being re-launched at a well-defined phase of the plate oscillation. Such low velocity impact, however, fails to be adequately represented by existing models of elastic collision. Indeed such model is but an approximation as it is well known that a ball bouncing off the floor will not keep bouncing forever, even in the absence of air. As common sense experience indicates, a ball will fail to bounce back when dropped from below a certain height. The consideration that a minimum amount of kinetic energy needs to be exchanged between colliding bodies—or equivalently, that a minimum relative velocity is required for rebound—leads to a new collision model relating incoming and outgoing velocities. Interestingly, this approach leads to an equation for velocity transformation that is very similar to that of relativistic velocity transformation. Like its relativistic counterpart, which closely represents Galilean kinematics up to nearly the speed of light, our new model is nearly identical to existing elastic collision models until the impact velocity becomes almost as small as the critical minimum required for rebound.

This apparently benign modification of the laws governing elastic collisions has a profound effect on the problem at hand. Indeed, the state of each bounce can be represented by two variables that are initial position and particle velocity, or equivalently initial plate acceleration and particle velocity. Successive impacts can thus be represented by a series of points in

---

an exceptional woman, friend, companion, confident, and mentor. No amount of work can ever repay her kindness, love and attention. No words but silent cries from the heart can ever pay tribute to her courage and strength. To Eliza Maria Haseganu who gave so much of herself in this life, may your next bring you the happiness and fulfillment you so much deserve.

the plane. Under the classical assumption of elastic impact, representative points for successive bounces form a cloud covering region of the plane. Under the resulting chaotic assumption, any velocity-acceleration combination is likely to happen. In contrast, when the new model for low-velocity impact is taken into account, it forces a quantization of the allowed states. For a given amplitude and frequency combination, only one pattern of discrete states is allowed. Representative points for successive bounces form a discrete and finite collection. This quantization effect can be understood as the effect of the new model expanding the soft landing conditions from a single phase to a continuous range. This will effectively allow the steady state pattern to occur after a series of apparently random transitional bounces. As soon as the particle impacts the plate with a low enough relative velocity, it will be captured by the plate and launched back at a precise phase corresponding to the plate deceleration greater than g. This will effectively lock the particle into a pattern of rebounds that will repeat ad-infinitum. Moreover, a perturbation of the particle motion will either have no effect, or will result in an apparently random pattern of bounces eventually returning to the stable pattern of allowed states. A perturbation of the plate motion will either have no effect if the non-dimensional acceleration is preserved, or will force the particle into a new "allowed state."

If such a minor chink in the constitutive laws of elastic collision does indeed exist, its consequences on the quantization of a bouncing particle should be noticeable by careful observation. To this end a series of experiments are to be conducted in which a spherical bead bounces off an oscillating platform. The experiment and its results however are outside the scope of this paper.

11.2. Review and Discussion of Prior Works

Our work is concerned with the vibrational response of shallow powder beds. In the behemoth field of vibrations and acoustics, the body of works dedicated to our aim is almost infinitesimal. This disproportion does not prejudice the relative importance of the topic. Rather, it bears witness to its difficulty. This review has a two-pronged objective. First, we intend to draw an objective portrait of the state of the art, this will be the topic of Section 11.2. Second, our theoretical and experimental advances enable us to revisit prior works and evaluate their methods, assumptions, and results. These remarks will be consigned in Section 11.3. Prior to that however, it is advisable to put some order in the presentation of the main concepts

and notations. The formulation of the problem is rather trivial, though its solution is not. However each author uses a different notation and formalism which makes it difficult to compare all publications on an equal footing. In order to compare objectively all works and insert our contribution as well, we shall start in Subsection 11.2.1 with an introduction of the topic and the notations used in modeling it.

11.2.1. *Notation*

In this section, we introduce the notation that will be used throughout this article. This early introduction will allow us to cover the existing body of prior works in a uniform and consistent manner. Although the notation and graphical representations used here to discuss prior works may be different from the original, every effort was made to preserve the intended meaning.

Representation of the plate kinematics:
Let $Z_{P/G}(t)$, $Z'_{P/G}(t)$ and $Z''_{P/G}(t)$ respectively represent the plate displacement, velocity, and acceleration along the vertical axis measured in the ground frame. Without loss of generality, we can represent the oscillatory motion of the plate by a cosine function of amplitude P and pulsation ω (or, equivalently, period $T = 2\pi/\omega$).

$$Z_{P/G}(t) = P\cos(\omega t). \tag{1}$$

It will be useful for the rest of this argument to write the first and second derivatives in forms that eliminate time:

$$Z'_{P/G}(t) = -P\omega\sin(\omega t), \tag{2}$$

$$Z''_{P/G}(t) = -P\omega^2\cos(\omega t) = -\omega^2 z_{P/G}. \tag{3}$$

A few researchers have characterized the motion in terms of non-dimensional parameters. This is also the convention we shall adopt in this article whenever applicable. Letting g stand for the acceleration of gravity, the non-dimensional position, velocity and accelerations are respectively defined as:

$$\xi_{P/G}(t) = \frac{Z_{P/G}(t)}{P} = \cos(\omega t), \tag{4}$$

$$\xi'_{P/G}(t) = \frac{Z'_{P/G}(t)}{P} = \pm\sqrt{1-\xi^2_{P/G}(t)}, \tag{5}$$

$$\xi''_{P/G}(t) = \frac{Z''_{P/G}(t)}{g} = -\frac{p\omega^2}{g}\xi_{P/G}. \tag{6}$$

An important parameter in this and other articles is the non-dimensional acceleration γ:

$$\gamma = \frac{P\omega^2}{g}. \tag{7}$$

Representation of the particle kinematics:

In this article, we shall denote by $Z_{B/G}$ and $Z_{B/P}$ the particle position relative to the ground and plate frames, respectively. The corresponding velocities and accelerations will be denoted by $Z'_{B/G}$, $Z_{B/P}$, $Z''_{B/G}$ and $Z''_{B/P}$. In order to be consistent with the rest of the literature, we also define the non-dimensional counterpart to these entities as:

$$\xi_{B/G} = \frac{Z_{B/G}}{P}, \qquad \xi_{B/P} = \frac{Z_{B/P}}{P}, \tag{8}$$

$$\xi'_{B/G} = \frac{Z_{B/G}}{P\omega}, \qquad \xi'_{B/P} = \frac{Z_{B/P}}{P\omega}, \tag{9}$$

$$\xi''_{B/G} = \frac{Z_{B/G}}{g}, \qquad \text{and} \quad \xi''_{B/P} = \frac{Z_{B/P}}{g}. \tag{10}$$

Representation of impact kinetics:

All published articles consider the plate to be perfectly rigid and of large mass. In effect, this hypothesis allows us to consider the plate motion to be unaffected by the particle impact. The relation between incoming and outgoing relative velocities is thus governed by the law of elastic impact with a coefficient of restitution η. Let us denote by ${}_it$ the time of the i^{th} impact.As a lexicographic rule, whenever a function f of time is expressed at ${}_it$, we shall use the following shorthand:

$${}_if = f({}_it). \tag{11}$$

The time of flight interval between the $(i-1)^{th}$ and the i^{th} impacts will be denoted by ${}_i\tau$:

$${}_i\tau = {}_i t - {}_{(i-1)} t. \tag{12}$$

The incoming and outgoing velocities at the i^{th} impact will be denoted respectively with a "+" or "-" prefix superscript. The law governing the velocity transformation relative to the plate is thus:

$${}^+_i Z'_{B/P} = -\eta_i^- Z'_{B/P} \tag{13}$$

or equivalently

$$\xi'_{B/P} = -\eta_i^- \xi'_{B/P}. \tag{14}$$

This relations (13) and (14) expressed in the ground reference frame becomes:

$$Z'_{B/G} = -\eta_i^- Z'_{B/G} + (1+\eta)_i Z'_{P/G} \tag{15}$$

which, when expressed in non-dimensional form becomes:

$$\xi'_{B/G} = -\eta_i^- \xi'_{B/G} + (1+\eta)_i \xi'_{P/G}. \tag{16}$$

Poincaré diagrams:

Each bounce can be represented by two variables, initial phase (or equivalently initial plate acceleration, or initial particle position) and velocity. This leads to a representation of the particle motion as a series of representative points in the plane, called a *Poincaré diagram* [Hjelmfelt and Allen (1989)][3]. Under classical models of chaotic behavior the Poincaré diagram will appear as a cloud of points covering an area of the plane. This phenomenon is illustrated in Figure 11.2, which records the first 300 bounces of a particle dropped from a 2 cm height onto a plate vibrating at 68 Hertz with 2mm amplitude.

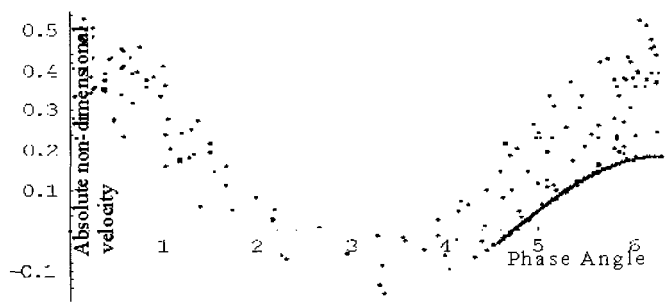

Fig. 11.2. Example of Poincaré diagram. Each point represents the phase angle and absolute non-dimensional velocity associated with each impact of a particle dropped from a height of 2 cm onto a plate vibrating at 68 Hz with 2mm amplitude. The first 300 bounces are plotted.

11.2.2. *Literature survey*

In the broad field of vibrations and acoustics, the body of published works dedicated to the study of granular material response to vibrations is minute.

Rather than pointing out a relative unimportance however, this disparity speaks to the difficulty of the subject matter. Among the few researchers to venture in this field, most have attempted an analytical approach or computer simulation. Our bibliography search turned up only a handful of experimental research papers. As our work is primarily concerned with shallow beds, the following review will be even more selective, highlighting the major theoretical approaches, and the one experimental work relevant to ours.

Analysis and simulation:

The seminal works in this field can be traced back to Wood and Byrne [Wood and Byrne (1981)][2], who established the impact governing equation (15), and [Holmes (1982)][1] who proposed an analytical solution. In order to solve the rather complex computational problem formulated by Wood and Byrne [Wood and Byrne (1981)][2], Holmes [Holmes (1982)][1] introduced a simplifying assumption by neglecting the plate position in computing the time of flight. In effect, only the plate velocity is accounted for in computing the rebound. Under this assumption, the time of flight becomes that of a particle in free fall departing from the plate's average position with a velocity imparted by the rebound. Hence the time of flight was given by the following equation:

$$ {}_{(i+1)}\tau = 2\frac{{}^{+}_{i}Z'_{B/G}}{g}. \tag{17} $$

Although this simple approximation allows solving for velocity transformation from one impact to the next, the phenomenon still remains highly complex, exhibiting irregular non-periodic solutions, as well as harmonic and sub-harmonic responses. In order to conduct a computationally tractable stability analysis, in [Holmes (1982)][1] it is further assumed that the collision is perfectly elastic (coefficient of restitution e=1.) Under these conditions, [Holmes (1982)][1] identifies transition from harmonic to stochastic responses. It is interesting to note that the patterns of responses are qualitatively similar to those obtained by other researchers, including ourselves, who did not resort to Holmes's simplifying assumptions. The appropriateness of theses assumptions and their results will be subjected to a critical analysis in our forthcoming discussion in Section 11.3.

Another analytical investigation of this phenomenon by means of simulations is due to Hjelmfelt [Hjelmfelt and Allen (1989)][3]. In contrast to [Holmes (1982)][1], Hjemfelt did not resort to a simplified kinematics but

used iterative marching methods to detect impacts between plate and particle. In this case the author points out that his approach is more representative of the actual physics of the phenomenon. In particular, Holmes model can occasionally produce negative rebound velocities. Such negative rebound velocities are perfectly valid physical solutions that can be handled by Hjemfelt, but are not compatible with Holmes's assumption since the particle would find itself below the table. Numerical experiments were conducted by Hjelmfelt with a coefficient of restitution of 0.4 and focus on a range of non-dimensional acceleration $0 \leq \gamma \leq 10$. These values are the same as used for simulation in prior works.

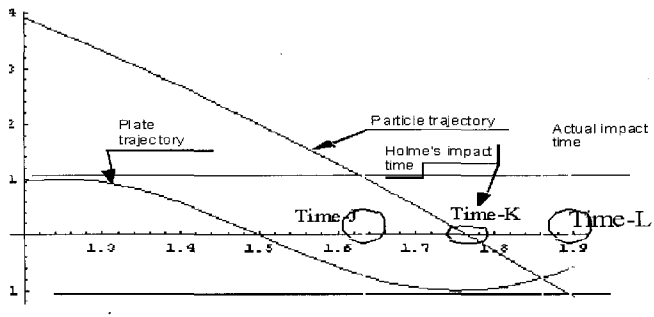

Fig. 11.3. The impact between the particle and the plate must occur during the interval when the particle trajectory intersects the plate's range of motion. Therefore the time of impact is bounded above and below by L and J respectively. Holmes' assumption would set the impact time at K, i.e. at the particle crossing height zero. Clearly, in the case illustrated here neither the velocity nor the position varies notably during the time interval (L-J). Hence Holmes' approximation would hold.

Hjelmfelt [Hjelmfelt and Allen (1989)][3] did not identify any of the periodic motions stressed by other researchers. Yet, and despite using a different approach than [Holmes (1982)][1], he eventually confirmed qualitatively a number of characteristics from prior studies with estimated measures of stability. Simulations show regions of transition to chaotic behavior, which are qualified by experimental estimation of their associated Lyapunov exponents.

The latest instance of simulated behavior studies is due to Luo and Han [Luo and Han (1996)][4] who focused on period-1 motions and their stability. In essence, the conditions for period-1 motions identified by Luo and Han

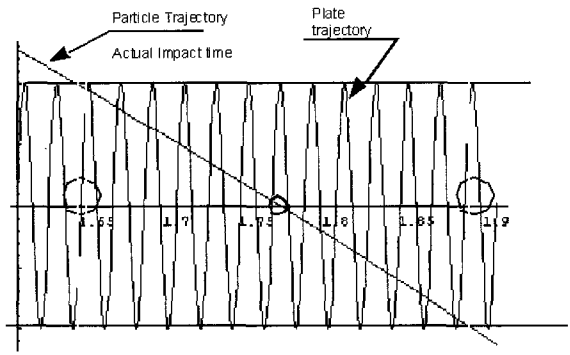

Fig. 11.4. For the same conditions as in Figure 11.3, but shorter period, the impact time and velocity are altered significantly. Holmes' approximation would yield time K for the impact, which is obviously off by many periods and occurs with a radically different velocity than the actual impact.

[Luo and Han (1996)][4] reduce to [Holmes (1982)][1], in the case of perfectly elastic impacts ($\eta = 1.$) For non-elastic collision, Luo and Han formulate a closed form expression of Eigenvalues of the differential mapping between impacts. With a few exceptions, periodic motions are shown to be unstable.

Experimental investigations:

Our only reference on these matters is [Brennen(1996)][5]. This article provides a good overview of prior research, and the results of their original experiment concur with other reports as well as our own. Brennen et al.'s setup uses a transparent rectangular box filled with shallow beds of ϕ 2.85mm spherical beads. The size of the beads allows them to neglect the effect of interstitial air flows. To observe the dynamic behavior of the bed, Brennen et al. top the bed with a light weight lid, and observe the bed expansion under a stroboscope.

The main remark from this experiment is that no significant expansion occurs for values of the non-dimensional acceleration γ between 1 and 2. Observations during this phase indicate that the flight time of the beads is less than 0.6 period and that the particles are riding on the plate for the rest of their periodic motion. Then at value of γ near 2, the bed experiences a sudden expansion, expanding gradually further afterward. In order to explain this phenomenon Brennen et al. surmise that the particles experience a period-1 motion. Using Holme's expression [Holmes (1982)][1]

for the period-1 non-dimensional acceleration, Brennen infers a coefficient of restitution of the order of 0.25 for such motion to occur.

11.2.3. *Discussion*

Assessment of Holmes' model:

Holmes' contribution [Holmes (1982)][1] rests on the approximation that the plate displacement does not affect significantly the impact time and rebound velocity. This approximation holds exactly in the case of period-1 motion since impact always occurs at the same phase angle of plate displacement. In this case [Holmes (1982)][1] rejoins that of Luo and Han [Luo and Han (1996)][4]. In most circumstances however our results concur with earlier criticisms by Luo and Han [Luo and Han (1996)][4] concerning the appropriateness of Holmes' approximation. First, we found that Holmes's only holds when the plate period is large compared to the particle travel time through the plate trajectory. Second, Holmes approximation requires that the particle velocity reverse course after impact, this often is not the case as judicially pointed by Luo and Han [Luo and Han (1996)][4]. Finally, we repeated Holmes' experiments and found that the assumption affects the Poincaré distribution. Yet, the qualitative results obtained by Holmes are strikingly similar to ours; most notably the horseshoe pattern of the Poincaré diagram and the existence of strange attractors.

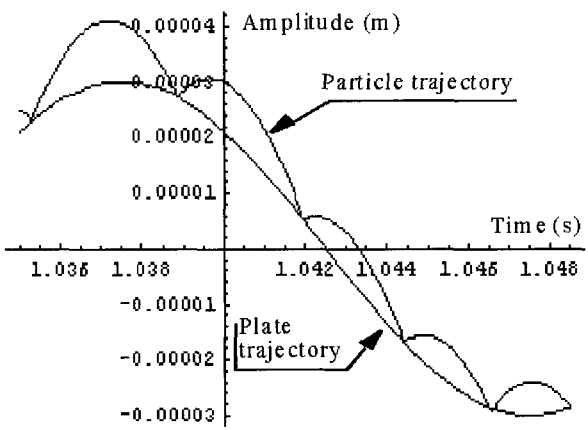

Fig. 11.5. When the particle time of flight is short with respect to the period, Holmes' approximation fails to capture the phenomenon accurately.

The first count is illustrated by Figure 11.3 and Figure 11.4. They show that Holmes' assumption does not hold when the particle transit through the plate's range of motion lasts more than a period. Another instance where Holmes approximation fails to capture the phenomenon is when the period is much longer than the time of flight. This is illustrated by Figure 11.5.

The second point was already discussed by other researchers [Luo and Han (1996)][4] and is illustrated by Figure 11.12. The third point concerning impact distribution is an original finding of our research that is illustrated further on in this article when we discuss strange attractors and point distribution in Section 11.4. Whereas Holmes' approximation yields a nearly uniform distribution of Poincaré points, our model shows an accumulation near phase zero (modulo 2π). This result is illustrated in Figure 11.10 and Figure 11.11.

Periodic motion and stability conditions in [Holmes (1982)][1] and [Luo and Han (1996)][4]:

To our knowledge, all prior works consider only elastic impact, regardless of approximation used. In all instances, the elastic impact assumption leads to chaotic models with occasional domains where the motion becomes periodic. Having identified such periodic modes, a few authors have sought to characterize their stability. Typically periodic modes are identified through fixed points $(\bar{\varphi}, \bar{\nu})$ of the mapping $(\varphi_{i+1}, \nu_{i+1}) = f(\varphi_i + \nu_i)$ yielding phase angle φ_{i+1} and velocity ν_{i+1} from the prior bounce conditions.

$$f(\bar{\phi}, \bar{V}) = (\bar{\phi}, \bar{V}). \tag{18}$$

As rightfully pointed out in [Holmes (1982)][1], focusing on fixed points alone will only yield period-1 motions. Other periodic modes may exist however when the motion cycles through a series of n points, thus experiencing period-n motion. Holmes' approximation allowed him to develop a recursive formulation relating the bounces. However, Holmes and other researchers that followed him failed to capture the conditions for period-n motion. Period-n motion occurs when the representative point on the Poincaré diagram cycles through n points. Hence, in order to characterize such period-n motion, one must identify the fixed point of an n-dimensional mapping. Below is an original finding of our research that formulates this fixed point in terms of Holmes' approximation. Letting X_i represent n successive bounces

on the Poincaré diagram,

$$X_i = \begin{bmatrix} \varphi_{i+n-1} \\ v_{i+n-1} \\ \varphi_{i+n-2} \\ v_{i+n-2} \\ \cdots \\ \varphi_i \\ v_i \end{bmatrix}, \tag{19}$$

the fixed points of the n-dimensional mapping corresponding to period-n motions must satisfy the following equation, which is obtained by applying the mapping and rotating the points:

$$X_i = \begin{bmatrix} \varphi_i + v_i \\ \gamma v_i - \alpha\cos(\varphi_i + v_i) \\ \varphi_{i+n-1} + v_{i+n-1} \\ \gamma v_{i+n-1} - \alpha\cos(\varphi_{i+n-1} + v_{i+n-1}) \\ \varphi_{i+n-2} + v_{i+n-2} \\ \gamma v_{i+n-2} - \alpha\cos(\varphi_{i+n-2} + v_{i+n-2}) \\ \cdots \\ \varphi_{i+1} + v_{i+1} \\ \gamma v_{i+1} - \alpha\cos(\varphi_{i+1} + v_{i+1}) \end{bmatrix} = X_i = \begin{bmatrix} \varphi_{i+n-1} \\ v_{i+n-1} \\ \varphi_{i+n-2} \\ v_{i+n-2} \\ \cdots \\ \varphi_i \\ v_i \end{bmatrix}. \tag{20}$$

Unfortunately, as we saw earlier, Holmes' approximation fails to adequately model but periodic motions that all land at a same plate height. For practical purposes, this limits Holmes to period-1 motions.

Armed with a fixed point formulation that characterizes period-n motions, one can now address the issue of stability of such periodic modes by studying the Jacobian of the mapping. This is what was achieved by Holmes [Holmes (1982)][1] and by Luo and Han [Luo and Han (1996)][4] for respectively approximated and numerically simulated period-1 motions. A corresponding stability analysis for period-n would require a similar analysis on the Jacobian of the mapping for Holmes, or a numerical equivalent for Luo and Han.

Compared to our research, the results in [Holmes (1982)][1] and [Luo and Han (1996)][4] appear to be an artifact of the elastic model. With the low velocity impact model that we introduce in Section 11.3, period-n motions are a necessary outcome. The proof of this assertion is not included here, but its outlines will be discussed in Section 11.5.

Observations of chaotic behavior by Hjelmfelt:

Hjelmfelt's research occupies a unique position in the field for its extensive analysis of chaos, using numerical simulation to estimate the Lyapunov exponent of the mapping. Without going into the numerical estimation of Lyapunov exponent, we repeated Hjelmfelt's experiments and compared his conclusions to ours.

Hjelmfelt's simulation [Hjelmfelt and Allen (1989)][3] concurred with prior observations of strange attractors by Holmes [Holmes (1982)][1], without resorting to approximations. He observed the phenomenon of the bounces being attenuated during plate downswing and the motion dying out on the plate upswing. This observation also concurs with ours, as Hjelmfelt's figure 1 should be compared to our Figure 11.12.

In plotting the non-dimensional impact velocities versus non-dimensional acceleration, Hjelmfelt [Hjelmfelt and Allen (1989)][3] identified downward parabolic shaped patterns that were assumed to be artifacts of the phenomenon. Our implementation of Hjelmfelt's approach [Hjelmfelt and Allen (1989)][3], illustrated in Figure 11.6, found these patterns to be characteristic of the initial conditions, and not of the ensuing chaotic behavior. Our simulation reproduced the patterns observed by Hjelmfelt [Hjelmfelt and Allen (1989)][3] even when the low velocity impact model introduced in Section 11.4 is used. The same parabolic patterns are observed corresponding to the first bounce off the plate.

11.3. Periodic Response with Soft Landing

Experiments indicate that amongst the apparently chaotic motion of a particle bouncing on a vibrating plate, there are small regions that are well-behaved with characteristically higher jumps. This can be explained in first approximation if we consider the case of a ball at rest on the plate at the origin. In such a case, if the plate's downward acceleration was ever to decrease below $-g$, then the plate and particle would separate, with the ball continuing on a parabolic trajectory in the ground frame until the next impact. This case is illustrated by Figure 11.7.

Particle initially at rest on a vibrating plate:

Using the non-dimensional notation introduced in Subsection 11.2.1, let us consider the initial condition of a particle riding on the plate. As illustrated in Figure 11.7, particle and plate trajectories will separate when the plate's

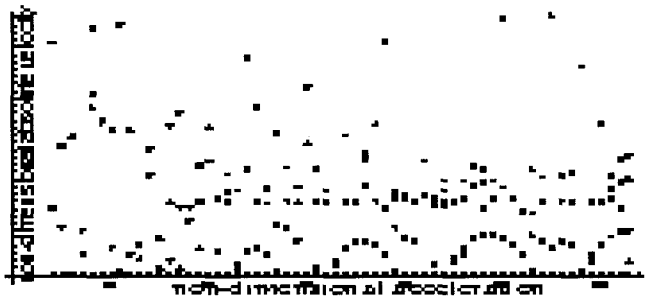

Fig. 11.6. Non-dimensional absolute impact velocities for the first five bounces off an oscillating plate with a 1mm amplitude. The graph shows the same characteristic downward parabolic pattern as Hjelmfelt [Hjelmfelt and Allen (1989)][3], which we found to be an artifact of initial conditions. The non-dimensional acceleration ranges from 4 to 64. The particle is dropped from an initial height of 2 cm at time 0.

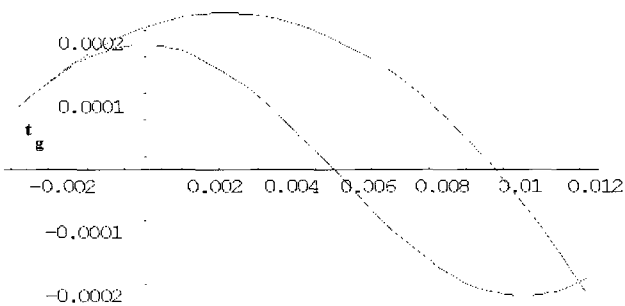

Fig. 11.7. Illustration of the case where the particle is initially at rest on a vibrating plate. The sine wave represents the vibrating plate trajectory. The parabolic, curve shows the particle trajectory after it separates from the plate. The horizontal lines show the amplitude at which the plate acceleration is equal in magnitude to gravity.

non-dimensional acceleration reaches -1; at which point the plate must have respective height and velocity:

$$ {}_g\xi = \frac{1}{\gamma}, \quad \text{and} \quad {}_g\xi' = \sqrt{1 - \frac{1}{\gamma^2}}. \tag{21} $$

The time at which this separation will happen is during the upward motion

of the plate, that is at time

$$ {}_g t = \frac{1}{\omega}(-a\cos({}_g\xi) + 2n\pi), \qquad n \in Z. \tag{22} $$

From this time and until the next impact, the particle then follows a parabolic trajectory with non-dimensional position and velocity respectively equal to:

$$ \xi_{B/G}(t) = -\frac{1}{2}\cdot\frac{\omega^2}{\gamma}(t -_g t)^2 + \omega \cdot_g \xi'(t -_g t) + \frac{1}{\gamma}, \tag{23} $$

$$ \xi'_{B/G}(t) = -\frac{\omega}{\gamma}(t -_g t) +_g \xi'. \tag{24} $$

The particle will reach its maximum height at time:

$$ {}_h t = \frac{\gamma}{\omega}\cdot_g \xi' +_g t, \tag{25} $$

where the height is

$$ \xi_{B/G}({}_h t) = \frac{\gamma}{2}\cdot_g \xi'^2 +_g \xi. \tag{26} $$

Boundary conditions so no bounce will occur:

The case studied above will, in most circumstances lead to the particle bouncing chaotically off the plate. There are however, instances where the particle will land on the plate with matching velocity, hence its motion will not be governed by the laws governing elastic impact. Rather, the ball will lift from the plate, follow a parabolic trajectory and meet the plate again at the only place where velocities can match, that is when the plate is at height ${}_g\xi$ during its downswing. Assuming, without loss of generality, that the particle separates from the plate at time

$$ {}_g t = -\frac{1}{\omega}a\cos({}_g\xi), \tag{27} $$

then the particle may only land at times

$$ {}_1 t = \frac{1}{\omega}(a\cos({}_g\xi) + 2n\pi), \qquad n = 0, 1, 2, \ldots, \tag{28} $$

or, equivalently,

$$ {}_l t = -{}_g t + nT. \tag{29} $$

From time ${}_l t$ until ${}_g t' =_l t + 2{}_g t + T$ the particle will then be stationary on the plate. Then at time ${}_g t'$ it will lift again from the plate and follow the same parabolic trajectory as before. We can see therefore that the particle will then adopt a periodic motion composed a section of free fall and a

section of vibratory motion. The period of the particle's motion is thus a multiple of the plate's period.

$$ {}_{B}T = (n+1)T, \qquad n = 0, 1, 2, \ldots \tag{30} $$

Classes of parabolic trajectories meeting boundary conditions:

In order not to experience an elastic impact, the particle must terminate its parabolic trajectory with matching plate position and velocity. Given that the particle time of flight to return to altitude ${}_{g}\xi$ with velocity $-{}_{g}\xi$ is:

$$ {}_{g}\tau = 2\omega\gamma \cdot {}_{g}\,\xi', \tag{31} $$

it must be that ${}_{g}\tau$ corresponds to the time interval between ${}_{g}t$ and ${}_{l}t$.

$$ {}_{g}\tau = -2 \cdot {}_{g}\,t + nT. \tag{32} $$

Given that ${}_{g}\tau$ and ${}_{g}t$ have explicit definitions in terms of the plate kinematics (31) and (27), respectively) we can establish a relation between plate amplitude and frequency:

$$ 2\omega\gamma \cdot {}_{g}\,\xi' = \frac{2}{\omega} a \cos(\frac{1}{\gamma}) + 2n\frac{\pi}{\omega}. \tag{33} $$

Using (21) to eliminate ${}_{g}\xi'$ we find that the plate amplitude and frequency must satisfy the following relation:

$$ \sqrt{\gamma^2 - 1} - a \cos \frac{1}{\gamma} = n\pi. \tag{34} $$

Note that the first four roots of (34) are 1, 4.60334, 7.78971, and 10.9499. After that the roots become large enough that we can approximate $\sqrt{\gamma^2 - 1}$ and $a\cos(1/\gamma)$ with γ and $\pi/2$, respectively, so the roots become uniformly spaced in first approximation:

$$ \gamma \approx n\pi - \frac{\pi}{2}, \qquad (n > 5). \tag{35} $$

At this venue, it is important to note that period-${}_{s}n$ phenomena are purely kinematic and independent of the coefficient of restitution η, as opposed to period-n motions identified by Holmes [Holmes (1982)][1] and Luo et al [Luo and Han (1996)][4].

Conclusion:

It is known that the problem of a particle bouncing elastically off a plate in sinusoidal motion will be chaotic. However, we have found that there exist domains in which, while we cannot talk of resonance proper, there will be

a definite well-behaved response. The modes at which such response will occur are such that the non-dimensional acceleration is a solution of (34).

Example 1: Consider a plate vibrating at 50 Hz (Pulsation $\omega = 100\pi$ radian/second). The corresponding first five amplitudes that will lead to the ball bouncing off the plate in singular mode are: 0.099, 0.457, 0.774, 1.088, 1.401 mm. The height z_g at which the particle and plate separate is the same for all amplitudes, in accordance with (21). For a frequency of 50 Hz, the value of z_g is 0.099 mm. Note that this is the same as the first mode amplitude, meaning that the parabolic arc reduces to a point which is the crest of the sine wave. Modes 2, 3, and 4 are shown in Figure 11.8.

Example 2: We consider now the case of a constant amplitude vibration of magnitude $P = 0.000774$ meters. The corresponding first five frequencies that will lead to the particle bouncing off the plate in singular mode are 17.9147, 38.4367, 50, 59.2808, and 67.2737 Hertz. Note that as before the first mode consists only of the crest of the sine wave. Modes 2, 3, and 4 are shown in Figure 11.9.

11.4. Low Velocity Impact Model

The typical model of elastic impact considers only kinetic losses proportional the velocity. Letting ${}^{-}\nu$ and ${}^{+}\nu$ stand respectively for incoming and outgoing impact velocities, the elastic model translates into the well-known formula:

$$ {}^{+}\nu = -\eta \cdot {}^{-}\nu. \tag{36}$$

This model is problematic however when the impact velocity becomes small and the kinetic energy assumed to be dissipated decreases without ever reaching zero. This model dictates that, contrary to experience, a particle bouncing elastically on a fixed plate will continue to bounce ad infinitum without ever coming to rest. Note that even the addition of linear damping would not resolve this quandary. We know that no matter the elasticity of the materials involved, a spherical object left to free fall will not bounce back if dropped from below a certain height $\tilde{h}$. Letting m stand for the mass of the particle, the height $\tilde{h}$ gives us a measure of the minimum energy $\tilde{\varepsilon}$ dissipated in the impact:

$$\tilde{\varepsilon} = mg\tilde{h}. \tag{37}$$

Equivalently, this experiment dictates the minimum impact velocity $\tilde{\nu}$ required for elastic bounce:

$$\tilde{\nu} = \sqrt{2g\tilde{h}}. \tag{38}$$

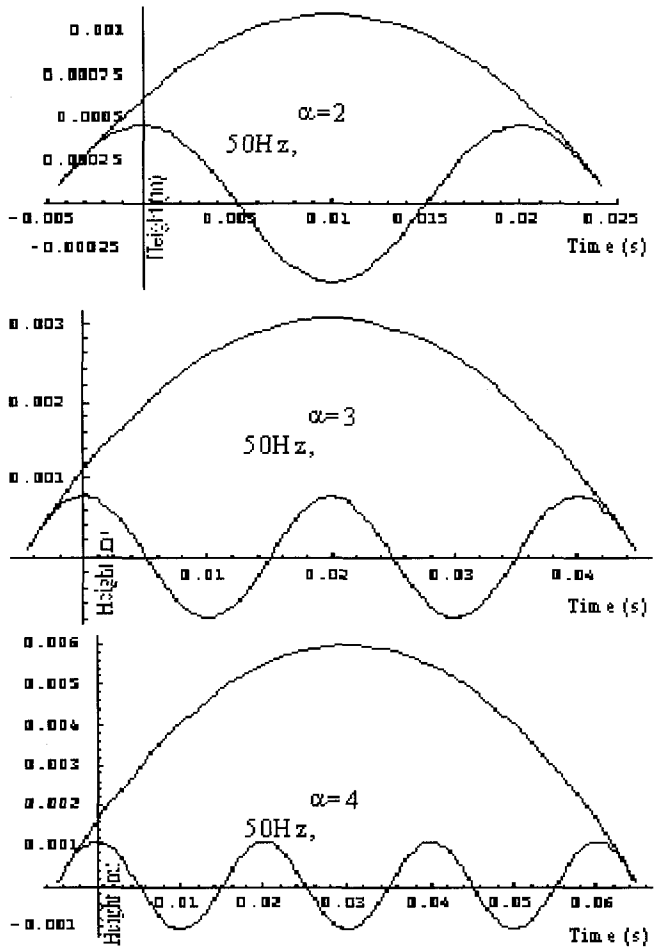

Fig. 11.8. Illustration of the second, third and fourth singular mode at 50 Hz.

For low velocity impact, we shall therefore consider that part of the kinetic energy corresponding to

$$\tilde{\varepsilon} = \frac{1}{2} m \tilde{\nu}^2 \tag{39}$$

is lost before the elastic bounce can even occur. In addition to incoming and outgoing velocities ${}^{-}\nu$ and ${}^{+}\nu$, we now need to introduce the equivalent incoming velocity ${}^{0}\nu$ after $\tilde{\xi}$ of the incoming kinetic energy is dissipated.

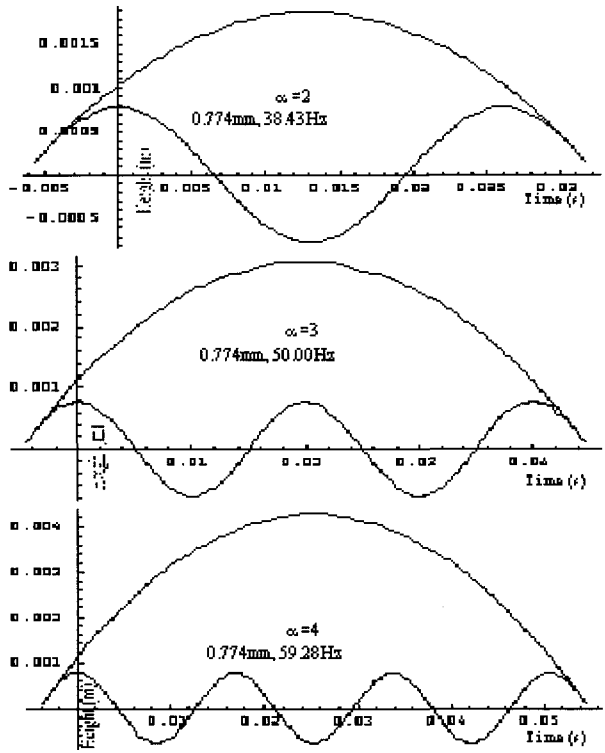

Fig. 11.9. Illustration of the second, third and fourth singular mode for constant amplitude of 0.774 mm.

We can relate ${}^0\nu$ to ${}^-\nu$ through a simple energy balance:

$$\begin{cases} {}^0\nu = {}^-\nu\sqrt{1-(\frac{\tilde{\nu}}{{}^-\nu})^2}, & {}^-\nu \geq \tilde{\nu}, \\ {}^0\nu = 0, & {}^-\nu < \tilde{\nu}. \end{cases} \tag{40}$$

Note the similarity of this law to that governing coordinate transforms in special relativity. Just like it, it will reduce to ${}^0\nu \approx {}^-\nu$ in most instances. The incoming velocity ${}^-\nu$ will have to come within twice of $\tilde{\nu}$ to even have a 10% influence on ${}^0\nu$. Nevertheless, it is an effect that we must account for if we are to model the bouncing of a particle on a vibrating plate.

Once the effect of dissipation for low velocity impact has been accounted for, we can return to the elastic model and assume the kinetic losses. This

leads us to the following formula to model both elastic and low velocity impact losses.

$$\begin{cases} {}^{+}\nu = -\eta \cdot {}^{0}\nu = -\eta \cdot {}^{-}\nu \sqrt{1 - (\frac{\tilde{\nu}}{-\nu})^2}, & {}^{-}\nu \geq \tilde{\nu}, \\ {}^{+}\nu = 0, & {}^{-}\nu < \tilde{\nu}. \end{cases} \tag{41}$$

11.5. Quantization Effects

Accounting for low velocity impact has a remarkable effect on the observed results. Comparative simulations were conducted with and without the low velocity impact model. They led to the discovery of a quantization of the particle states. For a given non-dimensional acceleration, a particle initially dropped at random on the plate will experience a series of apparently random bounces until it lands softly on the plate. From that point on, the particle will be locked in a complex pattern of bounces that repeats periodically. Perturbation of the plate motion will either have no effect, or result in a transition to another quantized state. The transition will be operated through a series of bounces akin to a random walk.

11.5.1. *Digital experiments*

A series of digital experiments were conducted whereby a particle is dropped from a given height at time zero, with zero initial velocity. Computation of the successive impacts relies on finding the first root of a rapidly oscillating function. As stated in prior works cited in Section 1.2, classical numerical methods are notedly unreliable for the purpose of finding such roots. In order to have a reliable solution, we have developed an ad-hoc approach involving recursive symbolic Taylor expansion and root isolation in Mathematica^{TM}. This method will not be exposed here and is the topic of an upcoming publication [Zhu and Pegna (2003)][6].

The particle under consideration is assumed to be a point, so that rotational inertia is negligible. For the purpose of this model, air resistance is also neglected. The resulting pattern of bounces was simulated under the classical and the low velocity impact models. Initial states are nearly identical, showing a motion akin to a random walk until the relative velocity of the particle with respect to the plate becomes small enough to trigger the low velocity impact model. The two model responses separate from that point on. In the case of the classical impact model, the particle appears engaged in a chaotic motion, while the low velocity impact results

in a quantization of the states. Once the particle is captured by the plate, it will repeat a periodic, albeit complex, pattern of bounces.

11.5.2. *Classical elastic impact model*

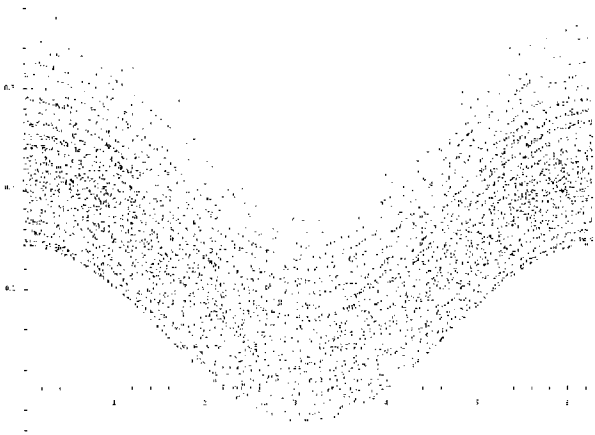

Fig. 11.10. Poincaré diagram for the same conditions as in [Holmes (1982), Figure 7.d][1], same acceleration ratio of 10 (amplitude 2 mm, frequency 35 Hz, coefficient of restitution 0.8) same number of representative points (5000).

A typical sample experiment conducted using this model was shown in Figure 11.2. The results concur with those of prior published research. In particular, one can observe the typical horseshoe pattern identified by Holmes [Holmes (1982)][1], even though his model neglected the influence of plate height. The experiment conducted by Holmes [Holmes (1982), Figure 7.d][1], showing 5000 representative points was repeated and the result is shown here as Figure 11.10. Observe that even though the general horseshoe pattern is preserved, the point density found in our simulation is not as uniform as Holmes'. There appears to be a higher density towards the 2π ends of the phase. The lowest density is found near phase π. Physically, this corresponds to an accumulation of points near the plate peak position.

Likewise, Holmes identified the existence of strange attractors near the 2π phase. The same feature is exhibited in our results. It can be explained however by noticing that it corresponds to a series of small bounces occurring from the damping on the plate downswing and continuing on the upswing until the particle is ejected. This phenomenon was already encoun-

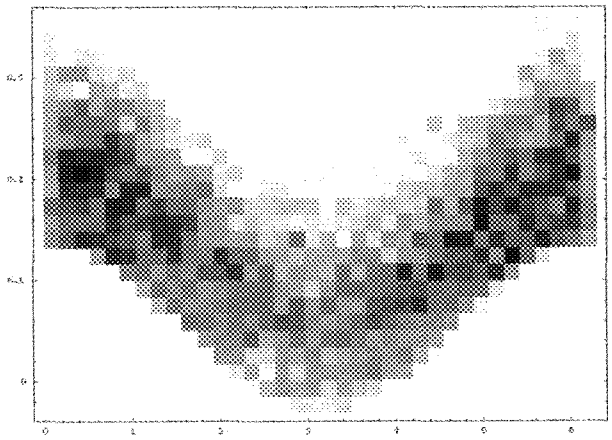

Fig. 11.11. Density plot for the data in Figure 11.10 (white = zero density) showing the accumulation of points on the plate downswing and upswing. The two vertical lines mark the phases at which the plate acceleration becomes greater than gravity. It clearly shows that accumulation occurs when the plate acceleration is less than gravity. As shown in Figure 11.12, the point accumulation corresponds to a dampening of the bounces during the downswing, followed by a succession of rapid small bounces on the upswing.

tered in Figure 11.5 and is repeated for an instance of Holmes' experimental conditions in Figure 11.12. It is however an artifact of the model. As we shall see in Section 11.4, it disappears when quantization of impact velocity is taken into account.

11.5.3. *Low velocity impact model*

Using the same conditions as in Figure 11.2, but accounting for what happens at low relative velocity alters the results in a significant manner. Figure 11.13 shows the Poincaré diagram for conditions that are identical to Figure 11.2, modified to account for a minimum impact relative velocity of 0.4625 m/s. Observe that even though the number of computed bounces is the same as in Figure 11.2 (300), the number of representative points is significantly lower. Indeed most points are representative of an initial transition akin to a random walk. This transition period is nearly identical for Figure 11.2 and Figure 11.13. The two phenomena however part as soon as the relative impact velocity becomes small enough to be affected by the low velocity impact model. From that point on, the pattern of bounces in Figure 11.13 locks into a period-$_s$4 motion while the pattern in Figure 11.2 continues into chaotic motion.

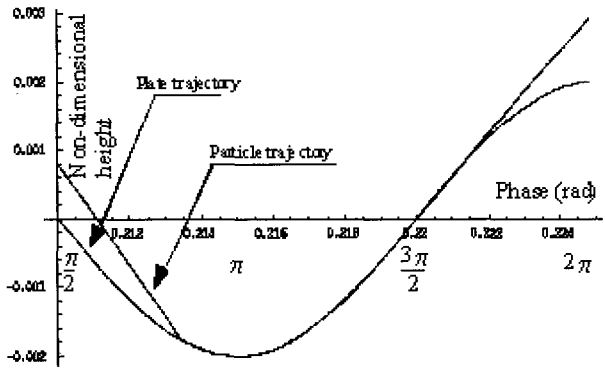

Fig. 11.12. Illustration of the particle trajectory near a strange attractor in Holmes' experiment [Holmes (1982)][1]. The particle bounce is dampened when landing during the plate downswing. A series of small bounces (6 in this instance) ensues until the particle is ejected again from the plate surface. To clarify the relation to Figure 11.11 the phase angle (in radians) is shown below the time scale.

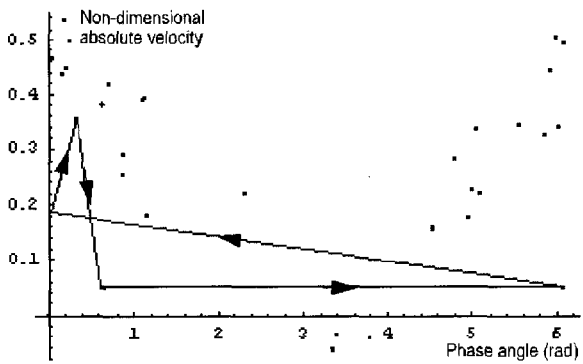

Fig. 11.13. Poincaré diagram accounting for low velocity impact for the same conditions and number of points (300) as in Figure 11.2. The non-dimensional critical impact relative velocity is 0.541 (corresponding to 0.46 m/s). After a series of apparently random bounces, represented by the collection of isolated points, the particle locks into a period-motion represented by the arrowed polygon. The corresponding pattern of bounces was shown in Figure 11.1

A similar experiment was conducted for the conditions in [Holmes (1982)][1] that were reproduced in Figure 11.10, but with a minimum impact velocity of 0.5 m/s. The resulting Poincaré diagram is in Figure 11.14. It shows that after an initial series of random bounces, the particle motion locks into a period$-_s6$ pattern, the trajectory of which is shown in Figure 11.15.

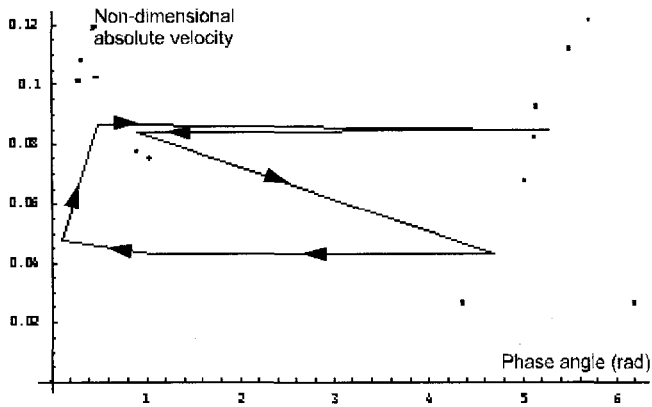

Fig. 11.14. Poincaré diagram accounting for low velocity impact for the same conditions and number of points (5000) as in Figure 11.10. The critical impact relative velocity is 0.5 m/s. After a series of apparently random bounces, represented by the collection of isolated points, the particle locks into a period- motion represented by the arrowed polygon. The trajectory corresponding to this diagram is shown in Figure 11.15.

11.5.4. *Quantum influence*

The main contribution of this work is the introduction of the low velocity impact model and the discovery of its quantization effect on the motion. If one omits to account for it, as was done in prior works, the motion generally appears to be chaotic. Hence, as one increases the number of simulated bounces, one also observes an increase in the number of representative points on the Poincaré diagram. As the minimum impact velocity is raised from zero, and the low velocity impact model is enabled, one observes that the motion will become periodic. Moreover the number of bounces in a period (i.e. number of cyclic points on the Poincaré diagram) will decrease as the minimum relative impact velocity increases. This effect is illustrated in the series of experiments shown in Figure 11.16. The figures illustrate the

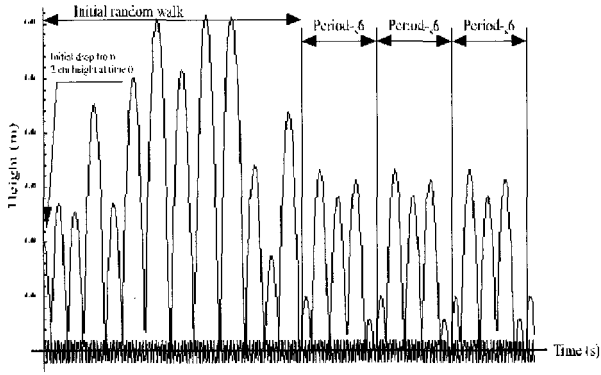

Fig. 11.15. Particle trajectory for the Poincaré diagram of Figure 11.14. Each bounce is represented as a point on the Poincaré diagram. The trajectory shows an initial seemingly random bounces followed by periodic patterns.

Poincaré diagrams for a range of non-dimensional acceleration from 4 to 53. For each value of the non-dimensional acceleration, the first 30 bounces are computed. As the minimum relative impact velocity is increased, the number of representative points decreases, indicating the presence of a periodic motion.

11.5.5. *Existence and uniqueness of quantized states*

The question of existence and uniqueness of quantized states remains open to further research. One can observe however that the chaotic nature of the classical model dictates that each point on the Poincaré diagram will be visited exactly once, for else the motion would engage in a repeating pattern from that point onward. The Poincaré diagram for the classical model of elastic bounce thus produces a region covered by a cloud of points. Since no points can be repeated, the diagram becomes denser as the number of bounces increases as indicated by the graphs in Figure 11.2 and Figure 11.10. Assuming that the point distribution is stable as the number of sample increases, one can assume the existence of a probability density function over the Poincaré diagram and produce an experimental measure such as the one in Figure 11.11.

If one accounts for the low velocity impact model, the behavior of the particle will match that of the classical model almost exactly during the initial series of seemingly random bounces. That is, until the relative impact velocity happens to be small enough that the particle will remain on the

plate. From that point on the particle will engage in a periodic motion. It is therefore legitimate to ask (1) if such low velocity impact will indeed occur and (2) if such impact were to occur, would the repeating pattern be indeed unique.

On the first count, one can surmise, on experimental grounds illustrated by Figure 11.11 that a low velocity impact is bound to occur unless the random bounces diverge away from zero velocity. Indeed, the probability of a bounce occurring with less than critical velocity is the integral of the probability density function (Figure 11.11) over a strip of height $\tilde{\nu}$. If the phenomenon is indeed chaotic, the probability of such an event will not be zero, hence the particle will eventually be captured by the plate.

While the above argument in the legitimacy of low velocity impact does not constitute a mathematical proof, it does however support the physics of the phenomenon. On that basis, we can answer on the second count, that of uniqueness. Once the particle is captured, the plate motion uniquely determines the boundary conditions for subsequent bounces. Since the mapping relating successive bounces is one to one [Holmes (1982)][1], it means that the periodic mode is uniquely determined.

11.5.6. *Stability of quantized states*

Assuming that quantized states exist and are unique for a given plate motion (frequency & amplitude) the next open research question is that of the stability of such states. While a formal analysis is not on the order of this article, one can nevertheless draw some conjecture on experimental grounds. The best illustration in that regard is that of Figure 11.16.

As the minimum critical impact velocity $\tilde{\nu}$ increases, so does the range of phase and impact velocities that will lead to the particle being captured. Hence, a small perturbation of the motion will simply have no effect on the observed bounces. Once the perturbation becomes large enough that the next impact will lie outside the permitted range, then the particle will engage in a random bounce pattern either returning to the initial pattern of settling into a pattern characteristic of the perturbed mode. As Figure 11.16 clearly shows, the order n of a period$-_s n$ motion decreases as the minimum critical impact velocity $\tilde{\nu}$ increases, resulting in increased stability. On the other end of the spectrum, Figure 11.16 also shows that as the order n becomes larger with decreasing velocity $\tilde{\nu}$, the number of random bounces before a periodic mode is reached also becomes larger. This indicates a greater sensibility to perturbations. Eventually, as $\tilde{\nu}$ goes to zero (classical

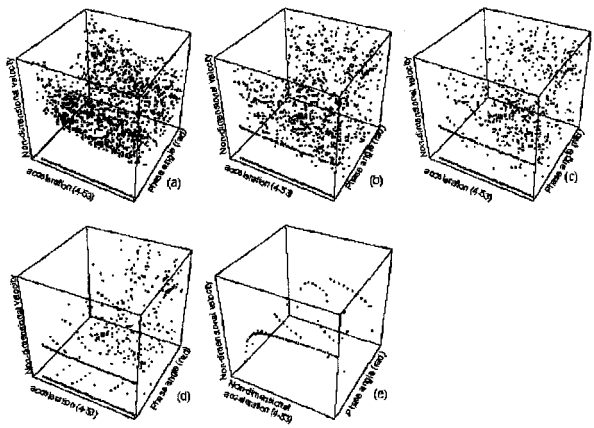

Fig. 11.16. Each figure shows the collection of Poincaré diagrams representing the first 30 points for an acceleration ratio between 4 and 53. The minimum impact velocity varies from 0 (a: classical model) to 0.2 m/s (b), 0.4 m/s (c), 0.6 m/s (d), 0.8 m/s (e). Note that the number of representative points decreases as the minimum impact velocity increases, denoting the occurrence of periodic bounce patterns over a decreasing number of points

elastic model) the number of random bounces increases without bounds, leading to chaos.

From an experimental standpoint, one must acknowledge that detecting periodic modes becomes extremely difficult in practice. As the phenomenon becomes more unstable as $\tilde{\nu}$ decreases, the motion will appear more and more chaotic. Moreover, experimental observations become ever less likely as the slightest perturbation will induce a chaotic response.

11.6. Conclusion

The question of the vibrational response of shallow powder bed arises in the context of powder mechanics. Typical theoretical analysis is conducted on the basis of the response of a single particle bouncing off a sinusoidally excited plate. The research presented here derives from an attempt to model experimentally observed, yet heretofore unexplained powder behavior in a novel dry powder nozzle. While experimental research is still ongoing, the model developed here is original and presents some striking features reminiscent of quantum mechanics.

The main contribution of this paper hinges on a heretofore undetected vibrational mode in which a particle bouncing off a vibrating plate lands with low relative velocity and is captured by the plate. In order to better model low velocity impact, a new model of elastic bounce is introduced whereby the particle is forced to exchange a minimum "quantum" of kinetic energy with the plate. The velocity transformation equation resulting from this model strikingly resembles velocity transformation in relativistic mechanics.

The main consequence of this model is the discovery that, contrary to most published results to date, the particle behavior is not chaotic. In fact, every plate vibration mode is associated to a "allowed" state. A particle bouncing off such plate will experience an apparently random series of bounces until it becomes "trapped" in this allowed state. A perturbation of the motion will either have no effect, or result in a random walk transition toward another allowed state.

Acknowledgments

Support for this work was provided in part by the Natural Science and Engineering Research Council of Canada under Discovery Grant #203515-1998. Our thanks also go to A. Drizo, of the Freeform Fabrication Laboratory at École Polytechnique de Montréal for her invaluable editorial suggestions.

References

1. Holmes, P.J., (1982), "The dynamics of repeated impacts with a sinusoidally vibrating table," J. of Sound Vibration, 84(2), 173–189.
2. Wood, L.A., and Byrne, K.P., (1981), "Analysis of a random repeated impact process," J. of Sound and Vibration 78, 329–345.
3. Hjelmfelt Jr., and Allen T., (1989), "Chaotic behavior of particle on vibrating plate," J. Eng. Mech., 115(7), 1458–1471.
4. Luo, A.C.J. and Han, R.P.S., (1996), "Dynamics of a bouncing ball with a sinusoidally vibrating table revisited," Nonlinear Dyn., 10(1), 1–18.
5. Brennen, C.E. (1996), "Vertical Oscillation of a Bed of Granular Material," J. Applied Mechanics, 63(1) 156–161.
6. Zhu, J., and Pegna, J., (2003), "Recursive Taylor expansion and chaotic root finding," manuscript in preparation.

This page is intentionally left blank

About the Authors

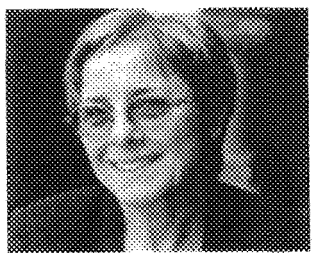

The present volume is dedicated to the memory of Prof. Eliza Maria Haseganu (1940 - 2002) a recognized researcher and a meticulous and loving teacher.

Educated in Romania, Professor Eliza M. Haseganu obtained her Diploma in Mechanical Engineering at the Polytechnic Institute of Brasov and had nearly finished her doctoral work when the political situation forced her to emigrate, and she had to begin her PhD all over again at the University of Alberta in Edmonton. Eliza got the Doctoral degree in 1994 for her thesis *Analytical Investigation of Tension Fields in Lightweight Membrane Structures* written under the supervision of Prof. David Steigmann.

In August 1994 Prof. Eliza Haseganu joined the Department of Mechanical and Industrial Engineering at the University of Concordia. For a short period of less than 8 years she has published about 30 research papers in international journals and conference proceedings and supervised one PhD and five Master's students. Her research and teaching interests were in solids and structural mechanics, dynamics, computational solids mechanics and biomechanics. She did research in the field of finite elasticity and nonlinear mechanics of thin shell and membrane structures, in the development of numerical models for stress analysis in a number of applications, such as

structural fabrics used in lightweight constructions and stressed biological tissues.

Prof. Haseganu intended to publish results from her dissertation research on the numerical solution of highly elastic wrinkled membranes under pressure. These are quite striking and reproduce unusual and unexpected features observed in experiments. Her numerical analysis was sufficiently robust to achieve this without the need for any special measures. However, she delayed publication in the expectation that she would find the time to refine some of her more important analyses to take the effect of self-contact of the membrane into account. Eliza's results are presented in this volume in the article by Prof. Steigmann on her behalf.

In the last years the objectives of Prof. Haseganu's research were also in the development of analytical vibration and buckling analysis techniques for thin walled structural elements made of composite materials by employing asymptotic methods. The research that had been started with Prof. Haseganu resulted in three other papers of the present volume.

Prof. Haseganu was a member of the scientific committee of several mechanical engineering conferences. At the time of her death, she was on sabbatical, and had made several trips to the United States and was planning a field trip to Russia as part of her work.

Mechanical and industrial engineering professor Eliza M. Haseganu, PhD, succumbed to cancer at the age of 62, depriving the international science community of a valuable colleague, gifted teacher and trusted mentor.

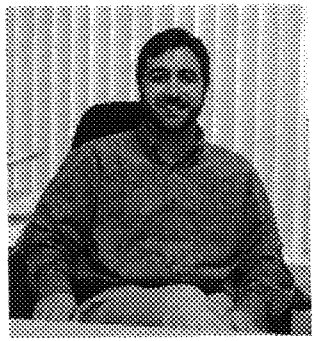

Ozan Akkus was born in Istanbul, Turkey in 1971. He obtained the B.Sc in mechanical engineering and the M.Sc in engineering sciences from the Middle East Technical University of Turkey. He received his Ph.D. in Mechanical Engineering from the Case Western Reserve University, USA. Following a post-doctoral training at the Orthopaedic Research Department of the Mount Sinai Hospital in New York City, Dr. Akkus joined the University of Toledo's College of Engineering as an Assistant Professor in the Department of Bioengineering. The research of Dr. Akkus is geared towards the understanding of the underlying factors for skeletal fragility during aging, disease and physical activity. His laboratory routinely conducts biomechanical tests, histological assays and laser spectroscopic assessment of bone tissue composition and mineral crystallinity.

Eveline Baesu was born in Bucharest, Romania in December 1963. She is an Assistant Professor in the Department of Engineering Mechanics at the University of Nebraska, Lincoln. She received her Diploma (M.S. equivalent) in Mathematics and Mechanics from the University of Bucharest in 1987. She received her Ph.D. in Solid Mechanics in 1998 from the University of California at Berkeley, with the thesis *A treatment of elastic-plastic constrained materials.* Her current research spans a number of areas including electroactive materials, plasticity, biomechanics, and fiber networks. She has published papers in these areas in a variety of journals including the Journal of Applied Mathematics and Physics (ZAMP), Mathematics and Mechanics of Solids, International Journal of Nonlinear Mechanics, and the Proceedings of the National Academy of Sciences (USA). In addition, she has served as Guest Editor of the Journal of Applied Mathematics and Physics and Mathematics and Mechanics of Solids.

Svetlana M. Bauer was born in Barnaul, Russia in 1954. She is Professor in the Department of Hydroelasticity of the Faculty of Mathematics & Mechanics, at St. Petersburg State University. She graduated in Applied Mathematics from St.PSU in 1975 and obtained from the same university her Ph.D. in Mechanics of Solids in 1980 and the degree of Doctor of Science in 2002 for her thesis: *Mathematical Simulation in Ophthalmology.* She is the author of ten books including *Asymptotic Methods in the Theory of Thin Shell Structures* (with P. E. Tovstik, S. B. Filippov, and A. L. Smirnov), 1995, *Asymptotic Methods in Problems and Examples* (with P. E. Tovstik, S. B. Filippov, and A. L. Smirnov), 1997, *The Elementary Analytical Models of Shells and Plates in Ophthalmology* (with P. E. Tovstik and B. A. Zimin), 2000, *Problems in the Theory of Stability* (with D. R. Merkin and A. L. Smirnov), 2002, *Asymptotic Methods in Mechanics of Solids* (with P. E. Tovstik, S. B. Filippov, and A. L. Smirnov), 2006, *Theory of Stability in Examples and Problems* (with A. L. Smirnov), 2006, and more than 60 papers on asymptotic methods in elastic stability of thin elastic shells and mathematical simulation in ophthalmology, published in *Vestnik Leningradskogo Universiteta, Technishe Mechanik, ACTA of Bioengineering and Biomechanics*, and other journals. She is a member of the National Comittee on Theoretical and Applied Mechanics.

Sergej B. Filippov was born in Leningrad, Russia in 1946. He is Professor in the Department of Theoretical and Applied Mechanics of the Faculty of Mathematics & Mechanics, St. Petersburg State University. He graduated in Applied Mathematics from St. Petersburg State University in 1970 and obtained his Ph.D. in Mechanics of Solids from the same university in 1975 and the degree of Doctor of Science in 1995 for his thesis *Vibrations and buckling of joined and stiffened shells.* He is the author of a monograph entitled *Theory of Joined and Stiffened Shells* and co-author of four other monographs, including *Asymptotic Methods in Mechanics of Solids* (with S. M. Bauer, P. E. Tovstik and A. L. Smirnov), 2006. More than 60 research papers of his are published in *Vestnik St. Petersburgskogo Universiteta, Mechanics of Solids, Technishe Mechanik*, it Mechanics Research Communications, and other journals.

Ardeshir Guran was born in Tehran, Iran, in 1957. He received his Master of Engineering (in Applied Mechanics) from McGill University (Montreal) in 1982. Both his M.Sc. (in Mathematics) and PhD (for the thesis *Contributions to Study of Instabilities in a Class of Conservative Systems*) were obtained from the University of Toronto. Professor Guran served as associate editor of the *International Journal of Modeling and Simulation* during 1993-95. He also served as guest editor of the special issue of *Technische Mechanik* dedicated to advances in theoretical and applied mechanics, and the special issue of *Meccanica* dedicated to Mechatronics. He has written a number of books. His book *Theory of Elasticity for Scientists and Engineers* (2000) has been published by Birkhäuser.

Dr. Guran has chaired a number of international scientific conferences: the First International Symposium on Impact and Friction of Solids, Structures and Intelligent Machines (Ottawa Congress Center, 1998), the First International Congress on Dynamics and Control of Systems (Chateau Laurier in Ottawa, 1999), the First International Conference on Acoustics, Noise and Vibrations (McGill University, 2000), the First International Congress on Mechatronics (Johannes Kepler University of Linz, 2002), the Second International Congress on Mechatronics (Technical University of Graz, 2003), and the Third International Congress on Mechatronics (Czech Technical University, 2004). He is the founder and editor-in-chief of the series on Stability, Vibration and Control of Systems.

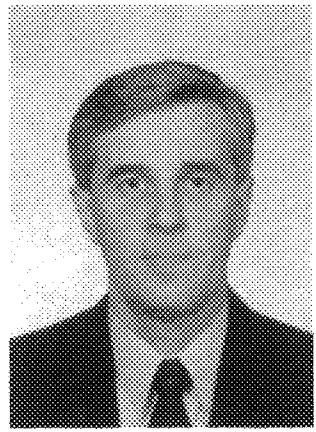

A. A. Kolyshkin was born in 1954 in Tallinn, Estonia. He graduated in applied mathematics from the Riga Technical University in Riga, Latvia, in 1976, and obtained his Ph.D. (Candidate in physics and mathematics) from Saint-Petersburg (then Leningrad) State University in 1981. In 1979–1980, he held a Research Fellowship in the Laboratory of Nondestructive Testing at the Riga Technical University. Since then he is with the Department of Engineering (formerly Applied) Mathematics of the Riga Technical University, as assistant in 1980–1983, senior lecturer in 1983–1990, associate professor in 1990–2002, and professor from 2002. From 1987 till 2003 he frequently visited the University of Ottawa and the Hong Kong University of Science and Technology as a visiting professor and a visiting researcher. He published more than 70 research papers. He co–authored, with M. Ya. Antimirov and R. Vaillancourt three monographs entitled "Applied Integral Transforms", "Mathematical Models in Eddy Current Testing", and "Complex Variables", published by AMS, CRM and Academic Press, respectively.

Irina Landman was born in St. Petersburg, USSR, in 1975. She graduated with honors in Applied Mathematics from St. Petersburg State University in 2000 and Concordia University, Montreal, Canada in Applied Science in 2001 under the supervision of E. M. Haseganu. She received a prize for an outstanding reasearch paper at SEECTAM XX Student Paper Competition in Alabama, USA.

Moyra McDill was born in Ottawa, Canada in 1956. She is Full Professor and Associate Chair (Undergraduate) in the Department of Mechanical and Aerospace Engineering in the Faculty of Engineering at Carleton University in Ottawa. She completed her Bachelor of Mechanical Engineering and her Master of Materials Engineering from Carleton University in 1979 and 1980 respectively. She worked during several years in the industry in Canada and then returned to Carleton where she completed her Ph.D. in Mechanical Engineering in 1988 with the thesis *An Adaptive Mesh-Management Algorithm for Three-Dimensional Finite Element Analysis.* Her research in the area of thermal-mechanical finite element analysis includes the development of several novel elements, adaptive techniques and constitutive modelling. She was a member of the Editorial Board of the Journal of Mathematical Modelling and Scientific Computing. In 1998 she received a Carleton University teaching award and a Students' Choice Best Professor Award. In 2000 and 2001 she was Associate Chair to the NSERC-NORTEL Joint Chair (Ontario) for Women in Science and Engineering. In 2002 she received a YMCA-YWCA Award as a Woman of Distinction in Ottawa for her contributions to engineering education. In 2002 she was also honoured by a Governor-in-Council appointment to the Canadian Nuclear Safety Commission.

Joseph Pegna received his Ph.D. from Stanford University. He is an Associate Professor and Canada Research Chair in Freeform Fabrication Laboratories of the Department of Mechanical Engineering, Manufacturing Division École Polytechnique de Montréal (Québec), Canada. Prof. Pegna's research involves free form fabrication, Rapid Prototyping/Rapid Manufacturing, testing computer-guided manufacturing techniques employing precision-injection technology and lasers, development of the next wave of industrial production tools. Joseph Pegna collaborated with the Angstrom Institute in Uppsala, Sweden.

Clare M. Rimnac received a B.S. in Metallurgy and Materials Science from Carnegie-Mellon University in 1978, and an M.S. in 1980 and a Ph.D. in 1983 in Metallurgy and Materials Engineering from Lehigh University. In 1983, she was a Research Fellow and from 1984 until 1996, she was a Scientist in the Department of Biomechanics at The Hospital for Special Surgery, in New York City. In 1996, Dr. Rimnac joined the faculty of the School of Engineering at Case Western Reserve University where she is currently an Associate Professor in the Departments of Mechanical and Aerospace Engineering and Orthopaedics. She is also Deputy Editor for Research for the Journal of Bone and Joint Surgery. Dr. Rimnac directs the Musculoskeletal Mechanics and Materials Laboratories at Case. Her research focuses on implant retrieval analysis, mechanical behavior and constitutive modeling of materials used in total joint replacements, and damage and fracture behavior of bone tissue. Her research is primarily funded by the NIH. Dr. Rimnac is the recipient of an AAOS Kappa Delta Award, the Hip Society Award, and the Knee Society Award.

Andrei L. Smirnov was born in Leningrad, USSR, in 1956. He is Associate Professor in the Department of Theoretical and Applied Mechanics of the Faculty of Mathematics and Mechanics and Senior Research Associate at the Laboratory of Applied Mechanics of the Institute of Mathematics & Mechanics at St. Petersburg State University (formerly Leningrad State University). He graduated in Applied Mathematics from the Leningrad State University in 1978 and obtained his Ph.D. in Mechanics of Solids from the same university in 1981 for the thesis: *Vibrations of the Rotating Shells of Revolution.* He is the author and/or the editor of 11 books including *Asymptotic Methods in Mechanics* (with R. Vaillancourt), *Asymptotic Methods in Problems and Examples* (with S. M. Bauer, S. B. Filippov and P. E. Tovstik) and *Asymptotic Methods in the Buckling Theory of Elastic Shells* (with P. E. Tovstik), *Asymptotic Methods in Mechanics of Solids* (with S. M. Bauer, P. E. Tovstik and S. B. Filippov), 2006, *Theory of Stability in Examples and Problems* (with S. M. Bauer), 2006, and papers on asymptotic and numerical methods in mechanics of thin structures published in *Transactions of the ASME*, *Transactions of the CSME*, *Technische Mechanik*, *Mechanics Research Communications*, *Vestnik Leningradskogo/Sankt-Peterburgskogo Universiteta*, *Review of industrial and Applied Mathematics* and other journals. He is a member of AMS.

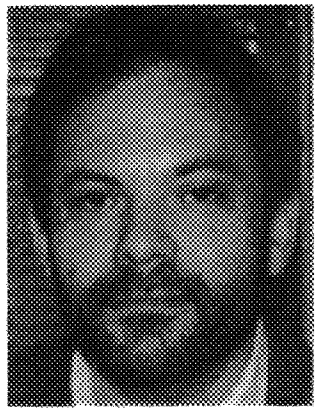

David J. Steigmann was born 25 October 1956 in Montreal, Canada. He obtained the B.Sc. degree from the University of Michigan, the M.Sc. from M.I.T. (both in Aerospace Engineering), and the Ph.D. from Brown University (in Engineering and Applied Mathematics). Following the Ph.D. he joined the faculty of the Department of Mechanical Engineering at the University of Alberta, Edmonton, and was subsequently promoted to Full Professor. Dr. Steigmann is currently Full Professor in the Department of Mechanical Engineering, UC Berkeley. His research is concerned with problems in continuum mechanics, shell theory, finite elasticity, variational methods, stability, surface stress, capillary phenomena, and the mechanics of thin films. He serves on the editorial boards of several journals including ZAMP, J. Elasticity, Int. J. Non-linear Mechanics, and Mathematics and Mechanics of Solids. He was Eliza Haseganu's dissertation advisor at Alberta.

Petr E. Tovstik was born in Leningrad, Russia, in 1935. He is presently Professor and Head of the Department of Theoretical and Applied Mechanics of the Faculty of Mathematics and Mechanics at St. Petersburg State University. He graduated in Applied Mathematics from St. Petersburg (Leningrad) State University in 1958, obtained his Ph.D. in Mechanics of Solids from the same university in 1963 and the degree of Doctor of Science in 1968 for the thesis: *Free Vibrations and the Stability of Thin Elastic Shells*. Prof. Petr Tovstik is a leading Russian specialist in the application of asymptotic methods in thin shell and plate theory. He is the author of 9 books including *Stability of Thin Shells*, *Free Vibrations of Thin Elastic Shells* (with A. L. Goldenveiser and V. B. Lidsky), *Asymptotic Methods in the Buckling Theory of Elastic Shells* (with A. L. Smirnov), *Asymptotic Methods in Mechanics of Solids* (with S. M. Bauer, S. B. Filippov, and A. L. Smirnov), and numerous papers on asymptotic methods in mechanics of thin structures published in *Doklady of the Academy of Science of the USSR*, *Mechanics of Solids*, *Transactions of the CSME*, *Differential Equations*, *Soviet Applied Mathematics*, *Technische Mechanik* and many other journals. He received the First Prize for Research at St. Petersburg (Leningrad) State University in 1970 and in 2004. In 1999 he got the highest scientific award in Russia, the State Prize. He is a member of the National Committee on Theoretical and Applied Mechanics and the editor of the journal *Vestnik Sankt-Peterburgskogo Universiteta*, series *Mathematics, Mechanics, Astronomy*. He is a member of AMS.

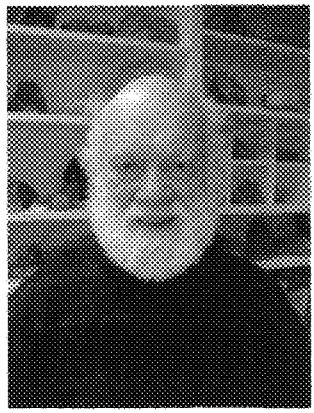

Rémi Vaillancourt was born in 1934 in Maniwaki, Québec, Canada. He took several bachelor's and master's degrees at the University of Ottawa, Ontario, Canada, and his Ph.D. under the direction of P. D. Lax and K. O. Friedrichs at the Courant Institute of Mathematical Sciences at New York University in 1969. He held an Office of Naval Research Fellowship at the University of Chicago where he worked under the direction of A. P. Calderón in 1960–1970. He is known for the Yamanugi–Nogi–Vaillancourt pseudo-difference operators and the Calderón–Vaillancourt theorem for non-classical pseudodifferential operators. Since 1970 he is with the department of Mathematics and jointly, since 1974, with the department of Computer Science at the University of Ottawa. He served as chairman of the former department in 1972–1976, as vice-president, president and past-president of the Canadian Mathematical Society in 1975–1981, and as chairman of the Canadian National Committee for the International Mathematical Union in 1979–1988. He collaborates with many mathematicians worldwide. His mathematical hobby is writing reviews for *Mathematical Reviews* and *Zentralblatt für Mathematik*. His home page is http://www.site.uottawa.ca/~remi

Inta Volodko was born in 1965 in Kraslava, Latvia. She graduated in applied mathematics from the Latvian State University in Riga, Latvia, in 1988, and obtained her Ph.D from the Latvian University in 1995. Since 1992 she has been with the Department of Engineering (formerly Applied) Mathematics of the Riga Technical University, as assistant in 1992–1996, lecturer in 1996–1998, assistant professor in 1998–2003 and associate professor from 2003. She also holds a position of assistant professor at the Latvian Agricultural University. Since 2002 she is the Head of the Department of Engineering Mathematics of the Riga Technical University. She published more than 20 papers. At present she is a Member of the Board of the Latvian Mathematical Society.

Jun Tonny Zhu was born in 1974. He got the degree of Bachelor on Mechatronics from Nanjing University of Science & Technology, China and Master's degree with major in Free Form Fabrication from Ecole Polytechnique de Montréal, when working as a Research Assistant at Freeform Fabrication Laboratories of the Department of Mechanical Engineering, Manufacturing Division Ecole Polytechnique de Montréal (Québec), Canada. At the present time he is a tool & die designer.

INDEX

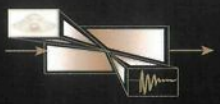

SERIES ON STABILITY, VIBRATION AND CONTROL OF SYSTEMS

Series B

Volume 15

Founder & Editor

Ardéshir Guran

Co-Editors

M. Cloud

W. B. Zimmerman

Advances in Mechanics of Solids

In Memory of Prof. E. M. Haseganu

The contributions in this volume are written by well-known specialists in the fields of mechanics, materials modeling and analysis. They comprehensively address the core issues and present the latest developments in these and related areas. In particular, the book demonstrates the breadth of current research activity in continuum mechanics. A variety of theoretical, computational, and experimental approaches are reported, covering finite elasticity, vibration and stability, and mechanical modeling. The coverage reflects the extent and impact of the research pursued by Professor Haseganu and her international colleagues.

25 World Scientific Years of Publishing 1981 – 2006

6161 hc

ISBN 981-256-867-0

9 789812 568670

www.worldscientific.com